Electronic magnetism in correlated systems: from quantum materials down to Earth's core

Dissertation zur Erlangung des
naturwissenschaftlichen Doktorgrades der
Julius-Maximilians-Universität Würzburg

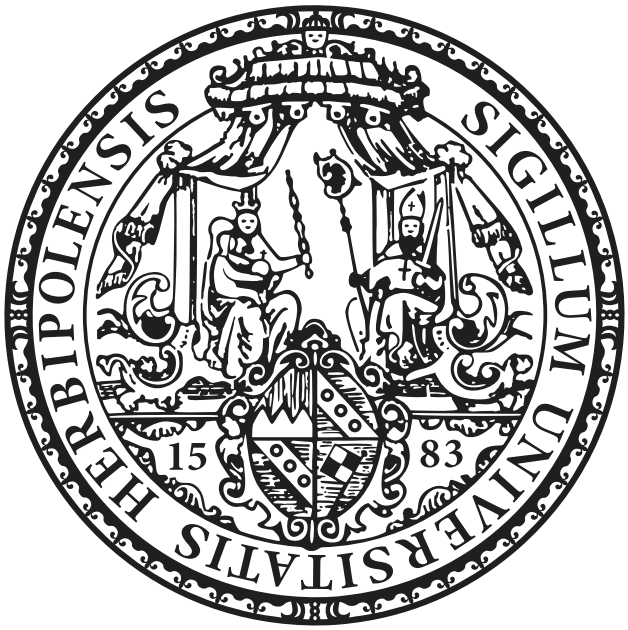

vorgelegt von
Andreas Hausoel
aus
Neumarkt in der Oberpfalz

Würzburg, 2022

Eingereicht am 20.11.20
bei der Fakultät für Physik und Astronomie

1. Gutachter: Prof. Dr. Giorgio Sangiovanni
2. Gutachter: Prof. Dr. Fakher Assaad
3. Gutachter:
der Dissertation

Vorsitzende(r):

1. Prüfer:
2. Prüfer:
3. Prüfer:
im Promotionskolloquium

Tag des Promotionskolloquiums:
Doktorurkunde ausgehändigt am:

Abstract

In the last decade continuous-time quantum Monte Carlo in the hybridization expansion (CTHYB) was one of the most successful Monte Carlo techniques to describe correlated quantum phenomena in conjunction with dynamical mean field theory (DMFT). The first part of the thesis consists of algorithmical developments regarding CTHYB and DMFT. I provide a complete derivation and an extensive discussion of the expansion formula. We generalized it to treat spin-orbit coupling, and invented the superstate sampling algorithm to make it efficient enough for describing systems with general interactions, crystal fields and spin-orbit coupling at low temperatures.

But CTHYB is known to fail in the standard implementation for equal-time correlators, certain higher-order Green's functions and the atomic limit; we discovered that its estimator for the Greens function is also inconsistent for Anderson impurities with finite, discrete baths. I focus then on further improvements of CTHYB that we have conceived and worked on, in particular for f-orbitals and for taking physical symmetries into account in the calculation of the Monte Carlo observables.

The second part of the thesis presents selected physical applications of these methods. I show DMFT calculations of highest accuracy for elemental iron and nickel and discover a new mechanism of magnetic ordering in nickel: the ordering of band structure-induced local moments. Then we analyze the stability of this phenomenon under pressure and temperatures, that characterize in the Earth's core. We find, that the mechanism survives these conditions and may give a significant contribution to the generation of the Earth's magnetic field. The next topic is the stability of double Dirac fermions against electronic correlations. We find, that the Coulomb interaction in the corresponding material Bi_2CuO_4 are strong enough to destroy the double Dirac cone, and substantial uniform pressure is necessary to restore them. In the last chapter I derive the properties of Higgs and Goldstone bosons from Ginzburg-Landau theory, and identify these excitations in a model of an excitonic magnet.

Zusammenfassung

Im letzten Jahrzehnt war die zeitkontinuierliche Hybridisierungsentwicklung (CTHYB) eine der erfolgreichsten Quanten Monte Carlo Methoden zur Behandlung stark korrelierter Elektronensysteme im Zusammenspiel mit der dynamischen Molekularfeldtheorie (DMFT). Im ersten Teil der Dissertation geht es um Algorithmenentwicklung bezüglich CTHYB und DMFT. Ich leite die CTHYB-Entwicklungsformel vollständig her und diskutiere ausführlich ihre Eigenschaften. Wir haben sie im Rahmen der Thesis für die Behandlung von Spin-Bahn gekoppelten Systemen verallgemeinert, und den Superstate-Sampling Algorithmus entwickelt, der unsere Implementation effizient genug macht, dass man Rechnungen mit allgemeinen Wechselwirkungen, Kristallfeldern und Spin-Bahn Kopplung bei tiefen Temperaturen effizient durchführen kann.

Es ist bekannt, dass CTHYB in der Standard-Implementation für Gleichzeit-Korrelationsfunktionen, bestimme Greenfunktionen höherer Ordnung und den atomaren Limes nicht funktioniert; wir haben entdeckt, dass der Standard-Estimator für die Greensche Funktion auch inkonsistent ist für Anderson-Störstellen mit endlich großem, diskretem Bad. Dann betrachte ich auch andere Verbesserungen von CTHYB, die wir uns ausgedacht haben, insbesondere für die Behandlung von Systemen mit f-Orbitalen, und wie man physikalische Symmetrien bei der Berechnung von Observablen bei CTHYB mit einbeziehen kann.

Im zweiten Teil der Arbeit präsentiere ich ausgewählte physikalische Anwendungen dieser Methoden. Ich zeige DMFT-Rechnungen mit größtmöglicher Präzision für die elementaren Metalle Eisen und Nickel, wobei wir einen neuartigen Mechanismus entdeckt haben, der in Nickel die magnetische Ordnung erzeugt: es ordnen sich lokale magnetische Momente, die von der Bandstruktur erzeugt worden sind. Dann untersuchen wir die Stabilität des Phänomens unter hohem Druck und hoher Temperatur, wie sie typischerweise im Erdkern herrschen. Wir finden, dass der Mechanismus diese Bedingungen übersteht und es denkbar ist, dass er einen signifikanten Beitrag zur Erzeugung des Magnetfelds der Erde liefert. Das nächste Beispiel ist, wie sich elektronische Korrelationseffekte auf doppel-Dirac Fermionen auswirken. Wir finden, dass die elektronische Wechselwirkung die doppel-Dirac Cones in Bi_2CuO_4 zerstört, und nur enormer hydrostatischer Druck sie wiederherstellen kann. Im letzten Kapitel leite ich die Eigenschaften von Higgs- und Goldstone-Bosonen mithilfe der Ginzburg-Landau Theorie her, und identifiziere dann diese Anregungen im Modell eines exzitonischen Magneten.

Man muss noch Chaos in sich haben!
(Friedrich Nietzsche)

Contents

Chapter 1

Introduction

The year 2019 may be remembered as that point in the history of computation, where a quantum computer for the first time gained supremacy over the most powerful existing classical computer (Arute et al., 2019). It uses the ability for superposition of quantum mechanical objects to perform a calculation for several inputs in parallel, whereas the classical computer has to calculate each input separately.

Another fascinating machine is the quantum simulator, which uses a very clean and well known reference quantum system, to gain access to properties about another quantum system of interest.

Two main features make quantum mechanics a very difficult task for classical computers. First, there is an exponential growth of the Hilbert space with regard to the size of the considered system. This alone was not a serious problem; but second, together with the anticommutation of the fermionic constituents, which equip half of the Hilbert space with a negative sign, it is impossible for Monte Carlo algorithms to pick out the important contributions. These two aspects together are believed to constitute a problem of non-polynomial complexity (Troyer and Wiese, 2005).

However, with current technology, it is also very delicate to build large quantum machines, because for performing the calculation and reading out the result, they have to be screened from all environmental perturbances and accessed in a very controlled way. There seems to be an exponential barrier as well. It is still true today, what physicists have said during the 1930s: "The Gods have set a limit for human drive to knowledge by the quantum mechanical many-body problem!".

A promising way towards quantum machines is trying to understand the properties of quantum matter to the point that one can make substantial steps forward in building hardware for quantum computers. For this however we rely on classical computation, which calls for heavy approximations and has many limitations at the moment. My thesis tries to contribute to the development of these methods, especially the dynamical mean field theory and quantum Monte Carlo.

The main physical subject of the thesis are emergent phenomena. Systems with many mutually interacting particles show fundamentally different behavior compared to the independent combination of the properties of the single particles. What emerges is not exactly definable, since the zoo of phenomena is species-rich and diverse. It is illuminating to collect some examples.

- The "classical" example is magnetism. Elementary magnets do not favor a specific orientation, but coupled together, they can give rise to spontaneous symmetry breaking and phase transitions to ferro-, anti-ferro, ferri-, anti-ferri and many other states. There exist analytically solvable models like the Ising model, or mathematically perfectly treatable models like the Heisenberg model. Many of these cases represent very well understood phenomena.

- Chrome-nickel-steel has a tensile strength greater than the sum of the tensile strengths of each of all its alloyed components together (Buckminster Fuller, 1969).
- Two humans (even though emergent phenomena on their own) have a conversation. Their interaction leads them to topics and conclusions, which they on their own never would be able to reach. A social emergent phenomenon.
- Furthermore there is right now a major change in the structure of society: we do not trust and listen to classical media any more, like TV or radio; instead we listen to each other via social media. This makes society a interacting many-body problem, that tends to show unpredictable emergent behavior.

Another feature of emergent phenomena is, that often two things compete against each other. The main model of this thesis is the Hubbard model and describes interacting electrons moving on a discrete lattice. Its playground is the competition of kinetic and potential energy. It has two simple limit. Around the non-interacting limit, the potential energy due to the interaction is so small, that they barely influence the properties of the freely moving electrons. Around the atomic limit, the electrons are localized on the sites and move so rarely, that they do not perturb the atomic properties significantly. In between there is the intermediate-coupling regime, which usually has a rich phase diagram of different states of matter, of which many are fundamentally different compared to analytically known or numerically calculable states of matter. Furthermore they sensitively depend on the external parameters: strength of the electron-electron interaction, crystal structure, crystal fields and spin-orbit coupling, filling and temperature.

The scope of the thesis is the following. The *first part* is about algorithmics. In **Chapter 2** I introduce the models and numerical methods which are used. In **Chapter 3** I discuss the continuous time quantum Monte Carlo method in hybridization expansion, before in **Chapter 4** I show one of its inadequacies that we discovered towards the end of my PhD studies. **Chapter 5** introduces the main approximation, the dynamical mean field theory, whereas in **Chapter 6** I discuss symmetry constraints, which dynamical mean-field and quantum Monte Carlo results have to fulfill. The *second part* shows selected physical applications. **Chapter 7** discusses the effects of electron-electron interactions on unconventional particles sharing the example of double Dirac fermions. In **Chapter 8** I introduce the Ginzburg-Landau theory for Higgs- and Goldstone-modes, and show their existence in an excitonic magnet, which is a Bose-Einstein condensate of excitons. In **Chapter 9** we solved a long standing riddle about elemental iron and nickel, and discovered a novel mechanism of magnetic ordering, which we called band-structure induced correlations.

Chapter 2

From the theory of everything to models and solutions

In the first part of this chapter I introduce the many-body Schrödinger equation (MBSGL) and discuss, to what extent statements about phenomena of our everyday world can be made on the basis of this equation.

The MBSGL can be treated in two distinctly different ways. First there are the *ab initio* methods around density functional theory. Second one can construct a *model*, which is a much simpler Hamiltonian that (hopefully) contains the essential processes to describe the phenomenons of interest, quantitatively if possible, or only qualitatively.

The main physical interest of this thesis is *correlated emergent* physics, i.e. properties of macroscopic systems which are not already properties of its microscopic constituents. Therefore I will not discuss DFT or how it connects to many-body methods, but only focus on the models of interest, the *Hubbard model* and the *Anderson impurity model*.

The second part of this chapter gives an overview of the methods used in this thesis to deal with these models of strong correlations. In order to obtain information about a quantum mechanical system, we must interact with the system and extract or add a particle to it.

Everything about the particle-in particle-out processes is contained the *Green's functions*. I explain the main framework used in this thesis to calculate Green's functions for the Hubbard model, the dynamical mean field theory. It treats the time domain in an exact way and applies a mean field approximation to the space. To solving the Anderson impurity model is devoted the much more detailed chapter 2. Finally I discuss the rather technically difficult analytic continuation of imaginary times Green's functions.

2.1 From the theory of everything to models

2.1.1 The theory of everything

Let's start with the microscopic *theory of everything*, the Hamiltonian of the many-body Schrödinger equation:

$$H_{\mathrm{TOE}} = -\sum_i \frac{\hbar^2}{2m}\boldsymbol{\nabla}_i^2 + \sum_i v^{\mathrm{ion}}(\boldsymbol{r}_i) + \sum_{i<j} \frac{e^2}{|\boldsymbol{r}_i - \boldsymbol{r}_j|}. \tag{2.1}$$

Electrons with charge $-e$ and mass m are located at positions $\boldsymbol{r}_i$ in space. They interact with each other according to Coulomb's law and move in the potential

$$v^{\text{ion}}(\boldsymbol{r}) = -\sum_I \frac{Z_I e^2}{|\boldsymbol{R}_I - \boldsymbol{r}|} \tag{2.2}$$

of lattice ions with charge $+Ze$. The interactions between the atomic nuclei are not included, instead their positions are kept fixed at positions $\boldsymbol{R}_I$ (Born-Oppenheimer approximation). According to non-relativistic quantum mechanics, the many-body wave function is obtained by solving the Schrödinger equation

$$i\hbar\frac{\partial}{\partial t}\left|\psi(\boldsymbol{r}_1, \boldsymbol{r}_2, \dots)\right\rangle = H_{\text{TOE}}\left|\psi(\boldsymbol{r}_1, \boldsymbol{r}_2, \dots)\right\rangle. \tag{2.3}$$

The expectation value of every static (time-independent) observable A can be computed via $\langle A\rangle = \langle\psi| A |\psi\rangle$.

With the solution of Eq. (2.3) it is in principle possible to calculate any desired observable, i.e. property of the physical system. But even for the smallest systems, a direct calculation of $|\psi\rangle$ is not possible. Let's take a single iron atom with 26 electrons. The wave function has 26 arguments, 3 dimensional each, i.e. 96 scalar arguments in total: $|\psi(\boldsymbol{r}_1, \boldsymbol{r}_2, ..., \boldsymbol{r}_{26})\rangle$. A very rough discretization of 10 values per dimension would give this function 10^{96} values, which is approximately equal the number of atoms in the universe (following Koch (2019)).

This was already foreseen in 1929 by Paul Dirac, that these equations are way too difficult to be solved exactly for any reasonable system. He asked for approximate practical methods to be developed, to gain access to the main features of complex quantum systems.

2.1.2 The reductionist hypothesis

The belief, that everything is encoded in underlying microscopic principles, here the many-body Schrödinger equation, is called the reductionist hypothesis. It is accepted by many scientists without question, that much of the animate and inanimate matter is controlled by Eq. (2.1): air, water, rocks, fire, people, the Coronavirus and so forth (Laughlin and Pines, 2000). Some important things like the existence of the planet Jupiter, nuclear power plants, the sun, and the curvature of space are not included in this equation, since gravity and inner-nuclear interactions are missing.

However the reductionist hypothesis does absolutely not imply a "constructionalist" one: The ability to reduce everything to fundamental laws does not imply the ability to start from those laws and reconstruct the universe (Anderson, 1972).

For example simple electrical measurements performed on superconducting rings determine to high accuracy the quantum of magnetic flux $hc/2e$. Four point conductance measurements on semiconductors in the quantum Hall regime accurately determine the quantity e^2/h. The magnetic field generated by a superconductor that is mechanically rotated, measures e/mc. These things are clearly true, yet they cannot be deduced by direct calculation from the theory of everything, because exact results cannot be predicted by approximate calculations (Laughlin and Pines, 2000).

2.1.3 The Hubbard model

A strategy opposite to applying approximations to the many-body Schrödinger equation is to build models that capture some physics of interest, and leave out other physics that is considered not to be important.

Transition metals and rare earth compounds have partially filled d- and f-orbitals besides also partially filled bands from s- and p-orbitals. Their behavior is in between that of a band model and that of an atomic model. For example, spin-waves in ferromagnets or the strong temperature dependence of the magnetic susceptibility in transition metals are atomic properties. In the same systems are non-integer magnetic moments (in units of Bohr magnetons), which are typical band properties. The desired model therefore must find the correct balance between atomic and band properties, and recover both cases in the appropriate limits. This was achieved by Hubbard (1963) by introducting the Hubbard model

$$H_{\text{Hubbard}} = -\sum_{ij\sigma} t_{ij} c^\dagger_{i\sigma} c_{j\sigma} + \text{H.c.} + \sum_i U n_{i\uparrow} n_{i\downarrow}, \tag{2.4}$$

here written down for one orbital. It consists of a lattice with discrete sites i. The operators $c^\dagger_{i\sigma}$ ($c_{i\sigma}$) create (annihilate) an electron on site i with spin σ, the density operators $n_{i\sigma}$ measure the occupation of the according site and spin. The first term is the kinetic energy, where electrons hop from site i to j with amplitude $-t_{ij}$. In the standard Hubbard model, there is only next nearest neighbor hopping, i.e. $t_{ij} = 0$ if i and j are not next nearest neighbors. The energy U that has to be paid, whenever a site is doubly occupied. The first term alone is the non-interacting limit, which is diagonal in momentum space, and the second term the atomic limit, which is diagonal in real space. However with both terms together, the model is currently not believed to be analytically solvable in general. An exception is the limiting case of a model with next-nearest neighbor hopping only in one spatial dimension. Then a crucial characteristic of quantum mechanics, the indistinguishability of particles, is absent. The leftmost electron of spin up can never bypass the second leftmost of spin up due to Pauli's principle, and so forth, which means they can be labeled just like classical particles. This makes an exact solution possible with the Bethe-ansatz (Lieb and Wu, 1994), and also numerical techniques are much more efficient in one dimension, compared to higher dimensions.

The Hubbard model (2.4) intrinsically contains many approximations in comparison to the many-body Schrödinger equation (2.3). The movement of the electrons has been discretized, they can only be on the sites and not in between sites. The far reaching Coulomb potential has been replaced by a delta function, i.e. only interactions on the same site are considered; the interaction energy of electrons further apart is neglected. Also the interplay of conduction orbitals with lower-lying valence orbitals is neglected in the single-orbital Hubbard model.

This thesis mainly deals with the multi-orbital Hubbard model, where each site has additional orbital degrees of freedom, or even consists of several atoms; these are much more complicated and will be discussed in Chapter 5.

2.1.4 The Anderson impurity model

Also very important in solid state physics is the Anderson impurity model (Philip Warren Anderson, 1961):

$$H_{\text{AIM}} = \sum_{\boldsymbol{k}\sigma} \epsilon_{\boldsymbol{k}\sigma} a^\dagger_{\boldsymbol{k}\sigma} a_{\boldsymbol{k}\sigma} + \sum_{\boldsymbol{k}\sigma} V_{\boldsymbol{k}\sigma} \left(c^\dagger_\sigma a_{\boldsymbol{k}\sigma} + a^\dagger_{\boldsymbol{k}\sigma} c_\sigma \right) + U n_\uparrow n_\downarrow. \tag{2.5}$$

The operators $a^\dagger_{\boldsymbol{k}\sigma}$ ($a_{\boldsymbol{k}\sigma}$) create (annihilate) electrons in a non-interacting conduction band with the dispersion $\epsilon_{\boldsymbol{k}\sigma}$. The operators $c^\dagger_\sigma$ (c_σ) create (annihilate) electrons with spin σ on the impurity, and $n_\sigma = c^\dagger_\sigma c_\sigma$ measures the number of electrons of spin σ on the impurity. $V_{\boldsymbol{k}\sigma}$ is the amplitude of an electron hopping from the impurity in the bath and vice versa, and U the strength of the electron-electron interaction on the impurity. The AIM is used to describe properties of doping

atoms in metallic hosts, like the formation of localized magnetic moments and their screening by conduction electrons, the Kondo effect (Kondo, 1964). It is also used as auxiliary model, as described in the next section.

For the scope of this thesis, a generalized AIM is necessary, which has multi-orbital structure and manifold hopping and interaction processes on the impurity. The generalized AIM and its treatment will be topic of Chapter 3.

2.2 From models to solutions

In this section I discuss, what we mean by saying to solve a model, namely to calculate its Green's function. I introduce Green's functions, derive some of their basic properties and show the main approximation used in this thesis to calculate them, the dynamical mean field theory. I close by commenting on the connection between Green's and spectral functions.

2.2.1 Green's functions

The Green's function in many-body physics

$$G_{\alpha\beta}(\boldsymbol{r},t;\boldsymbol{r}',t') = -i\left\langle T_t c_\alpha(\boldsymbol{r},t)c^\dagger_\beta(\boldsymbol{r}',t')\right\rangle \tag{2.6}$$

describes the amplitude of a process, where an electron is created in the system at $(\boldsymbol{r}',t')$. It propagates through the system and interacts with it, before it is removed again at $(\boldsymbol{r},t)$. The Greek indices denote an abbreviation of orbital and spin quantum numbers. For zero temperature the average goes only over the ground state, whereas for finite temperature a complete many-body basis needs to be considered

$$\langle ...\rangle = \begin{cases} \langle 0|\ ...\ |0\rangle & \text{for} \quad T=0 \\ \frac{1}{Z}\mathrm{Tr}\left[\mathrm{e}^{-\beta H}\right] & \text{for} \quad T>0. \end{cases} \tag{2.7}$$

Eq. (2.6) is the time-ordered Green's function, i.e. the order of the times is such that the operator of lesser time stands on the right side

$$T_t c_\alpha(t)c^\dagger_\beta(t') = \begin{cases} c_\alpha(t)c^\dagger_\beta(t') & t'<t \\ -c^\dagger_\beta(t')c_\alpha(t) & t<t', \end{cases} \tag{2.8}$$

where a minus sign appears if we are considering fermionic creation and annihilation operators.

When there is translational invariance in space, e.g. no boundaries or defects, G only depends on the differences of the spacial coordinates; When there is translational invariance in time, e.g. an equilibrium system and no explicit time dependence of the Hamiltonian, then G only depends on differences in time (Rohringer, 2013):

$$G_{\alpha\beta}(\boldsymbol{r},t;\boldsymbol{r}',t') \to G_{\alpha\beta}(\boldsymbol{r}-\boldsymbol{r}',t-t') = G_{\alpha\beta}(\boldsymbol{r},t). \tag{2.9}$$

Let's now discuss the time evolution:

$$\begin{aligned} G_{\alpha\beta}(\boldsymbol{r},t) &= -\frac{i}{Z}\mathrm{Tr}\left[\mathrm{e}^{-\beta H}T_t c_\alpha(\boldsymbol{r},t)c^\dagger_\beta(0,0)\right] \\ &= -\frac{i}{Z}\mathrm{Tr}\left[\mathrm{e}^{-\beta H}T_t \mathrm{e}^{iHt}c_\alpha(\boldsymbol{r})\mathrm{e}^{-iHt}c^\dagger_\beta(0)\right]. \end{aligned} \tag{2.10}$$

Combining the statistical weight and the time-evolution of the operators in Eq. (2.10) implies a time-evolution with a complex time argument $\tilde{t} = -\beta + it$. This causes complications in calculations. If one wanted to make an expansion of this object, one needed a two-dimensional expansion in time and temperature. Sampling this with a Markov chain gives a disastrous sign problem for two reasons. First, the imaginary time evolution is oscillating and therefore after a certain time one arrives at a state with same amplitude and opposite phase. Second, in two dimensions a random walker has many possibilities to make loops, go back to its starting point, but collect up a change in sign.

In 1955 Takeo Matsubara introduced his (in?)famous technique to fold together the two dimensions of time and temperature into one dimension, the imaginary time. This is formally done by the substitution $t \to -i\tau$, which makes the time-evolutions a real exponential

$$\mathrm{e}^{(-\beta+it)H} \to \mathrm{e}^{(-\beta+\tau)H}, \tag{2.11}$$

yielding the imaginary time Green's function

$$G_{\alpha\beta}(\boldsymbol{r},\tau) = -\left\langle T_\tau c_\alpha(\boldsymbol{r},\tau) c^\dagger_\beta(0,0)\right\rangle. \tag{2.12}$$

At first sight, this looks like simplifying things a lot, but as one might guess, a simple substitution cannot resolve problems of dealing with heavy oscillations of the time evolutions over all time scales. The Matsubara construction shifted the problem to the process of unfolding time and temperature after a calculation. This is necessary, since the physical response functions live on the real time or frequency axis. Unfolding is easy for analytic expressions (just apply the inverse substitution at any time), it is stable for deterministic techniques like exact diagonalization because of very precise data, but it is highly unstable and an unsolved problem for stochastic methods with slowly converging error bars (see more in section 2.2.4).

There are restrictions for the imaginary time τ. Assume $\tau > 0$, then

$$\mathrm{Tr}\left[\mathrm{e}^{-\beta H}\mathcal{T}_\tau \mathrm{e}^{H\tau} c_\alpha \mathrm{e}^{-H\tau} c^\dagger_\beta\right] = \frac{1}{Z}\sum_n \mathrm{e}^{-(\beta-\tau)E_n}... \tag{2.13}$$

Since we have fermions, we can assume the system's energy spectrum to be bound from below and set its ground state energy to zero. For this object to be convergent for any infinite system, the exponent must stay negative, which means $\tau < \beta$. Equivalently must for $\tau < 0$ the object

$$\mathrm{Tr}\left[\mathrm{e}^{-\beta H}\mathcal{T}_\tau \mathrm{e}^{H\tau} c_\alpha \mathrm{e}^{-H\tau} c^\dagger_\beta\right] = -\mathrm{Tr}\left[\mathrm{e}^{-\beta H} c^\dagger_\beta \mathrm{e}^{H\tau} c_\alpha \mathrm{e}^{-H\tau}\right] \tag{2.14}$$

$$= -\frac{1}{Z}\sum_n \mathrm{e}^{-\tau E_n}\mathrm{e}^{-\beta E_n}... \tag{2.15}$$

$$= -\frac{1}{Z}\sum_n \mathrm{e}^{-(\beta+\tau)E_n}... \tag{2.16}$$

be convergent, therefore $\tau > -\beta$. Overall the imaginary time Green's function is only defined in the interval

$$-\beta < \tau < \beta. \tag{2.17}$$

From the cyclicity of the trace follows (assume $\tau < 0$ here)

$$G_{\alpha\beta}(\tau) = \frac{1}{Z}\mathrm{Tr}\left[\mathrm{e}^{-\beta H}c_\beta^\dagger(0)c_\alpha(\tau)\right] \tag{2.18}$$
$$= \frac{1}{Z}\mathrm{Tr}\left[\mathrm{e}^{-\beta H}c_\beta^\dagger(0)\mathrm{e}^{H\tau}c_\alpha(0)\mathrm{e}^{-H\tau}\right] \tag{2.19}$$
$$= \frac{1}{Z}\mathrm{Tr}\left[\mathrm{e}^{H\tau}c_\alpha(0)\mathrm{e}^{-H\tau}\mathrm{e}^{-\beta H}c_\beta^\dagger(0)\right] \tag{2.20}$$
$$= \frac{1}{Z}\mathrm{Tr}\left[\mathrm{e}^{-\beta H}\mathrm{e}^{\beta H}\mathrm{e}^{H\tau}c_\alpha(0)\mathrm{e}^{-H\tau}\mathrm{e}^{-\beta H}c_\beta^\dagger(0)\right] \tag{2.21}$$
$$= \frac{1}{Z}\mathrm{Tr}\left[\mathrm{e}^{-\beta H}c_\alpha(\tau+\beta)c_\beta^\dagger(0)\right] \tag{2.22}$$
$$= -G_{\alpha\beta}(\tau+\beta). \tag{2.23}$$

This together with Eq. (2.17) allows one to study $G(\tau)$ in half of the interval. When having imaginary time objects, I will usually look at $[0,\beta]$.

The diagonal Green's function has a discontinuity at $\tau = 0$ of size one

$$G_{\alpha\alpha}(\tau = 0^-) = \left\langle c_\alpha(0)c_\alpha^\dagger(0^-)\right\rangle = n \tag{2.24}$$
$$G_{\alpha\alpha}(\tau = 0^+) = -\left\langle c_\alpha^\dagger(0^+)c_\alpha(0)\right\rangle = -1+n. \tag{2.25}$$

The values close to but smaller than β are

$$G_{\alpha\alpha}(\tau = \beta^-) = -G_{\alpha\alpha}(\tau = 0^-) \tag{2.26}$$
$$= \left\langle c_\alpha(0)c_\alpha^\dagger(0^-)\right\rangle = n. \tag{2.27}$$

From these follow the relation

$$G_{\alpha\beta}(0^+) + G_{\alpha\beta}(\beta^-) = \delta_{\alpha\beta}. \tag{2.28}$$

Since $G(\tau)$ is defined on a finite interval only, a well-behaved Fourier transform can be obtained by periodization over the full τ axis. Hence:

$$G(\boldsymbol{r}, i\omega_n) = \frac{1}{2}\int_{-\beta}^{\beta} \mathrm{d}\tau\; G(\boldsymbol{r},\tau)\mathrm{e}^{i\omega_n\tau} \tag{2.29}$$
$$G(\boldsymbol{r},\tau) = \frac{1}{\beta}\sum_n G(\boldsymbol{r}, i\omega_n)\mathrm{e}^{-i\omega_n\tau}. \tag{2.30}$$

Here the integration goes over the full interval $[-\beta,\beta]$ and we still have the unrestricted frequencies $\omega_n = \frac{2\pi}{2\beta}n$. Because of the analytic property $G(\tau) = -G(\tau+\beta)$ the full information is already contained in half the interval, therefore the integration can be rewritten such that it goes over $[0,\beta]$ only, together with a restriction for the frequencies:

$$G(\boldsymbol{r}, i\omega_n) = \frac{1}{2}\int_{-\beta}^{\beta} \mathrm{d}\tau\; G(\boldsymbol{r},\tau)\mathrm{e}^{i\omega_n\tau} \tag{2.31}$$
$$= \frac{1}{2}\int_{-\beta}^{0} \mathrm{d}\tau\; G(\boldsymbol{r},\tau)\mathrm{e}^{i\omega_n\tau} + \frac{1}{2}\int_{0}^{\beta} \mathrm{d}\tau\; G(\boldsymbol{r},\tau)\mathrm{e}^{i\omega_n\tau} \tag{2.32}$$
$$= -\frac{1}{2}\int_{-\beta}^{0} \mathrm{d}\tau\; G(\boldsymbol{r},\tau+\beta)\mathrm{e}^{i\omega_n\tau} + \frac{1}{2}\int_{0}^{\beta} \mathrm{d}\tau\; G(\boldsymbol{r},\tau)\mathrm{e}^{i\omega_n\tau} \tag{2.33}$$
$$= -\frac{1}{2}\int_{0}^{\beta} \mathrm{d}\tau'\; G(\boldsymbol{r},\tau')\mathrm{e}^{i\omega_n\tau'}\mathrm{e}^{i\omega_n\beta} + \frac{1}{2}\int_{0}^{\beta} \mathrm{d}\tau\; G(\boldsymbol{r},\tau)\mathrm{e}^{i\omega_n\tau} \tag{2.34}$$
$$= \frac{1}{2}\int_{0}^{\beta} \mathrm{d}\tau\; G(\boldsymbol{r},\tau)(1-\mathrm{e}^{i\omega_n\beta})\mathrm{e}^{i\omega_n\tau}. \tag{2.35}$$

In Eq. (2.32) the antiperiodic property was used. The fact that we have fermions manifests itself in the minus sign. In Eq. (2.33) a substitution $t' = t + \beta$ was done for the first integral. The bracket $(1 - \mathrm{e}^{i\pi/\beta n\beta}) = 1 - (-1)^n$ is 0 for n even, and 2 for n odd. Therefore the frequencies can be re-defined $\omega_n = (2n+1)\pi/\beta$ to match the standard definition for the fermionic Matsubara frequencies.

In summary, the Fourier transforms are as follows:

$$G_{\alpha\beta}(\boldsymbol{r}, i\omega_n) = \int_0^\beta \mathrm{d}\tau \; G_{\alpha\beta}(\boldsymbol{r}, \tau)\mathrm{e}^{i\omega_n\tau} \tag{2.36}$$

$$G_{\alpha\beta}(\boldsymbol{r}, \tau) = \frac{1}{\beta}\sum_n G_{\alpha\beta}(\boldsymbol{r}, i\omega_n)\mathrm{e}^{-i\omega_n\tau} \tag{2.37}$$

$$G_{\alpha\beta}(\boldsymbol{r}, \tau) = \frac{1}{(2\pi)^d}\int \mathrm{d}^d k \; G_{\alpha\beta}(\boldsymbol{k}, \tau)\mathrm{e}^{i\boldsymbol{k}\boldsymbol{r}} \tag{2.38}$$

$$G_{\alpha\beta}(\boldsymbol{k}, \tau) = \int \mathrm{d}^d r \; G_{\alpha\beta}(\boldsymbol{r}, \tau)\mathrm{e}^{-i\boldsymbol{k}\boldsymbol{r}} \tag{2.39}$$

For an extensive discussion of the many other types of Green's functions on the real axis, see the thesis of Ghanem (2017).

2.2.2 Fermi liquid theory

Often the strength of the Hubbard interaction U in metals is not small but rather of the order of the bandwidth W. Despite of that, the properties of such systems, as long as they stay metallic, can qualitatively be understood in terms of non-interacting calculations. Nevertheless numerical values of observables can become very different compared to the non-interacting ones. The non-interacting electrons become renormalized quasiparticles. Also the structure of the electronic excitations can be mapped onto the non-interacting ones. Since the quasiparticles are able to move, a Fermi surface exists and one can expand the self-energy around $\boldsymbol{k} \to \boldsymbol{k}_\mathrm{F}$ and $i\omega_n \to 0$:

$$\Sigma(\boldsymbol{k}, i\omega_n) \approx \underbrace{\mathrm{Re}\Sigma(\boldsymbol{k}_\mathrm{F}, i\omega_n \to 0)}_{\mu'} + \underbrace{\left.\frac{\partial \mathrm{Re}\Sigma(\boldsymbol{k}, i\omega_n \to 0)}{\partial \boldsymbol{k}}\right|_{\boldsymbol{k}\to\boldsymbol{k}_\mathrm{F}} (\boldsymbol{k} - \boldsymbol{k}_\mathrm{F})}_{\text{correction to } \epsilon_{\boldsymbol{k}}} \tag{2.40}$$

$$+ \underbrace{i\mathrm{Im}\Sigma(\boldsymbol{k}_\mathrm{F})}_{-i\gamma} + \underbrace{i\frac{\partial}{\partial i\omega_n}\Sigma(\boldsymbol{k}_\mathrm{F}, i\omega_n)\Big|_{i\omega_n\to 0} i\omega_n}_{-i\alpha\omega_n}. \tag{2.41}$$

The first term is a rigid shift μ' of the dispersion and is absorbed in the chemical potential. The second term is a correction to $\epsilon_{\boldsymbol{k}}$ linear in the wave vector $\boldsymbol{k}$. The third term $-i\gamma$ broadens the

levels and makes the lifetime of excitations finite. The effects caused by the fourth term will be clear in the following, after writing down the Fermi-liquid Green's function:

$$G(\boldsymbol{k}, i\omega_n) = \frac{1}{i\omega_n - \epsilon_{\boldsymbol{k}} - \Sigma(\boldsymbol{k}, i\omega_n)} \tag{2.42}$$

$$\approx \frac{1}{i\omega_n(1+\alpha) - \left(\frac{\partial \epsilon_{\boldsymbol{k}}}{\partial \boldsymbol{k}} + \frac{\partial \Sigma}{\partial \boldsymbol{k}}\right)_{\boldsymbol{k}\to\boldsymbol{k}_\mathrm{F}} (\boldsymbol{k} - \boldsymbol{k}_\mathrm{F}) + i\gamma} \tag{2.43}$$

$$= \frac{\frac{1}{1+\alpha}}{i\omega_n - \frac{1}{1+\alpha}\left(\frac{\partial \epsilon_{\boldsymbol{k}}}{\partial \boldsymbol{k}} + \frac{\partial \Sigma}{\partial \boldsymbol{k}}\right)_{\boldsymbol{k}\to\boldsymbol{k}_\mathrm{F}} (\boldsymbol{k} - \boldsymbol{k}_\mathrm{F}) + i\frac{1}{1+\alpha}\gamma} \tag{2.44}$$

$$= \frac{Z}{i\omega_n - Z\left(\frac{\partial \epsilon_{\boldsymbol{k}}}{\partial \boldsymbol{k}} + \frac{\partial \Sigma}{\partial \boldsymbol{k}}\right)_{\boldsymbol{k}\to\boldsymbol{k}_\mathrm{F}} (\boldsymbol{k} - \boldsymbol{k}_\mathrm{F}) + iZ\gamma} \tag{2.45}$$

$$= \frac{Z}{i\omega_n - \tilde{\epsilon}_{\boldsymbol{k}} + iZ\gamma} \tag{2.46}$$

In Eq. (2.45) the quasiparticle renormalization factor $Z = \frac{1}{1+\alpha} < 1$ has been introduced, and in Eq. (2.43) a renormalized and linearized dispersion $\tilde{\epsilon}_{\boldsymbol{k}}$.

In summary, the excitations of a non-interacting system around the Fermi level are particles of dispersion $\boldsymbol{v}_\mathrm{F}(\boldsymbol{k} - \boldsymbol{k}_\mathrm{F})$ and lifetime $\tau = \infty$. The low energy excitations of the Fermi liquid are quasi-particles with a dispersion of $\tilde{\epsilon}_{\boldsymbol{k}} = Z\left(\frac{\partial \epsilon_{\boldsymbol{k}}}{\partial \boldsymbol{k}} + \frac{\partial \Sigma}{\partial \boldsymbol{k}}\right)_{\boldsymbol{k}\to\boldsymbol{k}_\mathrm{F}} (\boldsymbol{k} - \boldsymbol{k}_\mathrm{F})$ and a finite life-time of $\tau = \frac{\hbar}{Z\gamma} < \infty$. In a non-interacting system the particles have the mass m_e of the electrons, whereas in the Fermi liquid they have an effective mass of

$$\frac{m^*}{m_e} = Z^{-1}\left[1 + \frac{m_e}{k_\mathrm{F}}\frac{\partial \Sigma}{\partial \boldsymbol{k}}\right] \geq 1. \tag{2.47}$$

Any Matsubara Green's function must have a definite high-frequency behavior of $\lim_{\omega_n\to\infty} G(i\omega_n) = 1/i\omega_n$ (Abrikosov et al., 2012). Therefore the Fermi-liquid expansion around the Fermi-level cannot be a full Green's function, since it has a high-frequency of $Z/i\omega_n$. Here we have only the coherent part of the Green's function with poles close to E_F. The incoherent part G^incoh with poles far away from ϵ_F and $\boldsymbol{k}_\mathrm{F}$ is missing, which is of course not contained in the Fermi-liquid expansion. Therefore:

$$G(\boldsymbol{k}, i\omega_n) = \frac{Z}{i\omega_n - \tilde{\epsilon}_{\boldsymbol{k}} + iZ\gamma} + (1-Z)G^\mathrm{incoh}(\boldsymbol{k}, i\omega_n) \tag{2.48}$$

The incoherent part describes electrons which are localized in atomic orbitals or Hubbard bands.

2.2.3 Dynamical mean field theory

The models of the last two sections, the Hubbard and Anderson impurity model, are connected via the dynamical mean field theory (DMFT). It was first observed that in infinite dimensions the self-energy of the Hubbard model is momentum-independent, thus all self-energy Feynman diagrams are local (Metzner and Vollhardt, 1989), before Georges and Kotliar (1992) introduced a formulation to calculate the momentum-independent self-energy with an auxiliary AIM.

The self-consistency condition demands that the local Green's function of the Hubbard model ($\boldsymbol{k}$-summed over the Brillouin zone)

$$G_\mathrm{loc}(i\omega_n) = \frac{1}{V_\mathrm{BZ}} \int \mathrm{d}\boldsymbol{k}\, G_{\text{Hubbard, DMFT}}(\boldsymbol{k}, i\omega_n) \tag{2.49}$$

equals the Green's function of the AIM

$$G_\mathrm{loc}(i\omega_n) \stackrel{!}{=} G_\mathrm{AIM}(i\omega_n) \tag{2.50}$$

The self-consistency can be performed in the following way: We start from an arbitrary Weiss field $\mathcal{G}(i\omega_n)$, which is the non-interacting Green's function of the (non-interacting) bath of the AIM. Note that this is not the same as the non-interacting Green's function of the Hubbard model. An impurity solver calculates the full Green's function $G_{\mathrm{AIM}}(i\omega_n)$ of the impurity. The self-energy

$$\Sigma_{\mathrm{AIM}}(i\omega_n) = G_{\mathrm{AIM}}(i\omega_n)^{-1} - \mathcal{G}(i\omega_n)^{-1} \tag{2.51}$$

of the AIM is calculated with Dyson's equation. We set this self-energy to be the self-energy of every site of the Hubbard model and calculate the Green's function of the Hubbard model

$$G_{\text{Hubbard, DMFT}}(\boldsymbol{k}, i\omega_n) = \frac{1}{i\omega_n + \mu - \epsilon_{\boldsymbol{k}} + \Sigma_{\mathrm{AIM}}(i\omega_n)}. \tag{2.52}$$

Out of $G_{\text{Hubbard, DMFT}}(\boldsymbol{k}, i\omega_n)$ the new $G_{\mathrm{loc}}(i\omega_n)$ is generated via Eq. (2.49). An inverse Dyson equation determines the new properties of the bath of the AIM

$$\mathcal{G}^{\mathrm{NEW}}(i\omega_n) = \left[G^{-1}_{\mathrm{loc}}(i\omega_n) + \Sigma_{\mathrm{AIM}}(i\omega_n)\right]^{-1}, \tag{2.53}$$

which closes the loop. The procedure is repeated until the self-consistency condition Eq. (2.50) is fulfilled.

For lattices in infinite coordination, DMFT gives the exact solution of the Hubbard model, since the self-energy is indeed $\boldsymbol{k}$-independent in this case. For systems in finite dimensions, DMFT is an approximation that assumes the self-energy of the Hubbard model to be the local DMFT one:

$$\Sigma(\boldsymbol{k}, i\omega_n) \approx \Sigma_{\mathrm{AIM}}(i\omega_n). \tag{2.54}$$

This is a reasonable approximation for three dimensions (Metzner and Vollhardt, 1989), but for two dimensions it gives large quantitative differences of 30%-40% (Rohringer et al., 2011) or even qualitatively wrong results. A DMFT approximation can only probe those phenomena of the Hubbard model, which are also present in the limit of infinite dimensions. Therefore when the physical phenomena are intrinsically described by non-local self-energies, like quantum-criticality or high-temperature superconductivity, they are absent in the DMFT approximation.

The strength of DMFT is to describe physics that is dominated by local processes within the atom in the solid. DMFT was the first theory capable of describing the metal to insulator Mott transition quantitatively, a localization of electrons on the lattice sites due to electron-electron interaction without the necessity of long-range order. It occurs at integer fillings (an integer number of electrons per site), when the interaction energy U becomes so large, that it is able to compete with the hopping amplitude t, or bandwidth energy scale W, respectively. Then it suppresses the hopping processes and gives an insulator.

DMFT is also exact in the non-interacting limit and atomic limit in any dimension. It is capable of describing the formation of localized magnetic moments due to electron electron interactions, as well as their screening by itinerant electrons, the Kondo-effect.

2.2.4 Analytic continuation

I have briefly mentioned above, that for the calculations we fold together temperature and time. This section discusses some aspects of the turmoil unfolding them again. The underlying mathematics, the Fredholm equation, also appears in many other occasions, whenever the dimension of a measured quantity is lower than the dimension of the desired observable. For example, computed

tomography scans make many two-dimensional, projected images of a human body, and then computers calculate a three-dimensional reconstruction. Also noisy pictures can be deblurred, if the distribution function of the noise in known.

But let us now go back to Green's functions. The relation between the spectral function and the Matsubara Green's function is given by a Fredholm equation of the first kind (Ghanem, 2017)

$$G(m) = \int_{-\infty}^{\infty} \mathrm{d}\omega \; K(m,\omega) A(\omega) \tag{2.55}$$

with a kernel K. For imaginary frequencies it is

$$K(i\omega_n, \omega) = -\frac{1}{i\omega_n - \omega}, \tag{2.56}$$

and for imaginary time

$$K(\tau, \omega) = -\frac{\exp(-\tau\omega)}{\exp(-\beta\omega) + 1}. \tag{2.57}$$

Transforming a spectral function from the real axis to the imaginary axis with these equations is easy and numerically stable, but vice versa it turns out to be very complicated. Equation (2.57) shows, that the features of $A(\omega)$ at large frequencies ω are damped exponentially, and become quickly hidden within the error bars of a stochastic method. This means, the inverse of the kernel amplifies the noise a lot, and results generated by numerical analytic continuation can only be trusted for low energy features. Appendix A demonstrates this with some examples.

If the data on the imaginary axis has noise or approximations applied, Eq. (2.55) does generally not have a solution at all. One ends up with the problem to find the most likely spectral function $A(\omega)$, that is compatible with the data and its precision. Generally, the deviation of the transform of a spectral function to the measured Green's function will be minimized, which means among the approximate solutions we look for the most likely one. In order to compare the two Green's functions we need a norm, and among the infinite possible choices come infinite many possible solutions $A(\omega)$. Everything boils down to find the compromise between smoothing the noise in $A(\omega)$ and not to oversmooth physical features.

The first attempts were made by Tikhonov (1943) to renormalize the exponentially damped eigenvalues of the inverse kernel. The Maxent procedure includes a standard model of the spectrum as prior information. Ghanem and Koch (2020) invented the average spectrum method, which samples over the free parameters of the Maxent procedure. Mishchenko (2012) sampled the space of possible (i.e. normalized and positive) spectral functions with a Markov chain; however this method still depends on the choice of a norm.

When doing a calculation on the imaginary axis, there are only two quantities, which can really be trusted: the density matrix and the value $A(\omega = 0)$, which can be related to $G(\tau = \frac{\beta}{2})$. Let me derive the latter relation. We examine the kernel

$$K(\tau = \frac{\beta}{2}, \omega) = -\frac{\exp(-\frac{\beta}{2}\omega)}{\exp(-\beta\omega) + 1} \tag{2.58}$$

$$= -\frac{1}{\exp(-\frac{\beta}{2}\omega) + \exp(\frac{\beta}{2}\omega)} \tag{2.59}$$

at this position. This is an inverse hyperbolic cosine. It gets very localized in frequency for low temperatures (see Fig. 2.1). The area under the curve is

$$A = \int \mathrm{d}\omega \; K(\tau = \frac{\beta}{2}, \omega) = \frac{\pi}{\beta} \tag{2.60}$$

and the variance

$$\sigma^2 = \int \mathrm{d}\omega\, \omega^2 K(\tau = \frac{\beta}{2}, \omega) = \frac{\pi^3}{\beta^3}. \tag{2.61}$$

A measure for the width is

$$\sigma = \sqrt{\frac{\sigma^2}{A}} = \frac{\pi}{\beta}, \tag{2.62}$$

i.e. proportional to the temperature T. This motivates the rule of thumb

$$G(\tau = \frac{\beta}{2}) = \frac{\pi}{\beta} A(\omega = 0) \tag{2.63}$$

in case the spectral function can be considered a constant within the integration region.

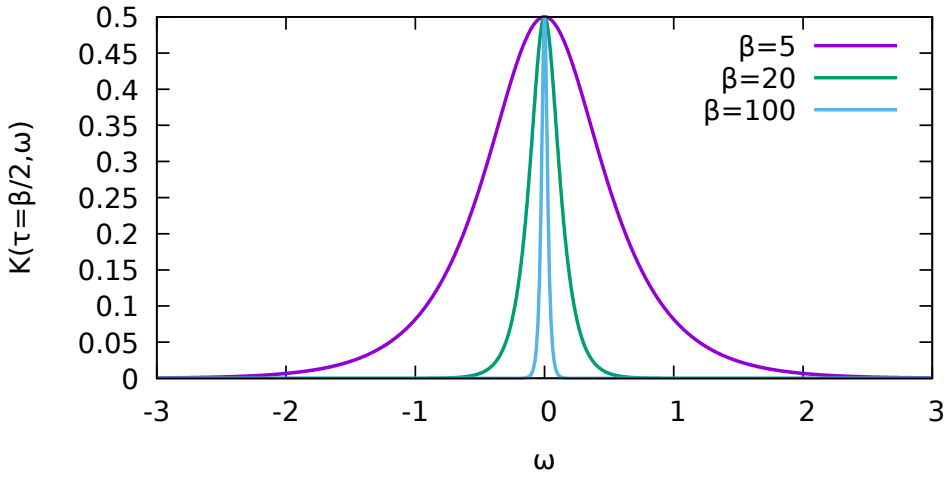

Figure 2.1: *The kernel plotted for $\beta = 5$, $\beta = 25$ and $\beta = 100$.*

Chapter 3

Continuous-time quantum Monte Carlo in hybridization expansion

Despite decades of intense research, a generic solution to the quantum many-body problem is still not found yet. The use of diagrammatic Monte Carlo techniques, however, has led to significant progress for special cases of interest, such as for the Anderson impurity model (AIM) and its generalizations to correlated molecules and retarded interactions.

Diagrammatic Monte Carlo techniques proceed in a three-step fashion: firstly, the Hamiltonian or the action is split into two parts, where one part is solved exactly. Secondly, the rest is treated by expanding an appropriate generating function (such as the partition function or free energy) with respect to it. Thirdly and finally, the resulting probability distribution is sampled using Markov chain Monte Carlo.

The hybridization expansion continuous time Quantum Monte Carlo (CTHYB) treats the impurity exactly, and expands in the so called hybridization function, which contains the effects of hybridization events and non-interacting bath terms combined. The impurity is a many-body problem itself and has to be solved with an exact diagonalization (ED) technique for each Monte Carlo move. This has on the one hand the disadvantage, that the computational effort grows exponentially with the size of the impurity, i.e. only small systems like correlated d- and f-shells are within reach. On the other hand it can deal with complicated one- and two-particle interaction terms on the impurity, which give no or only a moderate sign problem, since they are kept together within the ED and not sampled individually.

Since its invention, CTHYB has been one of the most powerful solvers for general impurities. At the moment it looks, that this will not stay that way, because non-probabilistic methods are moving forward fast, while CTHYB suffers from its unsolved deficiencies: a severe sign problem when the Hamiltonian has considerable complex terms, its exponential scaling in the number of impurity flavours, and finally, its operation on the imaginary time axis, which makes it very cumbersome if possible at all, to transfer the data to the real axis where the physics lives.

It has been written a lot about CTHYB, and the most powerful optimizations were developed the years following its invention. This makes it very difficult to write something meaningful without duplicating other works. Since a treatise of this topic can in any case only cover it partially, so I focus on aspects which have not been documented yet.

I decided to start with a complete derivation of the expansion formula, which I for a long time found confusing and complicated. I will discuss its properties and review the known optimizations. Then I show the superstate sampling algorithm, which discusses the optimal choice of the *size* of a Monte Carlo configuration. Next I discuss the so called *sliding technique*, which tries to cure one

of the minor deficiencies of CTHYB, namely that the estimators are delta functions in imaginary time, by smearing them out over a finite time-interval. With current supercomputer technology, the Hamiltonian and the operators of a full f-shell cannot be stored in memory without truncation; I propose the *mixbasis* algorithm, which tries to cure this issue with a time-memory trade-off. Last I describe and discuss two methods for measurements of density-density correlation functions, which were invented and implemented in the course of this thesis.

3.1 The hybridization expansion

The hybridization expansion formulas were first given by Werner et al. (2006). Here I want to provide three complete and different derivations of them, following what Einstein was supposed to have said: Make things as simple as possible, but not simpler. The main difference of the following three section is, how the hybridization function $\Delta(\tau)$ is created.

- Within the *operator formalism* $\Delta(\tau)$ emerges from Wick's theorem applied to the non-interacting bath operators.
- Using *Feynman's path integral technique*, where $\Delta(\tau)$ is generated by an integral over Gaussian fields. The result has to be symmetrized in the end.
- And by employing a *dual transformation*, known from the dual fermion techniques, where $\Delta(\tau)$ comes from evaluating Wick's theorem for non-interacting dual operators.

The starting point is the Hamiltonian

$$\hat{H}_{\mathrm{AIM}} = \hat{H}_{\mathrm{bath}} + \hat{H}^{\dagger}_{\mathrm{hyb}} + \hat{H}_{\mathrm{hyb}} + \hat{H}_{\mathrm{loc}} \tag{3.1}$$

$$= \sum_{p\mu} \epsilon_{p\mu} \hat{a}^{\dagger}_{p\mu} \hat{a}_{p\mu} + \sum_{p\mu\nu} \left(V^{*}_{p\mu\nu} \hat{c}^{\dagger}_{\nu} \hat{a}_{p\mu} + V_{p\mu\nu} \hat{a}^{\dagger}_{p\mu} \hat{c}_{\nu} \right) + \hat{H}_{\mathrm{loc}}[\hat{c}^{\dagger}, \hat{c}] \tag{3.2}$$

of the multi-orbital AIM. The operators $\hat{c}^{\dagger}_{\nu}$ ($\hat{c}_{\nu}$) create (annihilate) electrons on the impurity with flavour ν. The operators $\hat{a}^{\dagger}_{p\mu}$ ($\hat{a}_{p\mu}$) create (annihilate) electrons on the p-th bath site, which has an energy of $\epsilon_{p\mu}$ and belongs to impurity flavour μ. In the second term of Eq. (3.2), each impurity flavour ν couples to its own non-interacting bath sites with amplitudes $V_{p\nu\nu}$ (diagonal hybridization), but may also couple to the bath sites of other flavours μ via $V_{p\mu\nu}$ with $\mu \neq \nu$ (off-diagonal hybridization). The third term $\hat{H}_{\mathrm{loc}}[\hat{c}^{\dagger}, \hat{c}] = -t_{\mu\nu} \hat{c}^{\dagger}_{\mu} \hat{c}_{\nu} + U_{\kappa\lambda\mu\nu} \hat{c}^{\dagger}_{\kappa} \hat{c}^{\dagger}_{\lambda} \hat{c}_{\mu} \hat{c}_{\nu}$ contains the one- and two-particle interaction on the impurity; its actual form does not matter yet for the derivations, therefore I will not write it out until later in Chapter 5, when I discuss its terms explicitly.

3.1.1 Derivation with operator formalism

We take the partition function for Eq. (3.2), expand it within the operator formalism in a brute force way, and sort the terms into the known CTHYB formula. With Eq. (B.36) from appendix B

$$Z = \mathrm{Tr}\left\{ \mathrm{e}^{-\beta \hat{H}_0} \mathcal{T}_{\tau} \exp\left[-\int_0^{\beta} \mathrm{d}\tau \hat{V}(\tau) \right] \right\}, \tag{3.3}$$

and setting

$$\hat{H}_0 = \hat{H}_{\mathrm{bath}} + \hat{H}_{\mathrm{loc}} \tag{3.4}$$

$$\hat{V} = \hat{H}^{\dagger}_{\mathrm{hyb}} + \hat{H}_{\mathrm{hyb}}, \tag{3.5}$$

after expanding one gets

$$Z = \sum_{n=0}^{\infty} \frac{1}{n!} \int_0^\beta \mathrm{d}\tau_1 \int_0^\beta \mathrm{d}\tau_2 \cdots \int_0^\beta \mathrm{d}\tau_n \mathrm{Tr}_{ac} \left[\mathrm{e}^{-\beta \hat{H}_0} T_\tau (-\hat{V}(\tau_n)) \dots (-\hat{V}(\tau_2))(-\hat{V}(\tau_1)) \right]. \tag{3.6}$$

Tr_{ac} means, that the trace goes over a complete basis set of both the bath and the impurity. Furthermore in the absence of superconductivity, any term with not the same number of creation and annihilation operators of the same kind gives zero expectation value; therefore only terms with even expansion order n survive and the minus signs of the $\hat{V}$s disappear. After multiplying out the $\hat{V}$s, only terms with $n/2$ of the $\hat{H}_{\mathrm{hyb}}$ and $n/2$ of the $\hat{H}^\dagger_{\mathrm{hyb}}$ survive. Omitting all odd expansion orders, writing all even times primed and substituting $k = 2n$ gives

$$\begin{aligned}
Z &= \sum_{k=0}^{\infty} \frac{1}{k!} \int_0^\beta \mathrm{d}\tau_1 \int_0^\beta \mathrm{d}\tau_1' \cdots \int_0^\beta \mathrm{d}\tau_k \int_0^\beta \mathrm{d}\tau_k' && (3.7)\\
&\times \mathrm{Tr}_{ac} \left[\mathrm{e}^{-\beta \hat{H}_0} T_\tau \hat{H}_{\mathrm{hyb}}(\tau_k) \hat{H}^\dagger_{\mathrm{hyb}}(\tau_k') \dots \hat{H}_{\mathrm{hyb}}(\tau_1') \hat{H}^\dagger_{\mathrm{hyb}}(\tau_1) \right] \\
&= \sum_{k=0}^{\infty} \frac{1}{k!} \int_0^\beta \mathrm{d}\tau_1 \int_0^\beta \mathrm{d}\tau_1' \cdots \int_0^\beta \mathrm{d}\tau_k \int_0^\beta \mathrm{d}\tau_k' && (3.8)\\
&\times \sum_{p_1\mu_1\nu_1} \sum_{p_1'\mu_1'\nu_1'} \cdots \sum_{p_k\mu_k\nu_k} \sum_{p_k'\mu_k'\nu_k'} V_{p_1\mu_1\nu_1} V^*_{p_1'\mu_1'\nu_1'} \dots V_{p_k\mu_k\nu_k} V^*_{p_k'\mu_k'\nu_k'} \\
&\times \mathrm{Tr}_{ac} \left[\mathrm{e}^{-\beta \hat{H}_0} T_\tau \hat{a}^\dagger_{p_k\mu_k}(\tau_k) \hat{c}_{\nu_k}(\tau_k) \hat{c}^\dagger_{\nu_k'}(\tau_k') \hat{a}_{p_k'\mu_k'}(\tau_k') \dots \hat{a}^\dagger_{p_1\mu_1}(\tau_1) \hat{c}_{\nu_1}(\tau_1) \hat{c}^\dagger_{\nu_1'}(\tau_1') \hat{a}_{p_1'\mu_1'}(\tau_1') \right].
\end{aligned}$$

There is a special property here, namely that the operators always appear in connected pairs of one impurity and one bath operator with the same time argument. Thus time-ordering never generates minus signs. Since $\hat{H}_0$ does not couple the impurity with the bath states, one can factorize the trace into two traces

$$\begin{aligned}
Z &= \sum_{k=0}^{\infty} \frac{1}{k!} \int_0^\beta \mathrm{d}\tau_1 \int_0^\beta \mathrm{d}\tau_1' \cdots \int_0^\beta \mathrm{d}\tau_k \int_0^\beta \mathrm{d}\tau_k' && (3.9)\\
&\times \sum_{p_1\mu_1\nu_1} \sum_{p_1'\mu_1'\nu_1'} \cdots \sum_{p_k\mu_k\nu_k} \sum_{p_k'\mu_k'\nu_k'} V_{p_1\mu_1\nu_1} V^*_{p_1'\mu_1'\nu_1'} \dots V_{p_k\mu_k\nu_k} V^*_{p_k'\mu_k'\nu_k'} && (3.10)\\
&\times \mathrm{Tr}_c \left[\mathrm{e}^{-\beta \hat{H}_{\mathrm{loc}}} T_\tau \hat{c}_{\nu_k}(\tau_k) \hat{c}^\dagger_{\nu_k'}(\tau_k') \dots \hat{c}_{\nu_1}(\tau_1) \hat{c}^\dagger_{\nu_1'}(\tau_1') \right] && (3.11)\\
&\times \mathrm{Tr}_a \left[\mathrm{e}^{-\beta \hat{H}_{\mathrm{bath}}} T_\tau \hat{a}^\dagger_{p_k\mu_k}(\tau_k) \hat{a}_{p_k'\mu_k'}(\tau_k') \dots \hat{a}^\dagger_{p_1\mu_1}(\tau_1) \hat{a}_{p_1'\mu_1'}(\tau_1') \right], && (3.12)
\end{aligned}$$

where the first trace Tr_c now only goes over the impurity states, and the second trace Tr_a only over the non-interacting bath states. Note that separating the bath and impurity operators does not give minus signs, since in the ordering of Eq. (3.8) the impurity operators appear in pairs, which commute with the bath operators.[1]

[1] Fermionic operators follow anticommutation rules. However if the two systems under consideration A and B are completely decoupled, like the impurity and the bath in Eq. (3.8), a unitary *Klein transform* can transform B to C, where the operators of A and C commute instead of anticommute.

We want to use Wick's theorem to calculate the bath trace. For this purpose the time-ordered expectation value of one bath creator and annihilator is needed:

$$\Delta_{\nu\nu'}(\tau-\tau') = \sum_{pp'\mu\mu'} V_{p\mu\nu}V^*_{p'\mu'\nu'}\mathrm{Tr}_a\left[\mathrm{e}^{-\beta\hat{H}_{\mathrm{bath}}}T_\tau \hat{a}^\dagger_{p\mu}(\tau)\hat{a}_{p'\mu'}(\tau')\right] \tag{3.13}$$

$$= \begin{cases} \sum_{p\mu} V_{p\mu\nu}V^*_{p\mu\nu'}\mathrm{Tr}_a\left[\mathrm{e}^{-\beta\hat{H}_{\mathrm{bath}}}\hat{a}^\dagger_{p\mu}(\tau)\hat{a}_{p\mu}(\tau')\right], & \tau'<\tau \\ -\sum_{p\mu} V_{p\mu\nu}V^*_{p\mu\nu'}\mathrm{Tr}_a\left[\mathrm{e}^{-\beta\hat{H}_{\mathrm{bath}}}\hat{a}_{p\mu}(\tau')\hat{a}^\dagger_{p\mu}(\tau)\right], & \tau<\tau' \end{cases} \tag{3.14}$$

$$= \begin{cases} \Delta^{\mathrm{H}}_{\nu\nu'}(\tau-\tau'), & \tau'<\tau \\ \Delta^{\mathrm{P}}_{\nu\nu'}(\tau'-\tau), & \tau<\tau'. \end{cases} \tag{3.15}$$

In Eq. (3.14) I have already reduced the sums over the bath indices $p\mu p'\mu' \to p\mu$ from two to one, since the bath is diagonal, both bath operators must act on the same bath site. It is also possible in CTHYB to have off-diagonal baths, with electrons hopping among the bath sites, but for DMFT and the applications in this thesis, this does not occur, therefore I assume the bath to be always diagonal in the following.

Now let us calculate the propagators $\langle\hat{a}\hat{a}^\dagger\rangle$ and $\langle\hat{a}^\dagger\hat{a}\rangle$ separately, starting with the bath-hole propagator:

$$\Delta^{\mathrm{H}}_{\nu\nu'}(\tau-\tau') \overset{\tau'\leq\tau}{=} \sum_{p\mu} V_{p\mu\nu}V^*_{p\mu\nu'}\mathrm{Tr}_a\left[\mathrm{e}^{-\beta\hat{H}_{\mathrm{bath}}}\hat{a}^\dagger_{p\mu}(\tau)\hat{a}_{p\mu}(\tau')\right] \tag{3.16}$$

$$= \sum_{p\mu} V_{p\mu\nu}V^*_{p\mu\nu'}\left\langle\hat{a}^\dagger_{p\mu}\hat{a}_{p\mu}\right\rangle \mathrm{e}^{\epsilon_{p\mu}(\tau-\tau')} \tag{3.17}$$

$$= \sum_{p\mu} V_{p\mu\nu}V^*_{p\mu\nu'}\frac{1}{\mathrm{e}^{\beta\epsilon_{p\mu}}+1}\mathrm{e}^{\epsilon_{p\mu}(\tau-\tau')}. \tag{3.18}$$

This corresponds to a hole created at τ' which propagates through the bath with a time-evolution of $\mathrm{e}^{\epsilon_{p\mu}(\tau-\tau')}$.[2] The hole is annihilated at time τ. Separating out all time-evolutions leaves behind a expectation value $\left\langle\hat{a}^\dagger\hat{a}\right\rangle$, which is the Fermi distribution function.[3]

The same way the particle propagator is calculated, which creates a particle at τ' in the bath and annihilates it at τ:

$$\Delta^{\mathrm{P}}_{\nu\nu'}(\tau-\tau') \overset{\tau'\leq\tau}{=} -\sum_{p} V_{p\mu\nu}V_{p\mu\nu'}\mathrm{Tr}_a\left[\mathrm{e}^{-\beta\hat{H}_{\mathrm{bath}}}\hat{a}_{p\mu}(\tau)\hat{a}^\dagger_{p\mu}(\tau')\right] \tag{3.19}$$

$$= -\sum_{p} V_{p\mu\nu}V_{p\mu\nu'}\left\langle\hat{a}_{p\mu}\hat{a}^\dagger_{p\mu}\right\rangle \mathrm{e}^{-\epsilon_{p\mu}(\tau-\tau')} \tag{3.20}$$

$$= -\sum_{p} V_{p\mu\nu}V_{p\mu\nu'}\frac{\mathrm{e}^{\beta\epsilon_{p\mu}}}{\mathrm{e}^{\beta\epsilon_{p\mu}}+1}\mathrm{e}^{-\epsilon_{p\mu}(\tau-\tau')}. \tag{3.21}$$

The expectation value $\left\langle\hat{a}\hat{a}^\dagger\right\rangle$ is not the Fermi function, but one minus the Fermi function.[4] Let me stress, that in both expressions time ordering is fulfilled.

The relation between hole and particle propagator is

$$\Delta^{\mathrm{P}}_{\nu\nu'}(\tau) = -\Delta^{\mathrm{H}}_{\nu\nu'}(\beta-\tau). \tag{3.22}$$

[2] The time-evolution with regard to a non-interacting Hamiltonian $\hat{H}_{\mathrm{bath}} = \sum_{p\mu}\epsilon_{p\mu}\hat{a}^\dagger_{p\mu}\hat{a}_{p\mu}$ can be given explicitly: $\hat{a}_{p\mu}(\tau) = \mathrm{e}^{\hat{H}_{\mathrm{bath}}\tau}\hat{a}_{p\mu}\mathrm{e}^{-\hat{H}_{\mathrm{bath}}\tau} = \mathrm{e}^{-\epsilon_{p\mu}\tau}\hat{a}_{p\mu}$ and $\hat{a}^\dagger_{p\mu}(\tau) = \mathrm{e}^{\hat{H}_{\mathrm{bath}}\tau}\hat{a}^\dagger_{p\mu}\mathrm{e}^{-\hat{H}_{\mathrm{bath}}\tau} = \mathrm{e}^{\epsilon_p\tau}\hat{a}^\dagger_{p\mu}$, respectively.

[3] $\left\langle\hat{a}\hat{a}^\dagger\right\rangle = \langle\hat{n}\rangle = 1/(\exp[\beta\epsilon]+1)$

[4] $\left\langle\hat{a}^\dagger\hat{a}\right\rangle = 1-\langle\hat{n}\rangle = \exp[\beta\epsilon]/(\exp[\beta\epsilon]+1)$

Therefore the full object is

$$\Delta_{\nu\nu'}(\tau-\tau') = \begin{cases} \Delta^{\mathrm{H}}_{\nu\nu'}(\tau-\tau'), & \tau' < \tau \\ -\Delta^{\mathrm{H}}_{\nu\nu'}(\beta-(\tau-\tau')), & \tau < \tau' \end{cases}. \tag{3.23}$$

The antiperiodic property of Green's functions due to cyclicity of the trace appeared here through a particle-hole transformation of $\Delta^{\mathrm{P}}_{\nu\nu'}$. Now everything is prepared to evaluate the bath trace to a determinant using Wick's theorem:

$$\sum_{p_1\mu_1\nu_1}\sum_{p_1'\mu_1'\nu_1'}\cdots\sum_{p_k\mu_k\nu_k}\sum_{p_k'\mu_k'\nu_k'} V_{p_1\mu_1\nu_1}V^*_{p_1'\mu_1'\nu_1'}\ldots V_{p_k\mu_k\nu_k}V^*_{p_k'\mu_k'\nu_k'} \tag{3.24}$$

$$\times \mathrm{Tr}_a\left[\mathrm{e}^{-\beta\hat{H}_{\mathrm{bath}}}T_\tau \hat{a}^\dagger_{p_k\mu_k}(\tau_k)\hat{a}_{p_k'\mu_k'}(\tau_k')\ldots\hat{a}^\dagger_{p_1\mu_1}(\tau_1)\hat{a}_{p_1'\mu_1'}(\tau_1')\right] \tag{3.25}$$

$$= \sum_{\nu_1\nu_1'}\cdots\sum_{\nu_k\nu_k'} \tag{3.26}$$

$$\times \sum_{\substack{\text{permutations } \pi \\ \text{of } \{1,\ldots,k\}}} \mathrm{sign}(\pi)\sum_{p_1\mu_1} V_{p_1\mu_1\nu_1}V^*_{p_1\mu'_{\pi(1)}\nu'_{\pi(1)}}\left\langle T_\tau \hat{a}^\dagger_{p_1\mu_1}(\tau_1)\hat{a}_{p_1\mu'_{\pi(1)}}(\tau'_{\pi(1)})\right\rangle\ldots \tag{3.27}$$

$$\sum_{p_k\mu_k} V_{p_k\mu_k\nu_k}V^*_{p_k\mu'_{\pi(k)}\nu'_{\pi(k)}}\left\langle T_\tau \hat{a}^\dagger_{p_k\mu_k}(\tau_k)\hat{a}_{p_k\mu'_{\pi(k)}}(\tau'_{\pi(k)})\right\rangle$$

$$= \sum_{\nu_1\nu_1'}\cdots\sum_{\nu_k\nu_k'}\sum_{\substack{\text{permutations } \pi \\ \text{of } \{1,\ldots,k\}}} \mathrm{sign}(\pi)\prod_{i=1}^{k}\Delta_{\nu_i\nu'_{\pi(i)}}(\tau_i-\tau_{\pi(i)}) \tag{3.28}$$

$$= \sum_{\nu_1\nu_1'}\cdots\sum_{\nu_k\nu_k'}\det\boldsymbol{\Delta} \tag{3.29}$$

Here π is a element of the permutation group $\mathcal{P}$. $\mathrm{sign}(\pi) = +1$, if the number of permutations to restore the original order $\{1,\ldots,N\}$ is even, $\mathrm{sign}(\pi) = -1$, if the number is odd. In Eq. (3.27) all possible contractions according to Wick's theorem were made by keeping the creator's times and flavours fixed, and assigning the properties to the annihilators according to the permutation group. In Eq. (3.27) was also already used, that the bath propagator is diagonal in bath sites p_i. The two-operator expectation values evaluate to the hybridization function Eq. (3.28), and with the signs of the permutation, everything can be written as a determinant.

The final result is

$$Z = \sum_k \frac{1}{k!}\sum_{\nu_1\nu_1'}\cdots\sum_{\nu_k\nu_k'}\int_0^\beta \mathrm{d}\tau_1\int_0^\beta \mathrm{d}\tau_1'\cdots\int_0^\beta \mathrm{d}\tau_k\int_0^\beta \mathrm{d}\tau_k' \tag{3.30}$$

$$\times \mathrm{Tr}_c\left[\mathrm{e}^{-\beta\hat{H}_{\mathrm{loc}}}T_\tau \hat{c}_{\nu_k}(\tau_k)\hat{c}^\dagger_{\nu_k'}(\tau_k')\ldots\hat{c}_{\nu_1}(\tau_1)\hat{c}^\dagger_{\nu_1'}(\tau_1')\right]\det\boldsymbol{\Delta}. \tag{3.31}$$

Before discussing its properties, let me show the alternative ways to arrive at this formula.

3.1.2 Effective propagator formulation

The bath electrons are non-interacting, thus they can be integrated out analytically within Feynman's path integral formalism. This leaves behind an effective, retarded interaction for the electrons on the impurity. The topic of this section is to derive that action. Let's again start with the Hamiltonian

$$\hat{H} = \hat{H}_{\mathrm{bath}} + \hat{H}^\dagger_{\mathrm{hyb}} + \hat{H}_{\mathrm{hyb}} + \hat{H}_{\mathrm{loc}} \tag{3.32}$$

$$= \sum_{p\mu}\epsilon_{p\mu}\hat{a}^\dagger_{p\mu}\hat{a}_{p\mu} + \sum_{p\mu\nu}\left(V^*_{p\mu\nu}\hat{c}^\dagger_\nu\hat{a}_{p\mu} + V_{p\mu\nu}\hat{a}^\dagger_{p\mu}\hat{c}_\nu\right) + \hat{H}_{\mathrm{loc}}. \tag{3.33}$$

According to Eqs. (C.134) and (C.135) in appendix C the partition function is written as the path integral

$$Z = \int \mathcal{D}\bar{\boldsymbol{c}}\,\mathcal{D}\boldsymbol{c} \int \mathcal{D}\bar{\boldsymbol{a}}\,\mathcal{D}\boldsymbol{a}\, \exp(-S[\bar{\boldsymbol{c}}, \boldsymbol{c}, \bar{\boldsymbol{a}}, \boldsymbol{a}]) \tag{3.34}$$

with an action

$$S[\bar{\boldsymbol{c}}, \boldsymbol{c}, \bar{\boldsymbol{a}}, \boldsymbol{a}] = \int_0^\beta \mathrm{d}\tau \sum_\nu \bar{c}_\nu(\tau)[\partial_\tau - \mu]c_\nu(\tau) \tag{3.35a}$$

$$+ \int_0^\beta \mathrm{d}\tau\, \hat{H}_{\mathrm{loc}}(\tau) \tag{3.35b}$$

$$+ \int_0^\beta \mathrm{d}\tau \sum_{p\mu\nu} \left(V^*_{p\mu\nu}\bar{c}_\nu(\tau)a_{p\mu}(\tau) + V_{p\mu\nu}\bar{a}_{p\mu}(\tau)c_\nu(\tau) \right) \tag{3.35c}$$

$$+ \int_0^\beta \mathrm{d}\tau \sum_{p\mu} \bar{a}_{p\mu}(\tau)[\partial_\tau - \epsilon_{p\mu}]a_{p\mu}(\tau). \tag{3.35d}$$

The translation of second quantized operators into Grassmann number is done via $\hat{c}^\dagger \to \bar{c}$, $\hat{c} \to c$, and bath operators equivalently. A Fourier transform to Matsubara frequencies gives (see Eq. (C.148) in the appendix)

$$S[\bar{\boldsymbol{c}}, \boldsymbol{c}, \bar{\boldsymbol{a}}, \boldsymbol{a}] = \sum_n \sum_\nu \bar{c}_\nu(i\omega_n)[-i\omega_n - \mu]c_\nu(i\omega_n) \tag{3.36}$$

$$+ \sum_n \sum_{p\mu\nu} \left(V^*_{p\mu\nu}\bar{c}_\nu(i\omega_n)a_{p\mu}(i\omega_n) + V_{p\mu\nu}\bar{a}_{p\mu}(i\omega_n)c_\nu(i\omega_n) \right) \tag{3.37}$$

$$+ \sum_n \sum_{p\mu} \bar{a}_{p\mu}(i\omega_n)[-i\omega_n - \epsilon_{p\mu}]a_{p\mu}(i\omega_n) \tag{3.38}$$

$$+ \sum_n H_{\mathrm{loc}}(i\omega_n). \tag{3.39}$$

Now integrate out the bath fermions using Eqs. (C.47) and (C.63) of appendix C, which gives[5]

$$Z = \int \mathcal{D}\bar{\boldsymbol{c}}\,\mathcal{D}\boldsymbol{c}\, \exp[S_{\mathrm{eff}}[\bar{\boldsymbol{c}}, \boldsymbol{c}]] \cdot \det(-i\omega_n + \epsilon_{p\mu}) \tag{3.40}$$

with the effective action

$$S_{\mathrm{eff}}[\bar{\boldsymbol{c}}, \boldsymbol{c}] = \sum_n \sum_\nu \bar{c}_\nu(i\omega_n)[-i\omega_n - \mu]c_\nu(i\omega_n) \tag{3.41}$$

$$+ \sum_n H_{\mathrm{loc}}(i\omega_n) \tag{3.42}$$

$$+ \sum_n \sum_{p\mu\nu\nu'} V^*_{p\mu\nu}\bar{c}_\nu(i\omega_n)[-i\omega_n + \epsilon_{p\mu}]^{-1}V_{p\mu\nu'}c_{\nu'}(i\omega_n) \tag{3.43}$$

---

[5] The integral is $Z_G(\boldsymbol{M}, \boldsymbol{\eta}, \bar{\boldsymbol{\eta}}) = \int \mathrm{d}\theta_1 \mathrm{d}\bar{\theta}_1 \ldots \mathrm{d}\theta_n \mathrm{d}\bar{\theta}_N \exp\left(\sum_{ij=1}^N \bar{\theta}_i M_{ij}\theta_j + \sum_i \left(\bar{\eta}_i\theta_i + \bar{\theta}_i\eta_i \right) \right)$
$= \det\boldsymbol{M} \exp\left(-\sum_{ij} \bar{\eta}_i \Delta_{ij} \eta_j \right)$, with
$\bar{\theta}_i = \bar{a}_p$,
$\theta_j = a_p = \theta_i$,
$\eta_i = V_{p\mu\nu}c_\nu$,
$\bar{\eta}_i = V^*_{p\mu\nu}\bar{c}_\nu$, and
$M_{ij} = (-i\omega_n - \epsilon_{p\mu})\delta_{pp'}$.
The inversion of the matrix $\Delta_{ij} = \left(M^{-1}\right)_{ij}$ is done in the combined space of spin and bath-sites. Matsubara space is not affected by it.

The determinant in Eq. (3.40) $\det(-i\omega_n + \epsilon_{p\mu}) = \prod_{p\mu} \mathrm{diag}[-i\omega_n + \epsilon_{p\mu}]$ goes over the bath indices $p\mu$ and depends on the bath only, thus it will cancel out of all expectation values and can be omitted. A back-transform to imaginary time of the retarded object gives the explicit form in imaginary time

$$S_{\mathrm{eff}}[\bar{\boldsymbol{c}}, \boldsymbol{c}] = \int_0^\beta \mathrm{d}\tau \sum_\nu \bar{c}_\nu(\tau)[\partial_\tau - \mu]c_\nu(\tau) \tag{3.44}$$

$$+ \int_0^\beta \mathrm{d}\tau\, H_{\mathrm{loc}}(\tau) \tag{3.45}$$

$$+ \int_0^\beta \mathrm{d}\tau \int_0^\beta \mathrm{d}\tau' \sum_{p\mu\nu\nu'} \bar{c}_\nu(\tau)\Delta_{\nu\nu'}(\tau - \tau')c_{\nu'}(\tau'), \tag{3.46}$$

since the formulation with the partial derivative $\partial\tau$ is only formal. The hybridization function

$$\Delta_{\nu\nu'}(\tau - \tau') = \sum_{p\mu} \frac{V^*_{p\mu\nu} V_{p\mu\nu'}}{\mathrm{e}^{\beta\epsilon_{p\mu}} + 1} \mathrm{e}^{\epsilon_{p\mu}(\tau - \tau')} \tag{3.47}$$

is the retardation effect that an electron feels, which jumps in the bath at imaginary time τ' and comes back at imaginary time τ.

The final result of the action in effective formulation is

$$Z = \int \mathcal{D}\bar{\boldsymbol{c}}\, \mathcal{D}\boldsymbol{c}\, \exp(-S_{\mathrm{eff}}[\bar{\boldsymbol{c}}, \boldsymbol{c}]) \tag{3.48}$$

with an effective action

$$S_{\mathrm{eff}}[\bar{\boldsymbol{c}}, \boldsymbol{c}] = S_{\mathrm{at}}[\bar{\boldsymbol{c}}, \boldsymbol{c}] + \int_0^\beta \mathrm{d}\tau \int_0^\beta \mathrm{d}\tau' \sum_{\nu\nu'} \bar{c}_\nu(\tau)\Delta_{\nu\nu'}(\tau - \tau')c_{\nu'}(\tau'), \tag{3.49}$$

where the atomic action was introduced, which consists of Eqs. (3.44) and (3.45). We can now in principle continue in two different ways. Firstly, to expand in the hybridization term and then symmetrize the product of hybridization functions into the determinant. Secondly, we can perform another Hubbard-Stratonovich transformation to the retarded term (a dual transform), which re-introduces non-interacting operators, whose propagators will be the inverse hybridization function. Expanding with respect to the products of one impurity and one dual operator, and applying Wick's theorem to the latter, will also give the determinant.

3.1.3 Expansion with respect to Δ

We now take the effective action Eq. (3.49) and expand with respect to $\bar{c}\Delta c$:

$$Z = \int \mathcal{D}\bar{\boldsymbol{c}}\, \mathcal{D}\boldsymbol{c} \exp\left[S_{\mathrm{at}}[\bar{\boldsymbol{c}}, \boldsymbol{c}] + \int_0^\beta \mathrm{d}\tau \int_0^\beta \mathrm{d}\tau' \sum_{\nu\nu'} \bar{c}_\nu(\tau)\Delta_{\nu\nu'}(\tau - \tau')c_{\nu'}(\tau')\right] \tag{3.50}$$

$$= \sum_k \frac{1}{k!} \sum_{\nu_1\nu'_1 \ldots \nu_k\nu'_k} \int_0^\beta \mathrm{d}\tau_1 \int_0^\beta \mathrm{d}\tau'_1 \cdots \int_0^\beta \mathrm{d}\tau_k \int_0^\beta \mathrm{d}\tau'_k \exp[S_{\mathrm{at}}[\bar{\boldsymbol{c}}, \boldsymbol{c}]] \tag{3.51}$$

$$\mathcal{T}_\tau \bar{c}_{\nu_k}(\tau_k)c_{\nu'_k}(\tau'_k) \ldots \bar{c}_{\nu_1}(\tau_1)c_{\nu'_1}(\tau'_1) \tag{3.52}$$

$$\Delta_{\nu_k\nu'_k}(\tau_k - \tau'_k) \ldots \Delta_{\nu_1\nu'_1}(\tau_1 - \tau'_1). \tag{3.53}$$

Note that the integrations of the times all go from $[0, \beta]$. Therefore all permutations of the impurity operators will appear, which the time-ordering operator will put into time ordering. But the propagations through the bath will stay; no matter which position e.g. the impurity operators

$\bar{c}(\tau_1)$ and $c(\tau_1')$ will have in the local trace, they will always be connected by the bath propagator $\Delta(\tau_1 - \tau_1')$. This does not respect indistinguishability of quantum mechanical objects. It is not a fundamental problem, since in Feynman diagrams the particles and interactions are only of virtual type, and the result would converge to something that respects the indistinguishability of the particles. However, this expansion has a severe sign problem, because an exchange of two neighboring c and $\bar{c}$ would give a minus sign in the local trace, and have no effect on the sign of the bath part.

It is therefore necessary to symmetrize the bath part, which gives

$$\frac{1}{k!}\int_0^\beta \mathrm{d}\tau_1 \int_0^\beta \mathrm{d}\tau_1' \cdots \int_0^\beta \mathrm{d}\tau_k \int_0^\beta \mathrm{d}\tau_k' \; \mathcal{T}_\tau \bar{c}_{\nu_k}(\tau_k) c_{\nu_k'}(\tau_k') \ldots \bar{c}_{\nu_1}(\tau_1) c_{\nu_1'}(\tau_1') \tag{3.54}$$

$$\times \Delta_{\nu_k \nu_k'}(\tau_k - \tau_k') \ldots \Delta_{\nu_1 \nu_1'}(\tau_1 - \tau_1') \tag{3.55}$$

$$= \frac{1}{k!}\int_0^\beta \mathrm{d}\tau_1 \int_0^\beta \mathrm{d}\tau_1' \cdots \int_0^\beta \mathrm{d}\tau_k \int_0^\beta \mathrm{d}\tau_k' \; \mathcal{T}_\tau \bar{c}_{\nu_k}(\tau_k) c_{\nu_k'}(\tau_k') \ldots \bar{c}_{\nu_1}(\tau_1) c_{\nu_1'}(\tau_1') \tag{3.56}$$

$$\times \sum_{\substack{\text{permutations } \pi \\ \text{of } \{1,\ldots,k\}}} \operatorname{sign}(\pi) \prod_{i=1}^{k} \Delta_{\nu_i \nu_{\pi(i)}}(\tau_i - \tau_{\pi(i)}') \tag{3.57}$$

$$= \frac{1}{k!}\int_0^\beta \mathrm{d}\tau_1 \int_0^\beta \mathrm{d}\tau_1' \cdots \int_0^\beta \mathrm{d}\tau_k \int_0^\beta \mathrm{d}\tau_k' \; \mathcal{T}_\tau \bar{c}_{\nu_k}(\tau_k) c_{\nu_k'}(\tau_k') \ldots \bar{c}_{\nu_1}(\tau_1) c_{\nu_1'}(\tau_1') \tag{3.58}$$

$$\det \mathbf{\Delta}. \tag{3.59}$$

Now the exchange of two neighboring impurity operators gives a minus sign in both the impurity trace and in the determinant, where two rows are exchanged. Therefore no overall minus sign appears, analogous to Eq. (3.8) above. Switching back from Grassmann numbers to operators gives

$$Z = \sum_k \frac{1}{k!} \sum_{\nu_1 \nu_1'} \cdots \sum_{\nu_k \nu_k'} \int_0^\beta \mathrm{d}\tau_1 \int_0^\beta \mathrm{d}\tau_1' \cdots \int_0^\beta \mathrm{d}\tau_k \int_0^\beta \mathrm{d}\tau_k' \tag{3.60}$$

$$\times \operatorname{Tr}_c \left[\mathrm{e}^{-\beta H_{\mathrm{loc}}} T_\tau \hat{c}_{\nu_k}(\tau_k) \hat{c}_{\nu_k'}^\dagger(\tau_k') \ldots \hat{c}_{\nu_1}(\tau_1) \hat{c}_{\nu_1'}^\dagger(\tau_1') \right] \det \mathbf{\Delta}. \tag{3.61}$$

3.1.4 Expansion with respect to dual operators

Now I want to show a derivation of the hybridization expansion within the path integral formalism, where bath and impurity operators are treated on an equal footing: both appear as Grassmann numbers with their corresponding measure. For the impurity operators it is the inverse atomic Green's function, and for the dual bath operators it is the inverse hybridization function. This formulation has the advantage, that at no point combinatoric arguments or a symmetrization of the result are necessary. It was invented by Lewin Boehnke and Alexey Rubsov, and sketched in the thesis of Boehnke (2015).

So let us start with the effective action

$$S_{\mathrm{eff}}[\bar{\boldsymbol{c}}, \boldsymbol{c}] = S_{\mathrm{at}}[\bar{\boldsymbol{c}}, \boldsymbol{c}] - \int_0^\beta \mathrm{d}\tau \int_0^\beta \mathrm{d}\tau' \sum_{\nu\nu'} \bar{c}_\nu(\tau) \Delta_{\nu\nu'}(\tau - \tau') c_{\nu'}(\tau') \tag{3.62}$$

and apply the Hubbard-Stratonovich transformation a second time to the retarded term, which gives[6]

$$S_{\text{dual}}\Big[\bar{\boldsymbol{c}},\boldsymbol{c},\bar{\boldsymbol{f}},\boldsymbol{f}\Big] = S_{\text{at}}[\bar{\boldsymbol{c}},\boldsymbol{c}] - \int_0^\beta \mathrm{d}\tau \int_0^\beta \mathrm{d}\tau' \sum_{\nu\nu'} \bar{f}_\nu(\tau)\Delta^{-1}_{\nu\nu'}(\tau-\tau')f_{\nu'}(\tau') \tag{3.63}$$

$$+ \int_0^\beta \mathrm{d}\tau \sum_\nu \bar{c}_\nu(\tau)f_\nu(\tau) + \int_0^\beta \mathrm{d}\tau' \sum_{\nu'} \bar{f}_{\nu'}(\tau')c_{\nu'}(\tau'). \tag{3.64}$$

Let' briefly discuss this action. There are the impurity operators, whose integral measure is the atomic action S_{at}, which will later govern the time-evolution on the impurity. The new dual operators f and $\bar{f}$ have the measure

$$S_{\text{dual}}\Big[\bar{\boldsymbol{f}},\boldsymbol{f}\Big] = -\int_0^\beta \mathrm{d}\tau \int_0^\beta \mathrm{d}\tau' \sum_{\nu\nu'} \bar{f}_\nu(\tau)\Delta^{-1}_{\nu\nu'}(\tau-\tau')f_{\nu'}(\tau'). \tag{3.65}$$

Since they are non-interacting, their time-evolution can be encapsulated in a propagator, the inverse hybridization function. An expansion with regard to the mixed terms gives

$$Z = \int \mathcal{D}\bar{\boldsymbol{c}}\,\mathcal{D}\boldsymbol{c}\,\mathrm{e}^{S_{\text{at}}[\bar{\boldsymbol{c}},\boldsymbol{c}]} \int \mathcal{D}\bar{\boldsymbol{f}}\,\mathcal{D}\boldsymbol{f}\,\mathrm{e}^{S_{\text{dual}}[\bar{\boldsymbol{f}},\boldsymbol{f}]} \tag{3.66}$$

$$\cdot \exp\left[\int_0^\beta \mathrm{d}\tau \sum_\nu \bar{c}_\nu(\tau)f_\nu(\tau) + \int_0^\beta \mathrm{d}\tau' \sum_{\nu'} \bar{f}_{\nu'}(\tau')c_{\nu'}(\tau')\right] \tag{3.67}$$

$$= \int \mathcal{D}\bar{\boldsymbol{c}}\,\mathcal{D}\boldsymbol{c}\,\mathrm{e}^{S_{\text{at}}[\bar{\boldsymbol{c}},\boldsymbol{c}]} \int \mathcal{D}\bar{\boldsymbol{f}}\,\mathcal{D}\boldsymbol{f}\,\mathrm{e}^{S_{\text{dual}}[\bar{\boldsymbol{f}},\boldsymbol{f}]} \tag{3.68}$$

$$\cdot \sum_{k=0}^\infty \frac{1}{k!} \sum_{\nu_1\nu_1'\ldots\nu_k\nu_k'} \int \mathrm{d}\tau_1\mathrm{d}\tau_1'\ldots\mathrm{d}\tau_k\mathrm{d}\tau_k' \tag{3.69}$$

$$\cdot \mathcal{T}_\tau\Big[\bar{c}_{\nu_1}(\tau_1)f_{\nu_1}(\tau_1)\bar{f}_{\nu_1'}(\tau_1')c_{\nu_1'}(\tau_1')\ldots\bar{c}_{\nu_k}(\tau_k)f_{\nu_k}(\tau_k)\bar{f}_{\nu_k'}(\tau_k')c_{\nu_k'}(\tau_k')\Big] \tag{3.70}$$

$$= \int \mathcal{D}\bar{\boldsymbol{c}}\,\mathcal{D}\boldsymbol{c}\,\mathrm{e}^{S_{\text{at}}[\bar{\boldsymbol{c}},\boldsymbol{c}]} \int \mathcal{D}\bar{\boldsymbol{f}}\,\mathcal{D}\boldsymbol{f}\,\mathrm{e}^{S_{\text{dual}}[\bar{\boldsymbol{f}},\boldsymbol{f}]} \tag{3.71}$$

$$\cdot \sum_{k=0}^\infty \frac{1}{k!} \sum_{\nu_1\nu_1'\ldots\nu_k\nu_k'} \int \mathrm{d}\tau_1\mathrm{d}\tau_1'\ldots\mathrm{d}\tau_k\mathrm{d}\tau_k' \tag{3.72}$$

$$\cdot \mathcal{T}_\tau\Big[\bar{c}_{\nu_1}(\tau_1)c_{\nu_1'}(\tau_1')\ldots\bar{c}_{\nu_k}(\tau_k)c_{\nu_k'}(\tau_k')\Big] \tag{3.73}$$

$$\cdot \mathcal{T}_\tau\Big[f_{\nu_1}(\tau_1)\bar{f}_{\nu_1'}(\tau_1')\ldots f_{\nu_k}(\tau_k)\bar{f}_{\nu_k'}(\tau_k')\Big]. \tag{3.74}$$

The expectation value of the impurity operators will have to be calculated brute force for each Monte Carlo configuration, whereas for the dual operators we can apply Wick's theorem. The contraction of two dual operators gives[7]

$$\langle f_\nu(\tau)\bar{f}_{\nu'}(\tau')\rangle = \Delta_{\nu'\nu}(\tau-\tau'). \tag{3.75}$$

[6]The integral is $Z_G(\boldsymbol{M},\boldsymbol{\eta},\bar{\boldsymbol{\eta}}) = \int \mathrm{d}\theta_1\mathrm{d}\bar{\theta}_1\ldots\mathrm{d}\theta_N\mathrm{d}\bar{\theta}_N \exp\Big(\sum_{ij=1}^N \bar{\theta}_i M_{ij}\theta_j + \sum_i\left(\bar{\eta}_i\theta_i + \bar{\theta}_i\eta_i\right)\Big)$
$= \det\boldsymbol{M}\exp\Big(-\sum_{ij}\bar{\eta}_i\Delta_{ij}\eta_j\Big)$, with
$\eta_j(\tau') = c_{\nu'}(\tau')$,
$\bar{\eta}_i(\tau) = \bar{c}_\nu(\tau)$,
$\bar{\theta}(\tau) = \bar{f}(\tau)$,
$\theta(\tau') = f(\tau')$, and
$\Delta_{ij} = \Delta_{\nu\nu'}(\tau-\tau')$,

[7]The integral over the measure of the dual operators is of type $Z = \int \mathrm{d}\theta\mathrm{d}\bar{\theta}\exp\Big[\sum_{ij}\bar{\theta}_i M_{ij}\theta_j + \sum_i(\bar{\eta}_i\theta_i + \bar{\theta}_i\eta_i)\Big]$, which evaluates to $Z = \det M\exp(-\sum_{ij}\bar{\eta}_i\Delta_{ij}\eta_j)$. Then an expectation value of two thetas evaluates to $\langle\bar{\theta}_i\theta_j\rangle = \frac{\partial}{\partial\eta_i}\frac{\partial}{\partial\bar{\eta}_j}Z = \Delta_{ji}$. Note the exchange of the indices in the Delta compared to the thetas.

Therefore Eq. (C.75) from the appendix gives

$$\mathcal{T}_\tau \left[f_{\nu_1}(\tau_1)\bar{f}_{\nu'_1}(\tau'_1)\dots f_{\nu_k}(\tau_k)\bar{f}_{\nu'_k}(\tau'_k)\right] \tag{3.76}$$

$$= \sum_{\substack{\text{permutations } \pi \\ \text{of } \{1,\dots,k\}}} \operatorname{sign}(\pi) \left\langle f_{\nu_1}(\tau_1)\bar{f}_{\nu_{\pi(1)}}(\tau'_{\pi(1)})\right\rangle \dots \left\langle f_{\nu_k}(\tau_k)\bar{f}_{\nu_{\pi(k)}}(\tau'_{\pi(k)})\right\rangle \tag{3.77}$$

$$= \sum_{\substack{\text{permutations } \pi \\ \text{of } \{1,\dots,k\}}} \operatorname{sign}(\pi) \prod_{i=1}^{k} \Delta_{\nu_i\nu_{\pi(i)}}(\tau_i - \tau_{\pi(i)}) \tag{3.78}$$

$$= \det \mathbf{\Delta}. \tag{3.79}$$

The final result is

$$\begin{aligned} Z = \sum_k \frac{1}{k!} \sum_{\nu_1\nu'_1} \cdots \sum_{\nu_k\nu'_k} \int_0^\beta \mathrm{d}\tau_1 \int_0^\beta \mathrm{d}\tau'_1 \cdots \int_0^\beta \mathrm{d}\tau_k \int_0^\beta \mathrm{d}\tau'_k \\ \times \operatorname{Tr}_c \left[\mathrm{e}^{-\beta H_{\mathrm{loc}}} T_\tau c_{\nu_k}(\tau_k) c^\dagger_{\nu'_k}(\tau'_k) \dots c_{\nu_1}(\tau_1) c^\dagger_{\nu'_1}(\tau'_1)\right] \\ \times \det \mathbf{\Delta}. \end{aligned} \tag{3.80}$$

Let me note, that instead of two Hubbard-Stratonovich transforms, which go essentially back and forth, one can also cut short from Eq. (3.35) to Eq. (3.66) by a *non-unitary* transform of the bath operators via $\hat{f}_\nu(\tau) = \sum_{p\mu} V_{p\mu\nu}\hat{a}_{p\mu}(\tau)$.

3.2 Discussion of the expansion

In this section I will discuss the form of the CTHYB expansion formula, how it relates to Feynman diagrams, as well as the differences between the two types of measuring the Green's function: Z-sampling (corresponds to resampling) and G-sampling (worm sampling).

Let me start with the the second line of Eq. (3.80), the trace $\operatorname{Tr}_c[\dots] = \sum_s \langle s|\dots|s\rangle$. It sums over a complete many-body basis of the impurity, which for two flavours is $|s\rangle \in \{|0\rangle, |\uparrow\rangle, |\downarrow\rangle, |\uparrow\downarrow\rangle\}$. Its argument is a time-ordered product of impurity operators, whose time-evolution is governed by $\hat{H}_{\mathrm{loc}}$ via $\hat{c}_\nu(\tau) = \mathrm{e}^{\hat{H}_{\mathrm{loc}}\tau}\hat{c}_\nu \mathrm{e}^{-\hat{H}_{\mathrm{loc}}\tau}$. Let me introduce an abbreviated notation for the local weight of

$$w_{\mathrm{loc}}(\mathcal{C},\mathcal{C}') = \operatorname{Tr}_c \left[\mathrm{e}^{-\beta\hat{H}_{\mathrm{loc}}} T_\tau \prod_{(\nu,\tau)\in\mathcal{C}} \hat{c}^\dagger_\nu(\tau) \prod_{(\nu',\tau')\in\mathcal{C}'} \hat{c}_{\nu'}(\tau')\right], \tag{3.81}$$

where $\mathcal{C} = \{(\nu_1,\tau_1),\dots,(\nu_k,\tau_k)\}$ contains the flavours and times of the creators, and $\mathcal{C}' = \{(\nu'_1,\tau'_1),\dots,(\nu'_k,\tau'_k)\}$ those of the annihilators. I want to introduce a second notation, which will turn out useful for other purposes, namely to keep a symbolic representation of the time-ordered product of operators:

$$\hat{\mathcal{C}} = T_\tau \hat{c}_{\nu_k}(\tau_k)\hat{c}^\dagger_{\nu'_k}(\tau'_k)\dots\hat{c}_{\nu_1}(\tau_1)\hat{c}^\dagger_{\nu'_1}(\tau'_1). \tag{3.82}$$

Writing $w_{\mathrm{loc}}(\hat{\mathcal{C}})$ or $\operatorname{Tr}[\hat{\mathcal{C}}]$ shall be the same object as $w_{\mathrm{loc}}(\mathcal{C},\mathcal{C}')$, which allows to access or manipulate properties of operators and its neighbors in the time-ordered product via $\mathcal{C}[\dots\,\hat{c}_{\nu_i}(\tau_i)\hat{c}^\dagger_{\nu'_i}(\tau'_j)\dots]$.

Let's take a partition function configuration $\hat{c}^\dagger_\downarrow(\tau_1)\hat{c}^\dagger_\uparrow(\tau_2)\hat{c}_\downarrow(\tau'_1)\hat{c}_\uparrow(\tau'_2)$ of an AIM with two flavours $\uparrow$ and $\downarrow$ as an example (Fig. 3.1). This corresponds to $\mathcal{C} = \{(\downarrow,\tau_1),(\uparrow,\tau_2)\}$ and $\mathcal{C}' = \{(\downarrow,\tau'_1),(\uparrow,\tau'_2)\}$ in the abbreviated notation. The filled (empty) diamonds indicate the annihilation (creation) of an electron on the impurity. The dashed lines attached to an operator represent a connection of this operator to the bath. The bath weight $w_{\mathrm{bath}}(\mathcal{C},\mathcal{C}') = \det\mathbf{\Delta}$ (third line in Eq. (3.80))

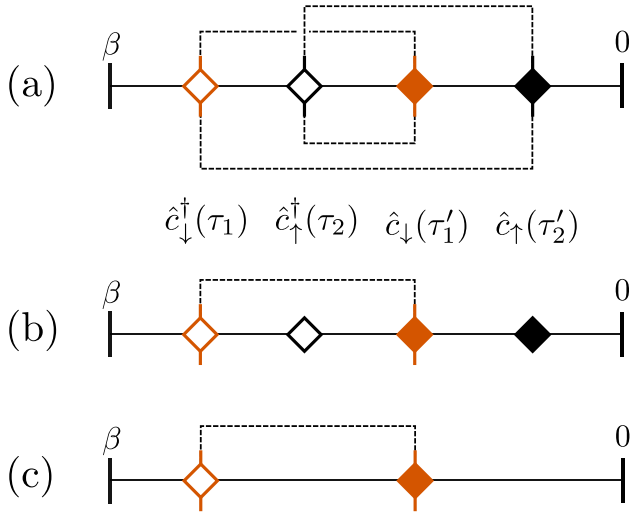

Figure 3.1: *a) Z-configuration for the Falicov-Kimball impurity. Empty diamonds denote creation operators, filled diamonds annihilation operators. The red dashed lines mean a propagation of the electron through the bath.*
b) Green's function configuration the Falicov-Kimball impurity. c) Z-configuration, which connects to configuration b) by inserting two worm operators.

describes the retardation effect of the bath on the impurity. It contains three processes combined: the hopping from impurity to bath, propagation through the bath, and hopping back from bath to impurity. In our example an impurity electron / bath hole pair is created at τ_2. The bath hole propagates to τ'_2, where it hops back to the impurity; the propagator for these three processes combined is $\Delta_{\uparrow\uparrow}(\tau_2 - \tau'_2)$. The same happens with another hole from τ_1 to τ'_1 via $\Delta_{\downarrow\downarrow}(\tau_1 - \tau'_1)$. A second possibility is that the hole at τ_2 goes to τ'_1 with propagator $\Delta_{\uparrow\downarrow}(\tau_2 - \tau'_1)$, then the hole from τ_1 must go to τ'_2 via $\Delta_{\downarrow\uparrow}(\tau_1 - \tau'_2)$. All these combinatorically possible propagations give the determinant

$$w_{\text{bath}}(\mathcal{C}_Z) = \det \begin{pmatrix} \Delta_{\downarrow\downarrow}(\tau_1 - \tau'_1) & \Delta_{\downarrow\uparrow}(\tau_1 - \tau'_2) \\ \Delta_{\uparrow\downarrow}(\tau_2 - \tau'_1) & \Delta_{\uparrow\uparrow}(\tau_2 - \tau'_2) \end{pmatrix}. \tag{3.83}$$

The general form of the bath weight is

$$w_{\text{bath}}(\mathcal{C}, \mathcal{C}') = \det \mathbf{\Delta}, \tag{3.84}$$

where the matrix elements are $\Delta_{ij} = \Delta_{\nu_i,\nu'_j}(\tau_i - \tau'_j)$ with $(\nu_i, \tau_i) \in \mathcal{C}$ and with $(\nu'_j, \tau'_j) \in \mathcal{C}'$.

Now let's discuss the two types of measuring the Green's function. The series expansion of the Green's function is

$$G_{\nu\nu'}(\tau - \tau') = \frac{1}{Z} \sum_{\mathcal{C}} w_{\text{loc}}(\mathcal{C} \cup \{\nu, \tau\}, \mathcal{C}' \cup \{\nu', \tau'\}) w_{\text{bath}}(\mathcal{C}, \mathcal{C}'). \tag{3.85}$$

It takes a partition function configuration $\mathcal{C}$, which was generated by the Markov chain, and adds a vertex $\{(\nu, \tau)\}$ to the set of creator vertices, and a vertex $\{(\nu', \tau')\}$ to the annihilator vertices in the local weight only (indicated by the union symbol). This is depicted in Fig. 3.1 (b), with Green's functions operators $\hat{c}^\dagger_\uparrow(\tau_2)$ and $\hat{c}_\uparrow(\tau'_2)$ added to the configuration (c). Sampling this expansion is referred to as worm sampling or G-sampling (Gunacker et al., 2015).

The standard way to measure the Green's function (Z-sampling) is different and a form of re-sampling. The Markov chain produces partition function configurations with weight $w_{\mathrm{loc}}(\mathcal{C},\mathcal{C}')w_{\mathrm{bath}}(\mathcal{C},\mathcal{C}')$, from which Green's function configurations are created via

$$\begin{aligned} G_{\alpha\alpha'}(\tau) &= \frac{1}{Z}\sum_{\mathcal{C}} w_{\mathrm{loc}}(\mathcal{C},\mathcal{C}')w_{\mathrm{bath}}(\mathcal{C},\mathcal{C}') \\ &\quad\times \sum_{n,m=1}^{k} \frac{w_{\mathrm{bath}}(\mathcal{C}\backslash\{(\alpha_n,\tau_n)\},\mathcal{C}'\backslash\{(\alpha'_m,\tau'_m)\})}{w_{\mathrm{bath}}(\mathcal{C},\mathcal{C}')} \\ &\quad\times \delta^-(\tau,\tau_n-\tau'_m)\delta_{\alpha\alpha_n}\delta_{\alpha'\alpha'_m} \qquad (3.86)\\ &= \frac{1}{Z}\sum_{\mathcal{C}} w_{\mathrm{loc}}(\mathcal{C},\mathcal{C}')w_{\mathrm{bath}}(\mathcal{C},\mathcal{C}') \qquad (3.87)\\ &\quad\times \sum_{n,m=1}^{k} M_{nm}\ \delta^-(\tau,\tau_n-\tau'_m)\delta_{\alpha\alpha_n}\delta_{\alpha'\alpha'_m}. \qquad (3.88) \end{aligned}$$

The object after the sum $\sum_{nm}$ is the estimated quantity, where the original bath weight $w_{\mathrm{bath}}(\mathcal{C},\mathcal{C}')$ is replaced by a bath weight, where $\{(\alpha_n,\tau_n)\}$ has been removed from the creator vertices and $\{(\alpha'_m,\tau'_m)\}$ from the annihilator vertices (indicated by the set difference). This leaves behind two operators in the local weight without hybridization lines, making them the Green's function operators. To exploit the full information of a Z-configuration, the procedure is applied for all possible pairs of annihilation and creation operators by the sum $\sum_{nm}$. The Green's function configuration in Fig. 3.1 (b) was created by removing the hybridization lines of two operators $\hat{c}^\dagger_\uparrow(\tau_2)$ and $\hat{c}_\uparrow(\tau'_2)$ compared to (a). The calculation of the fraction in Eq. (3.88), i.e. the ratio of two determinants, where in one of the matrices one row and column were removed, is usually done with fast Sherman Morrison formulas and gives a factor of M_{nm}, where $M=\Delta^{-1}$ is the inverse of the hybridization matrix. They are discussed extensively elsewhere (e.g. by Wallerberger (2016)) and therefore not reviewed in more detail here.

Finally let me illustrate the two sampling procedures (Fig. 3.2). In Z-sampling the sampling solely occurs in Z-space; for the measurment, Green's function configurations are created from Z-configurations. In G-sampling the random walk moves between Z-space and G-space and samples and measures in both.

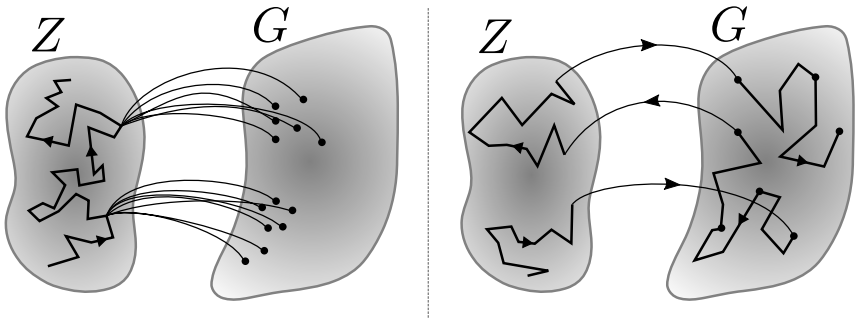

Figure 3.2: *Illustration of the two sampling procedures to measure the Green's function. Arrows indicate the direction that the random walker moves, black circles give the points in G-space where the Green's function is measured. In Z-sampling (left) the sampling only occurs in Z-space, and for generating Green's function configurations the Z-cofiguration is changed (two hybridization lines are removed). In G-sampling (right) also in G-space is sampled.*

3.3 State and superstate sampling

This chapter is based on the original work already published in Physical Review B (Kowalski et al., 2019). All figures and captions are taken from there, as well as some text (which is marked with a sidebar on the left).

3.3.1 State-of-the-art efficient implementation of CTHYB

CTHYB samples the space of atomic Green's functions of k-th order

$$G^{(k)}(\tau_1, \tau_1', \ldots, \tau_k, \tau_k') = \frac{1}{Z}\mathrm{Tr}_c \left[\mathrm{e}^{-\beta H_{\mathrm{loc}}} \hat{c}(\tau_k)\hat{c}^\dagger(\tau_k') \ldots \hat{c}(\tau_1)\hat{c}^\dagger(\tau_1') \right]. \tag{3.89}$$

The $G^{(k)}$ have to be calculated with an exact diagonalization method. Of course not the full, time-dependent object is calculated and stored. It is calculated on the fly for the specific times, which the Markov process demands.

While the exponential scaling with the number of flavours and the quadratic scaling with the inverse temperature are intrinsic to the local problem, potentially model-dependent improvements to the prefactor of this overall scaling can be achieved.

Common approaches to such optimization are block-diagonalization of the local Hamiltonian using conserved quantities (Haule, 2007; Parragh et al., 2012b) and binning, tree (Gull et al., 2011) or equivalent (Sémon et al., 2014) algorithms in so-called "matrix-matrix" implementations of CT-HYB. Additionally, with a similar motivation as for our method, outer truncation of the local trace to the few dominant contributions and calculation of those with more efficient sparse-matrix methods has been applied particularly to large systems at low temperatures (Läuchli and Werner, 2009). Other more advanced strategies are local updates in imaginary time (Shinaoka et al., 2014), a fast-rejection/acceptance algorithm by calculating upper/lower boundaries of the weight (Sémon et al., 2014), or a partial summation of diagrams to extract more information out of one Monte Carlo configuration (Augustinský and Kuneš, 2013).

In general, the local Hamiltonian H_{loc} conserves a set of quantum numbers. Consequently, the many-body Hilbert space can be partitioned into a set of linear subspaces $\{\mathcal{S}\}$, so-called "superstates" (Haule, 2007), and the Hamiltonian can be brought into a block-diagonal form with respect to these superstates.

3.3.2 Introduction

When designing a Monte-Carlo algorithm, there is a lot of freedom in what to define as a configuration. In Sec. 3.1.3 I have discussed, that summing up all combinatorically possible paths of electrons propagating through the bath, is necessary to avoid a disastrous sign problem.

In general, quantum mechanical expansions partition an observable into a sum of many terms. If one takes too few of these terms into one configuration, then the calculation of one weight is cheap, but there is likely a very bad sign problem. If one takes too many diagrams into one configuration, the calculation of one weight is very expensive, with a lighter sign problem (the extreme case would be to have one configuration with all diagrams, and the trivial Monte Carlo process has a sign of 1). Between these two limits exists an optimum of maximum efficiency, where the costs for calculating one configuration and the impact of the sign problem are balanced.

In this section I discuss, to what extent the local weight

$$w_{\mathrm{loc}}(\hat{\mathcal{C}}) = \sum_{\mathcal{S}} w_{\mathrm{loc},\mathcal{S}}(\hat{\mathcal{C}}) := \sum_{\mathcal{S}} \sum_{s\in\mathcal{S}} \langle s|\, \hat{\mathcal{C}}\, |s\rangle\,, \tag{3.90}$$

which the original algorithm always keeps together, can be decomposed into many smaller weights. Eq. (3.90) contains a sum over all superstates $\mathcal{S}$, whereas each superstate contains a sum over the states s it contains.

In other words, to what extent can the summands of $w_{\mathrm{loc}}(\hat{\mathcal{C}})$ be summed stochastically instead of deterministically?

We have the so called superstate-sampling algorithm, which takes $w_{\mathrm{loc},\mathcal{S}}(\hat{\mathcal{C}})$ as weight, and the states-sampling algorithm, which takes $\langle s|\, \hat{\mathcal{C}}\, |s\rangle$ as weight.

The method has been proposed by Markus Wallerberger in his thesis in 2016, but not implemented or tried out (Wallerberger, 2016).

3.3.3 Superstate sampling

The sampled distribution now is

$$Z = \underbrace{\sum_{\mathcal{C}} \sum_{\mathcal{S}}}_{\mathrm{QMC}} \sum_{s\in\mathcal{S}} \langle s|\, \hat{\mathcal{C}}\, |s\rangle\, w_{\mathrm{bath}}(\hat{\mathcal{C}}), \tag{3.91}$$

with an enlarged configuration space $\{\hat{\mathcal{C}}, \mathcal{S}\}$. This makes the calculation of one local weight faster, and thus also movement through configuration space. It is especially beneficial for systems with low symmetry, where the blocks of the Hamiltonian are large.

It must be carefully discussed, to what extent the newly defined configurations have different signs and this partitioning introduces a sign problem.

By just examining an example 5-orbital AIM (Fig. 3.3), the relative contribution of the second largest superstate is 0.01 % in average, and the contributions of the other superstates are damped exponentially. Thus the sign of w_{loc} is determined by its largest summand, which does not suggest the appearance of a sign problem.

A second argument in favor of this partitioning is the large-β limit, in which superstate sampling and the original algorithm are equivalent, since only one superstate survives in the local weight due to Pauli's principle. Therefore the average signs of the two algorithms in this limit must coincide. A sign-problem absent at low temperature and worsening at high temperature would contradict Troyer and Wiese (2005), which have proven that the sign problem becomes worse upon lowering the temperature.

In practice we indeed observe the same sign for both algorithms and all temperatures.

3.3.4 Window updates and τ-shift moves

As we have seen before, at low temperatures most of the configurations have only one possible outer superstate.

Since the effort of finding the possible superstates of a configuration is negligible compared to calculating the matrix-vector products (Haule, 2007), one might think superstate-sampling does not offer a benefit over the standard algorithm. But it does, since at this stage, it is already perfectly combinable with the window-sampling approach of Shinaoka et al. (2014). They showed that a tremendous speed-up can be achieved by proposing insertions of operator pairs only locally in imaginary time. If in window-sampling a proposed insert allows an additional another outer

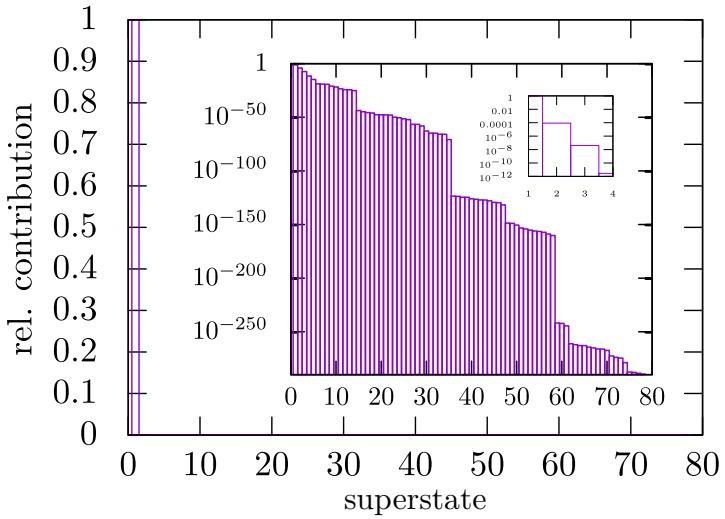

Figure 3.3: *Average relative contributions of outer superstates to the local weight per configuration for a typical simulation with five orbitals and Kanamori interaction. For comparability, the superstates are ordered by their contribution (i.e. absolute value of the part of the local weight sum from all states contained in the superstate) for each individual configuration, i.e. superstate "1" does not denote one specific constant superstate, but always refers to the biggest contributor.*

superstate than the current one, or requires the outer superstate to change, then for the new superstate the full operator sequence has to be calculated from scratch, which is expensive.

In superstate-sampling this case never happens, because the outer superstate is fixed when proposing insertions and removals.

To restore ergodicity, an additional move must be introduced to change the outer superstate. The naive choice of just proposing to change it, is highly inefficient, because as we have seen in Fig. 3.3, each configuration $\hat{\mathcal{C}}$ has a preferred superstate, and the contributions of the others are damped exponentially. Such a move would be expensive and have a very low acceptance rate.

Therefore we introduced the τ-shift move, which shifts the operator sequence in imaginary time. It is also an expensive move, since the whole operator sequence must be calculated from scratch, but it has an acceptance probability of one for superstate-sampling (for the proof see appendix of Kowalski et al. (2019)). This first means, that the infinite configurations connected by a τ-shift move can essentially be considered a single configuration. This is a nontrivial result, since it states that the cyclic property of the trace not only holds for the full trace, but also for each outer superstate.

Second, the ergodicity breaking cured by the τ-shifts is a tiny but crucial one. Let us divide all superstate sampling configurations into two classes: those ($\hat{\mathcal{C}}_{\mathcal{S}}$), which contain a certain superstate $\mathcal{S}$ at any imaginary time position, and those which do not ($\hat{\mathcal{C}}_{\bar{\mathcal{S}}}$). It holds $\hat{\mathcal{C}} = \hat{\mathcal{C}}_{\mathcal{S}} \cup \hat{\mathcal{C}}_{\bar{\mathcal{S}}}$. Fixing the outer superstate to $\mathcal{S}$ would only sample $\hat{\mathcal{C}}_{\mathcal{S}}$. Therefore the purpose of the τ-shift move is to also access $\hat{\mathcal{C}}_{\bar{\mathcal{S}}}$, which means it can be performed very rarely.

An example of a τ-shift move is depicted in Fig. 3.4.

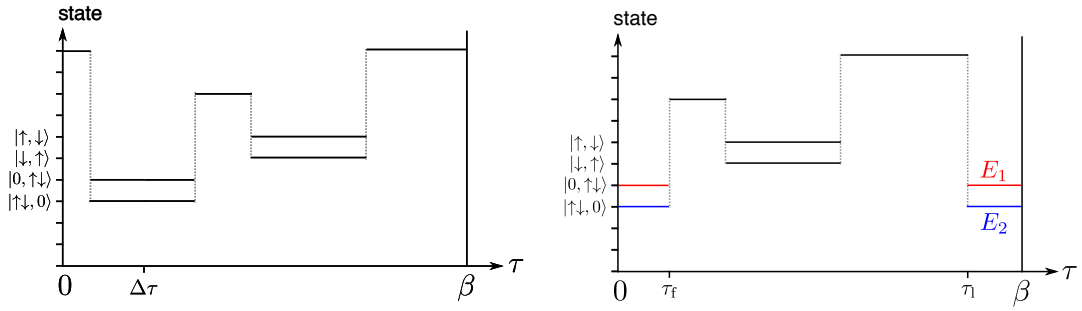

Figure 3.4: *Left: a superstate sampling configuration for a two orbital model with Kanamori interaction. Bold horizontal lines denote a time-evolution of an eigenstate, the dotted vertical lines the operators that cause transitions between superstates. Here all superstates have size 1, except the spin-flip and pair-hopping one. Right: the configuration resulting from application of a global τ-shift by $\Delta\tau$ to all operators of the one shown on the left. τ_f and τ_l denote the imaginary times of the first and last operator after the shift. In the superstate sampling algorithm the local weight is the sum of the red and blue state as outer state of the trace, whereas in the state sampling only one of the two is selected.*

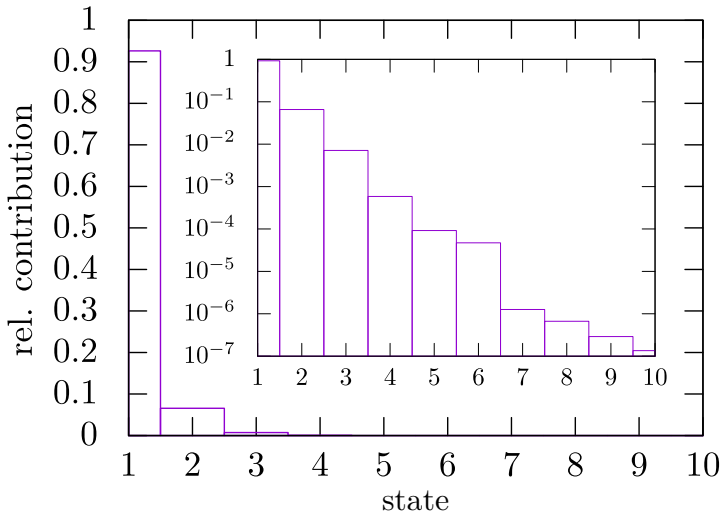

Figure 3.5: *Average relative contribution of outer states within one superstate, ordered by the size of contribution per configuration, normalized to the total weight of that superstate. This graph was obtained from a typical simulation of a 5-orbital system with Kanamori interaction.*

3.3.5 States sampling

Now I discuss the states-sampling algorithm, where both the summation over the superstates $\mathcal{S}$, and the summation over all states s within the chosen superstate, are done by the Monte Carlo:

$$Z = \underbrace{\sum_{\mathcal{C}} \sum_{\mathcal{S}} \sum_{s \in \mathcal{S}}}_{\text{QMC}} \langle s | \hat{\mathcal{C}} | s \rangle \, w_{\text{bath}}(\hat{\mathcal{C}}), \tag{3.92}$$

This corresponds to an enlarged configuration space of $\{\hat{\mathcal{C}}, \mathcal{S}, s \in \mathcal{S}\}$.

An argument as convincing as the large β limit in the previous section does not exist in favor for this algorithm. But a look at the relative contributions of states (Fig. 3.5) shows, that on average the largest state is one order of magnitude bigger than the second largest, the second largest one order of magnitude bigger than the third largest, and so on. One can hope, that the largest state determines the sign of the superstate often enough not to ruin the average sign. In practice, we observe a reduction of the average sign of a few percent.

Here the additional problem of choosing the outer state pops up; proposing it randomly would not give much benefit over a deterministic sum, since one would have to essentially try out all of them to find the dominant one.

We know that the candidates $|s\rangle$ at $\tau = 0$ and $\langle s|$ at $\tau = \beta$ are eigenstates of the local Hamiltonian. Therefore their time evolutions $\mathrm{e}^{-(E_s - E_0)\tau_f}$ and $\mathrm{e}^{(E_s - E_0)(\beta - \tau_l)}$ are known and act as multiplicative factor in $\langle s | \hat{\mathcal{C}} | s \rangle$. They are damped with an exponential factor, and we know that in advance. It is possible to transfer the first and last time-evolution (red and blue in Fig. 3.4) from the acceptance probability to the proposal probability. This has two advantages: the values of the acceptance probabilities are brought closer together, resulting in higher acceptance rates, and we are able to propose the likely outer states much more often. The proposal probability is an artificial Boltzmann distribution:

$$p_{\text{prop}}(s) = \frac{\exp[-(E_s - E_0) \cdot (\tau_f + \beta - \tau_l)]}{\sum_{k \in \mathcal{T}} \exp[-(E_k - E_0) \cdot (\tau_f + \beta - \tau_l)]}, \tag{3.93}$$

where $\mathcal{T}$ is the current outer superstate. Let me stress, that this procedure does not involve any approximation or assumption. It is an exact sampling, which enables the Monte Carlo to pick out the important parts of $w_{\text{loc}}(\hat{\mathcal{C}})$ and moves between them most of the time.

3.3.6 Performance and discussion

Figure 3.6 shows the average sign of an example calculation with a five orbital impurity. The Kanamori interaction has a constant sign of approximately 1, and the full Hubbard interaction a moderate sign problem with decreasing temperature. The sign of superstate sampling is not distinguishable to the original algorithm within the error bars for both interactions, and state-sampling has the sign reduced of about 5-10 %. The speed-up factors for superstate sampling compared to the original algorithm are 10-100 for Kanamori interaction and 150-250 for full-Hubbard interaction. Going from superstate- to state-sampling does not offer a benefit for the Kanamori interaction, since the blocks of the Hamiltonian are still quite small in this case; the largest ist a 10x10 matrix. State-sampling offers a noticeable speed-up or the full-Hubbard interaction compared to superstate-sampling, since the blocks are here considerably larger. For systems with lower symmetries these factors can still be orders of magnitude larger.

One might ask, may it be possible to apply the principle even one level deeper, namely to also sample the sums of the matrix-vector products when applying an operator to a state? We have

seen that sampling a sum reduces the average sign of about 5%. So for every additional 10 in the expansion order, the average sign drops by a multiplicative factor of $(0.95)^{20} \approx 0.35$. Clearly this is not acceptable, since typical expansion orders can be several hundreds.

In conclusion we find, that the states-sampling algorithm is the best compromise in balancing the costs for calculating one configuration and the impact of the sign problem.

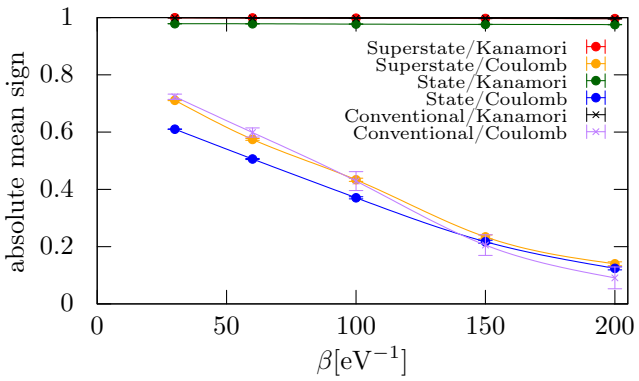

Figure 3.6: *Absolute value of the mean sign using our new sampling methods for a 5-orbital system with Kanamori or Coulomb interaction with cubic interpolation.*

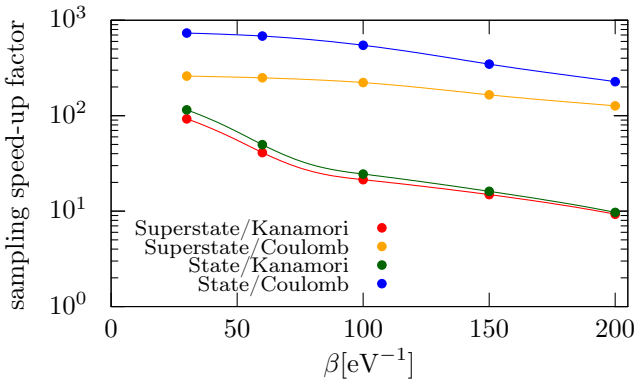

Figure 3.7: *Speed-up factors of the new sampling methods compared to conventional sampling for Kanamori and Coulomb interaction. For a 5-orbital system with Kanamori or full Hubbard interaction, not including measurement procedures of observables.*

3.4 The mixbasis algorithm

The treatment of general 7-orbital impurities (f-orbitals) poses a substantial challenge to CTHYB, which was up to now only feasible with approximations.

In these systems the non-Kanamori terms of the full-Hubbard interaction, spin-orbit coupling, as well as crystal fields are of the same order of magnitude. They are competing and thus have to be treated exactly. Because of these complicated one- and two-particle interactions the only conserved quantity on the impurity is the number of electrons. When there are n electrons on the

impurity, the blocks of the Hamiltonian have a size of $\binom{14}{n}$, or explicitly 1, 14, 91, 364, 1001, 2002, 3003, 3432, 3003, 2002, 1001, 364, 91, 14 and 1. An operator that describes the creation of an electron is a matrix. It has a size of 1x14 when going from zero to one electron, a size of 14x91 when going from one electron to two electrons, and so on. Therefore in order to save the operator matrices, the total number of nonzero matrix entries is

$$\sum_{n=0}^{13} \binom{14}{n} \cdot \binom{14}{n+1} = 37442160 \tag{3.94}$$

Storing a double precision number costs 64 bit, resulting in 2 396 298 240 bit, or 300 MB approximately. We need these operators $N_{\text{orbitals}} N_{\text{spins}} N_{\text{ca}} = 28$ times, giving a total memory requirement of 8400 MB for the operators on each processor, which is too much for the standard nodes of current supercomputers (SUPERMUC-NG has 304 000 cores with 2 GB per core, and 6900 cores with 16 GB per core).

Let's assume the system of interest has a filling of one electron on average. This means, in order to get that average, the number of electrons on the impurity must most of the time be zero, one, or two electrons, and the blocks with larger number of electrons must occur more and more rarely and are high excited states. It is reasonable to truncate them.

An outer truncation of the sum is to replace N with N_{trunc} in the local trace $\text{Tr}(\hat{\mathcal{C}}) = \sum_{n=1}^{N} \langle n| \hat{\mathcal{C}} |n\rangle$, assuming the eigenstates are ordered with increasing energy. This does not solve the memory issue; despite of starting with states $|n\rangle$ of low energy (and small matrix size), the configuration $\hat{\mathcal{C}}$ can also reach the highest excited states. An inner truncation means not to allow excitations in $\hat{\mathcal{C}}$ to exceed a certain energy level. In this case, all operators connecting to states above that level do not have to be stored, thus it alleviates the memory problem. However, both schemes are dangerous and give untrustworthy results.

In computer science there is a concept called time-memory trade-off. This means one can save memory by increasing the computation time by not storing objects, but instead calculating them on the fly whenever needed. In CTHYB such a trade-off is possible in the mixbasis algorithm.

The trace is usually calculated in the eigenbasis of the impurity Hamiltonian, i.e. the time-evolutions $\text{e}^{H_{\text{loc}}\tau}$ are diagonal matrices, and the operators are full matrices. It was shown by Läuchli and Werner (2009), that in the occupation number basis, the time-evolutions are complicated matrix exponentials, but the operator matrices are sparse and don't need notable space in memory at all.

The benefits of both bases can be combined. All time-evolutions are done in the eigenbasis, and whenever an operator has to be applied, the state vector is transformed from eigenbasis to occupation number basis. A sparse matrix-vector multiplication is performed, which has negligible costs compared to transformations between the bases. Then the state vector is transformed back to the eigenbasis, continuing with the time-evolution.

Let us estimate the additional costs of this procedure with the example of going from 6 to 7 electrons. The original algorithm needs a matrix-vector product with a 2002 x 3003 matrix, whereas in the mixbasis algorithm this is replaced by two matrix-vector products with matrix sizes 2002 x 2002 and 3003 x 3003. Assuming that the operator applications are the bottleneck, which definitely is the case for f-orbitals, the doubling of computation time completely removed the memory issues.

3.5 The sliding technique

CTHYB has the drawback, when measuring dynamic quantities, it always produces diagrams with delta-like information in imaginary time. The question arises, can out of such a configuration be extracted more information than that?

Another downside of delta peaks in imaginary time is that their Fourier transforms $e^{i\omega_n \tau}$ have essential singularities at $z = \infty$. Observables instead have a well defined high frequency behavior, therefore the singularities have to average away. This naturally causes large noise for the high frequency, which other methods like CTINT don't have, where each single measurement has a defined high frequency behavior (Gull et al., 2011).

The general idea of the sliding technique is to integrate out the time of one of the Greens function operators of a configuration. The delta-peaks in imaginary time now become continuous functions which still have steps, corresponding to essential singularities at $z = \infty$, but nevertheless the precision is increased since more information is extracted out of one configuration. The idea was originally developed by Augustinský and Kuneš (2013), but for density-density interactions only. The examinations in this chapter are a generalization thereof and valid for any kind of one- or two- particle interaction on the impurity.

A second application of the technique is to generate equal-time objects, which naturally never occur during simulation. They are necessary for physical susceptibilities or improved estimators. However I will show that the sliding-estimators of that kind are numerically not stable.

First I derive the sliding estimator for the single-particle Green's function, then I explain the general principle, and out of that re-derive the measurement of the single-particle Green's function. Last I derive and discuss the formulas for equal time objects.

3.5.1 Measuring the Green's function - heuristic derivation

Here I describe the sliding measurement procedure for the single-particle Green's function in Z-sampling.

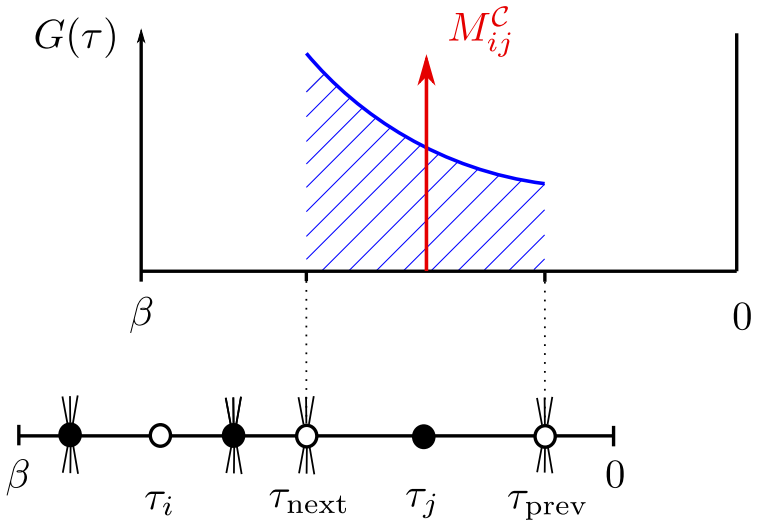

Figure 3.8: *This shows a configuration with four operators with hybridization lines (indicated by the three lines above and below them), and two Green's function operators without hybridization lines. Filled (empty) circles denote annihilation (creation) operators. The plot shows a single measurement of the standard estimator for the Green's function, which is a delta-function with prefactor $M_{ij}^{\mathcal{C}}$ (in red). The blue curve shows a single measurement of the sliding estimator. The area under the blue curve equals $M_{ij}^{\mathcal{C}}$.*

In Fig. 3.8 the standard measurement procedure for the Green's function in Z-sampling is depicted. The Markov chain has produced a Z-configuration, from which the hybridization lines (symbolized by the three lines above and below the operators) were removed from one creation and one annihilation operator in order to generate a Green's function configuration (see Eq. (3.88) in Sec. 3.2). At the time-difference $\tau_j - \tau_i$ of the two operators, in the Green's function array a delta-peak with integral M_{ij} appears (Eq. (3.96)). Now the operator at τ_j will be shifted to all possible τ positions, without changing the topology of the diagram, i.e. exchanging two operators. The objective is to sum up all the shifts. I call this procedure to *slide* the operator.

Moving the operator gives a multiplicative change of the weight of the configuration, which is not used to propose a new configuration, but to rescale the estimator of the Green's function. This results in a continuous curve. The area under this curve must be equal to M_{ij}, since the Markov chain asked to add a contribution of this size to the Green's function. Technically, we calculate the probability density of the moving operator.

Let's start with the measurement formula

$$G_{\alpha\beta}(\tau) = \frac{1}{\beta} \sum_{\mathcal{C}} \mathrm{Tr}[\hat{\mathcal{C}}]\det(\hat{\mathcal{C}}) \sum_{ij} M_{ij}^{\mathcal{C}}\, \delta^-(\tau, \tau_j - \tau_i)\delta_{\alpha\alpha_i}\delta_{\beta\beta_j} \tag{3.95}$$

$$= \frac{1}{\beta} \left\langle M_{ij}\delta^-(\tau, \tau_j - \tau_i)\right\rangle \tag{3.96}$$

for the Green's function in Z-sampling (Gull et al., 2011), where $M_{ij}^{\mathcal{C}}$ are the elements of the inverse hybridization matrix, and

$$\delta^-(\tau, \tau') = \begin{cases} \delta(\tau - \tau'), & \tau > \tau' \\ -\delta(\tau - \tau' - \beta), & \tau < \tau' \end{cases} \tag{3.97}$$

is the antiperiodic Dirac comb. The normalization factor for moving the operator τ_j is

$$N_j = \frac{1}{\int_{\tau_{\mathrm{prev}}}^{\tau_{\mathrm{next}}} \mathrm{d}\tau_j\ \mathrm{Tr}[\hat{\mathcal{C}}[..., c(\tau_j), ...]]}. \tag{3.98}$$

The integral boundaries τ_{prev} and τ_{next} are always the times of the neighboring operators of the slided operator in the time-ordered product. Actually all the operators have flavour indices, but since the concepts in this section do not fundamentally rely on the operator's flavours, I will omit them in the following. The estimator, where all annihilators are slided, is

$$G(i\omega_n) = \int \mathrm{d}\tau\ \mathrm{e}^{i\omega_n\tau} G(\tau) \tag{3.99}$$

$$= \frac{1}{\beta} \sum_{\mathcal{C}} \sum_{ij} \mathrm{Tr}[\hat{\mathcal{C}}]\det(\hat{\mathcal{C}})\ M_{ij}^{\mathcal{C}}\ \mathrm{e}^{i\omega_n(\tau_j - \tau_i)} \tag{3.100}$$

$$= \frac{1}{\beta} \sum_{\mathcal{C}} \sum_{ij} \mathrm{Tr}[\hat{\mathcal{C}}]\det(\hat{\mathcal{C}})\ M_{ij}^{\mathcal{C}} \frac{\int_{\tau_{\mathrm{prev}}}^{\tau_{\mathrm{next}}} \mathrm{d}\tau_j\ \mathrm{Tr}[\hat{\mathcal{C}}[...\hat{c}(\tau_j)...]]\ \mathrm{e}^{i\omega_n(\tau_j - \tau_i)}}{\int_{\tau_{\mathrm{prev}}}^{\tau_{\mathrm{next}}} \mathrm{d}\tau_j\ \mathrm{Tr}[...\hat{c}(\tau_j)...]}. \tag{3.101}$$

Note that it is not possible to formulate the estimator in imaginary time. This would correspond to Eq. (3.101) without the Fourier exponential, and the fraction would just cancel. When the trace is performed in the eigenbasis of the local Hamiltonian, the integration of the nominator

$$\int_{\tau_{\mathrm{prev}}}^{\tau_{\mathrm{next}}} \mathrm{d}\tau_j\ \mathrm{Tr}\left[... \mathrm{e}^{H_{\mathrm{loc}}(\tau_j - \tau_{\mathrm{next}})} c \mathrm{e}^{-H_{\mathrm{loc}}(\tau_j - \tau_{\mathrm{prev}})} ...\right] \mathrm{e}^{i\omega_n(\tau_j - \tau_i)} \tag{3.102}$$

boils down to integrating exponential functions.

Let me comment on the numerical stability of Eq. (3.101). One must investigate the possibility of the denominator becoming zero or very small. That could happen, if the neighboring operators are that close, that there is not much space for the operator to be slided. Assuming the trace does not change under tiny shifts, which is reasonable, we find

$$\int_{\tau_{\text{prev}}}^{\tau_{\text{next}}} \mathrm{d}\tau_j \ \mathrm{Tr}\left[\ldots \mathrm{e}^{H_{\text{loc}}(\tau_j-\tau_{\text{next}})} c \mathrm{e}^{-H_{\text{loc}}(\tau_j-\tau_{\text{prev}})} \ldots\right] \tag{3.103}$$

$$\sim (\tau_{\text{next}} - \tau_{\text{prev}}) \mathrm{Tr}(\hat{\mathcal{C}}), \tag{3.104}$$

where $\mathrm{Tr}(\hat{\mathcal{C}})$ is the trace of the original configuration. This object can become arbitrarily small, depending on how close the three operators at τ_{prev}, τ_j and τ_{next} get to each other. Since the integral appears in nominator and denominator, it cancels for $\tau_{\text{next}} - \tau_{\text{prev}} \to 0$ and leaves behind a well defined limit. The estimator therefore is numerically stable.

3.5.2 General Formalism

Here I describe the general mathematical theory of what we have done in the last paragraph.

All configurations $\hat{\mathcal{C}}$ are divided into equivalence classes $\hat{\mathcal{C}}_n$, denoted by integer subscript n[8]. Each diagram only belongs to one class, therefore the union amount of all classes corresponds to all diagrams

$$\hat{\mathcal{C}} = \bigcup_n \hat{\mathcal{C}}_n. \tag{3.105}$$

If we want to have all diagrams $\hat{\mathcal{C}}$ of one class $\hat{\mathcal{C}}_n$, we write $\hat{\mathcal{C}} \in \hat{\mathcal{C}}_n$. A class can also be represented by one of its diagrams; if we want to address all diagrams $\hat{\mathcal{C}}$ in one class $\hat{\mathcal{C}}_n$ by one representative $\hat{\mathcal{C}}'$ of this class, we write $\hat{\mathcal{C}} \sim \hat{\mathcal{C}}'$.

Now we derive the general sliding formula:

$$\sum_{\hat{\mathcal{C}}} f(\hat{\mathcal{C}}) g(\hat{\mathcal{C}}) = \sum_n \sum_{\hat{\mathcal{C}}' \in \hat{\mathcal{C}}_n} f(\hat{\mathcal{C}}') g(\hat{\mathcal{C}}') \tag{3.106}$$

$$= \sum_n \sum_{\hat{\mathcal{C}}'' \in \hat{\mathcal{C}}_n} f(\hat{\mathcal{C}}'') \frac{\sum_{\hat{\mathcal{C}}' \in \hat{\mathcal{C}}_n} f(\hat{\mathcal{C}}') g(\hat{\mathcal{C}}')}{\sum_{\hat{\mathcal{C}}''' \in \hat{\mathcal{C}}_n} f(\hat{\mathcal{C}}''')} \tag{3.107}$$

$$= \sum_{\hat{\mathcal{C}}} f(\hat{\mathcal{C}}) \frac{\sum_{\hat{\mathcal{C}}' \sim \hat{\mathcal{C}}} f(C') g(\hat{\mathcal{C}}')}{\sum_{\hat{\mathcal{C}}''' \sim \hat{\mathcal{C}}} f(\hat{\mathcal{C}}''')}, \tag{3.108}$$

Note how the only essential thing that has been done, was to insert a unity in Eq. (3.107). The final result, tidied up, is

$$\sum_{\hat{\mathcal{C}}} f(\hat{\mathcal{C}}) g(\hat{\mathcal{C}}) = \sum_{\hat{\mathcal{C}}} f(\hat{\mathcal{C}}) \frac{\sum_{\hat{\mathcal{C}}' \sim \hat{\mathcal{C}}} f(C') g(\hat{\mathcal{C}}')}{\sum_{\hat{\mathcal{C}}' \sim \hat{\mathcal{C}}} f(\hat{\mathcal{C}}')} \tag{3.109}$$

Eq. (3.109) means, when the Markov chain arrived at a configuration $\hat{\mathcal{C}}$, instead of measuring only $\hat{\mathcal{C}}$, we measure all configurations $\hat{\mathcal{C}}'$ that are in the same class as $\hat{\mathcal{C}}$.

[8] This is actually inaccurate, since the classes can not be counted nor ordered, but I will write it that way since it makes no difference.

3.5.3 Measuring the Green's function

In this subsection I will re-derive the result from Sec. 3.5.1 using the general formula Eq. (3.109). We find

$$G(i\omega_n) = \frac{1}{\beta}\sum_{\hat{\mathcal{C}}}\sum_{ij}\underbrace{\mathrm{Tr}[\hat{\mathcal{C}}]}_{f}\underbrace{\det(\hat{\mathcal{C}})\; M^{\hat{\mathcal{C}}}_{ij}\; \mathrm{e}^{i\omega_n(\tau_j-\tau_i)}}_{g} \tag{3.110}$$

$$= \frac{1}{\beta}\sum_{\hat{\mathcal{C}}}\sum_{ij}\mathrm{Tr}(\hat{\mathcal{C}})\frac{\sum_{\hat{\mathcal{C}}'\sim\hat{\mathcal{C}}}\mathrm{Tr}[\hat{\mathcal{C}}']\det(\hat{\mathcal{C}}')M^{\hat{\mathcal{C}}'}_{ij}\,\mathrm{e}^{i\omega_n(\tau_j-\tau_i)}}{\sum_{\hat{\mathcal{C}}'\sim\hat{\mathcal{C}}}\mathrm{Tr}(\hat{\mathcal{C}}')} \tag{3.111}$$

$$= \frac{1}{\beta}\sum_{\hat{\mathcal{C}}}\sum_{ij}\mathrm{Tr}(\hat{\mathcal{C}})\det(\hat{\mathcal{C}})M^{\hat{\mathcal{C}}}_{ij}\frac{\sum_{\hat{\mathcal{C}}'\sim\hat{\mathcal{C}}}\mathrm{Tr}[\hat{\mathcal{C}}']\mathrm{e}^{i\omega_n(\tau_j-\tau_i)}}{\sum_{\hat{\mathcal{C}}'\sim\hat{\mathcal{C}}}\mathrm{Tr}(\hat{\mathcal{C}}')} \tag{3.112}$$

$$= \frac{1}{\beta}\left\langle\sum_{ij}M_{ij}\frac{\sum_{\hat{\mathcal{C}}'\sim\hat{\mathcal{C}}}\mathrm{Tr}[\hat{\mathcal{C}}']\mathrm{e}^{i\omega_n(\tau_j-\tau_i)}}{\sum_{\hat{\mathcal{C}}'\sim\hat{\mathcal{C}}}\mathrm{Tr}(\hat{\mathcal{C}}')}\right\rangle. \tag{3.113}$$

The linear algebra identity

$$\det(\hat{\mathcal{C}}')M^{\hat{\mathcal{C}}'}_{ij} = \det(\hat{\mathcal{C}})M^{\hat{\mathcal{C}}}_{ij} \tag{3.114}$$

has been used in Eq. (3.112). The existence of a nontrivial identity like this can be motivated from the fact that by going from a configuration $\hat{\mathcal{C}}$ to $\hat{\mathcal{C}}'$ in two different ways, one must consistently obtain the same transition probability. The first way would be to start from a partition function configuration, remove two hybridization lines, and then shift one of the Green's function operators; the change of weight when shifting is obviously independent of the bath part $\det(\hat{\mathcal{C}})M^{\hat{\mathcal{C}}}_{ij}$. The second way of obtaining the final configuration is first to shift the operator, for which the bath $\det(\hat{\mathcal{C}})$ changes to $\det(\hat{\mathcal{C}}')$, and then remove the hybridization lines, which gives the factor $M^{\hat{\mathcal{C}}'}_{ij}$. From this considerations follows Eq. (3.114).

3.5.4 Measuring equal-time estimators

In this section I describe, how one might use the sliding technique to measure estimators with several operators at the same time, which are necessary for improved estimators, susceptibilities and the high-frequency dependency of 2-particle Green's functions. We will however find, that the equal-time estimators are numerically unstable.

I first discuss the most simple equal-time estimator, which is a density. We evaluate the Green's function at $\tau = 0^-$ and apply Eq. (3.109):

$$\langle n\rangle = G(\tau = 0^-) \tag{3.115}$$

$$= \sum_{\hat{\mathcal{C}}}\sum_{ij}\underbrace{\mathrm{Tr}[\hat{\mathcal{C}}]}_{f}\underbrace{\det[\hat{\mathcal{C}}]M_{ij}\delta[\tau_j = \tau_i - 0^-]}_{g} \tag{3.116}$$

$$= \sum_{\hat{\mathcal{C}}}\sum_{ij}\mathrm{Tr}[\hat{\mathcal{C}}]\frac{\sum_{\hat{\mathcal{C}}'\equiv\hat{\mathcal{C}}}\mathrm{Tr}[\hat{\mathcal{C}}']\det[\hat{\mathcal{C}}']M^{\hat{\mathcal{C}}'}_{ij}\delta[\tau_j = \tau_i - 0^-]\delta_{ai}\delta_{aj}}{\sum_{\hat{\mathcal{C}}'\equiv\hat{\mathcal{C}}}\mathrm{Tr}[\hat{\mathcal{C}}']} \tag{3.117}$$

$$= \sum_{\hat{\mathcal{C}}}\sum_{ij}\mathrm{Tr}[\hat{\mathcal{C}}]\det[\hat{\mathcal{C}}]M^{\hat{\mathcal{C}}}_{ij}\frac{\sum_{\hat{\mathcal{C}}'\equiv\hat{\mathcal{C}}}\mathrm{Tr}[\hat{\mathcal{C}}']\delta[\tau_j = \tau_i - 0^-]}{\sum_{\hat{\mathcal{C}}'\equiv\hat{\mathcal{C}}}\mathrm{Tr}[\hat{\mathcal{C}}']}\delta_{ai}\delta_{aj} \tag{3.118}$$

$$= \sum_{\hat{\mathcal{C}}}\sum_{ij}\mathrm{Tr}[\hat{\mathcal{C}}]\det[\hat{\mathcal{C}}]M^{\hat{\mathcal{C}}}_{ij}\frac{\mathrm{Tr}[\mathcal{C}_{\tau_j\to\tau_i+0^+}]}{\sum_{\hat{\mathcal{C}}'\equiv\hat{\mathcal{C}}}\mathrm{Tr}[\hat{\mathcal{C}}']}\delta_{ai}\delta_{aj} \tag{3.119}$$

$$= \left\langle M_{ij}\frac{\mathrm{Tr}[\hat{\mathcal{C}}_{\tau_j\to\tau_i+0^+}]}{\sum_{\hat{\mathcal{C}}'\equiv\hat{\mathcal{C}}}\mathrm{Tr}[\hat{\mathcal{C}}']}\delta_{ai}\delta_{aj}\right\rangle \tag{3.120}$$

This estimator now is much more dangerous that the one for the Green's function, since the integral in the denominator, which may become very small, is not canceled by an equally small nominator.

When the three operators $c^{(\dagger)}(\tau_{\text{next}})$, $c_i(\tau_j)$ and $c^{(\dagger)}(\tau_{\text{prev}})$ get very close to each other, the trace does not change upon sliding the middle operator and the fraction becomes

$$\frac{\mathrm{Tr}[\hat{\mathcal{C}}]}{\int_{\tau_{\text{prev}}}^{\tau_{\text{next}}} \mathrm{d}\tau_j \, \mathrm{Tr}[\dots c(\tau_{\text{next}})c(\tau_j)c^\dagger(\tau_{\text{prev}})\dots]} \approx \frac{\mathrm{Tr}[\hat{\mathcal{C}}]}{\mathrm{Tr}[\hat{\mathcal{C}}](\tau_{\text{next}} - \tau_{\text{prev}})} \tag{3.121}$$

$$= \frac{1}{(\tau_{\text{next}} - \tau_{\text{prev}})} \tag{3.122}$$

Some configurations will generate strong peaks, and when trying to remove them by increasing statistics, this generates just more peaks with even smaller $\tau_{\text{next}} - \tau_{\text{prev}}$, and the estimator never converges.

3.5.5 Measuring density correlation functions

For the sake of completeness, even though not recommendable to apply, I give here also the formula for measuring the one-time, two-particle Green's functions with the sliding technique, like for physical susceptibilities

$$\langle n(\tau)n(0)\rangle = \Big\langle c^\dagger(\tau)c(\tau)c^\dagger(0)c(0)\Big\rangle. \tag{3.123}$$

One begins with the measurement formula for the two-particle Green's function (Boehnke et al., 2011)

$$G_{abcd}(\tau_1,\tau_2,\tau_3,\tau_4) = \sum_{\hat{\mathcal{C}}}\sum_{ijkl} \mathrm{Tr}[\hat{\mathcal{C}}]\det[\hat{\mathcal{C}}](M_{ij}M_{kl} - M_{il}M_{jk}) \tag{3.124}$$

$$\cdot\, \delta(\tau_i - \tau_1)(\tau_j - \tau_2)(\tau_k - \tau_3)(\tau_l - \tau_4)\delta_{ai}\delta_{bj}\delta_{ck}\delta_{dl}. \tag{3.125}$$

The density correlation function is the special case

$$\langle n_a(\tau)n_b(0)\rangle = \sum_{\hat{\mathcal{C}}}\sum_{ijkl} \mathrm{Tr}[\hat{\mathcal{C}}]\det[\hat{\mathcal{C}}](M_{ij}M_{kl} - M_{il}M_{jk}) \tag{3.126}$$

$$\delta(\tau_i = \tau_j - 0^-)\delta(\tau_k = \tau_l - 0^-)\delta(\tau = \tau_i - \tau_k)\delta_{ai}\delta_{aj}\delta_{bk}\delta_{bl}. \tag{3.127}$$

Applying Eq. (3.109) to this expression twice, one finds

$$\langle n_a(\tau)n_b(0)\rangle = \sum_{\hat{\mathcal{C}}}\sum_{ijkl} \mathrm{Tr}[\hat{\mathcal{C}}]\det[\hat{\mathcal{C}}]\Big(M^{\hat{\mathcal{C}}}_{ij}M^{\hat{\mathcal{C}}}_{kl} - M^{\hat{\mathcal{C}}}_{il}M^{\hat{\mathcal{C}}}_{jk}\Big) \tag{3.128}$$

$$\cdot\, \frac{\mathrm{Tr}[\hat{\mathcal{C}}_{\tau_j\to\tau_i+0^+}]}{\sum_{\hat{\mathcal{C}}'_j\equiv\hat{\mathcal{C}}}\mathrm{Tr}(\hat{\mathcal{C}}'_j)} \frac{\mathrm{Tr}[\hat{\mathcal{C}}_{\tau_j\to\tau_i+0^+,\tau_l\to\tau_k+0^+}]}{\sum_{\hat{\mathcal{C}}'_l\equiv\hat{\mathcal{C}}_{\tau_j\to\tau_i+0^+}}\mathrm{Tr}[\hat{\mathcal{C}}'_l]}\delta_{ai}\delta_{aj}\delta_{bk}\delta_{bl}. \tag{3.129}$$

A possible procedure of accumulating would be the following (let's remind ourselves, that the result is independent of the order, but some orders may be much more complicated or impossible, since they contain an integral of the determinant):

- take a partition function configuration $\hat{\mathcal{C}}$
- remove the hybridization lines of the four operators involved
- calculate the norm for sliding the operator τ_j: $\sum_{\hat{\mathcal{C}}'_j\equiv\hat{\mathcal{C}}}\mathrm{Tr}(\hat{\mathcal{C}}'_j)$
- move operator τ_j to $\tau_i + 0^+$ and calculate trace: $\mathrm{Tr}[\hat{\mathcal{C}}_{\tau_j\to\tau_i+0^+}]$
- while the operator τ_j is kept at $\tau_i{+}0^+$, calculate the norm for sliding operator τ_l: $\sum_{\hat{\mathcal{C}}'_l\equiv\hat{\mathcal{C}}_{\tau_j\to\tau_i+0^+}}\mathrm{Tr}(\hat{\mathcal{C}}'_l)$
- then move operator τ_l to $\tau_k + 0^+$ and calculate the trace: $\mathrm{Tr}[\hat{\mathcal{C}}_{\tau_j\to\tau_i+0^+,\tau_l\to\tau_k+0^+}]$

3.5.6 Discussion

In this section I derived the sliding technique, which allows to integrate out the time of one Greens function operator. We have seen, that the method fails to produce configurations with equal-time operators because of divergent diagrams. The method works if it is used for smearing out the delta-estimators of Greens functions. This can be beneficial for systems with correlated f-shells. They are spatially rather localized and therefore expected to have low expansion order in CTHYB. Furthermore the sizes of the blocks of the local Hamiltonian is very large, making it very costly to calculate one Monte Carlo weight. This suggests that the sliding technique may be beneficial for f-impurities.

3.6 Measurement of density-density correlation functions

As last part of this chapter, I briefly show and discuss two estimators for the measurement of density-density correlation functions. Besides worm-sampling of $\langle \hat{n}(\tau)\hat{n}(0)\rangle$ there exist the shift-estimator, which shifts operators to make densities, and the insertion-estimator, which inserts densities in the Monte Carlo configuration.

3.6.1 Shift-estimators

A density can also be measured with the so-called shift-estimator. It works the following way: one changes the configuration, namely removes the hybridization lines of two neighboring operators, that have correct order to constitute a density, which gives a factor of M_{ij}. Then one shifts the creator into the annihilator, which gives a factor of $\mathrm{Tr}(\hat{\mathcal{C}}_{\tau_i\to\tau_j+0^+})/\mathrm{Tr}(\hat{\mathcal{C}})$.

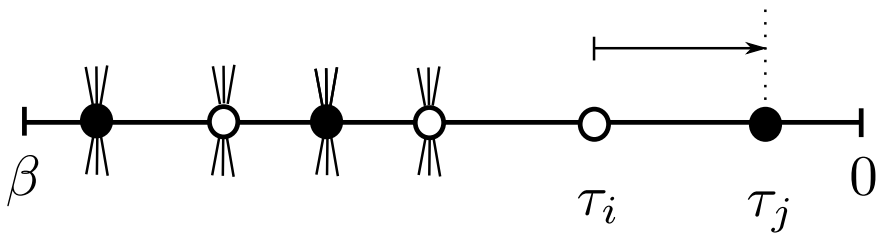

Figure 3.9: *The shift estimator. Creation operators (empty circles) are shifted close to annihilation operators to make densities.*

Therefore the estimator is

$$n = \left\langle \sum_{ij} M_{ij} \frac{\mathrm{Tr}(\hat{\mathcal{C}}_{\tau_i\to\tau_j+0^+})}{\mathrm{Tr}(\hat{\mathcal{C}})} \delta_{\tau_i \text{ and } \tau_j \text{ are neighbours}} \right\rangle . \tag{3.130}$$

Doing the thing twice with appropriate operators gives the density-density correlation function

$$\begin{aligned} \langle n(\tau)n(0)\rangle = \Bigg\langle \sum_{ijkl} \left(M^{\hat{\mathcal{C}}}_{ij} M^{\hat{\mathcal{C}}}_{kl} - M^{\hat{\mathcal{C}}}_{il} M^{\hat{\mathcal{C}}}_{jk} \right) \cdot \frac{\mathrm{Tr}[\hat{\mathcal{C}}_{\tau_i\to\tau_j+0^+,\tau_k\to\tau_l+0^+}]}{\mathrm{Tr}[\hat{\mathcal{C}}]} \\ \times \delta_{\tau_i \text{ and } \tau_j \text{ are neighbours}} \delta_{\tau_k \text{ and } \tau_l \text{ are neighbours}} \Bigg\rangle . \end{aligned} \tag{3.131}$$

The round brackets come from removing the hybridization lines of four operators, and in the trace of the nominator two densities are constructed.

3.6.2 Insertion estimators

It is known since the invention of CTHYB (Werner et al., 2006), that Green's functions cannot be measured by inserting a creation and an annihilation operator without hybridization lines into a configuration. That is because the application of an operator makes a transition to another block of the Hamiltonian, and thus also changes the superstate-sequence in between the two operators completely. It is likely that highly excited states are accessed, and thus the weight strongly damped. It generates many unlikely and few important Green's function diagrams. Very often also a Pauli violation happens between the inserted operators, which makes the contribution of the diagram exactly zero. Therefore this estimator only produces unlikely configurations and misses the likely ones and does not work.

Insertion estimators are only possible, if the operators inserted are projection operators, i.e. they bring a state back to the block of the Hamiltonian where it started, and thus the superstate-sequence between the operators is left unchanged. This is obviously true for densities.

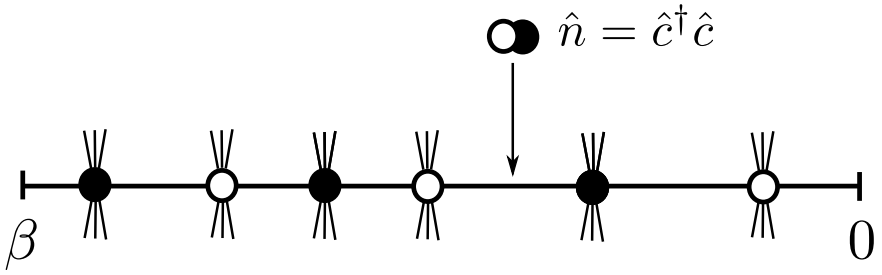

Figure 3.10: *insertion estimators*

The insertion estimator for measuring a density is

$$\langle n_a \rangle = \left\langle \frac{\mathrm{Tr}(\hat{\mathcal{C}}')}{\mathrm{Tr(C)}} \right\rangle, \tag{3.132}$$

where $\hat{\mathcal{C}}$ is the original Z-configuration and $\hat{\mathcal{C}}'$ the Z-configuration with a density operator n_a inserted (without hybridization lines).

For a density-density correlation function the estimator is

$$\langle n_a(\tau) n_b(0) \rangle = \left\langle \frac{\mathrm{Tr}(\hat{\mathcal{C}}'')}{\mathrm{Tr(C)}} \right\rangle, \tag{3.133}$$

where $\hat{\mathcal{C}}''$ is the Z-configuration $\hat{\mathcal{C}}$ with two density operators n_a and n_b (without hybridization lines) inserted at imaginary time difference τ.

`w2dynamics` has implemented the density-density and $\langle S_z(\tau) S_z(0) \rangle$ correlation function that way.

3.7 Conclusion

In this Chapter I first derived the CTHYB expansion formulas using three different paths: a brute force operator approach, the standard effective propagator formulation within Feynman's path integral technique, and with an elegant dual transform, that introduces the dual operators, which contain the effect of the bath and the hopping from bath to impurity within one operator.

I discussed the drawbacks of the technique, which is mainly the exponential scaling of the local problem, which has to be treated with an exact diagonalization method for every Monte Carlo move, and therefore constitutes the bottleneck of CTHYB.

The (super-)state sampling methods describes, how this local weight can be split up into smaller weights and sampled individually. This algorithmic improvementis the key part, which makes `w2dynamics` in its matrix-vector algorithm competitive to other implementations of CTHYB, which are mainly of matrix-matrix type (for a brief comparison of the two methods see Sec. 5.4).

I showed the mixbasis algorithm, which solves the memory-issue one faces with f-orbital impurities, and makes them accessible to CTHYB without truncation of the Hilbert space.

Then I discussed the sliding technique, which integrates over the time of one of the Greens function operators. It is not possible to generate equal-time estimators by applying the sliding technique, but it is possible to reduce the noise of Greens functions.

Last I briefly showed two estimators, which both can measure density-density correlation functions. The insertion estimator is highly perferable, since it can extract much more information out of a configuration compared to the shift estimator. The applicability of insertion estimators is restricted, such that the inserted operator applied on an impurity state must not change its conserved quantum numbers (for a discussion of quantum numbers see Sec. 5.1). With this reasoning, for systems where H_{loc} only conserves the number of electrons on the impurity, observables like $\langle J_x(\tau)J_x(0)\rangle$ or $\langle J_y(\tau)J_y(0)\rangle$ shall be measurable by insertions. Whether this is really true is subject of further work.

Chapter 4

Inconsistency of standard Green's function estimator in diagrammatic quantum Monte Carlo for finite systems

This chapter is an abbreviated version of what is being prepared for submission to Physical Review with co-authors Josef Kaufmann (TU Vienna), Markus Wallerberger (TU Vienna) and Giorgio Sangiovanni (University of Würzburg).

4.1 Abstract

In this chapter I describe an inconsistency of the standard Green's function estimator in CTHYB. It occurs due to Pauli's principle in finite baths of Anderson impurity models. We identify Feynman diagrams missing from the series and characterize the affected models. We argue that it can also manifest itself in systems with infinite bath size as very long autocorrelation times.

4.2 Introduction

Unlike in the classical case, in quantum mechanics each observable is operator-valued and comes with its own generating function, and thus after a series expansion, with its own probability distribution. In principle, Monte Carlo algorithms have to sample these distributions separately, e.g. the mean density, the one-particle propagator, and even the propagator evaluated at different times or orbitals.

Two methods are known to deal with this issue: (i) worm sampling, where one forms the direct sum over the probability spaces of all observables considered and samples that compound distribution. This quickly leads to an unwieldy number of computations. If the distributions of interest are similar in their structure, which is often the case, with (ii) resampling, one can sample only a single distribution and map all other observables to different estimators with respect to that distribution. Resampling is algorithmically simpler but yields an inconsistent estimator (and thus wrong results) if the mapping is not surjective. One also runs into autocorrelation problems if the mapping is indeed surjective, but the probability distributions are substantially different.

In this chapter I explore one such inconsistency for continuous-time quantum Monte Carlo in the hybridization expansion (CTHYB, Werner et al. (2006)). Here, the partition function is expanded with respect to the bath hybridization.

In measuring the Green's function, one usually employs resampling, relating each Green's function diagram to a process of "cutting" parts off a diagram in partition function space. This is already known to fail for equal-time correlators, certain higher order Green's functions, and close to the atomic limit. There, worm sampling must be used instead (Gunacker et al., 2015).

However, resampling is still widely used because it is believed to succeed away from these cases. We show that resampling yields inconsistent estimators also for certain finite systems, curtailing the viability of the method in quantum chemistry applications. We also show that for certain infinite systems, this form of resampling, while formally consistent, causes the autocorrelation length to grow significantly.

The chapter is organized as follows: We identify missing Feynman diagrams in systems with finite bath size in section 4.3. In section 4.4 we show an example and make the link to autocorrelation times. Finally in section 4.5, we show a system with infinite bath size and autocorrlation problems, before we conclude.

4.3 Inconsistency of the Z-estimator

Here we work out the inconsistency of the Z-estimator for the Green's function by closely examining Eq. (3.88) from chapter 3.2:

$$\begin{aligned} G_{\alpha\alpha'}(\tau) = \frac{1}{Z}\sum_{\mathcal{C}} & w_{\mathrm{loc}}(\mathcal{C},\mathcal{C}')w_{\mathrm{bath}}(\mathcal{C},\mathcal{C}') \\ & \times \sum_{n,m=1}^{k} \frac{w_{\mathrm{bath}}(\mathcal{C}\backslash\{(\alpha_n,\tau_n)\},\mathcal{C}'\backslash\{(\alpha'_m,\tau'_m)\})}{w_{\mathrm{bath}}(\mathcal{C},\mathcal{C}')} \\ & \times \delta^{-}(\tau,\tau_n-\tau'_m)\delta_{\alpha\alpha_n}\delta_{\alpha'\alpha'_m}. \end{aligned} \tag{4.1}$$

Suppose $w_{\mathrm{bath}}(\mathcal{C},\mathcal{C}')$ is zero, then the Z-configuration

$$w_{\mathrm{loc}}(\mathcal{C},\mathcal{C}')w_{\mathrm{bath}}(\mathcal{C},\mathcal{C}') \tag{4.2}$$

will never be reached. If now the cutting of the hybridization lines of two operators makes

$$w_{\mathrm{bath}}(\mathcal{C}\backslash\{(\alpha_n,\tau_n)\},\mathcal{C}'\backslash\{(\alpha'_m,\tau'_m)\}) \tag{4.3}$$

nonzero for any n and m, these Green's function configurations are missed by Z-sampling.

This can happen in systems with a finite number of bath sites, where the bath can only host a finite number of electrons due to Pauli's principle. If a Z-configuration wants to deposit more electrons in the bath than possible, its weight becomes exactly zero, and possible derived G-configurations are missed. The affected AIMs and diagrams can be exactly characterized, which we will do in the following.

Let us define a *cluster* on the impurity of size N, as the set of impurity flavors, which are connected by one- and two-particle interaction terms. As example we investigate a cluster of size $N = 4$ (see Fig. 4.1), where four impurity flavors (black circles) are connected by a hopping t. Without loss of generality, we analyze what happens at impurity flavor 1, by comparing the four-bath-site system A) to the three-bath-site system B).

In both systems the impurity cluster can host at most four electrons, therefore in the local configuration can be at most four consecutive annihilation operators of flavor 1. The diagram we

are going to discuss is a G-configuration with four annihilators of flavor 1 in a row, and one of them is a Green's function operator, which means it has no hybridization lines.

In G-sampling, these four operators are generated directly and need to deposit three electrons in the bath connected to impurity flavor 1, which is possible for both systems A) and B).

Now let us see what happens in Z-sampling. The Markov chain proposes a Z-configuration with four consecutive annihilators for flavor 1, which are all connected to the bath. For system A) this is possible, since there is space for four electrons in the bath. In system B) the weight of this configuration is always zero, since the attempt to deposit four electrons in this bath violates the Pauli principle. But by applying the resampling procedure and removing the hybridization lines of one of the four operators, the generated Green's function diagram is nonzero in both systems. It deposits three electrons in the bath, which is also possible in system B). Therefore by going the detour over a Z-configuration, Z-sampling misses this G-diagram in system B).

In summary, Z-sampling for the Green's function is inconsistent for a cluster of size N, if any flavor within the cluster has less than N bath sites.

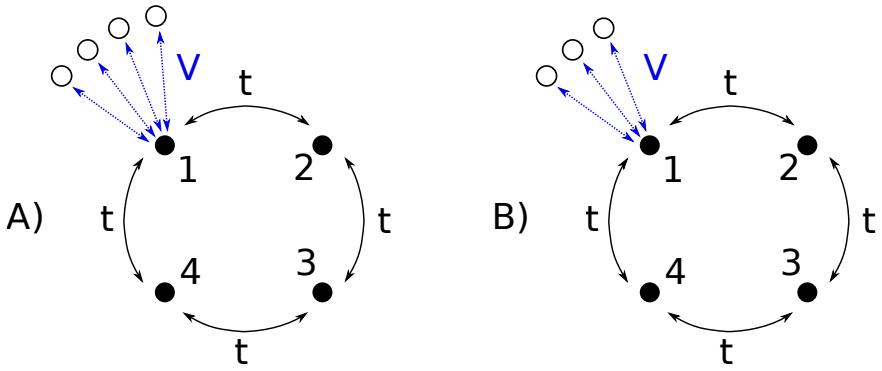

Figure 4.1: *An example cluster with 4 impurity flavors (black circles). They are connected by nearest-neighbor hopping with amplitude t. Flavor 1 is under consideration and has four bath sites (empty circles) in case A), and three bath sites in case B).*

4.4 Falicov-Kimball impurity

In this section we discuss the arguably smallest system violating the condition formulated at the end of the last section. It is an impurity with two flavors, which are both connected to only one and the same bath site. We show, that Z-sampling gives clearly wrong Green's functions, and interpret that with respect to autocorrelation times.

For another more physical example system, where each impurity flavor of an cluster of size $N = 2$ is connected to one bath site each, see appendix 4.8.5.

4.4.1 General description

The system under consideration is a one-orbital impurity (two spins with energy levels $E_\uparrow = E_\downarrow = -0.25V$). Both connect to a single bath site of energy $\epsilon = 0.0$ with hybridization amplitude V. Its Hamiltonian reads

$$\hat{H}_{\mathrm{FK}} = \begin{pmatrix} \hat{c}_\uparrow^\dagger & \hat{c}_\downarrow^\dagger & \hat{a}^\dagger \end{pmatrix} \begin{pmatrix} E_\uparrow & 0 & V \\ 0 & E_\downarrow & V \\ V & V & \epsilon \end{pmatrix} \begin{pmatrix} \hat{c}_\uparrow \\ \hat{c}_\downarrow \\ a \end{pmatrix} \tag{4.4}$$

$$= E_\uparrow \hat{c}_\uparrow^\dagger \hat{c}_\uparrow + E_\downarrow \hat{c}_\downarrow^\dagger \hat{c}_\downarrow + \epsilon \hat{a}^\dagger a + \sum_\sigma V(\hat{c}_\sigma^\dagger a + \hat{a}^\dagger \hat{c}_\sigma). \tag{4.5}$$

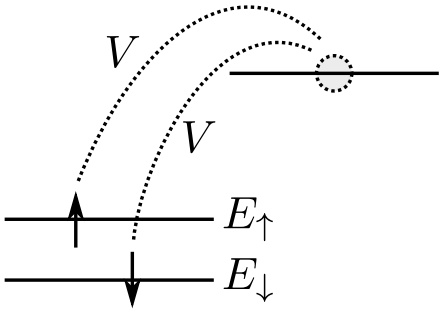

Figure 4.2: *Sketch of the discrete model considered in Sec. 4.4. Let us stress that this system can at most host 3 electrons, 2 on the impurity and 1 in the bath. There is no spin-degeneracy.*

This is equivalent to a Falicov-Kimball model by flavor rotation; for details see appendix 4.8.2. The two impurity flavors $E_\uparrow$ and $E_\downarrow$ of our model could differ by any quantum number like orbital, spin, or a combination thereof. In order to deal with one-orbital models, we choose this quantum number to be the spin. The inconsistency of the Z-estimator does not require electron-electron interaction, hence for simplicity we consider the system to be non-interacting.

The criterion, that each impurity flavor of an cluster of site N needs at least N bath sites, is violated here. We have two clusters of size one, and they are connected to the same bath site.

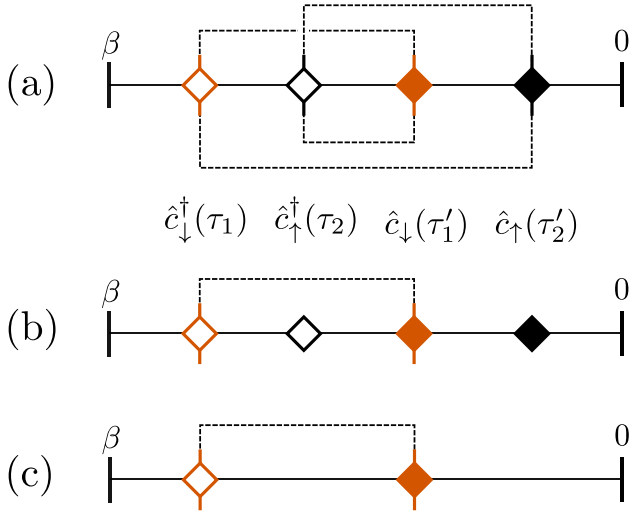

Figure 4.3: *a) Z-configuration for the Falicov-Kimball impurity. Empty diamonds denote creation operators, filled diamonds annihilation operators. The red dashed lines mean a propagation of the electron through the bath.*
b) Green's function configuration the Falicov-Kimball impurity. c) Z-configuration, which connects to configuration b) by inserting two worm operators.

We characterize the missing diagrams explicitly here, since in the section 4.4.2 we refer to them. The G-diagram in Fig. 4.3 (b) has nonzero weight; it annihilates an electron on each impurity flavor, creates them again and has only zero or one electron in the bath. In Z-sampling it would have to be generated out of the Z-diagram in Fig. 4.3 (a). This is however not possible, as it requires two electrons to occupy the same single bath site, which violates Pauli's principle and the Z-diagram has zero weight. Thus G-diagram (a) is never generated in Z-sampling, making this estimator inconsistent. For more details on how Pauli's principle is implemented in effective propagators, see appendix 4.8.3.

We confirm this numerically in Fig. 4.4. The Green's functions of Z-sampling are clearly wrong compared to G-sampling or exact diagonalization. The property $G_{\sigma\sigma'}(\tau = 0^+) + G_{\sigma\sigma'}(\tau = \beta^-) = \delta_{\sigma\sigma'}$ from the anticommutation relations of Fermionic operators is violated in Z-sampling.

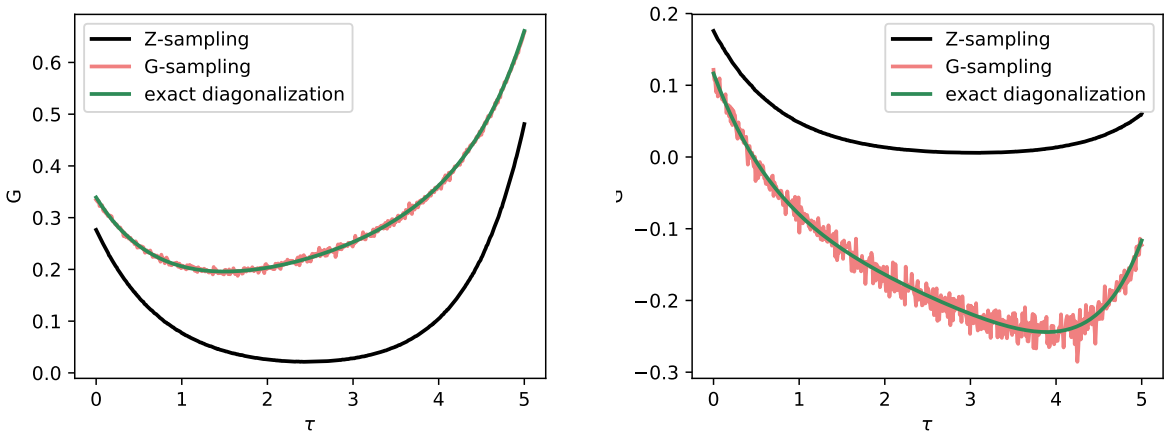

Figure 4.4: *Diagonal and offdiagonal Green's function of model Eq.* (4.4) *for inverse temperature* $\beta = 5\,V^{-1}$.

4.4.2 Autocorrelation time analysis

We have discussed in the previous section that for model (4.4) Z-sampling misses all Green's function diagrams with two creation or annihilation operators consecutively in a row. Such G-diagrams will be called *critical* in the following, and all remaining diagrams (with alternating $\hat{c}^\dagger$ and $\hat{c}$) *noncritical*. The Green's function can be decomposed in

$$G(\tau) = G_{\text{crit}}(\tau) + G_{\text{noncrit}}(\tau). \tag{4.6}$$

Now we show, that this can also be interpreted such that the autocorrelation time of the critical diagrams is infinite.

For this purpose we introduce a system, where the Pauli principle on the single bath-site can be switched on and off continuously. The single bath site is split into three and shifted apart by a parameter δ, creating an interpolation between an problematic and unproblematic system:

$$\hat{H}'_{\text{FK}}(\delta) = \begin{pmatrix} \hat{c}^\dagger_\uparrow \\ \hat{c}^\dagger_\downarrow \\ \hat{a}^\dagger_1 \\ \hat{a}^\dagger_2 \\ \hat{a}^\dagger_3 \end{pmatrix}^T \cdot \begin{pmatrix} E_\uparrow & 0 & v & v & v \\ 0 & E_\downarrow & v & v & v \\ v & v & \epsilon - \delta & 0 & 0 \\ v & v & 0 & \epsilon & 0 \\ v & v & 0 & 0 & \epsilon + \delta \end{pmatrix} \cdot \begin{pmatrix} \hat{c}_\uparrow \\ \hat{c}_\downarrow \\ \hat{a}_1 \\ \hat{a}_2 \\ \hat{a}_3 \end{pmatrix}. \tag{4.7}$$

We motivate this construction in appendix 4.8.4. For consistency with the previous model the new hybridization is $v = V/\sqrt{3}$. One can verify by using the resolvent expression $G = (\mathbb{1}i\omega - \hat{H})^{-1}$ or calculating the hybridization function, that the impurity Green's functions are identical for $\hat{H}_{\text{FK}}$ and $\hat{H}'_{\text{FK}}(\delta = 0)$.

A scan over the parameter δ is shown in Fig. 4.6 for the values $\delta \in \{0.3, 0.05, 0.01, 0.0\}$. Since the number of Monte Carlo steps and measurements is the same for all four panels, the noise can be directly interpreted as exclusive effect of the autocorrelation. Z-sampling gives correct results for the system with $\delta = 0.3$. The noise of the critical diagrams increases strongly upon decreasing δ, because the critical Z-diagrams occur less and less frequently. Therefore few and

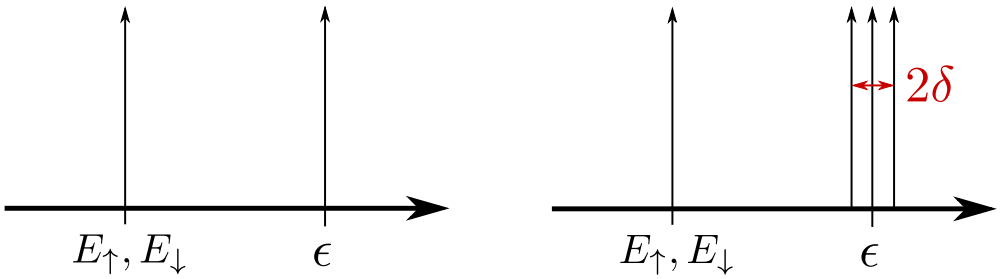

Figure 4.5: *Depiction of Hamiltonian* (4.7) *for zero and finite* δ.

fewer critical G-diagrams are generated, which explains the poor statistics in G_{crit}. For $\delta = 0.00$ no critical G-diagrams are produced any more. Their contribution is zero without noise and the result clearly wrong. Equivalently, the autocorrelation time of the critical diagrams became infinite here. Therefore, $\hat{H}'(\delta \gg 0)$ does not have the inconsistency problem, and for small δ it can be switched on continuously. A bias may occur for small δ and small N.

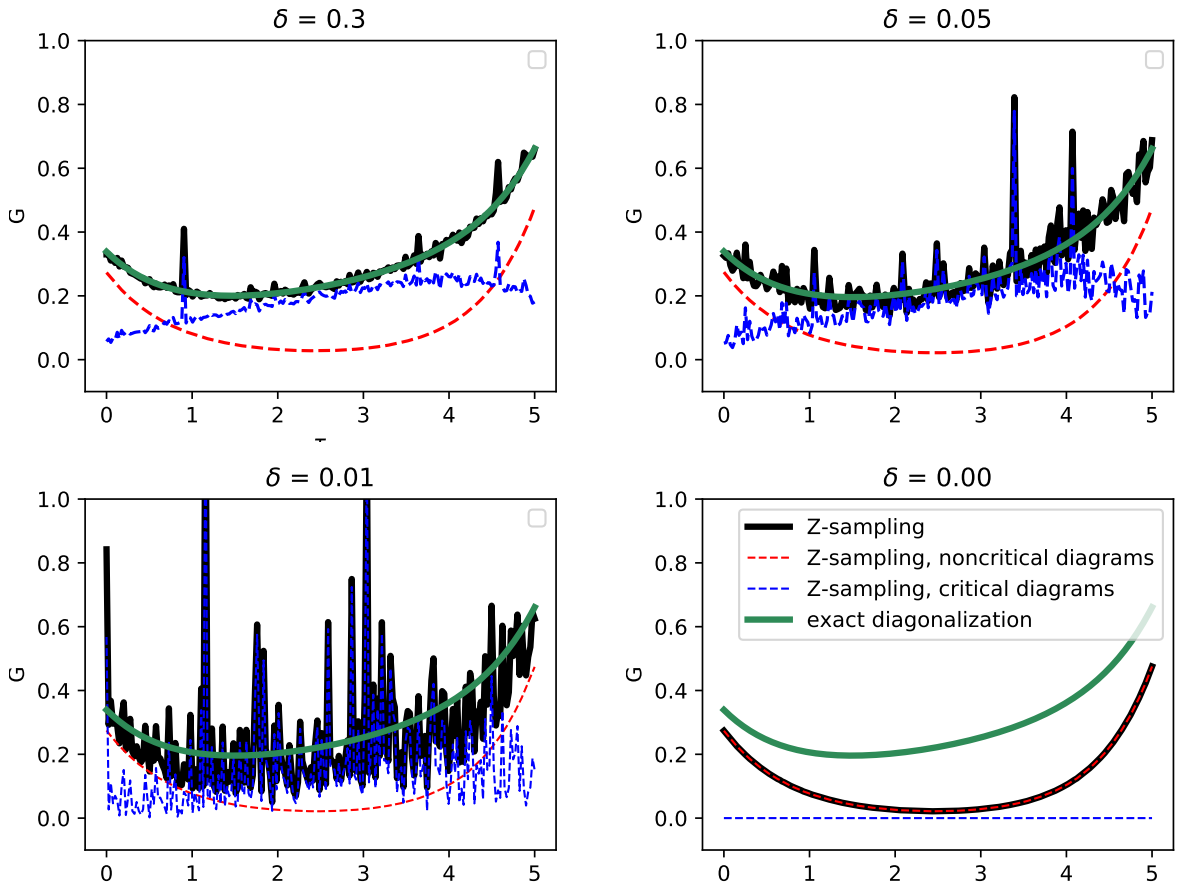

Figure 4.6: *Critical and non-critical contributions to the Green's function for various values of* δ. *The increasing autocorrelation time manifests itself in growing noise upon decreasing* δ. *For* $\delta = 0.00$ *the critical diagrams are not measurable, equivalent to an infinite autocorrelation time.*

The curve for the noncritical diagrams is smooth all the time, which means their autocorrelation times are small and independent of δ.

4.5 Infinite systems

Systems with baths of infinite size do not produce inconsistent estimators of the type discussed in section 4.3. However, the resampling may suffer from severe autocorrelation problems, as we will show in this section.

The system under consideration is an AIM with two flavors. We choose a specific bath hybridization function to illustrate the problem. The two impurity flavors are connected by a single-particle hopping t and have one bath site of energy $\epsilon = 0$ each. On its own, this system would violate the general condition and cause problems as shown in appendix 4.8.5 (the cluster size is $N = 2$ and there is one bath site per impurity flavor). But here we extend the bath hybridization function of a single delta-peak at $\epsilon = 0$ with some continuous hybridization bands at higher energies (from $-6t$ to $5t$ and $5t$ to $6t$), to create a bath of infinite size (see Fig. 4.7).

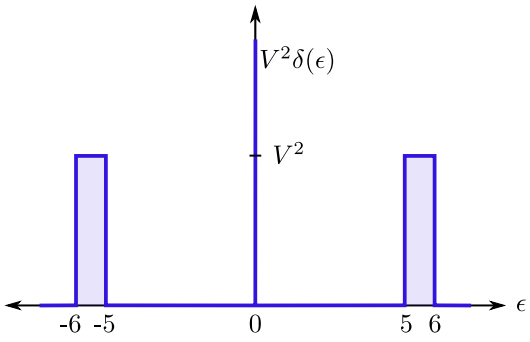

Figure 4.7: *An hybridization function made of a delta-peak at $\epsilon = 0$ and higher-energy bands, used to mimic a situation with a very narrow peak at the Fermi level and extended hybridization at higher energies.*

One discrete bath site, which on the real-frequency axis corresponds to a hybridization function of a delta-peak at energy position ϵ and amplitude V, becomes $V^2/(i\omega - \epsilon)$ after analytic continuation to the Matsubara axis. Therefore the full hybridization function becomes

$$\Delta(i\omega_n) = \frac{V^2}{i\omega - 0} + \int_{-6}^{-5} \mathrm{d}\epsilon \, \frac{V^2}{i\omega - \epsilon} + \int_{5}^{6} \mathrm{d}\epsilon \, \frac{V^2}{i\omega - \epsilon} \tag{4.8}$$

For the numerical calculation we set the hybridization parameter to $V = 0.3t$. In this case, the critical diagrams are those, which contain two creation or two annihilation operators of the same flavor consecutively in a row. As can be seen in Fig. 4.8, the noncritical part of $G(\tau)$ is smooth and thus has low autocorrelation time, whereas the critical part shows considerable more noise, which indicates a much larger autocorrelation time.

4.6 Conclusion

We found a strict criterion to identify the systems of finite size, for which the standard estimator of the Green's function (Z-Sampling) fails in CTHYB. Pauli's exclusion principle makes the weight of partition function configurations zero, out of which probably important, nonzero Green's function configuration had to be generated. In worm sampling (G-sampling), this kind of inconsistency does not occur. Furthermore our findings explain the occurrence of large autocorrelation times for systems with infinite bath size, and limit the application of CTHYB for quantum chemistry

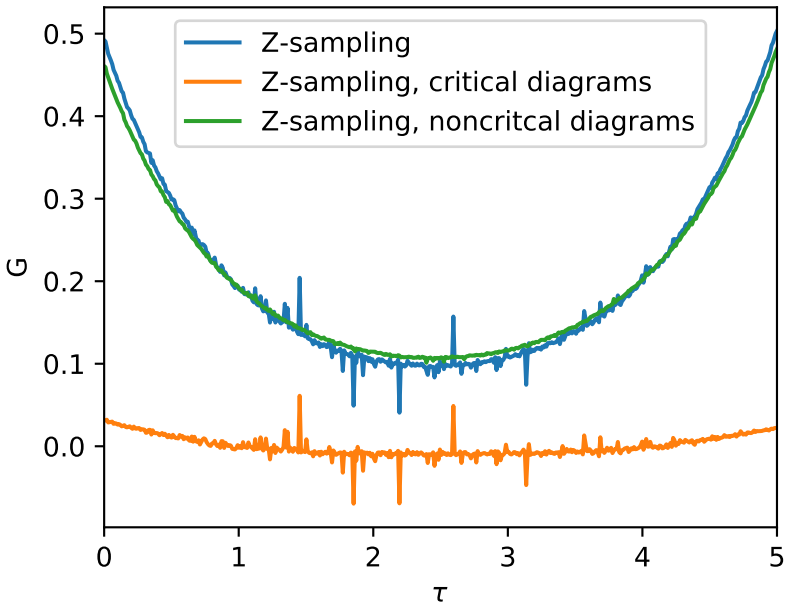

Figure 4.8: *Diagonal Green's function of infinite system (blue curve). It is divided into the critical and noncritical part, where the noise completely stems from the critical one.*

applications to worm sampling only. In general, our findings illustrate, that for any Markov Chain Monte Carlo algorithm of diagrammatic series, it is very important to carefully ensure surjectivity of the mapping between the sampled distribution and observable distribution.

4.7 Software

The CTHYB data was produced with w2dynamics (Wallerberger et al., 2019) using an interface (Hausoel et al., 2019) to the TRIQS library (Parcollet et al., 2015). The results shown in figures 4.4, 4.11 and 4.8 were confirmed with the CTHYB solver from TRIQS (Parcollet et al., 2015). The ED calculations were done with pomerol (Antipov and Krivenko, 2015), also using its interface to TRIQS.

4.8 Appendices

4.8.1 Some technical remarks

For large cluster sizes N the contributions of critical diagrams go rapidly to zero for combinatoric reasons.

The applicability of our criterion to systems with off-diagonal hybridizations is straightforward. Each flavor of an impurity cluster of size N must be connected to at least N bath sites, independently if these bath sites may also be connected to other impurity flavors.

Let us note that the inconsistency problem discussed here is not caused by an accidental zero of the weight due to numerical noise. However Z-configurations with exactly zero weight can have nonzero weight due to numerical instability, especially when using Sherman-Morrison formulas for updating the bath weight after insertion / removal of a diagram vertex. Then it is possible that the forbidden G-configurations can still be accessed with correct probabilities, since the "wrong"

but nonzero weights of the Z-configurations cancel out. The authors observed such a case, where in Z-sampling $G(\tau)$ first converged to a wrong result, then it became spiky and showed a very slow convergence towards the correct result. G-sampling instead immediately converged to the correct result.

4.8.2 Relation to Falicov-Kimball model

The system in Sec. 4.4 was labeled Falicov-Kimball impurity with rotated flavors. In order to motivate this name, we introduce new operators

$$\hat{d} = \frac{1}{\sqrt{2}}(\hat{c}_\uparrow + \hat{c}_\downarrow) \tag{4.9}$$

$$\hat{f} = \frac{1}{\sqrt{2}}(\hat{c}_\uparrow - \hat{c}_\downarrow). \tag{4.10}$$

They are a unitary transform of the original operators $\hat{c}_\uparrow$ and $\hat{c}_\downarrow$, which can be written as

$$\hat{c}_\uparrow = \frac{1}{\sqrt{2}}(\hat{d} + \hat{f}) \tag{4.11}$$

$$\hat{c}_\downarrow = \frac{1}{\sqrt{2}}(\hat{d} - \hat{f}). \tag{4.12}$$

Inserting these expressions into the Hamiltonian of Eq. (4.4), we obtain

$$\hat{H} = \begin{pmatrix} \hat{d}^\dagger & \hat{f}^\dagger & \hat{a}^\dagger \end{pmatrix} \begin{pmatrix} E & \Delta E & \sqrt{2}V \\ \Delta E & E & 0 \\ \sqrt{2}V & 0 & \epsilon \end{pmatrix} \begin{pmatrix} \hat{d} \\ \hat{d} \\ \hat{a} \end{pmatrix}, \tag{4.13}$$

where the abbreviations $E = \frac{1}{2}(E_\uparrow + E_\downarrow)$ and $\Delta E = \frac{1}{2}(E_\uparrow - E_\downarrow)$ were used. The bath operators $\hat{a}^\dagger$ and $\hat{a}$ remain unchanged. Eq. (4.13) clearly shows that the f-electrons do not hybridize with the bath.

4.8.3 Discussion of Pauli's principle for effective propagators by the example of the Falicov-Kimball model

Here we will discuss how Pauli's principle is implemented for effective propagators using the Z-diagram in Fig. 4.3 (a) as example. The hybridization function of its Hamiltonian (4.4) is

$$\Delta(\tau) = \frac{V^2}{\mathrm{e}^{\beta\epsilon} + 1} \times \begin{cases} \mathrm{e}^{\epsilon\tau}, & \text{if } \tau > 0 \\ -\mathrm{e}^{\epsilon(\beta-\tau)}, & \text{if } \tau < 0 \end{cases}, \tag{4.14}$$

where the bath site was integrated out. Summing the effective propagators to a determinant for the Z-configuration gives

$$\begin{aligned} w_{\mathrm{bath}}(\mathcal{C}_Z) &= \det \begin{pmatrix} \Delta(\tau_1 - \tau_3) & \Delta(\tau_2 - \tau_3) \\ \Delta(\tau_1 - \tau_4) & \Delta(\tau_2 - \tau_4) \end{pmatrix} \\ &= \det \begin{pmatrix} \mathrm{e}^{\epsilon(\tau_1-\tau_3)} & \mathrm{e}^{\epsilon(\tau_2-\tau_3)} \\ \mathrm{e}^{\epsilon(\tau_1-\tau_4)} & \mathrm{e}^{\epsilon(\tau_2-\tau_4)} \end{pmatrix} \\ &= 0, \end{aligned} \tag{4.15}$$

because the matrix in Eq. (4.15) is rank deficient: the rows are the same, but the first is multiplied with a factor $\mathrm{e}^{-\epsilon\tau_3}$, the second with a factor $\mathrm{e}^{-\epsilon\tau_4}$. This is Pauli's exclusion principle in the language of effective propagators, which allows at a certain time only one electron to propagate through the bath for the Falicov-Kimball impurity.

The generalization to bigger matrices is straightforward.

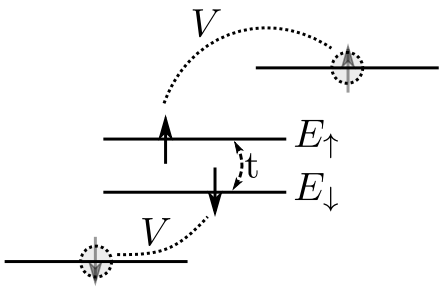

Figure 4.9: *Sketch drawing of the discrete model considered in Sec. 4.8.5.*

4.8.4 Adding dummy bath sites

Here we discuss how a single bath site, which can only host one electrons, can artificially be split into two bath sites, which together also can only host one electron. Take a system with one impurity flavor and one bath site for simplicity

$$\hat{H} = \begin{pmatrix} \hat{c}^\dagger & \hat{a}_1^\dagger \end{pmatrix} \begin{pmatrix} E & V \\ V & \epsilon \end{pmatrix} \begin{pmatrix} c \\ \hat{a}_1 \end{pmatrix}. \tag{4.16}$$

A dummy bath site with the same energy ϵ is added, which is not coupled to the impurity:

$$\hat{H} = \begin{pmatrix} \hat{c}^\dagger & \hat{a}_1^\dagger & \hat{a}_2^\dagger \end{pmatrix} \begin{pmatrix} E & V & 0 \\ V & \epsilon & 0 \\ 0 & 0 & \epsilon \end{pmatrix} \begin{pmatrix} c \\ \hat{a}_1 \\ \hat{a}_2 \end{pmatrix}. \tag{4.17}$$

Then $\hat{H}$ is rotated with a unitary matrix

$$A = \begin{pmatrix} 1 & 0 & 0 \\ 0 & \frac{1}{\sqrt{2}} & \frac{1}{\sqrt{2}} \\ 0 & \frac{1}{\sqrt{2}} & -\frac{1}{\sqrt{2}} \end{pmatrix}, \tag{4.18}$$

which gives a Hamiltonian

$$A^\dagger \hat{H} A = \begin{pmatrix} \hat{c}^\dagger & b_1^\dagger & b_2^\dagger \end{pmatrix} \begin{pmatrix} E & V/\sqrt{2} & V/\sqrt{2} \\ V/\sqrt{2} & \epsilon & 0 \\ V/\sqrt{2} & 0 & \epsilon \end{pmatrix} \begin{pmatrix} c \\ b_1 \\ b_2 \end{pmatrix}. \tag{4.19}$$

The bath of Hamiltonian (4.19) looks like it was able to host two electrons, because one could assign an additional quantum number to them, a site number. But there can only be one electron in the bath, since (4.19) is a rotation of (4.17). Also the hybridization functions of the Hamiltonians (4.16), (4.17) and (4.19) coincide.

Now shifting the energies ϵ apart continuously switches off Pauli's principle in the bath.

4.8.5 Impurity with single bath site

We consider a physically more realistic example here: an impurity with two flavors $E_\uparrow = E_\downarrow = 0$, where each flavor has its own bath. There is a hopping t between the impurity flavors.

$$\hat{H} = \begin{pmatrix} \hat{c}_\uparrow^\dagger & \hat{c}_\downarrow^\dagger & \hat{a}_\uparrow^\dagger & \hat{a}_\downarrow^\dagger \end{pmatrix} \begin{pmatrix} E_\uparrow & t & V & 0 \\ t & E_\downarrow & 0 & V \\ V & 0 & \epsilon_\uparrow & 0 \\ 0 & V & 0 & \epsilon_\downarrow \end{pmatrix} \begin{pmatrix} \hat{c}_\uparrow \\ \hat{c}_\downarrow \\ \hat{a}_\uparrow \\ \hat{a}_\downarrow \end{pmatrix} \tag{4.20}$$

$$= \sum_\sigma (E_\sigma \hat{c}_\sigma^\dagger \hat{c}_\sigma + t \hat{c}_\sigma^\dagger \hat{c}_{\bar{\sigma}}) + \sum_\sigma \epsilon_\sigma \hat{a}_\sigma^\dagger \hat{a}_\sigma \tag{4.21}$$

$$+ \sum_\sigma V (\hat{c}_\sigma^\dagger \hat{a}_\sigma + \hat{a}_\sigma^\dagger \hat{c}_\sigma). \tag{4.22}$$

The bath parameters are $\epsilon_\uparrow = 0.1t$, $\epsilon_\downarrow = -0.1t$, $V = 0.3t$, and the inverse temperature $\beta = 5/t$. There is no interaction among the electrons.

The criterion is violated here, since the cluster size is $N = 2$, and each impurity flavor has only one bath-site.

Critical diagrams are those with two annihilation operators of same kind after each other, like shown in Fig. 4.10. The Green's function from Z-sampling is clearly wrong (Fig. 4.11).

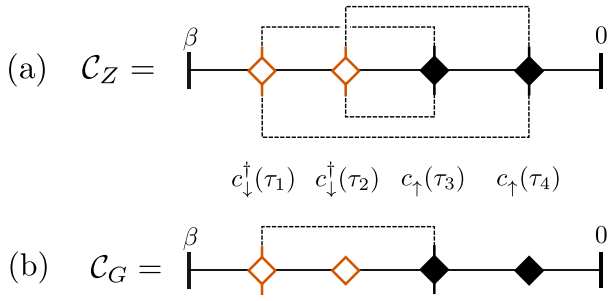

Figure 4.10: *A critical diagram for the impurity of model in Eq.* (4.20).

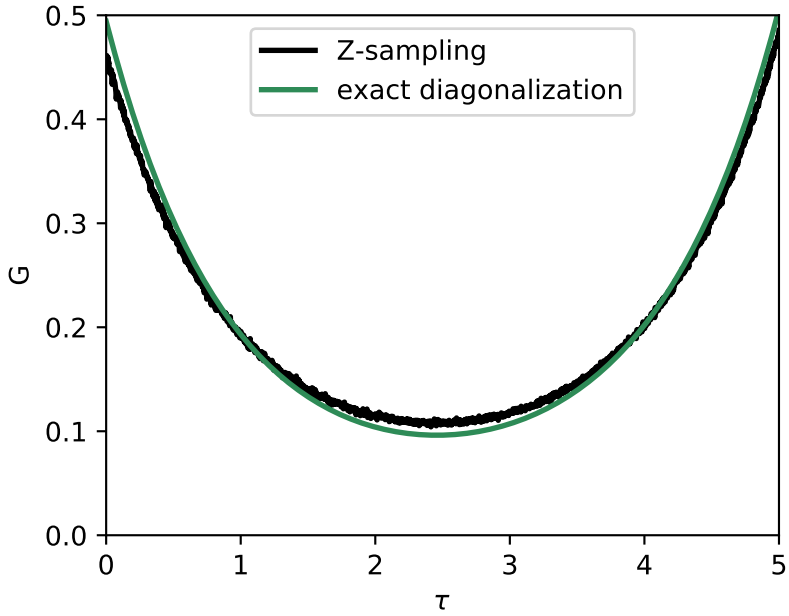

Figure 4.11: *Diagonal Green's function of the impurity Eq.* (4.20).

Chapter 5

DMFT with general interactions

One of the main tasks of this thesis was to generalize the DFMT package `w2dynamics` to treat Hubbard models with the most general, one- and two-particle on-site terms

$$H_{\mathrm{loc}} = H_{\mathrm{loc,1P}} + H_{\mathrm{loc,2P}} \tag{5.1}$$

$$= \sum_{\mu\nu} t_{\mu\nu} c^\dagger_\mu c_\nu + \frac{1}{2} \sum_{\kappa\lambda\mu\nu} U_{\kappa\lambda\mu\nu} c^\dagger_\kappa c^\dagger_\lambda c_\nu c_\mu. \tag{5.2}$$

In this chapter I first discuss the physical content and technical implications of certain H_{loc}. Then I discuss, how to change the basis of the AIM and the DMFT loop. A major reason for a change of basis is the symmetry of the local problem. When the crystal structure or the presence of complicated spin-orbit terms reduces the symmetry of the Weiss field $\mathcal{G}(i\omega_n)$, then partial rotations can make calculations feasible, e.g. because they alleviate the sign problem or reduce the size of offdiagonal hybridizations. Further choosing the right basis may help to interpret and understand the results physically better. Another reason is the so-called *rotation test*. One performs calculations for the same system in two different bases and checks for consistency. Last I briefly introduce the interface of the CTHYB solver `w2dynamics` to the `TRIQS` library.

5.1 Properties of the local Hamiltonian

In this section I discuss the properties of the local impurity Hamiltonian H_{loc}, which governs the time evolution via $c^{(\dagger)}(\tau) = \mathrm{e}^{-H_{\mathrm{loc}}\tau} c^{(\dagger)} \mathrm{e}^{H_{\mathrm{loc}}\tau}$, as we have seen in Chapter 3. It contains the microscopic processes, which happen on the impurity during time evolution and mix different states with each other. The mixing states are grouped together in blocks of H_{loc}. The fact that during time evolution the system cannot go from one to another block means, that each block has a set of conserved quantum numbers, which are different for each block. Since the size of the blocks directly determines the exponential scaling of CTHYB, a minimization of the block sizes is desirable. Since there is an equal number of creation an annihilation operators in each term of Eq. (5.2) and we don't consider superconductivity, the total number of electrons (in `w2dynamics` called `Nt`) is always conserved.

Let me further separate the discussion for one- and two-particle terms.

5.1.1 Two-particle terms

It is more intuitive to start from the most severe approximation that sometimes is adopted, which is the *density-density* interaction

$$H_{\mathrm{loc,2P}}^{\mathrm{density}} = \sum_i U n_{i\uparrow} n_{i\downarrow} + \sum_{i<j,\sigma\sigma'} (V - J\delta_{\sigma\sigma'}) n_{i\sigma} n_{j\sigma'}, \tag{5.3}$$

that sometimes is adapted. It only consists of density terms, therefore the time evolution is not able to change a many body state, but just assigns an energy to it. The orbital occupations $n_{i\sigma}$ (called `Azt` in `w2dynamics`) are conserved quantities on the impurity.

A step away from the most serious approximation is represented by the *Kanamori* Hamiltonian

$$H_{\mathrm{loc,2P}}^{\mathrm{Kanamori}} = H_{\mathrm{loc,2P}}^{\mathrm{density}} - J \sum_{i<j} \left(c_{i\uparrow}^\dagger c_{i\downarrow}^\dagger c_{j\uparrow} c_{j\downarrow} + c_{i\uparrow}^\dagger c_{j\downarrow}^\dagger c_{j\uparrow} c_{i\downarrow} \right), \tag{5.4}$$

which adds spin-flip and pair-hopping terms. As can be seen from figure (5.1), these processes conserve the PS quantum number, which is the pattern of single occupied orbitals (depicted in blue here and called `Qzt` in `w2dynamics`).

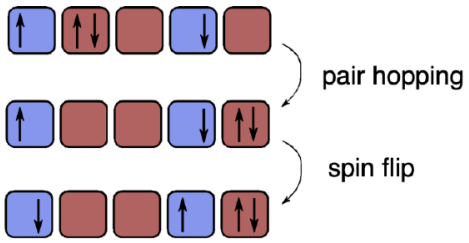

Figure 5.1: *Illustration of pair-hopping and spin-flip processes on the impurity. The five boxes represent five orbitals. Taken from Parragh et al. (2012a).*

The *full-Hubbard* interaction

$$H_{\mathrm{loc,2P}}^{\text{full Hubbard}} = \sum_{ijkl\sigma\sigma'} U_{ijkl} c_{i\sigma}^\dagger c_{j\sigma'}^\dagger c_{l\sigma'} c_{k\sigma} \tag{5.5}$$

also allows all correlated hopping processes beyond spin-flip and pair-hopping. These are for example two single electrons hopping, or two electrons of a double occupied orbital hopping apart, as depicted in Fig. 5.2. They obviously break the PS quantum number.

`w2dynamics` also has the *Coulomb* interaction implemented, which is the local part of a spherical Coulomb tensor written in the basis of the tesseral harmonics (real spherical harmonics) for d-orbitals. This poses constraints on the numerical values of U_{ijkl} in Eq. (5.5) and gives the angular momentum in z-direction as additional conserved quantity (`Lzt` in `w2dynamics`).

In summary, the parametrizations of the 2-particle interaction $H_{\mathrm{loc,2P}}$ discussed here conserve the number of electrons and the spin in z-direction. According to the chosen approximation additionally come the conserved quantities above. The one-particle terms can break these quantum numbers, which I will discuss in the following.

5.1.2 One particle terms

The one particle terms that consist of density terms only describe the energy levels on the impurity and do not disturb the conserved quantities of the two particle terms.

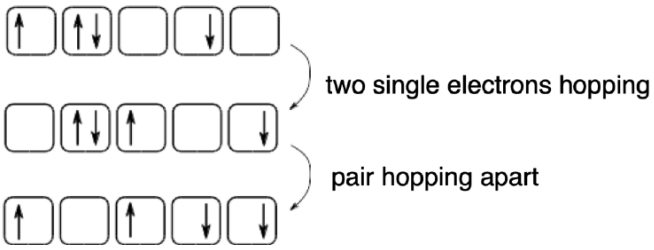

Figure 5.2: *Illustration of full-Hubbard processes on the impurity; for a more detailed discussion see Ref. Valli et al. (2020). The five boxes represent five orbitals. Adapted from Parragh et al. (2012a).*

There can be a one-particle hopping of conserving spin, which come from the $\boldsymbol{k}$-averaged DMFT Hamiltonian (see Eq. (5.33) later in this chapter), or to describe non-local correlations with cluster DMFT. The conserved quantities these terms leave are `Nt` and `Szt`.

There can be terms that flip the spin and conserve the orbital, for example magnetic fields in other than z-direction. And there can be single-particle hopping terms which flip the spin, when there is spin-orbit coupling. In `w2dynamics` in both cases only `Nt` is left as conserved quantity.

5.1.3 Discussion

In `w2dynamics` the conserved quantities have to be given explicitly in the parameter file, for example as `QuantumNumbers = Nt Szt Qzt`. Then the block structure of H_{loc} is fixed that way and all terms outside of the blocks are neglected. One can play around with the quantum numbers and check the sensitivity of the results upon truncating classes of terms, in order to find out about their importance or to find a computationally cheaper model. The computation time may vary over orders of magnitude upon change of the quantum numbers.

There is also an algorithm implemented, which automatically finds the order and grouping of the many-body states in the numerical representation of H_{loc} minimizing the size of the blocks (add `All` to the list of `QuantumNumbers`, which are known to be conserved). In this case, one should especially closely look at the offdiagonal elements of $H_{\mathrm{loc,1P}}$, since in a calculation of a real material they are generated from the $\boldsymbol{k}$-averaged Hamiltonian $\langle H(\boldsymbol{k})\rangle$ (see Eq. (5.33) later in this chapter). They may be effectively zero, but have numerical noise and lead to larger blocks in the automatic minimization procedure.

5.2 The solver

In this section I show how to change the single-particle basis of the CTHYB solver. First I discuss the impurity operators, then the Green's functions, and last the one- and two-particle interactions.

5.2.1 Rotation of impurity operators

The transforms of the impurity operators are

$$d_\alpha = \sum_\beta A^*_{\beta\alpha} c_\beta \qquad d = A^\dagger c \tag{5.6}$$

$$d^\dagger_\alpha = \sum_\beta A_{\beta\alpha} c^\dagger_\beta \qquad d^\dagger = c^\dagger A, \tag{5.7}$$

where $c_\alpha^{(\dagger)}$ are the original impurity operators with $\{c_\alpha, c_\beta^\dagger\} = \delta_{\alpha\beta}$. The transformed operators have to fulfill the same anticommutation relation, therefore

$$\left\{d_\alpha, d_\beta^\dagger\right\} = \sum_{\gamma\delta} A_{\gamma\alpha}^* A_{\delta\beta} \left\{c_\gamma, c_\delta^\dagger\right\} \tag{5.8}$$

$$= \sum_{\gamma} A_{\gamma\alpha}^* A_{\gamma\beta} \tag{5.9}$$

$$\stackrel{!}{=} \delta_{\alpha\beta} \tag{5.10}$$

For this to be the case, A must be a unitary matrix ($A^\dagger A = \mathbb{1}$). The inverse transforms are

$$c_\alpha = \sum_\beta A_{\alpha\beta} d_\beta \qquad\qquad c = Ad \tag{5.11a}$$

$$c_\alpha^\dagger = \sum_\beta A_{\alpha\beta}^* d_\beta^\dagger \qquad\qquad c^\dagger = d^\dagger A^\dagger. \tag{5.11b}$$

5.2.2 Rotation of impurity quantities

Now I will find the relations between the impurity quantities and their rotations into the new basis. The rotation of the Green's function $G(\tau) = \left\langle T_\tau c(\tau) c^\dagger(0) \right\rangle$ is

$$A^\dagger G(\tau) A = \left\langle T_\tau A^\dagger c(\tau) c^\dagger(0) A \right\rangle \tag{5.12}$$

$$= \left\langle T_\tau d(\tau) d^\dagger(0) \right\rangle \tag{5.13}$$

$$= G'(\tau), \tag{5.14}$$

or explicitly with indices

$$G'_{\alpha\beta}(\tau) = \sum_{\gamma\delta} A_{\gamma\alpha}^* A_{\delta\beta} G_{\gamma\delta}(\tau). \tag{5.15}$$

Transforming the single-particle interaction yields

$$H_{\mathrm{loc,1P}} = \sum_{\mu\nu} t_{\mu\nu} c_\mu^\dagger c_\nu \tag{5.16}$$

$$= \sum_{\mu\nu} t_{\mu\nu} \sum_\alpha A_{\mu\alpha}^* d_\alpha^\dagger \sum_\beta A_{\nu\beta} d_\beta \tag{5.17}$$

$$= \sum_{\alpha\beta} \left(\sum_{\mu\nu} t_{\mu\nu} A_{\mu\alpha}^* A_{\nu\beta} \right) d_\alpha^\dagger d_\beta \tag{5.18}$$

$$= \sum_{\alpha\beta} t'_{\alpha\beta} d_\alpha^\dagger d_\beta, \tag{5.19}$$

or $t' = A^\dagger t A$ in short. The same way the two-particle interaction transforms

$$H_{\mathrm{loc,2P}} = \sum_{\kappa\lambda\mu\nu} U_{\kappa\lambda\mu\nu} c_\kappa^\dagger c_\lambda^\dagger c_\nu c_\mu \tag{5.20}$$

$$= \sum_{\kappa\lambda\mu\nu} U_{\kappa\lambda\mu\nu} \sum_\alpha A_{\kappa\alpha}^* d_\alpha^\dagger \sum_\beta A_{\lambda\beta}^* d_\beta^\dagger \sum_\gamma A_{\nu\gamma} d_\gamma \sum_\delta A_{\mu\delta} d_\delta \tag{5.21}$$

$$= \sum_{\alpha\beta\gamma\delta} \left(\sum_{\kappa\lambda\mu\nu} U_{\kappa\lambda\mu\nu} A_{\kappa\alpha}^* A_{\lambda\beta}^* A_{\nu\gamma} A_{\mu\delta} \right) d_\alpha^\dagger d_\beta^\dagger d_\gamma d_\delta \tag{5.22}$$

$$= \sum_{\alpha\beta\gamma\delta} U'_{\alpha\beta\gamma\delta}\, d_\alpha^\dagger d_\beta^\dagger d_\gamma d_\delta \tag{5.23}$$

with the new interaction matrix

$$U'_{\alpha\beta\gamma\delta} = \sum_{\kappa\lambda\mu\nu} U_{\kappa\lambda\mu\nu} A^*_{\kappa\alpha} A^*_{\lambda\beta} A_{\nu\gamma} A_{\mu\delta}, \tag{5.24}$$

or $U' = A^\dagger A^\dagger U A A$ in short.

5.3 DMFT loop

In this section I describe the DMFT loop. First I establish the connection between the Weiss field and the hybridization function, which was introduced in chapter 3. Then I formulate the rotation test for DMFT, discuss its purpose and limitations, and last show an easy example.

5.3.1 The hybridization function

When there is CTHYB as impurity solver in the DMFT loop (see figure 5.3), the Weiss field / non-interacting Green's function $\mathcal{G}(i\omega_n)$ of the AIM needs to be transformed to the hybridization function $\Delta(i\omega_n)$ as input for CTHYB. Also in order to calculate the self-energy of the impurity, we need the non-interacting Green's function

$$\mathcal{G}(i\omega_n) = [i\omega_n \mathbb{1} + \mu_{\text{imp}} - \Delta(i\omega_n)]^{-1} \tag{5.25}$$

of the AIM (Bruus and Flensberg, 2004), with a yet undefined, matrix valued impurity chemical potential μ_{imp}. Then the hybridization function for particles is

$$\Delta^{\text{P}}(i\omega_n) = i\omega_n \mathbb{1} + \mu_{\text{imp}} - [\mathcal{G}(i\omega_n)]^{-1}. \tag{5.26}$$

In CTHYB holes propagate through the bath, therefore we find by a particle-hole transform

$$\Delta^{\text{H}}(-i\omega_n) = i\omega_n \mathbb{1} + \mu_{\text{imp}} - [\mathcal{G}(i\omega_n)]^{-1} \tag{5.27}$$

$$\Delta^{\text{H}}(i\omega_n) = -i\omega_n \mathbb{1} + \mu_{\text{imp}} - [\mathcal{G}(-i\omega_n)]^{-1}, \tag{5.28}$$

which now is the proper input for the CTHYB, suitable for Eq. (3.23).

The impurity chemical potential μ_{imp} still needs to be properly defined. We demand, that the impurity has the same average filling as one site of the corresponding Hubbard model. It is well known, that the high-frequency behavior of one-particle Matsubara objects does not contain dynamical processes, but depends on static properties or densities only (Wang et al., 2011). Therefore we fix μ_{imp} by inspecting high frequency expansions of the corresponding Matsubara objects.

I first take the local Green's function of the lattice

$$G_{\text{loc}}(i\omega_n) = \frac{1}{N_k} \sum_k [(i\omega_n + \mu)\mathbb{1} - \Sigma(i\omega_n) - H(\boldsymbol{k})]^{-1} \tag{5.29}$$

and expand its inverse around $i\omega_n \to \infty$. This gives[1]

$$\lim_{i\omega_n \to \infty} G^{-1}_{\text{loc}}(i\omega_n) = (i\omega_n + \mu)\mathbb{1} - \Sigma(i\omega_n) - \langle H(\boldsymbol{k}) \rangle \tag{5.30}$$

[1] The inverse of $g(z) = \frac{1}{N}\sum_{i=1}^{N} \frac{1}{z - c_i}$ expanded around $z = \infty$ gives $\frac{1}{g(z)} = z + \frac{1}{N}\sum_{i=1}^{N} c_i$. A generalization to matrix valued z and c_i is straightforward.

with the local, Brillouin-zone averaged Hamiltonian $\langle H(\boldsymbol{k})\rangle = 1/N_{\boldsymbol{k}} \sum_{\boldsymbol{k}} H(\boldsymbol{k})$.[2] The second equation needed is the hybridization function Eq. (5.28), with the Weiss field is eliminated by Dyson's equation $\mathcal{G}^{-1} = G^{-1} + \Sigma$, which gives

$$\Delta(-i\omega_n) = (i\omega_n + \mu_{\mathrm{imp}})\mathbb{1} - G^{-1}_{\mathrm{loc}}(i\omega_n) - \Sigma(i\omega_n). \tag{5.31}$$

Plugging $G_{\mathrm{loc}} + \Sigma = (i\omega_n + \mu)\mathbb{1} - \langle H\rangle$ from Eq. (5.30) into Eq. (5.31) gives

$$\Delta(-i\omega_n) = (i\omega_n + \mu_{\mathrm{imp}})\mathbb{1} - (i\omega_n + \mu)\mathbb{1} + \langle H(\boldsymbol{k})\rangle\,. \tag{5.32}$$

Applying the limit $i\omega_n \to \infty$ makes the hybridization function disappear, and the defining equation for the impurity chemical potential is found to be

$$\mu_{\mathrm{imp}}\mathbb{1} = \mu\mathbb{1} - \langle H(\boldsymbol{k})\rangle\,. \tag{5.33}$$

5.3.2 Rotation test for DMFT

Possible problems of the solver may be so subtle, that they are not visible in a single-shot calculation or they can be smaller than the error bars. However, they may act as a "force" on the self-consistency procedure in phase space, making it end up somewhere completely else compared to where it is supposed to end. One sometimes also needs to test the DMFT loop. Here I describe the rotation test of the DFMT cycle, which essentially means doing the same calculation in two different bases.

Let us see how the quantities transform starting the self-consistency with $\Sigma = 0$. We have to modify the single particle dispersion by hand via

$$H'(\boldsymbol{k}) = U^\dagger H(\boldsymbol{k}) U. \tag{5.34}$$

It can be seen in figure 5.3, that the quantities

$$G'_{\mathrm{latt}}(\boldsymbol{k}, i\omega_n) = U^\dagger G_{\mathrm{latt}}(\boldsymbol{k}, i\omega_n) U \tag{5.35}$$

$$G'_{\mathrm{loc}}(i\omega_n) = U^\dagger G_{\mathrm{loc}}(i\omega_n) U \tag{5.36}$$

$$\mathcal{G}'(i\omega_n) = U^\dagger \mathcal{G}(i\omega_n) U \tag{5.37}$$

change together with the basis accordingly. Within the solver,

$$\mu_{\mathrm{imp}} \to U^\dagger \mu_{\mathrm{imp}} U \tag{5.38}$$

$$\Delta(i\omega_n) \to U^\dagger \Delta(i\omega_n) U \tag{5.39}$$

change together with their basis automatically, leaving the interaction matrix, that has to be changed by hand via

$$U' = A^\dagger A^\dagger U A A. \tag{5.40}$$

Then the solver delivers a transformed impurity Green's function and self-energy

$$G'_{\mathrm{imp}}(i\omega_n) = A^\dagger G_{\mathrm{imp}}(i\omega_n) A \tag{5.41}$$

$$\Sigma'(i\omega_n) = A^\dagger \Sigma(i\omega_n) A, \tag{5.42}$$

which closes the DMFT loop. The lattice chemical potential is independent of the basis, since it is proportional to the unit matrix, but double-counting schemes are usually basis dependent. If for the rotation test a system with double counting shall be rotated in another basis, one has to fix the double counting in one basis, and rotate it to the new basis, instead of applying the scheme to the new basis.

[2] Since in `w2dynamics` the dispersion $H(\boldsymbol{k})$ of the lattice is always given at a finite set of $\boldsymbol{k}$-points, the actual Brillouin-zone average $1/V_{\mathrm{BZ}} \int_{\mathrm{BZ}} \mathrm{d}\boldsymbol{k}$ is here also approximately written as a discrete sum $1/N_k \sum_k$, which is implemented.

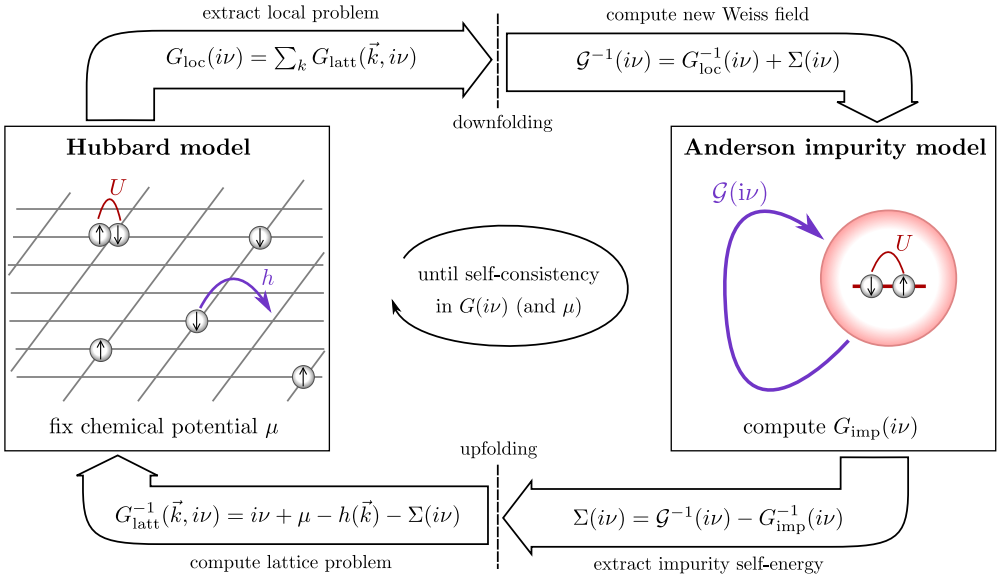

Figure 5.3: *Illustration of the DMFT loop. On the left side the observables of the Hubbard model, which are the lattice Green's function G_{latt} local Green's function G_{loc}. On the right side the impurity quantities, which are the Weiss field $\mathcal{G}$ and self-energy Σ. Taken from Wallerberger (2016).*

5.3.3 A two orbital example

As an example, I show the rotation test for a two orbital Hubbard model with simple cubic lattice and a Hamiltonian of

$$H(\boldsymbol{k}) = \begin{pmatrix} -2t[\cos(k_x) + \cos(k_y)] & 0 \\ 0 & -2t[\cos(k_x) + \cos(k_y)] \end{pmatrix} \tag{5.43}$$

for both spins. There is a Kanamori interaction with Parameters $U = 2.0t$, $J = 0.5t$ and $V = 1.0t$. A magnetic field of strength $h = 0.2t\sigma_z$ in z-direction is applied[3]. The DMFT Green's function for a temperature of $\beta = 10t$ in the original basis is shown in figure 5.4. Since the orbitals are degenerate and all quantities diagonal in the orbitals, I show only one orbital in the following and also omit the orbital indices. The magnetic field induces a finite magnetization of $m = n_\uparrow - n_\downarrow = G_{\uparrow\uparrow}(\tau = \beta^-) - G_{\downarrow\downarrow}(\tau = \beta^-)$. As expected, the offdiagonal Green's functions are zero.

In the following I discuss this calculation in different bases. The general rotation of a spin around an axis $\boldsymbol{n}$ is given by (Sakurai and Commins, 1995)

$$R_{\boldsymbol{n}}(\alpha) = \cos(\alpha/2)\mathbb{1} - i\boldsymbol{\sigma}\sin(\alpha/2) \tag{5.44}$$

$$= \begin{pmatrix} \cos(\alpha/2) - in_z\sin(\alpha/2) & (-in_x - n_y)\sin(\alpha/2) \\ (-in_x + n_y)\sin(\alpha/2) & \cos(\alpha/2) + in_z\sin(\alpha/2) \end{pmatrix}. \tag{5.45}$$

The system is rotated with

$$R_{\boldsymbol{n}_y}(\alpha) = \begin{pmatrix} \cos(\alpha/2) & -\sin(\alpha/2) \\ \sin(\alpha/2) & \cos(\alpha/2) \end{pmatrix} \tag{5.46}$$

$$R_{\boldsymbol{n}_y}(\pi) = \begin{pmatrix} 1/\sqrt{2} & -1/\sqrt{2} \\ 1/\sqrt{2} & 1/\sqrt{2} \end{pmatrix} \tag{5.47}$$

by an angle of $\alpha = \pi$ around the y-axis $\boldsymbol{n}_y = (0, 1, 0)$. Fig. 5.5 shows two calculations:

[3] All technical details about running this (called "A-two-orbital-model-with-magnetic-field") and other examples with `w2dynamics` can be found on the tutorial part of the website of the code: https://github.com/w2dynamics/w2dynamics/wiki/Tutorials

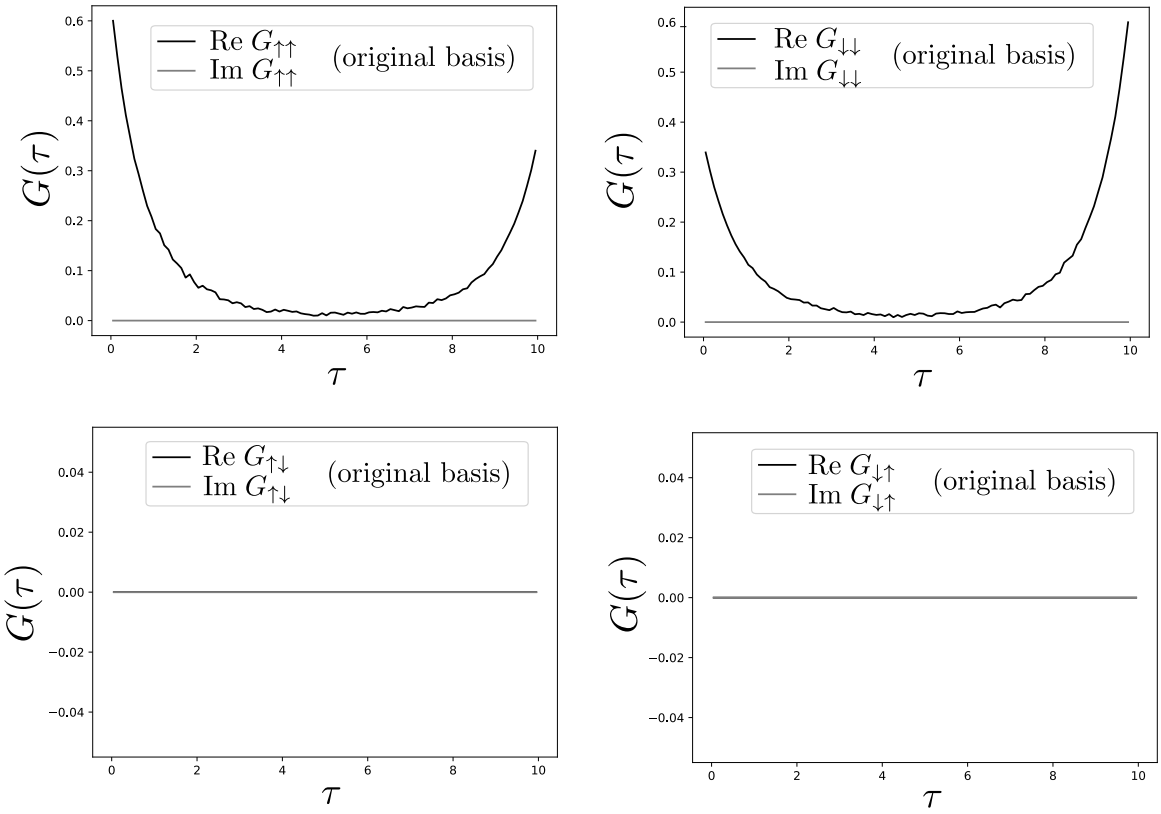

Figure 5.4: *Converged DMFT results for the system with magnetic field in z-direction. The pictures above show the spin-diagonal Green's function, which have a spin polarization. The pictures below show the spin-offdiagonal part, which is zero.*

- one of DMFT convergence, where the Hamiltonian $H(\boldsymbol{k})$ and the interaction matrix were rotated with $R_{\boldsymbol{n}_y}(\pi)$[4],
- and one where the DMFT convergence was done with the original Hamiltonian (with magnetic field in z-direction), and the resulting $G(\tau)$ rotated with $R_{\boldsymbol{n}_y}(\pi)$.

They have to coincide, which is the case. We see, that the magnetic field no longer splits up the occupations of the spins, but its effect is encoded in the real offdiagonal part of $G(\tau)$.

Figure 5.6 shows the same procedure, but with a rotation around the x-axis with a matrix

$$R_{\boldsymbol{n}_x}(\pi) = \begin{pmatrix} \cos(\alpha/2) & -i\sin(\alpha/2) \\ -i\sin(\alpha/2) & \cos(\alpha/2) \end{pmatrix} \tag{5.48}$$

$$= \begin{pmatrix} 1/\sqrt{2} & -i/\sqrt{2} \\ -i/\sqrt{2} & 1/\sqrt{2} \end{pmatrix}. \tag{5.49}$$

Now the magnetic field is encoded in the imaginary offdiagonal part of $G(\tau)$. Note the different symmetry properties of the real and imaginary offdiagonal parts of $G(\tau)$, which come from the hermiticity of the Hamiltonian discussed in Sec. 6.2, especially Eq. (6.17).

5.3.4 Discussion

Performing a calculation in two different bases and comparing the results in one basis is a very powerful test, which sensitively points towards problems. These can be for example not enough

[4]Note that because the Kanamori interaction for two orbitals is SU(2) spin-rotationally invariant, this also corresponds to a magnetic field of $\boldsymbol{h} = 0.2t\sigma_x$ applied to the original system.

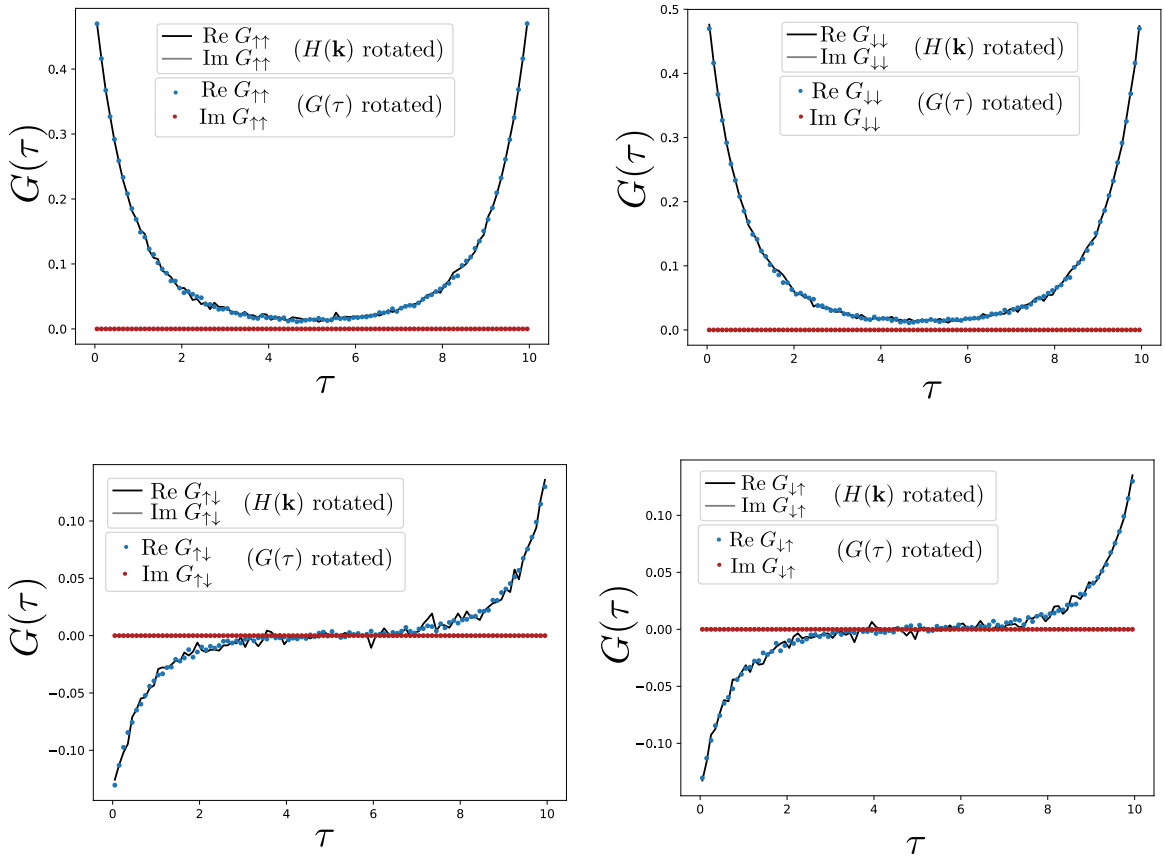

Figure 5.5: *These figures show the results of two calculations. 1) The black and gray solid lines show the system, where the DMFT calculation was done with the Hamiltonian $H(\boldsymbol{k})$ rotated with $R_{\boldsymbol{n}_y}(\pi)$, where the magnetic field now points in x-direction. The diagonal parts of the Greens function are spin-degenerate again, and the effect of the magnetic field is encoded in the real offdiagonal parts of the Greens function (figures below). 2) In order to test the implementation and the input, here are also shown the Green's functions of Fig. 5.4 rotated with $R_{\boldsymbol{n}_y}(\pi)$ (red and blue dots).*

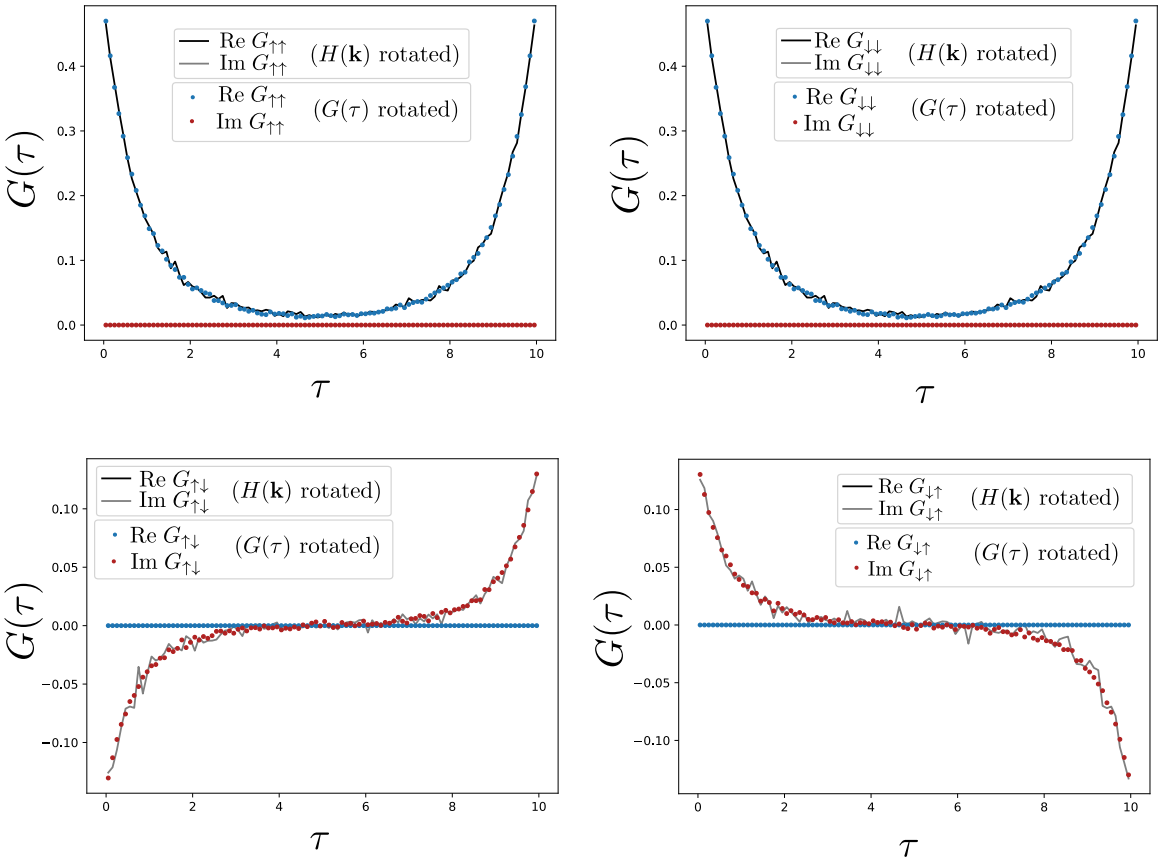

Figure 5.6: *This shows the same as Fig. 5.5, but with a rotation of* $R_{\boldsymbol{n}_x}(\pi)$.

Matsubara frequencies and therefore inaccurate Fourier transforms, omission of important terms of H_{loc} by enforcing too much quantum numbers, or ergodicity problems in the Monte Carlo sampling.

However the rotation test only works for paramagnetic systems. In the example of Sec. 5.3.3 a magnetic field was used to induce a magnetization in order to enable a nontrivial rotation, and the rotation test was found to succeed. This would be very different, if the ordering was an emergent phenomenon. For magnetization in z-direction the order parameter is a scalar ($m = n_\uparrow - n_\downarrow$), but for a magnetization in any other direction it is a frequency-dependent, complex $N_{\text{flav}} \times N_{\text{flav}}$ matrix. In the latter case, the system has many more degrees of freedom to minimize its energy, therefore one cannot expect that a rotation exists, which maps the two systems onto each other. This is also what we observe.

One can force the magnetization into the xy-plane by applying Eq. (6.71) only to the diagonal part of $G(\tau)$, i.e. to symmetrize over the spins on the diagonal only. Since magnetization in z-direction is described by σ_z, this suppresses its z-component. If the paramagnetic solution $G(\tau)$ is completely real, by keeping it real, the magnetization can be forced into the xz-plane. Furthermore applying the two constraints together forces the magnetization to point in x-direction. This is especially useful, if a system is non-uniform in space like layered structures, where one can create in-plane and out-of-plane magnetizations this way.

In any case, the choice of the basis is crucial. First, the average Monte Carlo sign depends on it (Shinaoka et al., 2015), since CTHYB does not like large, offdiagonal imaginary hybridization functions. Second, for ordered solutions the results may become very difficult to interpret, when there is a mixed orbital and spin order, also basis dependent of course. Then one must use physical intuition or a priori knowledge from experiment about what kind of orderings are expected, and which basis is best to examine them.

5.4 The w2dynamics_interface - a link to the TRIQS library

As seen in the previous section, rotation tests are not practical to check ordered solutions. They are however of great interest, therefore one must compare to other implementations of CTHYB and DMFT.

For this and other purposes we made an the `w2dynamics_interface`[5] to `TRIQS`[6], the Toolbox for Research on Interacting Quantum Systems. It provides C++ and python libraries for the treatment of strongly correlated quantum systems, e.g. to quickly build DMFT loops, and also contains complete applications[7] like a CTHYB solver. With the interface it is possible to run the same calculation with two different implementation of the DMFT loop and two solvers:

- `w2dynamics` DMFT loop & `w2dynamics` solver
- `TRIQS` DMFT loop & `w2dynamics` solver
- `TRIQS` DMFT loop & `TRIQS` solver

These three setups give identical results for paramagnetic calculations, but not yet for magnetic ones. Further work has to be done in this direction.

Another motivation for the interface was to compare the two CTHYB solvers. Even though their algorithm is conceptually the same, their interior, especially their implementation of the fermionic trace $\mathrm{Tr}(\hat{\mathcal{C}}) = \sum_n \langle n| \hat{\mathcal{C}} |n\rangle$ can be considered *orthogonal* to each other, making this comparisons valuable. I will briefly describe the differences here.

`triqs_cthyb` calculates $\mathrm{Tr}(\hat{\mathcal{C}}) = \sum_n \langle n| \hat{\mathcal{C}} |n\rangle$ in a matrix-matrix algorithm. This means it multiplies the matrix representations of the operators and saves them in a binary tree, and in the very end contracts one matrix with the eigenstates $|n\rangle$. `w2dyn_cthyb` has a matrix-vector algorithm, which means it multiplies the matrix representations of the operators repeatedly on the eigenstates $|n\rangle$.

`w2dyn_cthyb` employs an importance sampling of the sum over the outer states $|n\rangle$ (the superstate-sampling or state-sampling algorithm of Kowalski et al. (2019)), whereas `triqs_cthyb` performs this sum explicitly.

`triqs_cthyb` uses a lazy trace evaluation Sémon et al. (2014), which is a method to quickly calculate upper and lower bounds of the trace by using the norms of the matrices instead of full matrices. This allows it to reject very unlikely configurations quickly without wasting time to calculating the exact trace. `w2dyn_cthyb` instead uses the sliding window technique to propose only updates local in imaginary time Shinaoka et al. (2014). This enhances acceptance rates a lot, since the weight of a configuration is known to be damped exponentially with the distance of the inserted operators in imaginary time.

[5] https://triqs.github.io/w2dynamics_interface/latest/
[6] https://triqs.github.io/triqs/latest/
[7] https://triqs.github.io/cthyb/latest/

Chapter 6

From system symmetries to Green's function's symmetries

This chapter discusses constraints of Green's functions due to symmetries. For complicated systems it is desirable to know the symmetries of the Green's function and enforce them in DMFT calculations. This improves the statistics and stabilizes the convergence.

First I derive what hermiticity of the Hamiltonian ($\hat{H} = \hat{H}^\dagger$) implies, then I discuss time-reversal symmetry. Last comes a method, to transfer invariances of the Hamiltonian with respect to unitary transforms to constraints for the Green's function.

I consider multi-orbital AIMs with general one- and two-particle interactions, but restrict myself on one-particle Green's functions.

6.1 Some repetitions

For the sake of completeness, I repeat some properties already derived in former chapters. The definition of the imaginary time Green's function is

$$G_{\alpha\beta}(\tau) = -\left\langle T_\tau \hat{c}_\alpha(\tau)\hat{c}^\dagger_\beta(0)\right\rangle, \tag{6.1}$$

where already the symmetry of time translational invariance is applied, which is caused by energy-conservation in the system. The Green's function then only depends on time differences, or equivalently one time can put to zero. The Fourier transforms are

$$G_{\alpha\beta}(i\omega_n) = \int_0^\beta \mathrm{d}\tau\; G_{\alpha\beta}(\tau)\mathrm{e}^{i\omega_n\tau} \tag{6.2}$$

$$G_{\alpha\beta}(\tau) = \frac{1}{\beta}\sum_n G_{\alpha\beta}(i\omega_n)\mathrm{e}^{-i\omega_n\tau}. \tag{6.3}$$

The cyclic property of the trace leads to

$$G_{\alpha\beta}(\tau) = -G_{\alpha\beta}(\tau+\beta). \tag{6.4}$$

6.2 Symmetries from hermiticity

A fundamental property of equilibrium quantum systems is the hermiticity of the Hamilton operator ($\hat{H} = \hat{H}^\dagger$). This is connected to a symmetry of the one-particle Green's function, which I

will derive in the following. Generally, the complex conjugate of a matrix element with hermitian operators $\hat{A}_1, \ldots, \hat{A}_n$ is

$$\langle m| \hat{A}_1 ... \hat{A}_n |n\rangle^* = \langle n| \hat{A}_n^\dagger ... \hat{A}_1^\dagger |m\rangle . \tag{6.5}$$

The order of all objects is inversed and the operators are daggered. We take the definition of the Green's function without time-translational symmetry

$$G_{\alpha\beta}(\tau_1, \tau_2) = \left\langle T_\tau [\hat{c}_\alpha(\tau_1) \hat{c}_\beta^\dagger(\tau_2)] \right\rangle \tag{6.6}$$

$$= \frac{1}{Z} \mathrm{Tr}\left[\mathrm{e}^{-\beta \hat{H}} T_\tau \hat{c}_\alpha(\tau_1) \hat{c}_\beta^\dagger(\tau_2) \right] \tag{6.7}$$

and write the Heisenberg time-evolution explicitly

$$\hat{c}_\alpha^\dagger(\tau) = \mathrm{e}^{\hat{H}\tau} \hat{c}_\alpha^\dagger \mathrm{e}^{-\hat{H}\tau} \tag{6.8}$$

$$\hat{c}_\alpha(\tau) = \mathrm{e}^{\hat{H}\tau} \hat{c}_\alpha \mathrm{e}^{-\hat{H}\tau}. \tag{6.9}$$

Unlike for real times, the dagger of an imaginary-time dependent operator is not just obtained by removing / adding the dagger. Instead the time additionally picks up a minus sign:

$$\left[\hat{c}_\alpha^\dagger(\tau)\right]^\dagger = \left[\mathrm{e}^{\hat{H}\tau} \hat{c}_\alpha^\dagger \mathrm{e}^{-\hat{H}\tau}\right]^\dagger \tag{6.10}$$

$$= \mathrm{e}^{-\hat{H}\tau} \hat{c}_\alpha \mathrm{e}^{\hat{H}\tau} \tag{6.11}$$

$$= \hat{c}_\alpha(-\tau) \tag{6.12}$$

$$[\hat{c}_\alpha(\tau)]^\dagger = \hat{c}_\alpha^\dagger(-\tau). \tag{6.13}$$

Applied to the Green's function Eq. (6.5), this gives

$$G_{\alpha\beta}^*(\tau_1, \tau_2) = \left\langle T_\tau [\hat{c}_\alpha(\tau_1) \hat{c}_\beta^\dagger(\tau_2)] \right\rangle^* \tag{6.14}$$

$$= \left\langle T_\tau [\hat{c}_\beta(-\tau_2) \hat{c}_\alpha^\dagger(-\tau_1)] \right\rangle \tag{6.15}$$

$$= G_{\beta\alpha}(-\tau_2, -\tau_1). \tag{6.16}$$

With time translational invariance one finds

$$G_{\alpha\beta}^*(\tau) = G_{\beta\alpha}(\tau), \tag{6.17}$$

where the time τ is defined as the first minus the second time argument of G. From this follows, that the diagonal part $G_{\alpha\alpha}(\tau)$ is always real for any equilibrium Green's function.

To find the corresponding Matsubara relations first write the original definition, then the complex conjugate of it, and the Fourier representation of the right side of Eq. (6.17):

$$G_{\alpha\beta}(\tau) = \frac{1}{\beta} \sum_n G_{\alpha\beta}(i\omega_n) \mathrm{e}^{-i\omega_n \tau} \tag{6.18}$$

$$G_{\alpha\beta}^*(\tau) = \frac{1}{\beta} \sum_n G_{\alpha\beta}^*(i\omega_n) \mathrm{e}^{i\omega_n \tau} \tag{6.19}$$

$$G_{\beta\alpha}(\tau) = \frac{1}{\beta} \sum_n G_{\beta\alpha}(i\omega_n) \mathrm{e}^{-i\omega_n \tau}. \tag{6.20}$$

According to Eq. (6.17), the right sides of Eqs. (6.19) and (6.20) must be the same. Performing a substitution $i\omega_n \to -i\omega_n$ and remembering that Fourier exponentials are a orthonormal basis set, one finds

$$G_{\alpha\beta}^*(i\omega_n) = G_{\beta\alpha}(-i\omega_n). \tag{6.21}$$

In `w2dynamics`, Eq. (6.21) is enforced by default for the hybridization function $\Delta(i\omega_n)$.

6.3 Time reversal symmetry

Here I first discuss the time reversal of the Schrödinger equation, both time-dependent and time-separated, and in real as well as in imaginary time, to find the properties of states, operators and the time-evolution under time reversal. Then I discuss the time reversal operator and how it transforms the Green's function.

6.3.1 The real time Schrödinger equation (full)

To find out, how states and operators transform under time-reversal, it is convenient to go back to first quantization and Schrödinger's equation

$$i\hbar\frac{\partial}{\partial t}\left|\psi(t)\right\rangle = \hat{H}\left|\psi(t)\right\rangle. \tag{6.22}$$

A complex conjugation of it gives

$$-i\hbar\frac{\partial}{\partial t}\left|\psi(t)\right\rangle^* = \hat{H}^*\left|\psi(t)\right\rangle^*. \tag{6.23}$$

The system is time-reversal invariant, if and only if there exists a unitary transform U_T, which is applied from the left to Eq. (6.23)

$$i\hbar\frac{\partial}{\partial(-t)}U_T\left|\psi(t)\right\rangle^* = U_T\hat{H}^*U_T^{-1}U_T\left|\psi(t)\right\rangle^*, \tag{6.24}$$

and for which $U_T\hat{H}^*U_T^{-1} = \hat{H}$ holds. Then if $\left|\psi(t)\right\rangle$ is a solution of the Schrödinger equation, also $U_T\left|\psi(-t)\right\rangle^*$ is a solution.

6.3.2 The real time Schrödinger equation (time-separated)

To better understand, I now do the same again with the time-separated SGL. There the wave function can be written as $\left|\psi(t)\right\rangle = \mathrm{e}^{-iHt}\left|\psi(0)\right\rangle$ and the SGL becomes

$$i\hbar\frac{\partial}{\partial t}\mathrm{e}^{-iHt}\left|\psi(0)\right\rangle = \hat{H}\mathrm{e}^{-iHt}\left|\psi(0)\right\rangle. \tag{6.25}$$

The complex conjugate of it is

$$(-i)\hbar\frac{\partial}{\partial t}\mathrm{e}^{iH^*t}\left|\psi(0)\right\rangle^* = \hat{H}^*\mathrm{e}^{iH^*t}\left|\psi(0)\right\rangle^*. \tag{6.26}$$

The unitary transform U_T again comes from the left

$$i\hbar\frac{\partial}{\partial(-t)}U_T\mathrm{e}^{iH^*t}U_T^\dagger U_T\left|\psi(0)\right\rangle^* = U_T\hat{H}^*U_T^\dagger U_T\mathrm{e}^{iH^*t}U_T^\dagger U_T\left|\psi(0)\right\rangle^* \tag{6.27}$$

and with $U_T\hat{H}^*U_T^{-1} = \hat{H}$ we have

$$i\hbar\frac{\partial}{\partial(-t)}\mathrm{e}^{iHt}U_T\left|\psi(0)\right\rangle^* = \hat{H}\mathrm{e}^{iHt}U_T\left|\psi(0)\right\rangle^* \tag{6.28}$$

$$i\hbar\frac{\partial}{\partial(-t)}U_T\mathrm{e}^{iH^*t}\left|\psi(0)\right\rangle^* = \hat{H}U_T\mathrm{e}^{-iH^*t}\left|\psi(0)\right\rangle^* \tag{6.29}$$

$$i\hbar\frac{\partial}{\partial(-t)}U_T\left|\psi(t)\right\rangle^* = \hat{H}U_T\left|\psi(t)\right\rangle^* \tag{6.30}$$

$$i\hbar\frac{\partial}{\partial t}U_T\left|\psi(-t)\right\rangle^* = \hat{H}U_T\left|\psi(-t)\right\rangle^*. \tag{6.31}$$

In Eq. (6.29) the antilinear property $U_T\hat{H}^* = \hat{H}U_T$ was used, in Eq. (6.30) the time evolution was put again back into the state via $\mathrm{e}^{iH^*t}\left|\psi(0)\right\rangle^* = \left(\mathrm{e}^{-iHt}\left|\psi(0)\right\rangle\right)^* = \left|\psi(0)\right\rangle^*$ and in Eq. (6.31) a substitution $t \to -t$ was performed.

6.3.3 The imaginary time Schrödinger equation (full)

Since in this thesis all calculations are performed in imaginary time, I briefly have to write down the derivation also for the imaginary time SGL.

$$-\hbar\frac{\partial}{\partial\tau}\left|\psi(\tau)\right\rangle = \hat{H}\left|\psi(\tau)\right\rangle. \tag{6.32}$$

A complex conjugation of it gives

$$-\hbar\frac{\partial}{\partial\tau}\left|\psi(\tau)\right\rangle^* = \hat{H}^*\left|\psi(\tau)\right\rangle^*. \tag{6.33}$$

U_T comes from the left and with $U_T\hat{H}^*U_T^{-1} = \hat{H}$ there is

$$-\hbar\frac{\partial}{\partial\tau}U_T\left|\psi(\tau)\right\rangle^* = U_T\hat{H}^*U_T^{-1}U_T\left|\psi(\tau)\right\rangle^* \tag{6.34}$$

$$= \hat{H}U_T\left|\psi(\tau)\right\rangle^* \tag{6.35}$$

If $|\psi(\tau)\rangle$ is a solution of the imaginary time Schrödinger equation and time-reversal symmetry holds, $U_T\left|\psi(\tau)\right\rangle^*$ is also a solution. It might seem strange that under a time-reversal operation, here the time is unaffected. But time-reversal may also be thought as a mirroring along $i\tau$ in the t–$i\tau$ plane, and therefore leaving only the mirroring axis $i\tau$ invariant.

6.3.4 The time reversal operator

The above considerations motivate to define the time reversal operator T such that it acts on states and operators like

$$T\left|\psi(t)\right\rangle = U_T\left|\psi(-t)\right\rangle^* \tag{6.36}$$

$$T\hat{A}T^{-1} = U_T\hat{A}^*U_T^{-1}. \tag{6.37}$$

It consists of the complex conjugation operator K and a yet undefined, unitary transform U_T:

$$T = U_TK. \tag{6.38}$$

The overlap $\langle\psi|\phi\rangle$ between two time independent states transforms under time reversal like

$$\left\langle\psi\right|T^{-1}T\left|\phi\right\rangle = \left\langle\psi\right|KU_T^\dagger U_TK\left|\phi\right\rangle \tag{6.39}$$

$$= (\left\langle\psi\right|K)\underbrace{U_T^\dagger U_T}_{=\mathbb{1}}(K\left|\phi\right\rangle) \tag{6.40}$$

$$= (\langle\psi|\phi\rangle)^* \tag{6.41}$$

$$= \langle\phi|\psi\rangle, \tag{6.42}$$

i.e. it complex conjugates the overlap. With an operator $\hat{A}$ in between there is

$$\left\langle\psi\right|T^{-1}\hat{A}T\left|\phi\right\rangle = \left\langle\psi\right|KU_T^\dagger\hat{A}U_TK\left|\phi\right\rangle \tag{6.43}$$

$$= (\left\langle\psi\right|K)U_T^\dagger\hat{A}U_T(K\left|\phi\right\rangle) \tag{6.44}$$

$$= \Big(\left\langle\psi\right|(U_T^\dagger\hat{A}U_T)^*\left|\phi\right\rangle\Big)^*, \tag{6.45}$$

where the complex conjugate of the inner bracket must not be mistaken for a Hermitian conjugate. Now there is still the form of the unitary transform U_T to be defined. For this, one precondition

from the correspondence principle has to be used, namely that the spin $\boldsymbol{S} = \hbar/2\boldsymbol{\sigma}$ flips under time reversal

$$T\boldsymbol{S}T^\dagger = -\boldsymbol{S}, \tag{6.46}$$

like any angular momentum in classical mechanics does. With the standard representation of the spin via the Pauli matrices

$$\sigma_x = \begin{pmatrix} 0 & 1 \\ 1 & 0 \end{pmatrix}, \quad \sigma_y = \begin{pmatrix} 0 & -i \\ i & 0 \end{pmatrix}, \quad \sigma_z = \begin{pmatrix} 1 & 0 \\ 0 & -1 \end{pmatrix} \tag{6.47}$$

the transformations under time reversal are

$$T\sigma_x T^{-1} = U_T K \sigma_x K U_T^\dagger = U_T \sigma_x U_T^\dagger = -\sigma_x \tag{6.48}$$
$$T\sigma_y T^{-1} = U_T K \sigma_y K U_T^\dagger = -U_T \sigma_y U_T^\dagger = -\sigma_y \tag{6.49}$$
$$T\sigma_z T^{-1} = U_T K \sigma_z K U_T^\dagger = U_T \sigma_z U_T^\dagger = -\sigma_z. \tag{6.50}$$

Thus U_T must commute with σ_y and anticommute with σ_x and σ_z. Since any unitary matrix of size 2×2 can be decomposed like $U_T = \alpha\mathbb{1} + \beta\sigma_x + \gamma\sigma_y + \delta\sigma_z$, the only possibility that Eqs. (6.48) to (6.50) allow is $U_T = \sigma_y$ (up to phase). The phase can conveniently be chosen such that the result is real:

$$U_T = i\sigma_y = \begin{pmatrix} 0 & -1 \\ 1 & 0 \end{pmatrix}. \tag{6.51}$$

A typical feature of time reversal for fermions is, that applied twice, it restores the original state, but with an minus sign:

$$TT = U_T K U_T K = U^2 = -\mathbb{1}. \tag{6.52}$$

6.3.5 Time reversal of 2nd quantization operators

To figure out, how time reversal acts on 2nd quantized operators, I switch to a spinor notation with

$$|\uparrow\rangle = \begin{pmatrix} 1 \\ 0 \end{pmatrix}, \quad |\downarrow\rangle = \begin{pmatrix} 0 \\ 1 \end{pmatrix}. \tag{6.53}$$

Therefore:

$$U_T |\uparrow\rangle = |\downarrow\rangle \tag{6.54}$$
$$U_T^2 |\uparrow\rangle = -|\uparrow\rangle \tag{6.55}$$
$$U_T^3 |\uparrow\rangle = -|\downarrow\rangle \tag{6.56}$$
$$U_T^4 |\uparrow\rangle = |\uparrow\rangle. \tag{6.57}$$

With the shorthand notation $\sigma = 1$ for spin-up and $\sigma = -1$ for spin-down, the operators transform like

$$U_T^\dagger \hat{c}_\sigma U_T = \sigma \hat{c}_{-\sigma}. \tag{6.58}$$

6.3.6 Time reversal of the Green's function

To get the behavior of the Green's function under time reversal, I write the trace explicitly as a sum over the eigenstates and use the fact, that the time-reversed states $U_T \left|N\right\rangle^*$ also form a complete basis set (here I closely follow Bányai and el Sayed (1994))

$$G_{\sigma\sigma'}(\tau) = \frac{1}{Z}\mathrm{Tr}\left[\mathrm{e}^{-\beta\hat{H}}T_\tau \mathrm{e}^{\hat{H}\tau}\hat{c}_\sigma \mathrm{e}^{-\hat{H}\tau}\hat{c}^\dagger_{\sigma'}\right] \tag{6.59}$$

$$= \frac{1}{Z}\sum_N \mathrm{e}^{-\beta E_N}\left\langle N\right| T_\tau \mathrm{e}^{\hat{H}\tau}\hat{c}_\sigma \mathrm{e}^{-\hat{H}\tau}\hat{c}^\dagger_{\sigma'}\left|N\right\rangle \tag{6.60}$$

$$= \frac{1}{Z}\sum_N \mathrm{e}^{-\beta E_N}(\left\langle N\right| K)U_T^\dagger T_\tau \mathrm{e}^{\hat{H}\tau}\hat{c}_\sigma \mathrm{e}^{-\hat{H}\tau}\hat{c}^\dagger_{\sigma'}U_T(K\left|N\right\rangle). \tag{6.61}$$

We complex conjugate it (not Hermitian conjugate!), where the second quantized operators and the U_T (since they are real) stay unaffected:

$$G^*_{\sigma\sigma'}(\tau) = \frac{1}{Z}\sum_N \mathrm{e}^{-\beta E_N}\left\langle N\right| U_T^\dagger T_\tau \mathrm{e}^{\hat{H}^*\tau}\hat{c}_\sigma \mathrm{e}^{-\hat{H}^*\tau}\hat{c}^\dagger_{\sigma'}U_T\left|N\right\rangle. \tag{6.62}$$

Now if time reversal invariance holds $U_T\hat{H}U_T^\dagger = \hat{H}^*$, or $U_T^\dagger\hat{H}^*U_T = \hat{H}$ respectively, one can restore the original Hamiltonian and relate to the original Green's function

$$G^*_{\sigma,\sigma'}(\tau) = \frac{1}{Z}\sum_N \mathrm{e}^{-\beta E_N}\left\langle N\right| U_T^\dagger T_\tau \mathrm{e}^{\hat{H}^*\tau}\hat{c}_\sigma \mathrm{e}^{-\hat{H}^*\tau}\hat{c}^\dagger_{\sigma'}U_T\left|N\right\rangle \tag{6.63}$$

$$= \frac{1}{Z}\sum_N \mathrm{e}^{-\beta E_N}\left\langle N\right| T_\tau U_T^\dagger \mathrm{e}^{\hat{H}^*\tau}U_T U_T^\dagger\hat{c}_\sigma U_T U_T^\dagger \mathrm{e}^{-\hat{H}^*\tau}U_T U_T^\dagger\hat{c}^\dagger_{\sigma'}U_T\left|N\right\rangle \tag{6.64}$$

$$= \frac{1}{Z}\sum_N \mathrm{e}^{-\beta E_N}\left\langle N\right| T_\tau \mathrm{e}^{\hat{H}\tau}\sigma\hat{c}_{-\sigma}\mathrm{e}^{-\hat{H}\tau}\sigma'\hat{c}^\dagger_{-\sigma'}\left|N\right\rangle \tag{6.65}$$

$$= \sigma\sigma' G_{-\sigma,-\sigma'}(\tau), \tag{6.66}$$

therefore

$$G_{\sigma\sigma'}(\tau) = (\sigma\sigma')G^*_{-\sigma,-\sigma'}(\tau). \tag{6.67}$$

The relations in Matsubara space are found equivalently to Sec. 6.2

$$G_{\sigma\sigma'}(\tau) = \frac{1}{\beta}\sum_n G_{\sigma\sigma'}(i\omega_n)\mathrm{e}^{-i\omega_n\tau} \tag{6.68}$$

$$(\sigma\sigma')G^*_{-\sigma,-\sigma'}(\tau) = \frac{1}{\beta}\sum_n (\sigma\sigma')G^*_{-\sigma,-\sigma'}(i\omega_n)\mathrm{e}^{i\omega_n\tau} \tag{6.69}$$

$$(\sigma\sigma')G^*_{-\sigma,-\sigma'}(\tau) = \frac{1}{\beta}\sum_n (\sigma\sigma')G^*_{-\sigma,-\sigma'}(-i\omega_n)\mathrm{e}^{-i\omega_n\tau}, \tag{6.70}$$

which yields

$$G_{\sigma\sigma'}(i\omega_n) = (\sigma\sigma')G^*_{-\sigma,-\sigma'}(-i\omega_n). \tag{6.71}$$

For multi-orbital systems one obtains the final result by adding orbital indices a and b

$$G_{a\sigma b\sigma'}(i\omega_n) = (\sigma\sigma')G^*_{a,-\sigma b,-\sigma'}(-i\omega_n), \tag{6.72}$$

or in imaginary time, respectively:

$$G_{a\sigma b\sigma'}(\tau) = (\sigma\sigma')G^*_{a,-\sigma b,-\sigma'}(\tau). \tag{6.73}$$

In `w2dynamics`, one can set the parameter `magnetism=para` to force the Green's functions to be time-reversal invariant, and therefore not develop magnetic order.

6.4 General symmetries

A unitary transformation U of the Hamiltonian is called symmetry of the system, if it commutes with the Hamiltonian: $[U, \hat{H}] = 0$. In this section I discuss a method, how a general symmetry of the Hamiltonian can be transferred to symmetry relations for the Green's function. This section is based on section 2.2.2 of the thesis of Georg Rohringer (2013).

I change the notation a little and write the Green's function as a function of the operators and the Hamiltonian:

$$G(c_\alpha, c_\beta^\dagger, \hat{H}) = G_{\alpha\beta}(\tau_1, \tau_2) \tag{6.74}$$

$$= \left\langle T_\tau[\hat{c}_\alpha(\tau_1)\hat{c}_\beta^\dagger(\tau_2)] \right\rangle . \tag{6.75}$$

The idea is the following: The symmetry transform leaves the Hamiltonian invariant $U\hat{H}U^{-1} = \hat{H}' = \hat{H}$. Via its associative property it can be detached from the Hamiltonian and applied to the operators, which then transform the Green's function and deliver a symmetry relation. As a convention I write the transformed quantities primed: G', c' and $c'^\dagger$.

As a simple example one could take the one-orbital Hamiltonian and a SU(2) symmetry, i.e. spin-rotational invariance. By physical intuition this means, that the labels spin-up and spin-down can be exchanged in the Hamiltonian without changing any property of the system. Transferring this symmetry from the Hamiltonian to the Green's function operators, suggests relations $G_{\uparrow\uparrow}(\tau) = G_{\downarrow\downarrow}(\tau)$ and $G_{\uparrow\downarrow}(\tau) = G_{\downarrow\uparrow}(\tau)$, which will show to be correct. However, for multi-orbital systems with general interactions and more complicated symmetries, we have to go through the mathematics.

So let us apply the procedure to a Green's function of a transformed Hamiltonian $\hat{H}'$:

$$G'(c_\alpha, c_\beta^\dagger, \hat{H}') = \left\langle T_\tau[\hat{c}_\alpha(\tau_1)\hat{c}_\beta^\dagger(\tau_2)] \right\rangle \tag{6.76}$$

$$= \left\langle T_\tau[\mathrm{e}^{-\beta\hat{H}'}\mathrm{e}^{\hat{H}'\tau_1}\hat{c}_\alpha\mathrm{e}^{-\hat{H}'\tau_1}\mathrm{e}^{\hat{H}'\tau_2}\hat{c}_\beta^\dagger\mathrm{e}^{-\hat{H}'\tau_2}] \right\rangle \tag{6.77}$$

$$= \left\langle T_\tau[\mathrm{e}^{-\beta UHU^{-1}}\mathrm{e}^{UHU^{-1}\tau_1}\hat{c}_\alpha\mathrm{e}^{-UHU^{-1}\tau_1}\mathrm{e}^{UHU^{-1}\tau_2}\hat{c}_\beta^\dagger\mathrm{e}^{-UHU^{-1}\tau_2}] \right\rangle \tag{6.78}$$

$$= \left\langle T_\tau[U\mathrm{e}^{-\beta\hat{H}}U^{-1}U\mathrm{e}^{\hat{H}\tau_1}U^{-1}\hat{c}_\alpha U\mathrm{e}^{-\hat{H}\tau_1}U^{-1}U\mathrm{e}^{\hat{H}\tau_2}U^{-1}\hat{c}_\beta^\dagger U\mathrm{e}^{-\hat{H}\tau_2}U^{-1}] \right\rangle \tag{6.79}$$

$$= \left\langle T_\tau[\mathrm{e}^{-\beta\hat{H}}\mathrm{e}^{\hat{H}\tau_1}U^{-1}\hat{c}_\alpha U\mathrm{e}^{-\hat{H}\tau_1}\mathrm{e}^{\hat{H}\tau_2}U^{-1}\hat{c}_\beta^\dagger U\mathrm{e}^{-\hat{H}\tau_2}] \right\rangle \tag{6.80}$$

$$= \left\langle T_\tau[\hat{c}'_\alpha(\tau_1)\hat{c}'^\dagger_\beta(\tau_2)] \right\rangle \tag{6.81}$$

$$= G'(\hat{c}'_\alpha, \hat{c}'^\dagger_\beta, \hat{H}). \tag{6.82}$$

The transformed operators were defined as

$$\hat{c}'^\dagger_\alpha = U^{-1}\hat{c}_\alpha^\dagger U \tag{6.83}$$

$$\hat{c}'_\alpha = U^{-1}\hat{c}_\alpha U. \tag{6.84}$$

Note that going from Eq. (6.78) to Eq. (6.79) the transformation matrices have been dragged out of the exponentials.[1] Now if U is a symmetry of the system with $[U, \hat{H}] = 0$, the Hamiltonians are the same $\hat{H}' = U\hat{H}U' \stackrel{!}{=} \hat{H}$, and therefore also the Green's functions:

$$G'(c'_\alpha, c'^\dagger_\beta, \hat{H}) \stackrel{!}{=} G(c_\alpha, c_\beta^\dagger, \hat{H}). \tag{6.85}$$

On the right side, the operators $c'^\dagger$ and c' have to be expressed in terms of the untransformed operators $c^\dagger$ and c, of course. Practically, once $[U, \hat{H}] = 0$ was shown, one applies the transformations to the operators, and Eq. (6.85) delivers constraints for G.

[1] This can be seen by $\mathrm{e}^{UHU^{-1}\tau} = I + UHU^{-1}\tau + \frac{1}{2}UHU^{-1}\tau UHU^{-1}\tau + \cdots = U[I + \hat{H}\tau + \frac{1}{2}\hat{H}\tau\hat{H}\tau + \ldots]U^{-1} = U\mathrm{e}^{\hat{H}\tau}U^{-1}$, and also using $U^{-1}U = \mathbb{1}$.

6.5 SU(2) symmetry

As application of the method from the last section and an example for a transform described by a unitary matrix, I want to discuss the SU(2) symmetry here, which is the invariance under rotation in spin-space. I employ a spinor notation $\hat{\boldsymbol{c}}^\dagger = (\hat{c}_\uparrow^\dagger, \hat{c}_\downarrow^\dagger)^T$ and $\hat{\boldsymbol{c}} = (\hat{c}_\uparrow, \hat{c}_\downarrow)^T$, where the original system is such that the spin quantization axis is in z-direction. A rotation around a axis $\boldsymbol{n}$ of an angle φ is described by (Rohringer, 2013)

$$\hat{\boldsymbol{c}}'(\boldsymbol{n},\varphi) = \Big[\cos(\varphi/2)\mathbb{1} - i\sin(\varphi/2)\boldsymbol{n}\cdot\boldsymbol{\sigma}\ \Big]\hat{\boldsymbol{c}} \tag{6.86}$$

$$\hat{\boldsymbol{c}}'^\dagger(\boldsymbol{n},\varphi) = \Big[\cos(\varphi/2)\mathbb{1} + i\sin(\varphi/2)\boldsymbol{n}\cdot\boldsymbol{\sigma}^T\Big]\hat{\boldsymbol{c}}^\dagger. \tag{6.87}$$

Again orbital indices will be neglected in the following, and added again in the end, because the symmetry only acts on spin space. A rotation around the y-axis $\boldsymbol{n} = (0,1,0)$ gives explicitly

$$\begin{pmatrix}\hat{c}_\uparrow(\varphi)\\ \hat{c}_\downarrow(\varphi)\end{pmatrix} = \begin{pmatrix}\cos(\varphi/2) & -\sin(\varphi/2)\\ \sin(\varphi/2) & \cos(\varphi/2)\end{pmatrix}\begin{pmatrix}\hat{c}_\uparrow\\ \hat{c}_\downarrow\end{pmatrix} \tag{6.88}$$

$$\begin{pmatrix}\hat{c}_\uparrow^\dagger(\varphi)\\ \hat{c}_\downarrow^\dagger(\varphi)\end{pmatrix} = \begin{pmatrix}\cos(\varphi/2) & -\sin(\varphi/2)\\ \sin(\varphi/2) & \cos(\varphi/2)\end{pmatrix}\begin{pmatrix}\hat{c}_\uparrow^\dagger\\ \hat{c}_\downarrow^\dagger\end{pmatrix}. \tag{6.89}$$

Note that in general, the annihilators rotate different compared to the creators, but for this special case the minus in Eq. (6.86) cancels the transpose in Eq. (6.87).

6.5.1 Rotation of $\varphi = \pi$ (spin rotation of 180°)

Now I want to perform some rotations of specific angles explicitly, to derive the constraints of a SU(2)-invariant Green's function. Starting with an angle of $\varphi = \pi$ gives the rotations

$$\begin{pmatrix}c'_\uparrow\\ c'_\downarrow\end{pmatrix} = \begin{pmatrix}-\hat{c}_\downarrow\\ \hat{c}_\uparrow\end{pmatrix} \quad \text{and} \quad \begin{pmatrix}c'^\dagger_\uparrow\\ c'^\dagger_\downarrow\end{pmatrix} = \begin{pmatrix}-\hat{c}^\dagger_\downarrow\\ \hat{c}^\dagger_\uparrow\end{pmatrix} \tag{6.90}$$

for the operators. The diagonal Green's function then transforms like

$$\begin{aligned} G'(\hat{c}'_\uparrow, \hat{c}'^\dagger_\uparrow, \hat{H}) &= \left\langle T_\tau \hat{c}'_\uparrow(\tau)\hat{c}'^\dagger_\uparrow\right\rangle && (6.91)\\ &= \left\langle T_\tau(-\hat{c}_\downarrow(\tau))\left(-\hat{c}^\dagger_\downarrow\right)\right\rangle && (6.92)\\ &= G_{\downarrow\downarrow}(\tau) && (6.93)\\ &\stackrel{!}{=} G(\hat{c}_\uparrow, \hat{c}^\dagger_\uparrow, \hat{H}), && (6.94)\end{aligned}$$

therefore

$$G_{\uparrow\uparrow}(\tau) = G_{\downarrow\downarrow}(\tau). \tag{6.95}$$

The same procedure for the offdiagonal Green's function gives

$$\begin{aligned} G'(\hat{c}'_\uparrow, \hat{c}'^\dagger_\downarrow, \hat{H}) &= \left\langle T_\tau \hat{c}'_\uparrow(\tau)\hat{c}'^\dagger_\downarrow\right\rangle && (6.96)\\ &= \left\langle T_\tau(-\hat{c}_\downarrow(\tau))\hat{c}^\dagger_\uparrow\right\rangle && (6.97)\\ &= -G_{\downarrow\uparrow}(\tau) && (6.98)\\ &\stackrel{!}{=} G(\hat{c}_\uparrow, \hat{c}^\dagger_\downarrow, \hat{H}), && (6.99)\end{aligned}$$

therefore

$$G_{\uparrow\downarrow}(\tau) = -G_{\uparrow\downarrow}(\tau). \tag{6.100}$$

6.5.2 Rotation of $\varphi = \pi/2$ (spin rotation of $90°$)

Let us try one more angle, namely $\varphi = \pi/2$. This gives the rotations

$$\begin{pmatrix} \hat{c}'_\uparrow \\ \hat{c}'_\downarrow \end{pmatrix} = \begin{pmatrix} \frac{1}{\sqrt{2}}(\hat{c}_\uparrow - \hat{c}_\downarrow) \\ \frac{1}{\sqrt{2}}(\hat{c}_\uparrow + \hat{c}_\downarrow) \end{pmatrix} \quad \text{and} \quad \begin{pmatrix} \hat{c}'^\dagger_\uparrow \\ \hat{c}'^\dagger_\downarrow \end{pmatrix} = \begin{pmatrix} \frac{1}{\sqrt{2}}(\hat{c}^\dagger_\uparrow - \hat{c}^\dagger_\downarrow) \\ \frac{1}{\sqrt{2}}(\hat{c}^\dagger_\uparrow + \hat{c}^\dagger_\downarrow) \end{pmatrix} \tag{6.101}$$

for the operators. The diagonal Green's function then transforms like

$$\begin{aligned} G'_{\uparrow\uparrow}(\tau) &= \left\langle T_\tau \hat{c}'_\uparrow(\tau)\hat{c}'^\dagger_\uparrow \right\rangle && (6.102)\\ &= \left\langle T_\tau \frac{1}{\sqrt{2}}(\hat{c}_\uparrow(\tau) - \hat{c}_\downarrow(\tau))\frac{1}{\sqrt{2}}\left(\hat{c}^\dagger_\uparrow - \hat{c}^\dagger_\downarrow\right) \right\rangle && (6.103)\\ &= \left\langle T_\tau \frac{1}{2}\left(\hat{c}_\uparrow(\tau)\hat{c}^\dagger_\uparrow + \hat{c}_\downarrow(\tau)\hat{c}^\dagger_\downarrow - \hat{c}_\uparrow(\tau)\hat{c}^\dagger_\downarrow - \hat{c}_\downarrow(\tau)\hat{c}^\dagger_\uparrow\right) \right\rangle && (6.104)\\ &= \frac{1}{2}(G_{\uparrow\uparrow} + G_{\downarrow\downarrow} - G_{\uparrow\downarrow} - G_{\downarrow\uparrow}) && (6.105)\\ &\stackrel{!}{=} G_{\uparrow\uparrow}(\tau), && (6.106) \end{aligned}$$

and the offdiagonal Green's function like

$$\begin{aligned} G'_{\uparrow\downarrow}(\tau) &= \left\langle T_\tau \hat{c}'_\uparrow(\tau)\hat{c}'^\dagger_\downarrow \right\rangle && (6.107)\\ &= \left\langle T_\tau \frac{1}{\sqrt{2}}(\hat{c}_\uparrow(\tau) - \hat{c}_\downarrow(\tau))\frac{1}{\sqrt{2}}\left(\hat{c}^\dagger_\uparrow + \hat{c}^\dagger_\downarrow\right) \right\rangle && (6.108)\\ &= \left\langle T_\tau \frac{1}{2}\left(\hat{c}_\uparrow(\tau)\hat{c}^\dagger_\uparrow - \hat{c}_\downarrow(\tau)\hat{c}^\dagger_\downarrow + \hat{c}_\uparrow(\tau)\hat{c}^\dagger_\downarrow - \hat{c}_\downarrow(\tau)\hat{c}^\dagger_\uparrow\right) \right\rangle && (6.109)\\ &= \frac{1}{2}(G_{\uparrow\uparrow} - G_{\downarrow\downarrow} + G_{\uparrow\downarrow} - G_{\downarrow\uparrow}) && (6.110)\\ &\stackrel{!}{=} G_{\uparrow\downarrow}(\tau) && (6.111) \end{aligned}$$

Using the results of the previous section, this does not give additional constraints.

6.5.3 A general rotation

Last let me show, that any general rotation

$$\begin{pmatrix} c'_\uparrow \\ c'_\downarrow \end{pmatrix} = \begin{pmatrix} \cos(\frac{\varphi}{2})\hat{c}_\uparrow - \sin(\frac{\varphi}{2})\hat{c}_\downarrow \\ \sin(\frac{\varphi}{2})\hat{c}_\uparrow + \cos(\frac{\varphi}{2})\hat{c}_\downarrow \end{pmatrix} \quad \text{and} \quad \begin{pmatrix} c'^\dagger_\uparrow \\ c'^\dagger_\downarrow \end{pmatrix} = \begin{pmatrix} \cos(\frac{\varphi}{2})\hat{c}^\dagger_\uparrow - \sin(\frac{\varphi}{2})\hat{c}^\dagger_\downarrow \\ \sin(\frac{\varphi}{2})\hat{c}^\dagger_\uparrow + \cos(\frac{\varphi}{2})\hat{c}^\dagger_\downarrow \end{pmatrix} \tag{6.112}$$

does not provide more information, compared to what we already have. The diagonal Green's function transforms like

$$\begin{aligned} G'_{\uparrow\uparrow}(\tau) &= \left\langle T_\tau \left[\cos(\frac{\varphi}{2})\hat{c}_\uparrow(\tau) - \sin(\frac{\varphi}{2})\hat{c}_\downarrow(\tau)\right]\left[\cos(\frac{\varphi}{2})\hat{c}^\dagger_\uparrow - \sin(\frac{\varphi}{2})\hat{c}^\dagger_\downarrow\right] \right\rangle && (6.113)\\ &= \left\langle T_\tau \left[\cos^2(\frac{\varphi}{2})\hat{c}_\uparrow(\tau)\hat{c}^\dagger_\uparrow + \sin^2(\frac{\varphi}{2})\hat{c}_\downarrow(\tau)\hat{c}^\dagger_\downarrow\right] - \cos(\frac{\varphi}{2})\sin(\frac{\varphi}{2})\left(\hat{c}_\uparrow(\tau)\hat{c}^\dagger_\downarrow + \hat{c}_\downarrow(\tau)\hat{c}^\dagger_\uparrow\right) \right\rangle \\ &= \cos^2(\frac{\varphi}{2})G_{\uparrow\uparrow} + \sin^2(\frac{\varphi}{2})G_{\downarrow\downarrow} && (6.114)\\ &\stackrel{!}{=} G_{\uparrow\uparrow}(\tau) && (6.115) \end{aligned}$$

and the offdiagonal like

$$G'_{\uparrow\downarrow}(\tau) = \left\langle T_\tau \left[\cos(\frac{\varphi}{2})\hat{c}_\uparrow(\tau) - \sin(\frac{\varphi}{2})\hat{c}_\downarrow(\tau) \right] \left[\sin(\frac{\varphi}{2})\hat{c}^\dagger_\uparrow + \cos(\frac{\varphi}{2})\hat{c}^\dagger_\downarrow \right] \right\rangle \tag{6.116}$$

$$= \left\langle T_\tau \left[\cos^2(\frac{\varphi}{2})\hat{c}_\uparrow(\tau)\hat{c}^\dagger_\downarrow - \sin^2(\frac{\varphi}{2})\hat{c}_\downarrow(\tau)\hat{c}^\dagger_\uparrow \right] + \cos(\frac{\varphi}{2})\sin(\frac{\varphi}{2}) \left(\hat{c}_\uparrow(\tau)\hat{c}^\dagger_\uparrow - \hat{c}_\downarrow(\tau)\hat{c}^\dagger_\downarrow \right) \right\rangle$$

$$= \cos^2(\frac{\varphi}{2})G_{\uparrow\downarrow} - \sin^2(\frac{\varphi}{2})G_{\downarrow\uparrow} \tag{6.117}$$

$$\stackrel{!}{=} G_{\uparrow\downarrow}(\tau) \tag{6.118}$$

When using the results of $\varphi = \pi$ and the trigonometric Pythagorean identity, one sees, that this gives no additional information.

Let me summarize the findings of this section by adding orbital indices:

$$G_{a\uparrow b\uparrow} = G_{a\downarrow b\downarrow} \tag{6.119}$$

$$G_{a\uparrow b\downarrow} = G_{a\downarrow b\uparrow} \tag{6.120}$$

Chapter 7

Unconventional fermions in the presence of interactions

This chapter is based on the original work already published in Physical Review B (Di Sante et al., 2017). All figures and captions are taken from there (if not otherwise cited), as well as some text (which is marked with a sidebar on the left).

7.1 Unconventional excitations in the solid

Electrons in solids witness a reduced spatial symmetry in comparison to the space-time continuum. While the high-energy perspective constrains us to Majorana, Weyl, and Dirac fermions in accordance with the inhomogeneous Lorentz (or Poincaré) group, electronic quasiparticles in solids at low energies can display emergent fermionic behavior within and even beyond this classification (Bradlyn et al., 2016; Wieder et al., 2016). Graphene constitutes one of the most prominent material discoveries where Dirac-type quasiparticles have been realized (Neto et al., 2009). The current rise of Weyl semimetals (Wan et al., 2011), along with Majorana quasiparticles in superconducting heterostructures (Fu and Kane, 2008; Read and Green, 2000), complements this evolution in contemporary condensed-matter physics.

Recently, Wieder et al. (2016) have brought up the possibility to realize double Dirac quasiparticles in certain 3D crystals with specific non-symmorphic point group symmetry. Such a type of fermion does not exist in high-energy physics due to its incompatibility with the Lorentz group, and highlights the relevance of lattice fermion realizations not only in terms of quantum many-body, but also single-particle states of matter. Double Dirac fermions were identified by a systematic analysis of all double space groups (SGs) accounting for $S = 1/2$ electrons in spin-orbit coupled crystals with time reversal symmetry (Bradlyn et al., 2016). In particular, SG 130 and 135 were found to establish eminently suited ground for generic double Dirac fermions protected by point group symmetry. Among all material candidates for SG 130, it was already realized by Bradlyn et al. (2016) that Bi_2CuO_4 might be a prime candidate due to its filling-enforced semimetallicity (Po et al., 2016), nurturing the hope to observe double Dirac fermions close to the Fermi level. All such band structure classifications, however, always need to be extended to account for the role of interactions in the material, which turn out to be of vital relevance in Bi_2CuO_4. Most of the topological band properties, even the metallic ones, display a certain degree of persistence against weak interactions as long as those do not break any protecting symmetry. Interaction-induced instabilities, however, do change

the symmetry class of the quantum state, possibly affecting the whole range of constituting symmetries including charge conservation, time reversal, and point group operations.

7.1.1 Role of electron-electron interactions

As a paradigmatic change, the concept of topological quantum chemistry is firmly emerging, based on the idea that quantum chemistry and topology conspire to provide a new search principle for topological quantum states of matter (Bradlyn et al., 2017). Many new topological insulator and semimetal candidates were revealed within such a framework, where however strong electron interactions are neglected. In this Letter, to show how crucial for this search is to go beyond the single-particle description, we study strong interaction effects of double Dirac fermions, analyzing the band structure properties and electronic correlations in Bi_2CuO_4. From density functional theory, we distill an effective eight-band tight-binding Hubbard model which is dominated by the $d_{x^2-y^2}$ orbital of the four Cu atoms in the unit cell. Spin-orbit coupling (SOC) is found to be weak because the heavy atoms of the compound do not significantly contribute to the low-energy density of states. As expected, the double Dirac dispersion is located close to the Fermi energy, as identified by an 8-fold band degeneracy at the A point.

7.1.2 Band structure and effective tight-binding model

Bi_2CuO_4 crystallizes in the tetragonal spage group P4/ncc (SG 130), see Fig. 7.1(a) (Garcia-Munoz et al., 1990). Four inequivalent Cu atoms in the unit cell share a square-planar CuO_4 coordination, stacked along the out-of-plane direction and intercalated by Bi atoms, as depicted in Fig. 7.1(b). The Cu-O hybridization is quite strong, leading to a mixed *d-p* character of the band structure of the occupied states. The Bi-*p* manifold only starts ≈ 1.5 eV above the Fermi level, suggesting that the low energy model is given by Cu and O electronic states. The square-planar crystal field is characterized by a higher-in-energy $d_{x^2-y^2}$ orbital experiencing a head-to-head interaction with the O-*p*. The level separation is schematically drawn in the left inset of Fig. 7.1(c). Cu is nominally in the oxidation state 2+ (i.e. d^9 configuration). For this reason, a half-filled $d_{x^2-y^2}$-derived single spin-degenerate band per Cu atom in the unit cell is expected to dominate at low energies. Fig. 7.1(c) displays the band dispersion of the electronic states around the Fermi level. Due to the dominant Cu orbital, the effect of SOC is almost negligible, only inducing small spin splittings. We estimate the energy scale of SOC to be ≈ 20 meV. Despite its small scale, however, SOC is a crucial ingredient for the symmetries in the double SG representation that ensures the existence of a double Dirac fermion with linear dispersion at the Brillouin zone corner $A = (\pi, \pi, \pi)$. As the band filling is given by an odd multiple of 4 ($180 = 8\times22+4$), the double Dirac fermion in Bi_2CuO_4 is located almost at the Fermi level, as visible in the right inset of Fig. 7.1(c).

From the DFT band structure of the system in the metallic, paramagnetic phase a effective tight binding model is derived using maximally localized Wannier functions. Despite the UFO-structure of the CuO_4 may suggest that the system has a rather 2-dimensional character, the band-structure between Γ and Z is not constant. It has a strong three-dimensional character and thus is within the range of applicability of DMFT.

The strength of the electron-electron interaction has been estimated by cRPA to be $U_{\mathrm{CRPA}} = 1.58$ eV.

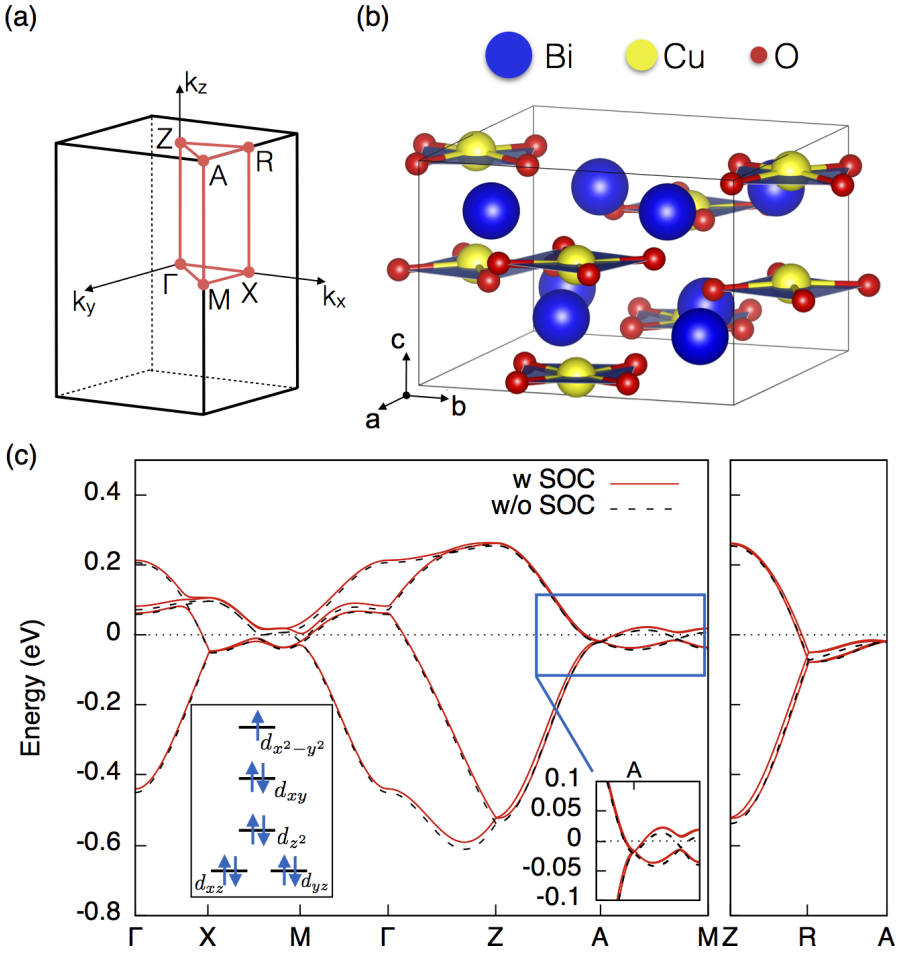

Figure 7.1: *(a) with corresponding high-symmetry points. (b) Crystal structure of Bi2CuO4. Atom colors: Bi (blue), Cu (yellow), and O (red). Blue plaquettes highlight the square-planar CuO4 coordination. (c) DFT band structure in the paramagnetic metallic phase with (red solid line) and without (black dashed line) SOC. The left inset is a schematic representation of the square-planar crystal field and orbital filling for Cu-type d9. The right inset shows a zoom around the eightfold degenerate A point, which comes along a characteristic fourfold degeneracy along the R-Z line.*

7.2 Mott transition and spectral function

Comparing this strength of the interaction with the bandwidth, one may already guess that Bi_2CuO_4 is deep in the Heisenberg limit.

Fig. 7.2(a) displays the quasiparticle weight

$$Z = \lim_{\omega \to 0} \left(1 - \frac{\partial}{\partial \omega} \mathrm{Re}\Sigma(\omega)\right)^{-1}. \tag{7.1}$$

Before reaching U_{cRPA}, we encounter a Mott-type metal-to-insulator transition (MIT) at $U_{\mathrm{Mott}} \approx 0.85$ eV. At the Mott transition, the quasiparticle weight is suppressed by interactions, and the fraction of doubly-occupied Cu-sites $\langle n_\uparrow n_\downarrow \rangle$ reduces from the free-particle value of 1/4 towards zero (inset in Fig. 7.2(a)). At intermediate U, the spectral function, as depicted in Fig. 7.2(b), is well described by the DFT single particle band structure renormalized in terms of bandwidth by the quasiparticle weight Z, along with the appearance of incoherent lower and upper Hubbard bands. Since the double Dirac fermion is located close to the Fermi level, it contributes to the quasiparticle peak for interaction strengths below the Mott transition. Even though the eightfold-degeneracy at the A-point remains discernible up to U_{Mott}, the Coulomb repulsion has a dramatic effect on the double Dirac feature. The velocities are substantially reduced and the linewidths increase rapidly due to the strong scattering. Even if the protecting symmetry is not yet broken by the magnetic ordering, the damping of the band structure as well as the transfer of spectral weight towards high-energy (Hubbard) bands are so pronounced that the whole double Dirac feature looses most of its distinctness already for $U \ll U_{\mathrm{Mott}}$.

7.2.1 Magnetic ordering

At $U_{\mathrm{cRPA}} = 1.58$ eV, allowing for magnetic ordering, the ground state of Bi_2CuO_4 is not paramagnetic, but displays a intra-unit-cell magnetic order. As a consequence, the Mott regime and the breaking of time-reversal symmetry independently suggest the absence of double Dirac cones.

Fig. 7.3 shows some DMFT magnetization curves for interaction values already larger than the cRPA value $U_{\mathrm{cRPA}} = 1.58$ eV. The system is in the Heisenberg limit, which means the Hubbard model can be mapped very well onto a Heisenberg model. Note that the DMFT Neel temperature is proportional to $1/U$, which is typical of the Heisenberg limit. The Heisenberg exchange interaction scales indeed like $J \sim t^2/U$. For this compound, DMFT does not describe very well its G-antiferromagnetism (the magnetic moments aligned antiferromagnetically in all directions). The calculated ordering temperatures are way too large. We instead assume the electrons to be localized in the orbitals and construct a Heisenberg model, whose behavior is governed by the exchange interaction between the spins of the localized electrons. Solving this with a classical quantum Monte Carlo technique (for details see appendix of Di Sante et al. (2017)), gives essentially the experimental value (see Fig. 7.3). Since DMFT describes the local electronic correlations within one atom exactly, but non-local correlations only within a mean-field approximation, the cause for the different Neel temperatures comes from non-local correlations (Rohringer et al., 2011).

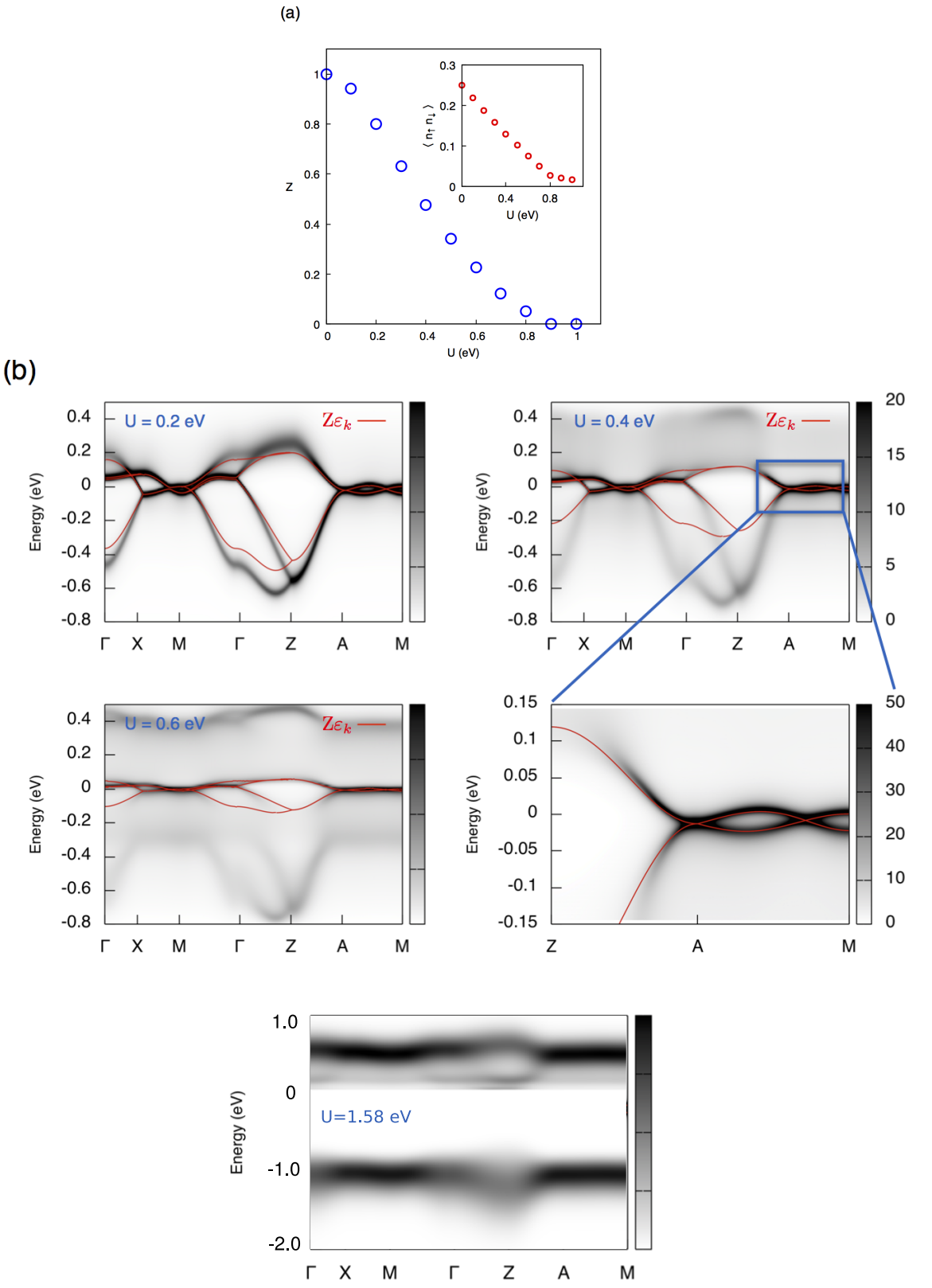

Figure 7.2: *(a) DMFT quasiparticle weight Z (main panel) and double occupancies (inset) as a function of U in the paramagnetic phase for a temperature $\beta = 100$ eV^{-1}. The Mott transition occurs at UMott ≈ 0.85 eV. (b) Momentum-resolved DMFT spectral function $A(k, \omega)$ for $U = 0.2$, 0.4, 0.6 and the cRPA value of 1.58 eV. Red lines denote the DFT band structure renormalized by the DMFT quasiparticle weight Z. For $U = 0.4$ eV, the zoom shows the preservation of the eightfold degenerate A point along with an already significant band renormalization.*

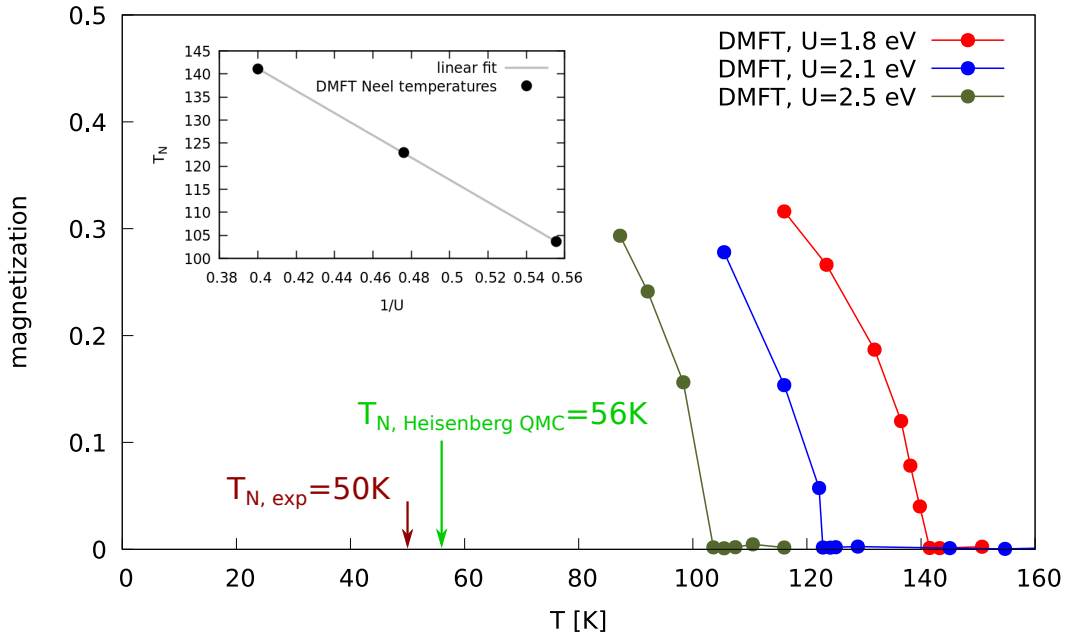

Figure 7.3: *This figure shows DMFT results of the Neel temperature for the interaction values $U = 1.8$, 2.1 and 2.5 eV. Also shown is the experimental value and the value of classical Monte Carlo for the corresponding Heisenberg model. The inset shows that T_N is proportional to $\frac{1}{U}$, which means it follows the behavior expected for a Heisenberg model.*

7.2.2 Hydrostatic pressure

Pressure has a profound impact on the electronic properties of a solid. Here we study the effects of hydrostatic pressure, i.e. uniform pressure from all spacial directions. Uniform pressure makes the unit cell smaller, and widens the Brillouin zone. This increases the overlaps between the orbitals, thus makes the hopping terms larger and the DOS broader. On the other hand, orbitals become larger, which reduces the electronic interaction energies. Both effects make uniform pressure a method to reduce the strength of electronic correlations. The question arises, whether in reasonable experimental setups the double Dirac cones in Bi_2CuO_4 can be restored. This is the topic of this section.

As illustrated in Fig. 7.4(a-c), the bands above and below the $d_{x^2-y^2}$ manifold get closer to the Fermi level. This results in a more efficient screening of the Coulomb interaction for the target $d_{x^2-y^2}$ states. Fig. 7.4(d) (...) report the corresponding reduction of U_{cRPA}. In addition, the slight increase of the $d_{x^2-y^2}$ bandwidth ($\sim 10\%$) leads to a larger critical U_{Mott} for the Mott transition. Even though U_{cRPA} remains larger than U_{Mott} all the way up to 50 GPa, the trend towards the restoration of the metallic phase is evident, as shown in Fig. 7.4(d,e,f). The most reliable feature is the trend observed as a function of pressure rather than the absolute values of the Coulomb interaction strength obtained through cRPA. The absolute accuracy of cRPA is challenged by (i) the slight tendency to underestimate the Coulomb matrix elements, (ii) the mapping of the non-local cRPA Coulomb interaction onto a local Hubbard model, and (iii) the absence of all non-local correlations within the DMFT approximation. The latter is known to reduce the Néel temperature of about 30-40% in 3D systems (Rohringer et al., 2011). Assuming the absence of a structural phase transition, this suggests a transition into a high-pressure double Dirac metal for $\simeq 60$ GPa. So far, pressure effects have been hardly

investigated in Bi_2CuO_4. In Zhang et al. (2006), the occurrence of a structural phase transition might have been observed within 20 GPa and 37 GPa, but demands further analysis.

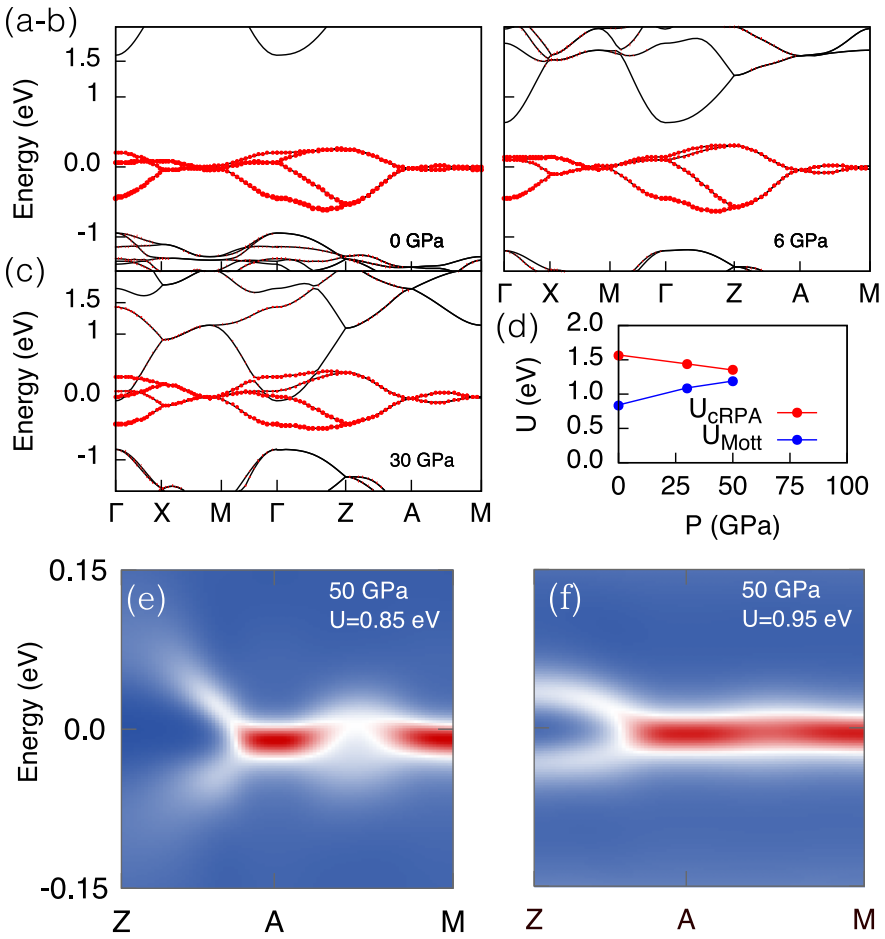

Figure 7.4: *(Color online) (a-c) Evolution of the DFT band structure for $P = 0$ (ambient pressure), 6, and 30 GPa. Red symbols refer to the $d_{x^2-y^2}$ character. (d) U_{cRPA} and U_{Mott} as a function of pressure. It is suggestive to expect an insulator to metal transition around $P = 50-60$ GPa. (e-f) Momentum-resolved DMFT spectral function $A(k, \omega)$ for $U = 0.85$ and 0.95 eV at a pressure $P = 50$ GPa. A two-color palette has been used to better highlight the linear dispersion along the Z-A line. The maximum color intensity (arb. units) in panel (e) is twice as larger as that in panel (f).*

7.2.3 Conclusion

Our analysis identifies Bi_2CuO_4 as a prototypical material where crystal structure and orbital character, under pressure, conspire to give rise to correlated double Dirac fermions close to the Fermi level. At ambient pressure, the interactions turn out to drive the system into a Mott state along with magnetic intra-cell ordering where the double Dirac cone is absent. As a function of hydrostatic pressure, we find that the material could be driven into a metallic state where the double Dirac features would emerge. For this, our ab initio calculations indicate a pressure regime of ≈ 60 GPa, which is still within the range of experimental pressure cell transport setups. Our study suggests several routes to realize a double-Dirac metal in Bi_2CuO_4 at low temperatures. For instance, a combined pressure and doping approach could establish

a convenient perturbation of the pristine material in order to render correlated double Dirac fermions accessible to experimental investigation.

Beside the specific example of double Dirac fermions in Bi_2CuO_4, (...) we communicate a rather general message, namely that all these new topological quantum chemistry developments need to be looked at more carefully, as interactions are systematically neglected (Bradlyn et al., 2017). This may constitute the most severe and harsh drawback of the whole approach, largely based on the single-particle band theory of electrons. On the other hand, we demonstrated how it is possible to restore the nontrivial new quasiparticles physics by means of external handles, curing this way the intrinsic failure of the topological quantum chemistry machinery.

This is crucial in light of future technological applications of such new quasiparticles. To give an example, it will be of relevant interest to study the effects of a magnetic field imposed on the double Dirac particle dispersion, similarly to what has been done in the case of Dirac and Weyl semimetals (Jeon et al., 2014; Klier et al., 2015). Centered in the same conal center, the double Dirac particle features two Dirac cones of different opening angles. As a function of these angles, it is reasonable to foresee an unprecedented variety of band decompositions that promises to happen in response to a magnetic field, along with a likely highly non-trivial magnetoresistance profile. However, in analogy to the Fermi velocity renormalization effect by interactions in graphene (Elias et al., 2011), the renormalization of the double Dirac cone dispersion will play a quantitative key role.

Chapter 8

Higgs and Goldstone modes in excitonic magnets

This chapter is based on the original work already published in Physical Review Letters (Geffroy et al., 2019). All figures and captions are taken from there (if not otherwise cited), as well as some text (which is marked with a sidebar on the left).

In this chapter I will first derive the properties of Higgs and Goldstone modes within the theory of Ginzburg and Landau. Then I introduce the concept of excitonic condensation, and identify these modes in a model of an excitonic magnet. Finally we will make a connection of the excitonic susceptibilities, which are not measurable by experiment, to spin-spin susceptibilities, which are accessible by experiments.

8.1 Effective field theory of Higgs and Goldstone bosons

The Ginzburg-Landau description of emergent ordering phenomena in terms of spontaneously broken symmetries is one of the most successful concepts in physics. The system is characterized by an order parameter, which is zero above the critical temperature and nonzero below. Since it is an effective theory, the precise microscopic expression for the order parameter, which might be very difficult to determine, is not required to find the macroscopic consequences. In many cases the order parameter can be measured directly like a magnetization, but it might as well be out of reach for current experimental technologies.

In this section I closely follow Pekker and Varma (2015) and supplement their derivations with additional details.

8.1.1 Static Ginzburg Landau theory

The order parameter of interest for this chapter is a space and time dependent, complex number

$$\Psi(\boldsymbol{r},t) = |\Psi(\boldsymbol{r},t)|\mathrm{e}^{i\phi(\boldsymbol{r},t)}, \tag{8.1}$$

for which we write the Ginzburg-Landau action density. Its lowest order static terms are

$$\begin{aligned} S_{\text{static}} &= -r\Psi^*\Psi + \frac{U}{2}(\Psi^*\Psi)^2 + \zeta^2(\nabla\Psi^*)(\nabla\Psi) \\ &= S_1 + S_2 + S_3. \end{aligned} \tag{8.2}$$

It is not a priori clear, that such an expansion is possible, since the point of the phase transition is a singular point. The coefficients must behave innocuously, which is an assumption (that turns out to be possible). Because of the gradients in S_3, non-uniform solutions in space are possible, but the uniform solution is the ground state.

The parameter $r = r_0(T - T_c)$ determines, whether the system Eq. (8.2) is in the normal state ($r < 0$), the ordered state ($r > 0$) or at the critical point ($r = 0$). I will not derive this here, since it follows from standard Landau theory (Nolting, 2007).

I start the derivations with the solution of the static action in the long-wavelength limit, i.e. where the gradients are very small and thus can be neglected. In order to find the minimum of the potential energy, we set the derivative

$$\frac{\partial S_{\text{stat}}}{\partial \Psi} = -r\Psi^* + U\Psi^*\Psi\Psi^* \tag{8.3}$$

$$= -r|\Psi|\mathrm{e}^{-i\phi} + U|\Psi|^2|\Psi|\mathrm{e}^{-i\phi} \tag{8.4}$$

$$= 0 \tag{8.5}$$

to zero and obtain the solution[1]

$$\Psi_0(\boldsymbol{r}) = \sqrt{\frac{r}{U}}\mathrm{e}^{-i\phi} \tag{8.6}$$

for nonzero $|\Psi|$. This is the minimum of the famous Mexican hat or wine-bottle potential depicted in Fig. 8.1. One can already see that there are two kinds of low-energy excitations: oscillations of $|\Psi|$ in radial direction, which are the amplitude or Higgs modes, and oscillations in azimuthal direction (corresponds to a variation of ϕ), which are the phase or Goldstone modes. I will derive and discuss their properties in the next section.

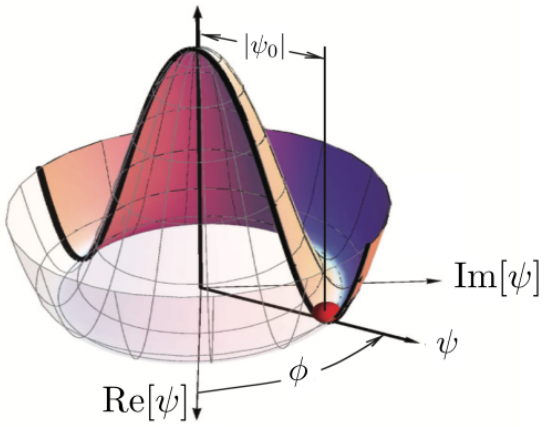

Figure 8.1: *Mexican hat potential of a complex order parameter Ψ in the symmetry broken phase. Taken from Coleman (2015) and adapted to my notation.*

8.1.2 Dynamic Ginzburg Landau theory

To access the low energy excitations, dynamic terms must also be considered. The lowest order terms, which are time-reversal invariant and fulfill a global U(1)-gauge symmetry, are

$$S_{\text{dynamic}} = iK_1\Psi^*\frac{\partial}{\partial t}\Psi - K_2\left(\frac{\partial}{\partial t}\Psi^*\right)\left(\frac{\partial}{\partial t}\Psi\right) \tag{8.7}$$

$$= S_4 + S_5.$$

[1]The derivative with respect to Ψ^* gives the same expression.

To find the minima of $S = S_{\text{static}} + S_{\text{dynamic}}$, we need to solve the equations $\frac{\partial S}{\partial \Psi^*} = 0$ and $\frac{\partial S}{\partial \Psi} = 0$. Then we take the equilibrium solution Ψ_0 and expand to first order in amplitude fluctuations $\delta\Psi$ and phase fluctuations $\delta\phi$, where the calculation is done at $\phi_0 = 0$:

$$\begin{aligned}
\Psi(\boldsymbol{r}, t) &= (\Psi_0 + \delta\Psi)\mathrm{e}^{i(\phi_0+\delta\phi)} && (8.8)\\
&= (\Psi_0 + \delta\Psi)(1 + i\delta\phi) && (8.9)\\
&= \Psi_0 + \delta\Psi + i\delta\phi && (8.10)\\
\Psi^*(\boldsymbol{r}, t) &= \Psi_0 + \delta\Psi - i\delta\phi. && (8.11)
\end{aligned}$$

The Fourier transforms are

$$\begin{aligned}
\Psi(\boldsymbol{r}, t) &= \int \mathrm{d}\omega \int \mathrm{d}\boldsymbol{q}\ \mathrm{e}^{i\boldsymbol{q}\boldsymbol{r}+i\omega t}\Psi(\boldsymbol{q}, \omega) && (8.12)\\
\Psi^*(\boldsymbol{r}, t) &= \int \mathrm{d}\omega \int \mathrm{d}\boldsymbol{q}\ \mathrm{e}^{-i\boldsymbol{q}\boldsymbol{r}-i\omega t}\Psi^*(\boldsymbol{q}, \omega). && (8.13)
\end{aligned}$$

By deriving with respect to Ψ, we find the terms

$$\begin{aligned}
\frac{\partial S_1}{\partial \Psi} &= -r\Psi^*\\
&= -r(\Psi_0 + \delta\Psi - i\delta\phi) && (8.14)\\
\frac{\partial S_2}{\partial \Psi} &= U\Psi^*\Psi\Psi^*\\
&= U(\Psi_0 + \delta\Psi - i\delta\phi)(\Psi_0 + \delta\Psi + i\delta\phi)(\Psi_0 + \delta\Psi - i\delta\phi)\\
&= 3r\delta\Psi - ir\delta\phi && (8.15)\\
\frac{\partial S_3}{\partial \Psi} &= -\zeta^2\nabla^2\Psi^*\\
&= -\zeta^2((-q^2)\Psi_0 + (-q^2)\delta\Psi - (-q^2)i\delta\phi) && (8.16)\\
\frac{\partial S_4}{\partial \Psi} &= -iK_1\frac{\partial}{\partial t}\Psi^*\\
&= -iK_1(-i\omega)(\delta\Psi - i\delta\phi) && (8.17)\\
\frac{\partial S_5}{\partial \Psi} &= K_2\frac{\partial^2}{\partial t^2}\Psi^*\\
&= K_2(-\omega^2)(\delta\Psi - i\delta\phi), && (8.18)
\end{aligned}$$

and with respect to Ψ^* we find

$$\begin{aligned}
\frac{\partial S_1}{\partial \Psi^*} &= -r\Psi \\
&= -r(\Psi_0 + \delta\Psi + i\delta\phi) && (8.19)\\
\frac{\partial S_2}{\partial \Psi^*} &= U\Psi^*\Psi\Psi \\
&= U(\Psi_0 + \delta\Psi - i\delta\phi)(\Psi_0 + \delta\Psi + i\delta\phi)(\Psi_0 + \delta\Psi + i\delta\phi) \\
&= 3r\delta\Psi + ir\delta\phi && (8.20)\\
\frac{\partial S_3}{\partial \Psi^*} &= -\zeta^2\nabla^2\Psi \\
&= -\zeta^2((-q^2)\Psi_0 + (-q^2)\delta\Psi + (-q^2)i\delta\phi) && (8.21)\\
\frac{\partial S_4}{\partial \Psi^*} &= -iK_1\frac{\partial}{\partial t}\Psi \\
&= -iK_1(i\omega)(\delta\Psi + i\delta\phi) && (8.22)\\
\frac{\partial S_5}{\partial \Psi^*} &= K_2\frac{\partial^2}{\partial t^2}\Psi \\
&= K_2(-\omega^2)(\delta\Psi + i\delta\phi). && (8.23)
\end{aligned}$$

Only terms of linear order are kept in the fluctuations $\delta\Psi$ and $\delta\phi$. In Eq. (8.15) the equilibrium solution $\Psi_0 = \sqrt{r/U}$ was inserted, and in Eqs. (8.17) and (8.18) I used that Ψ_0 is time-independent. Writing $\frac{\partial S}{\partial \Psi} + \frac{\partial S}{\partial \Psi^*}$ and $\frac{\partial S}{\partial \Psi} - \frac{\partial S}{\partial \Psi^*}$ gives the equations

$$\Big(2r + \zeta^2 q^2 - K_2\omega^2\Big)\delta\Psi + iK_1\omega\delta\phi = 0 \tag{8.24a}$$

$$-i\omega K_1\delta\Psi + \Big(\zeta^2 q^2 - K_2\omega^2\Big)\delta\phi = 0, \tag{8.24b}$$

which are also given in Pekker and Varma (2015). One can see from Eq. (8.24b), that with all the given terms in the expansion, the amplitude and phase modes are coupled via

$$\delta\Psi = \frac{\zeta^2 q^2 - K_2\omega^2}{i\omega K_1}\delta\phi. \tag{8.25}$$

Inserting this into Eq. (8.24a) gives

$$\Big[\Big(2r + \zeta^2 q^2 - K_2\omega^2\Big)\Big(\zeta^2 q^2 - K_2\omega^2\Big) - (K_1\omega)^2\Big]\delta\phi = 0, \tag{8.26}$$

which is a biquadratic equation and easy to solve:

$$\omega(q) = \sqrt{\frac{K_1^2 + 2K_2(r + q^2\zeta^2) \pm \sqrt{\left(K_1^2 + 2K_2 r\right)^2 + 4K_1^2 K_2 q^2\zeta^2}}{2K_2^2}}. \tag{8.27}$$

In front of the outer root there is actually also a $\pm$, which I omit since it has no physical relevance.

8.1.3 Particle-hole symmetric case ($K_1 = 0$)

One can see from Eq. (8.24), that the equations decouple and amplitude and phase fluctuations become independent. Then the amplitude (Higgs) mode has a dispersion of

$$\omega^2(q) = \frac{2r + \zeta^2 q^2}{K_2}, \tag{8.28}$$

which at zero momentum has a finite dispersion $\omega(q=0)=\sqrt{2r/K_2}$. The phase (Goldstone) mode has a dispersion of

$$\omega^2(q)=\frac{\zeta^2 q^2}{K_2} \tag{8.29}$$

and zero energy at zero momentum. This is consistent with physical intuition, which states that due to the global $U(1)$-symmetry there must exist a gapless excitation along the minimum of the Mexican hat in Fig. 8.1.

8.1.4 Particle-hole asymmetric case ($K_1 \neq 0, K_2 \neq 0$)

In the particle-hole asymmetric case, amplitude and phase modes are coupled. Here I discuss their behavior in the limit of small wavevectors. With $\sqrt{1+x}\approx 1+1/2\,x$ the inner root of the general solution Eq. (8.27) expands to $\sqrt{\left(K_1^2+2K_2r\right)^2+4K_1^2K_2q^2\zeta^2}=K_1^2+2K_2r+\frac{2K_1^2K_2q^2\zeta^2}{\left(K_1^2+2K_2r\right)^2}$, and we receive

$$\omega(q)=\sqrt{\frac{2K_1^2+4K_2r+\left(2K_2+\frac{2K_1^2K_2}{K_1^2+2K_2r}\right)\zeta^2q^2}{2K_2^2}} \tag{8.30}$$

for the Higgs mode. It is always gapped $\left(\omega(q=0)=\frac{\sqrt{2K_2r+K_1^2}}{K_2}\right)$, even at the phase transition ($r=0$).

The Goldstone mode becomes

$$\omega(q)=\frac{1}{K_2}\sqrt{K_2-\frac{K_1^2K_2}{K_1^2+2K_2r}}\zeta^2q^2. \tag{8.31}$$

It is always gapless for all values of the parameters K_1 and K_2.

8.1.5 Summary

Let me here summarize the main properties of the Higgs and Goldstone modes, which we will later identify in the excitonic magnet.

Some examples of the general dispersion Eq. (8.27) are shown in Fig. 8.2. The Goldstone modes are always gapless. At the critical point ($r=0$), the Higgs mode is also gapless, but it opens a gap upon entering the ordered phase, and upon breaking particle-hole symmetry.

For half-filling, Goldstone- and Higgs-modes are decoupled, for out-of-half-filling they are coupled.

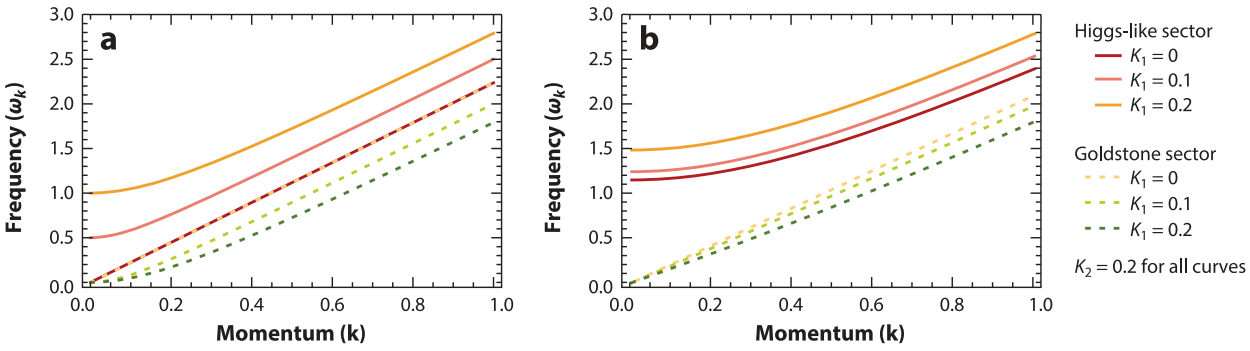

Figure 8.2: *a) The dispersion of Higgs and Goldstone modes at the critical point ($r=0$). b) The dispersion in the ordered phase ($r=0.15$). Taken from Pekker and Varma (2015).*

8.2 Excitonic insulators in a nutshell

An exciton is a bound state of an electron and a hole, which carries energy but no charge. Mott (1961), as well as Halperin and Rice (1968) proposed the excitonic insulator, a Bose-Einstein condensate of excitons. Conclusive experimental evidence for its existence was first given by Kogar et al. (2017) half a century later. The case of spinful excitons is known as excitonic magnet (Khaliullin, 2013) and proposed in the material $Pr_{0.5}Ca_{0.5}CoO_3$ (Kuneš and Augustinský, 2014; Tsubouchi et al., 2002; Yamaguchi et al., 2017).

The minimal model to describe the excitonic condensation is a two-orbital model with interaction between the orbitals (inter-band hybridization, hopping or correlated hopping). Characteristic for such a condensate is the spontaneous coherence between valence and conduction electrons, represented by orbital offdiagonal elements of the one-particle density matrix

$$\boldsymbol{\phi}_i = \sum_{\alpha\alpha'} \boldsymbol{\sigma}_{\alpha\alpha'} \left\langle a^\dagger_{i\alpha} b_{i\alpha'} \right\rangle \tag{8.32}$$

as order parameter. $\boldsymbol{\sigma}$ is the vector of Pauli matrices, a and b fermionic operators for the two orbitals, and i the site index of the lattice. The emergence of this nonzero order parameter generates offdiagonal elements in the self energy, which open a gap in the spectral function $A(\omega)$, making the system an insulator.

8.3 The model and observables

Here we calculate dynamical susceptibilities in the normal and ordered phase of an excitonic magnet. We identify Higgs and Goldstone modes via the properties that I derived in Sec. 8.1. Further we observe, that the spin susceptibility shows a qualitative change at the phase boundary, which gives experiment a direct observable to probe the excitonic condensate.

The Hamiltonian of our model reads

$$\begin{aligned} H = &\sum_{ij,\sigma} \begin{pmatrix} a^\dagger_{i\sigma} & b^\dagger_{i\sigma} \end{pmatrix} \begin{pmatrix} t_{aa} & t_{ab} \\ t_{ab} & t_{bb} \end{pmatrix} \begin{pmatrix} a_{j\sigma} \\ b_{j\sigma} \end{pmatrix} + \frac{\Delta}{2} \sum_{i,\sigma} (n^a_{i\sigma} - n^b_{i\sigma}) \\ &+ U \sum_{i,\alpha} n^\alpha_{i\uparrow} n^\alpha_{i\downarrow} + \sum_{i,\sigma\sigma'} (U' - J\delta_{\sigma\sigma'}) n^a_{i\sigma} n^b_{i\sigma'}, \end{aligned} \tag{8.33}$$

where $a^\dagger_{i\sigma}$ and $b^\dagger_{i\sigma}$ are fermionic operators that create electrons with the respective orbital flavors and spin σ at site i of a square lattice. The first term describes the nearest neighbor hopping. The rest, expressed in terms of local densities $n^c_{i,\sigma} \equiv c^\dagger_{i\sigma} c_{i\sigma}$, captures the crystal-field Δ, the Hubbard interaction U and Hund's exchange J in the Ising approximation. Parameters $U = 4$, $J = 1$, $U' = U - 2J$, $t_{aa} = 0.4118$, $t_{bb} = -0.1882$, t_{ab} =0, 0.02, 0.06 with magnitudes (in eV) typical for $3d$ transition metal oxides were used in previous studies (Kuneš, 2014; Kuneš and Augustinský, 2014; Kuneš and Geffroy, 2016). The results are little sensitive to variation of U' and J as long as the ratio Δ/J is fixed.

The model is solved within the DMFT approximation, from which the lattice Green's function $G_{\mathrm{latt}}(\boldsymbol{k}, i\omega_n)$ and generalized two-particle susceptibility of the AIM are calculated. The real-frequency susceptibilities $\chi^{OO}_{\eta\eta}(\mathbf{k}, \omega)$ are obtained by solving the Bethe-equation in the particle-

hole channel and analytic continuation (Gubernatis et al., 1991; Kunes, 2019) of the Matsubara representations

$$\chi^{OO}_{\eta\eta}(\mathbf{k}, i\nu_n) = \sum_{\mathbf{R}} \int_0^\beta \mathrm{d}\tau \, e^{i(\nu_n\tau + \mathbf{k}\cdot\mathbf{R})} \langle O^\eta_{\mathbf{i}+\mathbf{R}}(\tau) O^\eta_{\mathbf{i}}(0)\rangle - \langle O^\eta\rangle^2,$$

with the observables O of interest being the two excitonic fields and the z-component of spin moment:

$$R^\eta_i = \sum_{\alpha\beta} \sigma^\eta_{\alpha\beta} (a^\dagger_{i\alpha} b_{i\beta} + b^\dagger_{i\alpha} a_{i\beta}) \tag{8.34}$$

$$I^\eta_i = i \sum_{\alpha\beta} \sigma^\eta_{\alpha\beta} (a^\dagger_{i\alpha} b_{i\beta} - b^\dagger_{i\alpha} a_{i\beta}) \tag{8.35}$$

$$S^z_i = \sum_{\alpha\beta} \sigma^z_{\alpha\beta} (a^\dagger_{i\alpha} a_{i\beta} + b^\dagger_{i\alpha} b_{i\beta}). \tag{8.36}$$

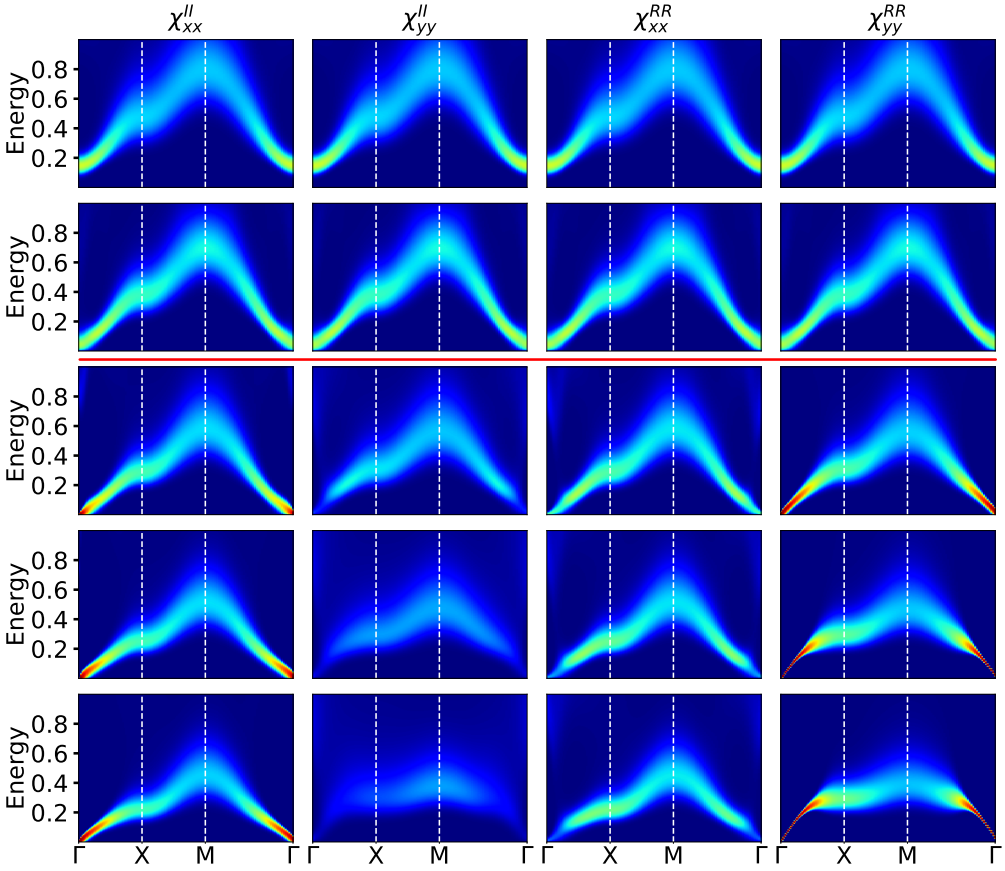

Figure 8.3: *Evolution of the excitonic modes of dynamical susceptibility in the $U^2(1)$ model (t_{ab}=0) across Δ-driven transition ($T = 1/40$). The columns correspond to $-\operatorname{Im}\chi^{OO}_{\gamma\gamma}(\mathbf{k},\omega)$ with $O^\gamma = I^x, I^y, R^x, R^y$ (left to right) along the high-symmetry lines in the 2D Brillouin zone. The rows from top to bottom correspond to Δ =3.9, 3.8, 3.65, 3.55, 3.45 with $\Delta_c \approx 3.75$ (Red line separates the normal state from the PEC phase).*

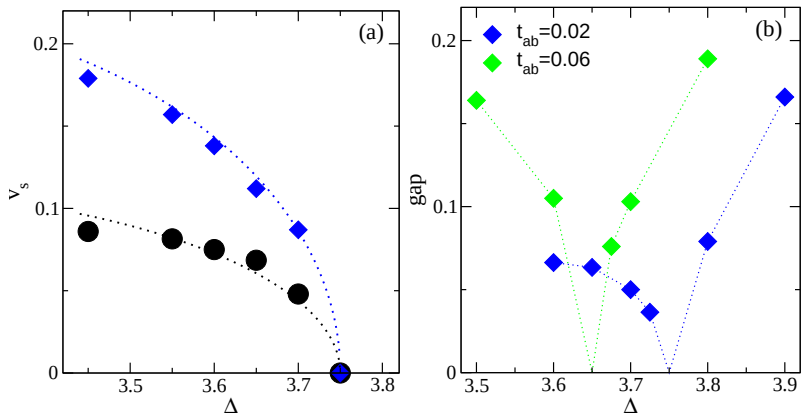

Figure 8.4: *(a) The sound velocity v_s of the GMs, the phase mode (χ^{RR}_{yy}, blue symbols) and the spin rotation mode (χ^{II}_{xx}, black symbols) in the $U^2(1)$ model as a function of the crystal field Δ. The dotted lines show the corresponding strong-coupling results. (b) The Higgs gap in the $U(1)$ model with t_{ab} =0.02 and 0.06 as a function of Δ. The line is a guide for eyes.*

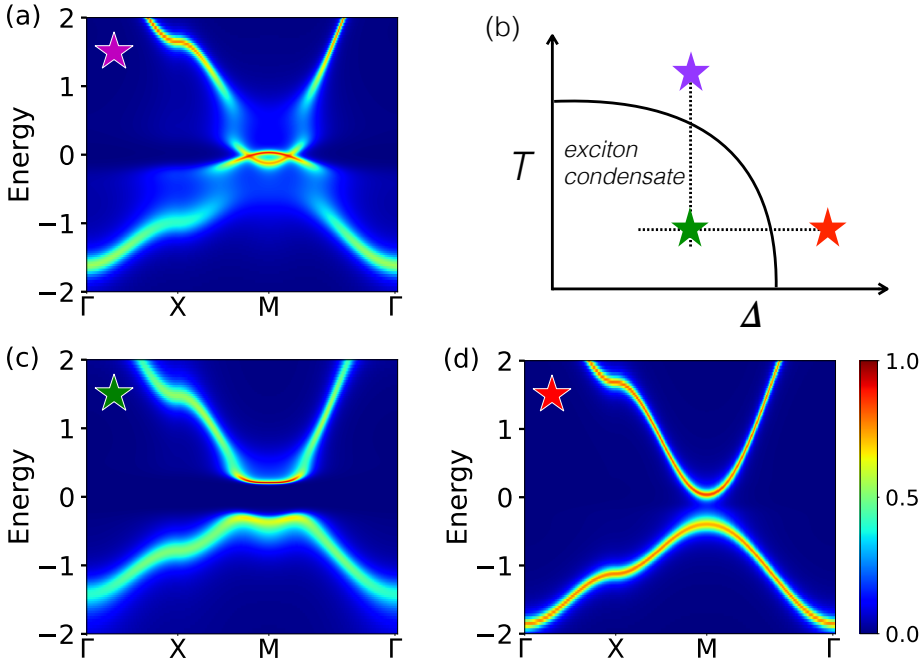

Figure 8.5: *Sketch of the crystal field vs temperature ($\Delta - T$) phase diagram (b) with marked cuts, along which the susceptibilities are calculated. The 1P spectral function at the (Δ, T)-points violet (3.55, 1/11), green (3.55, 1/40) and blue (3.8, 1/40).*

8.4 Results and Discussion

Model Eq. (8.33) at half-filling has a rich phase diagram exhibiting a metal-insulator transition (Werner and Millis, 2007) as well as various types of LRO including antiferromagnetism, spin-state order or superconductivity (Hoshino and Werner, 2016; Kaneko and Ohta, 2014; Kaneko et al., 2015; Kuneš and Augustinský, 2014). For the present parameters it undergoes a temperature- or crystal-field-controlled transition to polar exciton condensate (PEC) (Kuneš, 2015), as shown in Fig. 8.5b. PEC is characterized by a finite excitonic field. Throughout the paper we choose the orientation $\langle I^y \rangle = \phi$, while R^y, I^x and R^x remain fluctuating. This phase is an instance of spin nematic state, which breaks spin-rotation symmetry without appearance of spin polarization.

The behavior of the collective modes depends on the continuous symmetry broken by the LRO (Watanabe and Murayama, 2012). Here, it is the $U(1)$ spin (z-axis) rotation. If $t_{ab} = 0$, an additional $U(1)$ gauge symmetry due to conservation of $\sum_{i,\sigma}(n^a_{i,\sigma} - n^b_{i,\sigma})$ makes the total broken symmetry $U(1) \times U(1)$. We will refer to the general $t_{ab} \neq 0$ case as $U(1)$ model and the $t_{ab} = 0$ case as $U^2(1)$ model.

8.4.1 Crystal field driven transition.

While the system exhibits a sizable 1P gap throughout the studied Δ-range, horizontal line in Fig. 8.5b, low-energy 2P-excitations show up in the excitonic susceptibilities, Fig. 8.3. In the normal phase ($\Delta > \Delta_c$), these can be viewed as spinful Frenkel excitons. The spin symmetry ensures the equivalence of x and y directions, while the gauge symmetry leads to equivalence of the excitonic fields R and I in the $U^2(1)$ model.

Reducing Δ closes the excitation gap and the system undergoes transition to the PEC phase. For the exctionic field, which freezes in an arbitrary direction both in the xy-plane and the RI-plane in the $U^2(1)$ case, we choose the orientation discussed above. Linear gapless GMs (Kunes, 2019) corresponding to the spin rotation and phase fluctuation (RI-rotation) are observed in χ^{II}_{xx} and χ^{RR}_{yy}, respectively. The intensities of both GMs diverge as $1/|\mathbf{k}|$ (Kunes, 2019). The corresponding sound velocities are shown in Fig. 8.4a.

Finite cross-hopping t_{ab} leads to a generic $U(1)$ model. The equivalence between the R and I fields is lost, see Fig. 8.6. The excitonic field freezes in the I-direction (Geffroy et al., 2018; Kuneš, 2015), while the xy-orientation remains arbitrary. For the small t_{ab} studied here, the changes to the excitonic spectra (Kunes, 2019) are concentrated in the low-energy region shown in Fig. 8.6. The spin-rotation GM, visible in χ^{II}_{xx}, remains gapless and linear. The 'phase' mode acquires a Higgs gap that vanishes at the transition, Fig. 8.4b, a behavior observed in bi-layer Heisenberg system $TlCuCl_3$ (Merchant et al., 2014).

Interestingly the character of this mode changes as we proceed deeper into the ordered phase, Fig. 8.6. Close to the phase boundary, its spectral weight is dominated by χ^{II}_{yy}, i.e., amplitude fluctuation of the condensed I^y field. Deeper in the ordered phase the spectral weight is mostly in χ^{RR}_{yy}, corresponding to phase fluctuation (RI-rotation) as in the $U^2(1)$ model. We offer an interpretation in terms of the relative strength of the symmetry breaking term (t_{ab}) in the Hamiltonian and the spontaneously generated Weiss field. The Weiss field, the off-diagonal $F^{\uparrow\downarrow}_{ab}(\omega)$ part of the hybridization function in the present method, is in general a fluctuating (frequency dependent) object, which prohibits a direct comparison to

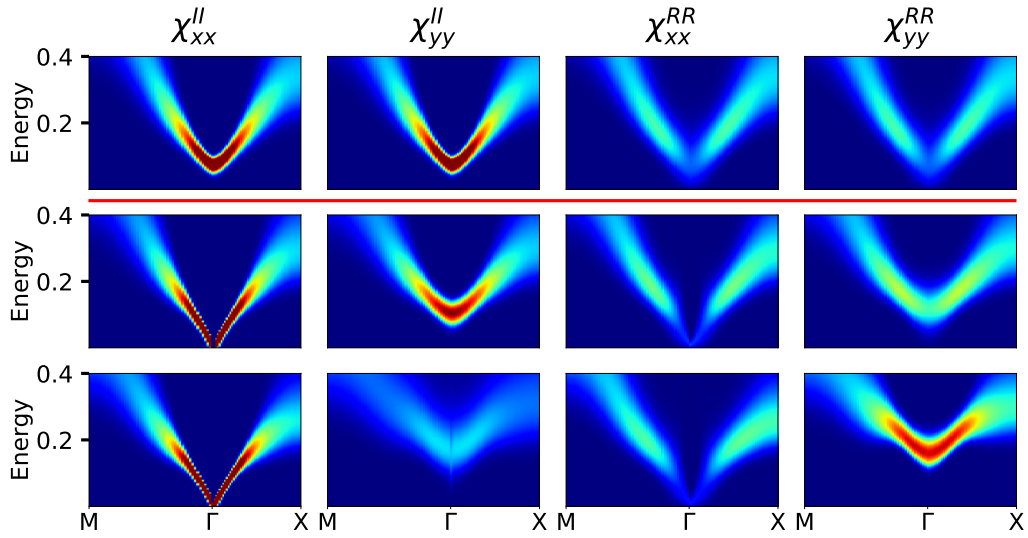

Figure 8.6: *The same susceptibilities as in Fig. 8.3 ($T = 1/40$) in the vicinity of* Γ*-point for $U(1)$ model with cross-hopping $t_{ab} = 0.06$. The rows from top to bottom correspond to Δ =3.675, 3.60, 3.5, with $\Delta_c \approx 3.65$ (Red line separates the normal state from the PEC phase) .*

t_{ab}. Nevertheless, we can compare their dynamical effects. A Weiss field dominating over the Hamiltonian term (t_{ab}) results in a gapped GM found deep in the ordered phase. A common example of such situation is a gap in spin-wave spectra of magnets due to magneto-crystalline anisotropy. Dominance of the Hamiltonian term (t_{ab}) close to the phase boundary, where the Weiss field is small, results in amplitude fluctuations. This is a generic situation in cases without an approximate symmetry. This interpretation is supported by the observation that the extent of the amplitude-fluctuation regime shrinks when t_{ab} is reduced (Kunes, 2019). Moreover, the strong-coupling calculations (see supplementary material of Kunes (2019)), which make an explicit comparison possible, lead to the same conclusions.

Next, we discuss the impact of exciton condensation on the spin susceptibility χ^{SS}_{zz}, shown in Fig. 8.7. In the normal phase, $\chi^{SS}_{zz}(\mathbf{k}, \omega)$ exhibits no distinct dispersion and essentially vanishes throughout the Brillouin zone, Fig. 8.7b, as expected in a band insulator. In the PEC phase, it develops a sharp spin-wave-like dispersion although there are no ordered moments present. We point out a similarity of $\chi^{SS}_{zz}(\mathbf{k}, \omega)$ to $\chi^{RR}_{xx}(\mathbf{k}, \omega)$ that we discuss later. A distinct feature of $\chi^{SS}_{zz}(\mathbf{k}, \omega)$ is the suppression of the spectral weight close to the Γ-point. This suppression can be overcome by doping, which results in appearance of ferromagnetic exciton condensate (Kuneš, 2014).

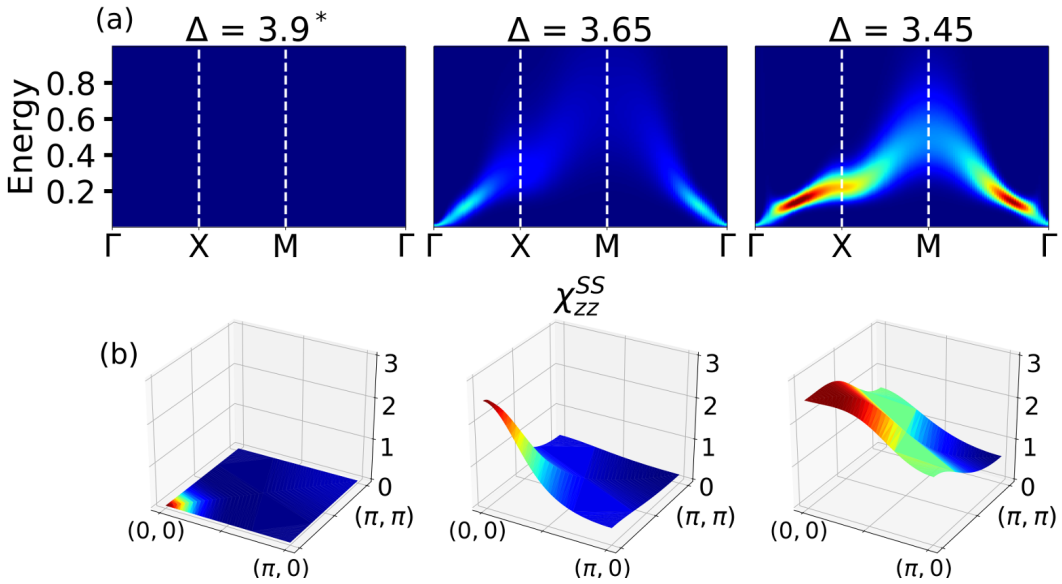

Figure 8.7: *(a) Evolution of dynamical spin susceptibility* $-\operatorname{Im}\chi^{SS}_{zz}(\mathbf{k},\omega)$ *across the* Δ*-driven transition in the* $U^2(1)$ *model of Fig. 8.3 (Asterisk marks the normal phase). (b) The corresponding static susceptibilities* $\operatorname{Re}\chi^{SS}_{zz}(\mathbf{k},0)$ *throughout the Brillouin zone.*

Table 8.1: *The parameters of Eq. 8.38. The variational parameter* $0 \leq \alpha^2 \leq 1$*, corresponding to the LS density, assumes 1 in the normal phase and* $\frac{\mu+z(\mathcal{T}+\mathcal{W})+z\mathcal{V}}{2z(\mathcal{T}+\mathcal{W})+z\mathcal{V}}$ *in the condensate.*

μ_x	$\alpha^2\mu + z\alpha^2(1-\alpha^2)(2\mathcal{T}+2\mathcal{W}+\mathcal{V})$
$\mathcal{T}_x$	$\alpha^2\mathcal{T} - (1-\alpha^2)\mathcal{J}$
$\mathcal{W}_x$	$\alpha^2\mathcal{W} + (1-\alpha^2)\mathcal{J}$
μ_y	$z(\mathcal{T}+\mathcal{W})$; μ if $\alpha^2 = 1$
$\mathcal{T}_y$	$\mathcal{T} - \alpha^2(1-\alpha^2)(2\mathcal{T}+2\mathcal{W}+\mathcal{V})$
$\mathcal{W}_y$	$\mathcal{W} - \alpha^2(1-\alpha^2)(2\mathcal{T}-2\mathcal{W}+\mathcal{V})$

8.4.2 Strong-coupling limit

To understand the numerical results, it is instructive to analyze the strong-coupling limit of (8.33), which can be expressed in terms of two-flavor hard-core bosons (Balents, 2000; Kuneš, 2015; Nasu et al., 2016)

$$\begin{aligned}\mathcal{H} =&\mu \sum_i n_i - \sum_{ij,\nu} \Big[\mathcal{T} d^\dagger_{i\nu} d_{j\nu} - \frac{\mathcal{W}}{2}(d^\dagger_{i\nu} d^\dagger_{j\nu} + d_{i\nu} d_{j\nu})\Big] \\ &+\frac{\mathcal{V}}{2}\sum_{ij} n_i n_j + \frac{\mathcal{J}}{2}\sum_{ij} S^z_i S^z_j,\end{aligned} \tag{8.37}$$

Bosonic operators $d^\dagger_{i\nu}$ ($\nu = x, y$), which create high-spin (HS) states out of the low-spin (LS) state, are related to the excitonic fields by $R^\nu_i(I^\nu_i) \to \sqrt{\pm 1}(d^\dagger_{i\nu} \pm d_{i\nu})$. The number operators $n_i = \sum_\nu d^\dagger_{i\nu} d_{i\nu}$ measure the HS concentration and $S^z_i = -i(d^\dagger_{ix} d_{iy} - d^\dagger_{iy} d_{ix})$ is the z-component of the spin operator. The relations of the coupling constants μ, $\mathcal{T}$, $\mathcal{W}$, $\mathcal{V}$, and $\mathcal{J}$ to the parameters of (8.33) can be found in SM (Kunes, 2019) and Ref. (Kuneš and Augustinský, 2014). Since $\mathcal{W} \sim t^2_{ab}$, the gauge symmetry of the $U^2(1)$ model reflects conservation of d-charge for $\mathcal{W} = 0$.

Generalized spin wave treatment (Nasu et al., 2016; Sommer et al., 2001) of the excitations over the variational ground state $|G\rangle = \prod_i (\alpha + i\sqrt{1-\alpha^2} d^\dagger_{iy})|0\rangle$, see SM (Kunes, 2019) for details, leads to a free boson model

$$\tilde{\mathcal{H}}_\nu = \mu_\nu \sum_i \tilde{n}_{i\nu} - \sum_{ij} \Big[\mathcal{T}_\nu \tilde{d}^\dagger_{i\nu} \tilde{d}_{j\nu} - \frac{\mathcal{W}_\nu}{2}(\tilde{d}^\dagger_{i\nu} \tilde{d}^\dagger_{j\nu} + H.c.)\Big]. \tag{8.38}$$

Note that the parameters of this effective model in the ordered phase, given in Table 8.1, depend on the flavor $\nu = x, y$. The elementary excitations of (8.38) have the dispersion $\epsilon_\nu(\mathbf{k}) = \sqrt{(\mu_\nu - 2\mathcal{T}_\nu \delta(\mathbf{k}))^2 - (2\mathcal{W}_\nu \delta(\mathbf{k}))^2}$ with $\delta(\mathbf{k}) = \cos k_x + \cos k_y$. In the $U^2(1)$ case with $\mathcal{W} = 0$ both x and y modes are gapless with sound velocities $v_\nu \equiv \nabla_{\mathbf{k}} \epsilon_\nu(\mathbf{k} = 0) = \sqrt{8|\mathcal{W}_\nu|(\mathcal{T}_\nu + |\mathcal{W}_\nu|)}$ vanishing at the transition. Finite $\mathcal{W}$ in the $U(1)$ case leads to opening of a gap for y-excitations. The ratio of the spectral weights of $I-$ and $R-$ propagators corresponding to χ^{II}_{yy} and χ^{RR}_{yy} at Γ point is given by (Kunes, 2019)

$$\frac{\operatorname{Im} \chi^{II}_{yy}(0, \nu_{\text{gap}})}{\operatorname{Im} \chi^{RR}_{yy}(0, \nu_{\text{gap}})} \approx \frac{4\mathcal{W}}{(2\mathcal{T} + \mathcal{V})\phi^2},$$

which supports the interpretation that a dominant Hamiltonian term ($\mathcal{W}$) favors the amplitude fluctuations, while a dominant Weiss field ($\sim \mathcal{T}\phi$) favors the gapped Goldstone fluctuations.

Finally, we address the behavior of the spin susceptibility χ^{SS}_{zz} in Fig. 8.7 We observe that replacing the operator d_{iy} in the strong-coupling expression for S^z_i by its finite PEC value yields $S^z_i \sim (d^\dagger_{ix} + d_{ix})\phi/2$. In the ordered phase, the spin susceptibility χ^{SS}_{zz} therefore follows χ^{RR}_{xx}, while they are decoupled in the normal phase.

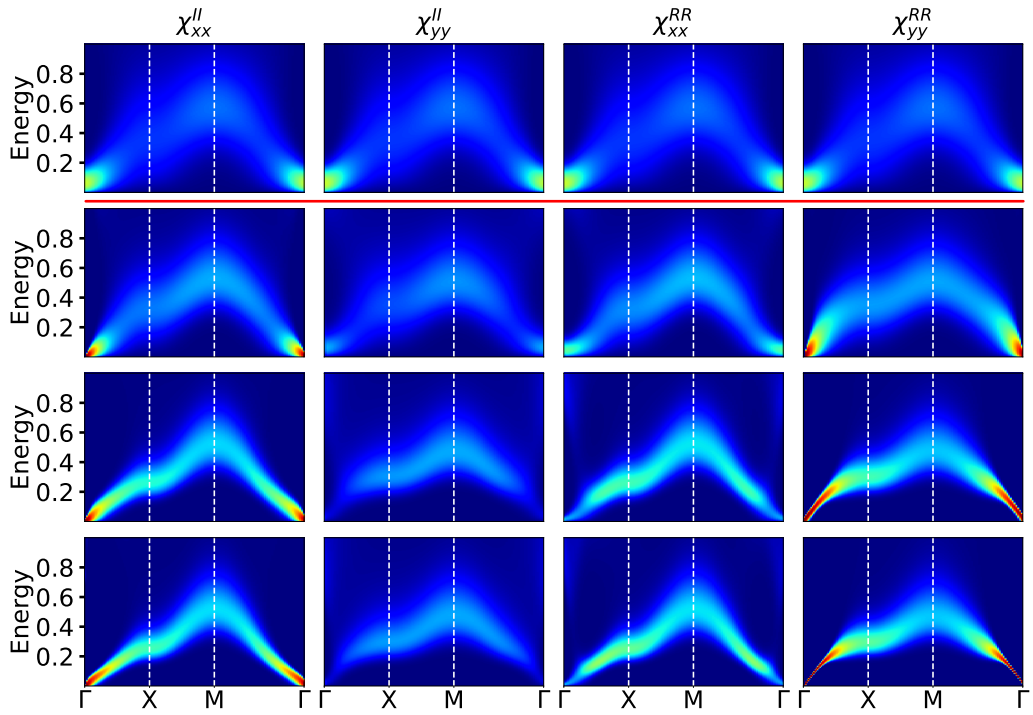

Figure 8.8: *The same susceptibilities of $U^2(1)$ model as in Fig. 8.3 calculated across the thermally driven transition for Δ =3.55. The rows from top to bottom correspond to temperatures $T = 1/11$, $1/16$, $1/30$, $1/40$ with $T_c \approx 1/13$.*

8.4.3 Thermally driven transition

Since the transition observed in $Pr_{0.5}Ca_{0.5}CoO_3$ (Tsubouchi et al., 2002) is driven by temperature we investigate the behavior of the $U^2(1)$ model along the vertical trajectory in Fig. 8.5b. We observe that the 1P gap in the normal state is closed, Fig. 8.5d. The excitonic susceptibilities possess a peak at finite frequency, whose tail extends to zero frequency, Fig. 8.8 Cooling is accompanied by a downward shift of the damped dispersive features, i.e., the phase transition can be viewed as a mode softening, an observation also made experimentally on $TlCuCl_3$ (Merchant et al., 2014).

The normal state spin susceptibility χ^{SS}_{zz} in Fig. 8.9 does not vanish as in Fig. 8.7. The presence of thermally excited HS states gives rise to **k**-featureless susceptibility with spectral weight concentrated at low energies. Nevertheless, $\chi^{SS}_{zz}(\mathbf{k}, \omega)$ changes qualitatively at the transition in this case as well. The dispersion becomes sharper and its bandwidth increases significantly. As a result, upon cooling below T_c, the low-energy region is depleted of spectral weight throughout the Brillouin zone, except in the vicinity of the Γ-point. Recently, this behavior was reported in inelastic neutron scattering in the putative excitonic material $(Pr_{1-y}Y_y)_{1-x}Ca_xCoO_3$ (Moyoshi et al., 2018).

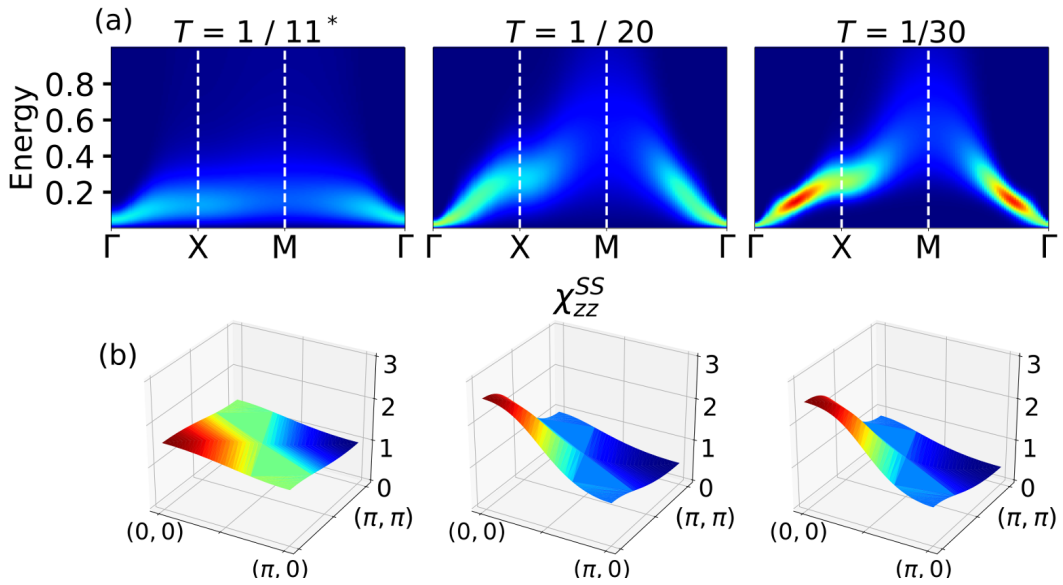

Figure 8.9: *(a) Evolution of dynamical spin susceptibility* $-\operatorname{Im}\chi^{SS}_{zz}(\mathbf{k},\omega)$ *across the thermally driven phase transition as in Fig. 8.8 for temperatures* $T = 1/11,\ 1/20,\ 1/30$ *(Asterisk marks the normal phase). (b) The corresponding static susceptibilities* $\operatorname{Re}\chi^{SS}_{zz}(\mathbf{k},0)$ *throughout the Brillouin zone.*

8.4.4 Summary

In conclusion, we used DMFT to study the 2P response across exciton condensation transition in two-orbital Hubbard model. We observed the formation of GMs as predicted by symmetry considerations (Watanabe and Murayama, 2012). Explicit breaking of continuous symmetry led to appearance of a gapped mode (Pekker and Varma, 2015), characterized by vanishing of the gap at the phase transitions similar to observations in $TlCuCl_3$ (Merchant et al., 2014). We have observed that the character of this mode changes from Higgs-like amplitude fluctuations close to the phase boundary, to Goldstone-like phase fluctuations deep in the ordered phase. We suggest that this behavior shall be common to systems with weakly broken symmetry and provide an interpretation in terms of the relative strengths of the spontaneously generated Weiss field and the explicit symmetry-breaking term in the Hamiltonian.

Experimental observation of excitonic modes is in principle possible (Kim et al., 2014; Wang et al., 2018) using resonant inelastic x-ray scattering, however, practical limitations in energy resolution and **k**-space accessibility (Wang et al., 2018) exist at the moment. We have shown that the measurement of dynamical spin susceptibility provides an alternative, that can used to identify spinful excitonic condensates with current experimental technology (Bryan, 1990; Jarrell and Gubernatis, 1996; Kraberger et al., 2017; Luttinger, 1961; Otsuki et al., 2017; Sandvik, 1998).

Chapter 9

Band structure-induced correlations in iron and nickel at ambient and Earth's core conditions

This chapter is based on the original work already published in Nature Communications (Hausoel et al., 2017). All figures and captions are taken from there (if not otherwise cited), as well as some text (which is marked with a sidebar on the left).

9.1 Introduction

The ferromagnetism of the elements iron and nickel is one of the most ancient phenomena known to mankind and the natural sciences. Iron and nickel have vast areas of technical appliance, in pure form, as well as in combination with other elements. They are also present in the Earth's core and responsible for the magnetic field of our planet, which deflects cosmic particles and rays, which can damage the cells of living beings severely. Without or a significantly weaker field, life would definitely look different compared to as we know it. Animals needed much thicker skin to screen the radiation that comes from the sky, and also electronic devices needed special shielding from cosmic particles to work properly.

However while it is widely accepted that a geodynamo is at work in the outer core of the Earth, a consistent theory of it does not exist yet. Especially there is a lively debate about the detailed mechanisms how it is created and sustained. In 2012 Pozzo et al. found, that under the assumption of the Earth's core consisting of iron only, there is not enough convection to sustain the geodynamo (Olson, 2013; Pozzo et al., 2012). A search for the missing ingredients began. The physical conditions at the core are out of reach for most experiments, therefore computer simulations of the material's properties at the core and comparing the results to geological experiments like shock-waves or particle absorption measurements are a way to go.

In this project I describe the effect of band structure-induced correlations in pure nickel and iron-nickel alloy, as well as possible implications for geodynamo theory. The properties of sharp features in the density of states (so called van-Hove singularities) are very well known. It has been predicted with models (Vonsovskii et al. (1993), among others), that under special conditions they can shape the properties of a system and make it strongly correlated. However here for the first time, I present materials existing in nature, where this mechanism is actually at work. Simultaneously I also resolve the old riddle of determining the strength of correlations in iron and nickel and which way they come about.

The chapter is structured as follows: First I briefly review standard geodynamo theory and explain its main problem. Then I discuss some of the known magnetic properties of iron and nickel at the one-particle level, before I show a careful comparison of the two at the two particle level. There I uncover their different microscopic mechanisms, which lead to correlation effects of similar strength. Finally I discuss how this mechanism can survive Earth's core conditions and may give a significant contribution to the thermal resistivity of the outer core.

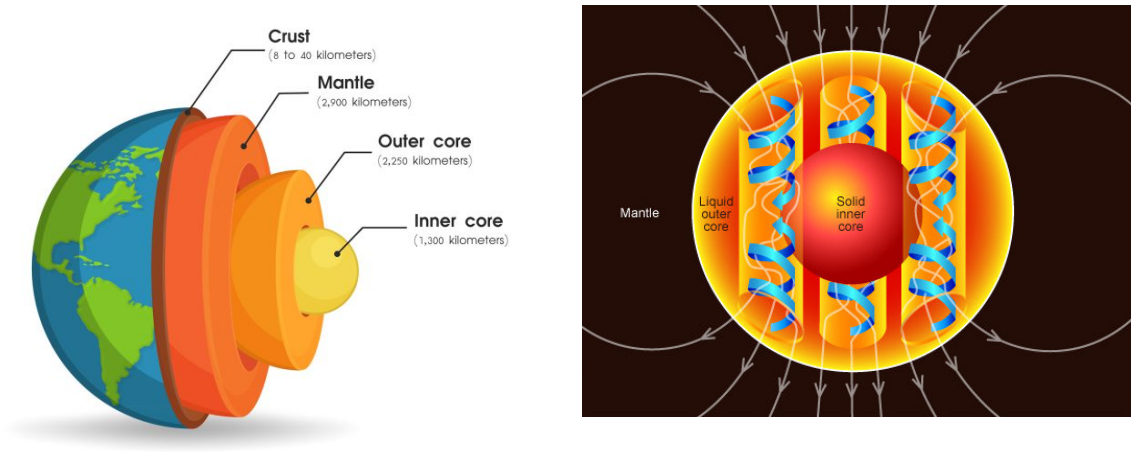

Figure 9.1: *The structure of the Earth (left) and a cartoon of the geodynamo (right): the inner core is solid an has a temperature of 5,000-7,000K the outer core is liquid and has 4,000-5,000K, and the mantle which consists of rock, but is still so hot that it flows like road tar. Taken from Geggel (1998) and Christensen (2019).*

9.2 Geodynamo theory

I start with a brief review of geodynamo theory here and make the connection to the topic of this thesis, strongly correlated materials.

The Earth's interior consists of the Earth's inner core, which is believed to be solid and made of about 80% iron and 10-20% nickel (National Geographic, 1998). One layer above is the outer core, which contains mostly liquid iron and also some nickel, but less compared to the inner core. The Earth's mantle consists mainly of silicate rocks and also some iron. But it is only partially molten and considering the relevant time-scale, it can be considered as solid and does not play a role for the geodynamo.

The Earth's magnetic field cannot come from the known mechanism of ferromagnetism, since the temperatures are way too high (4,000 to 5,000K in the outer, 5,000 to 7,000K in the inner core). At ambient conditions the ordering temperature of iron is $1,043$K (Wohlfarth, 1986), and hydrostatic pressure can only reduce this number, since it widens the density of states and thus reduces correlation effects.

Instead, the field is believed to be generated by the geodynamo the following way. The inner core produces heat by various processes: radioactive elements decay, material condensates at the surface of the inner core, and by friction from dense material sinking downwards. This energy has to get outwards, which can happen by convection (i.e. material is carried with the transport of heat) and by conduction (heat is transferred without transport of material). The convecting

material is forced into rotating columns by the Coriolis force, which then generates the field, see Fig. 9.1.

Bcc-iron is strongly correlated at standard conditions for temperature and pressure, and would have enough thermal resistivity to sustain the geodynamo, but under pressure it makes a structural phase transition to hcp-iron (Leonov et al., 2011). In 2012 Pozzo et al. calculated the thermal conductivity of hcp-iron with DFT + molecular dynamics at Earth's core conditions. They found that it is a factor of 2-3 too high in order to create sufficient convection for a geodynamo of sufficient strength for the magnetic field we observe on the surface of the Earth. Thus the thermal conductivity must be low enough, that the heat transport carries enough material in order to sustain the geodynamo. Back then a vivid search for the missing compounds and mechanisms was started. In 2017 Belonoshko et al. noted, that a diffusion mechanism may stabilize bcc-iron in the inner core.

In this project we show, that the effect of band structure-induced correlations in nickel and hcp-iron-nickel alloy delivers an important contribution to the thermal resistivity of the outer core, since it significantly increases electron-electron scattering processes and thus increases thermal resistivity.

9.3 Ferromagnetism and correlations in iron and nickel

Let's first take a look at the applicability of the DFT+DMFT method reproducing and discussing known magnetic transition temperatures and spectra of iron and nickel.

Surprisingly, we still lack a complete theoretical comprehension of these two textbook materials. The reason can be ascribed to the intrinsic quantum many-body nature of their electronic structure, which makes a standard treatment in terms of independent electrons and conventional band theory inapplicable. The calculated Coulomb interaction is large and comparable in size in iron and nickel, which instead differ in the number of $3d$ electrons filling the bands close to the Fermi level. Iron is not too far from half-filling, where the Coulomb interaction has the strongest effect and can easily drive a system Mott insulating. On the contrary, nickel has an almost full shell. A situation in which Landau-theory of Fermi-liquids is in general recovered, even if the Coulomb interaction is significant. Yet, nickel was originally considered the more correlated of the two, because of photoemission satellites far away from the Fermi level, believed to originate from spectral weight transfer due to the Coulomb interaction (Hüfner and Wertheim, 1975; Tanaka et al., 1992). A theoretical study by one of us (Lichtenstein et al., 2001) put the two materials on a similar level, stressing the existence in both of them of well-formed local moments, despite their marked itinerant character.

9.3.1 Ferromagnetic transition temperatures

The Curie temperature (T_C) of iron and nickel has been the object of several studies, in particular using the merger of density functional theory and dynamical mean-field theory (DFT+DMFT) (Georges et al., 1996; Held, 2007; Kotliar et al., 2006). This theoretical approach gives reliable results for three-dimensional materials with large coordination number, and is able to access the magnetic as well as the non-ordered phase above T_C. The latter is described by DFT+DMFT as non-vanishing local magnetic moments with strong quantum fluctuations, which is crucial for the physics of correlated itinerant magnets (Drchal et al., 2013; Kudrnovskỳ et al., 2012; Liechtenstein et al., 1987; Ruban et al., 2007).

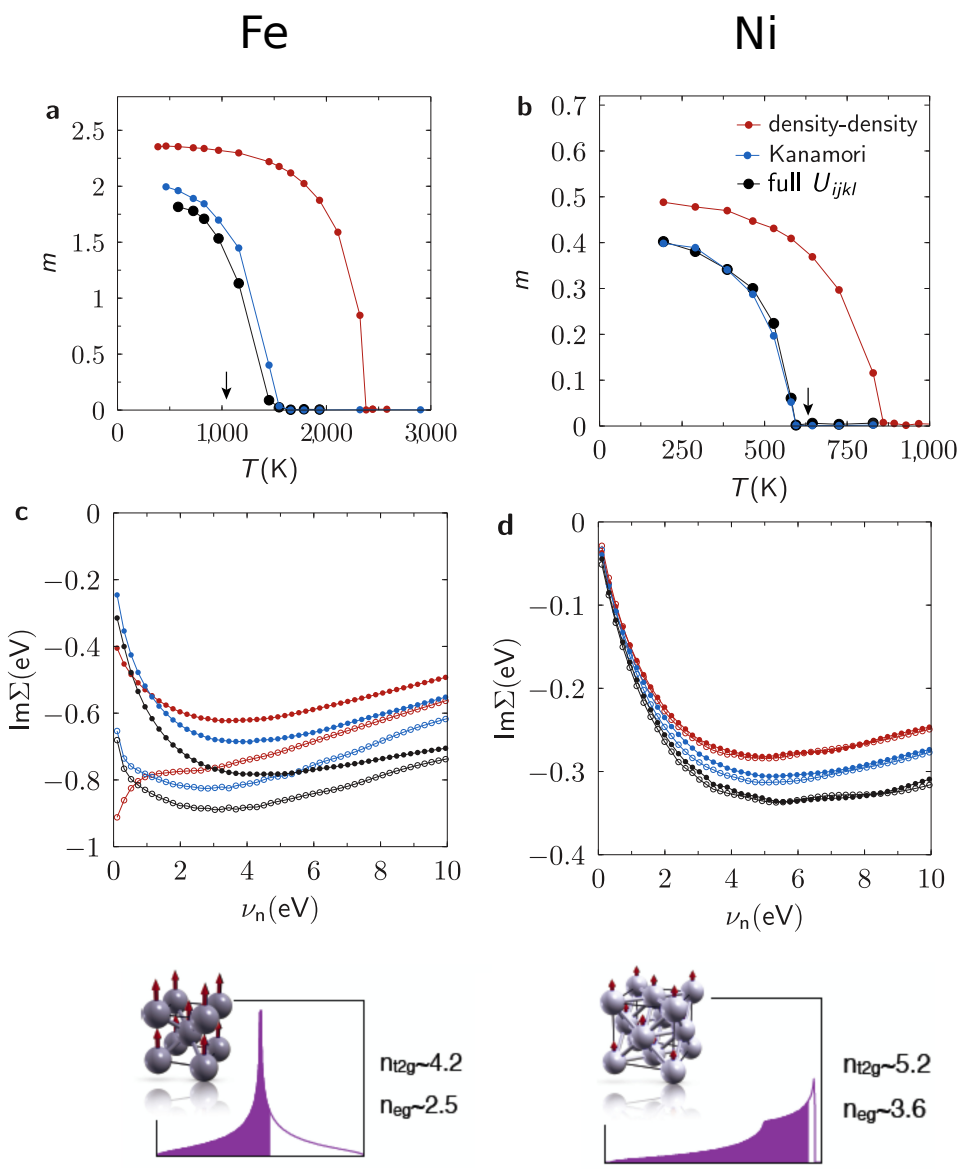

Figure 9.2: Curie temperatures and self energies of iron and nickel. *Ferromagnetic order parameter* $m = N_\uparrow - N_\downarrow$ *in bcc-iron* (**a**) *and in fcc-nickel* (**b**) *as a function of temperature, whereas* $N_\uparrow$ *(*$N_\downarrow$*) are the total number of spin-up (-down) electrons in the correlated d-orbitals. The Curie temperature* T_C *is signaled by the magnetization dropping to zero. For nickel we obtain* $T_C = 600\,\mathrm{K}$*, very close to the experimental value of* $633\,\mathrm{K}$ *(Wohlfarth, 1986), indicated by the black arrow in* **b**. *Our estimated* T_C *for iron is around* $1,500K$*, i.e. roughly 30% larger than the experimental one of* $1,043K$ *(Wohlfarth, 1986), marked by the black arrow in* **a** *(for a discussion, see Methods, where also a description of the three parametrization used for the Coulomb interaction is given). Imaginary part of the Matsubara self-energies of iron* (**c**) *and nickel* (**d**)*. The curves with filled circles show one of the degenerate* t_{2g} *orbitals, with empty circles one of the degenerate* e_g *orbitals. The lifetime of the quasiparticles is inversely proportional to* $Im\Sigma(i\nu_n \to 0)$*. Contrary to nickel, the scattering rate in iron at ambient pressure is large, even though the insulating-like shape of the density-density* e_g*-self-energy is replaced by an upturn at small frequencies in Kanamori and full Coulomb.*

In the literature about ab-initio calculations for iron and nickel, there were made severe approximations on the parametrization of the electron-electron interaction. Most of them kept density-density interaction terms only (Leonov et al., 2011; Lichtenstein et al., 2001) or restored spin-rotation symmetry within the density-density interaction (Belozerov et al., 2013). In order to see the effects, which the different types of approximations make on the results, we did our calculations for three types of interaction. (see Fig. 9.2).

The three references given above overestimated T_C for nickel substantially; with Kanamori or full-Hubbard interaction instead we find the experimental value. For iron, Kanamori or full-Hubbard interaction still overestimates T_C of about 30 %.

This makes sense, since iron (6.7 electrons in the d-manifold) is much closer to half-filling than nickel (8.8 electrons in d-manifold), and going from half to full filling, the Fermi liquid state is recovered. DMFT is exact in the non-interacting limit, which corresponds here to the system being completely full, therefore DMFT is expected to work better for nickel. The same also for the coordination number, which is 8 for iron's bcc-lattice, and 12 for nickel's fcc-lattice, expecting DMFT to perform better for nickel.

The 30 % off observed for iron can thus be accounted for non-local correlations (Rohringer et al., 2011). They are strongly present in iron and not captured by DMFT, whereas in nickel they seem to have minor influence on T_c.

9.3.2 Self energies

We have seen, that the magnetic transition temperatures strongly depend on on the parametrization of the Coulomb interaction. A similar picture also holds for the self energies.

Iron's self energies are much larger compared to those of nickel, and also differ strongly between e_g and t_{2g} contributions.

Nickel's self energies are smaller a factor of 2-3 and don't differentiate much between the types of interaction, as well as between e_g and t_{2g}.

From the perspective of the self-energies only, iron looks like a strongly correlated metal at these temperatures, and nickel rather close to a Fermi-liquid state.

9.3.3 DFT + DMFT spectral functions

In the previous two sections we argued that nickel seems to be a Fermi-liquid and iron a strongly correlated metal. However looking at the spectral functions, nickel has a very pronounced Hubbard satellite, and therefore must also be a strongly correlated metal. This contradiction will be resolved later in Sec. 9.4. But let's now discuss the spectral functions first.

Our DFT+DMFT spectra are consistent with previous calculations of similar kind (Belozerov et al., 2013; Lichtenstein et al., 2001; Sánchez-Barriga et al., 2009; Schickling et al., 2016) and agree reasonably well with angular resolved photoemission data (see Fig. 9.5). They also reproduce the known signatures of correlation in both materials, in particular the visible spin-polarized photoemission satellite around $-6e$V for nickel.

k-averaged spectral functions

The results for Fe at $T = 386$K are shown in Fig. 9.3 for the three parametrizations of the interaction used. The spectra generally agree well with photoemission experiments (Hüfner

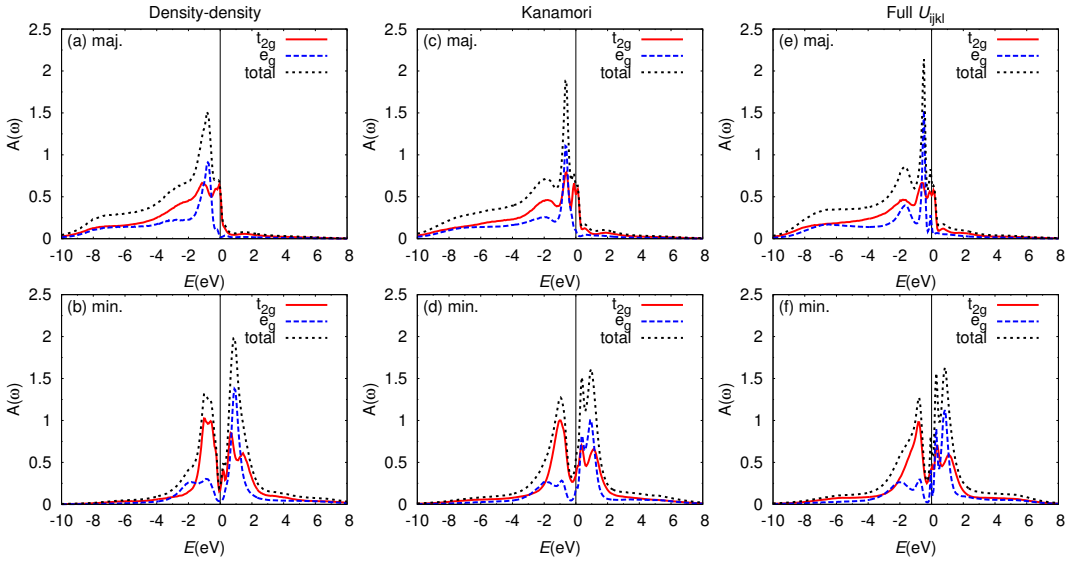

Figure 9.3: ***Iron spectral functions.*** *Spectra of the 3d shell for Fe at $T = 386K$ using the three parametrizations of the interaction as discussed above. The top row shows the majority, the bottom row the minority spin channel.*

and Wertheim, 1974; Pessa et al., 1976; Schulz et al., 1979), showing a principal peak below the Fermi level, a secondary peak at about 2eV binding energy, as well as additional features at higher binding energies with a potential satellite at about 6-7eV. The spectra undergo an evolution as a function of the parametrization of the Coulomb interaction, showing more multiplet features when going form density-density (panels a,b in Fig. 9.3) towards the full inclusion of U_{ijkl} (e,f in Fig. 9.3). This is somewhat expected, due to the large effects of the Coulomb interaction on the electronic structure of iron in general.

For Ni the situation is complicated by the long history of the satellites in the photoemission spectrum. Our results for Ni ($T = 386$K) are shown in Fig. 9.4 for the three parametrizations of the interaction used. Here, the spectra do not vary as strongly as in the case of iron. This is again not unexpected, since the different parametrizations do not have such a strong effect in Ni. Only small changes in the intensities and positions of features are observed. Comparing to experiments we identify a large principal peak, a shoulder next to it, as well as an additional peak at about 2eV binding energy (Hüfner and Wertheim, 1974; Mårtensson et al., 1984; Nakajima et al., 2004; Okane et al., 1993). Apart from these, we see only one additional satellite around $6-8$eV binding energy, which we identify as the "6eV valence band satellite".

k-resolved spectral functions

We have also performed a preliminary comparison of our calculations with angle-resolved photoemission spectroscopy (ARPES) data, which is shown in Fig. 9.5. We compare our results with ARPES of Himpsel et al. (Himpsel et al., 1979) for Ni and of Schäfer et al. (Schäfer et al., 2005) for Fe. We have used the results of the density-density interaction, since the QMC data at low temperature have the least noise here.

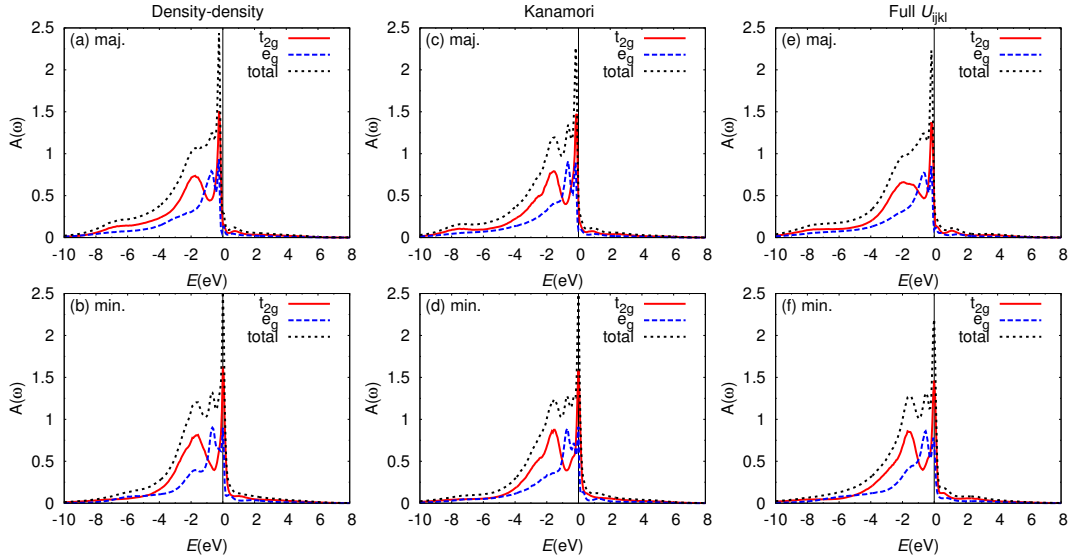

Figure 9.4: ***Nickel spectral functions.*** *Spectra of the 3d shell for Ni $T = 386K$ using the three parametrizations of the interaction as discussed above. The top row shows the majority, the bottom row the minority spin channel.*

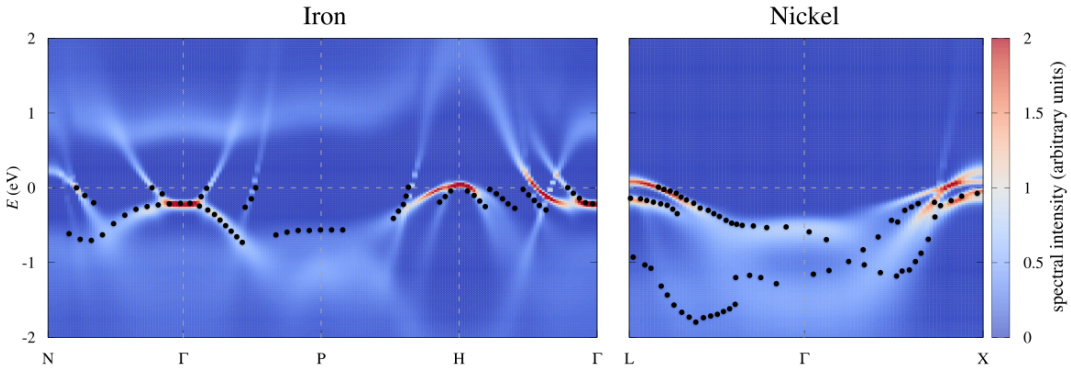

Figure 9.5: ***Momentum resolved spectra.*** *Total momentum resolved spectral functions of the 3d shell for Fe and Ni at $T = 386K$ using the density-density parametrization of the interaction as discussed above.*

For Ni the agreement is quite satisfactory only close to the Fermi level along L-Γ, but worsens at larger binding energies as well as along Γ-X. From the analytically continued Green's function at the L-point we have estimated the exchange splitting to be about 0.25eV in good agreement with experiments that give values between 0.26 ± 0.05eV (Eberhardt and Plummer, 1980) and 0.31 ± 0.03eV (Himpsel et al., 1979).

For Fe the agreement between our data and ARPES is very good along the N-Γ-P lines of the band structure. Larger quantitative discrepancies appear along P-H-Γ, which is a trend also seen in the Gutzwiller-DFT of Schickling et al. (Schickling et al., 2016). Since we can reasonably describe the ARPES spectrum of the ferromagnetic phase of Fe, it appears that local correlations play an important role here. On the other hand it was shown in Ref. (Sponza et al., 2017) that the ARPES spectrum of Fe is also very well described within QSGW alone, neglecting local correlations. In this case, only a simultaneous analysis of one- and two-particle quantities within the same theoretical scheme can clarify the relative role of local (DMFT) and non-local (QSGW) correlations.

9.4 The mechanisms of ordering in the antipodal ferromagnets iron and nickel

Here we show, that iron is the typical textbook strong coupling ferromagnet. Strong electron-electron interactions localize electrons in the atomic orbitals, which then can order by an exchange type of interaction. Nickel instead is also a strong-coupling ferromagnet, but goes a different way: its van-Hove singularities close to the Fermi level first slow down the electrons, which are then able to localize in the atomic orbitals and order. Thus only the combination of its peculiar DOS and electron-electron interactions create the Curie-Weiss susceptibilities and non-Fermi liquid scattering rates observed in nickel.

One year after this publication, one of the coauthors disentangled in a separate work the effects of large DOS at the Fermi level and an asymmetric DOS. He showed that both effects increase the amount of electronic correlations (Belozerov et al., 2018).

9.4.1 Iron as typical strong-coupling ferromagnet

The onset of ferromagnetic long-range order is signaled by a divergence of the $\mathbf{Q} = 0$ spin susceptibility at the Curie temperature. For a ferromagnetic metal, such as nickel or iron, the local spin susceptibility is instead a regular function of T. The latter is defined as

$$\chi_{\mathrm{loc}}^{\omega=0} = \int_0^\beta \mathrm{d}\tau \chi_{\mathrm{loc}}(\tau), \tag{9.1}$$

i.e. the $\omega = 0$-Fourier component of the spin-spin response function

$$\chi_{\mathrm{loc}}(\tau) = g^2 \sum_{ij} \left\langle S_z^i(\tau) S_z^j(0) \right\rangle, \tag{9.2}$$

where $S_z^i(\tau)$ is the local spin operator for the orbital i on nickel or iron, at the imaginary time τ. g denotes the electron spin gyromagnetic factor. By studying $\chi_{\mathrm{loc}}^{\omega=0}(T)$, the formation of local magnetic moments can be inferred. A Stoner-like ferromagnet does not have pre-formed local moments, whereas a strong-coupling ferromagnetic instability can be pictured as the emergence of localized spin moments at high temperatures, which acquire phase coherence

and order throughout the crystal upon cooling. With DFT+DMFT we can access $\chi_{\rm loc}^{\omega=0}(T)$ also below the Curie temperature, as if magnetism was not present (paramagnetic solution). This is useful to study the intrinsic local spin response, independently of the actual long range order. If the local moments are created by the electron-electron interaction, $\chi_{\rm loc}^{\omega=0}(T)$ must go, at sufficiently high temperatures, as $1/T$ (Curie law). This clearly happens in iron (Fig. 9.6a and b) for both parametrizations of the Coulomb interaction used in this case. Plotted on the same scale of the interacting one, the $U_{ijkl}=0$-susceptibility (green dots), as well as the dressed convolution of two DMFT Green's functions ("bubble" approximation, gray squares), are small and weakly temperature dependent. They are completely overwhelmed by the pronounced Curie behavior obtained, as soon as the Coulomb interaction is considered.

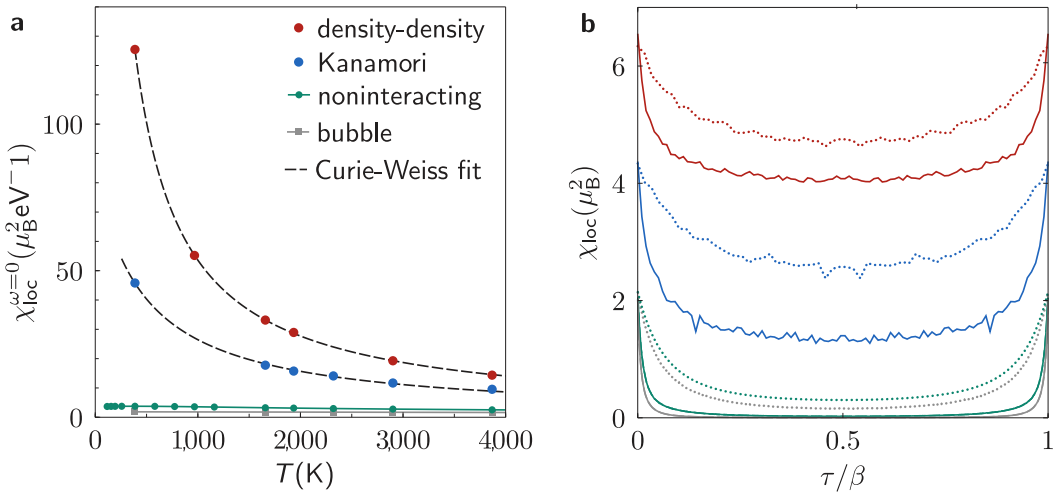

Figure 9.6: Paramagnetic spin response of iron at ambient pressure. a, *Temperature dependence of the local spin susceptibility* $\chi_{\rm loc}^{\omega=0}(T) = g^2\int_0^\beta {\rm d}\tau \sum_{ij}\left\langle S_z^i(\tau)S_z^j(0)\right\rangle$ *in iron, calculated with DFT+DMFT. Calculations are performed following the non-ordered magnetic solution, also below the ferromagnetic transition temperature* T_C *at which the uniform* ($\mathbf{Q}=0$) *susceptibility diverges (not shown).* $\chi_{\rm loc}^{\omega=0}(T)$ *in iron displays a marked "*$1/T$*"-Curie-Weiss behavior, above as well as below* T_C*, indicating the existence of robust local magnetic moments. The fits are least-square fits with fit function* $\chi_{\rm loc}^{\omega=0}(T) = \frac{\mu_{\rm eff}^2}{3(T+2T_K)}$*. For density-density we obtain an effective local moment of* $\mu_{\rm eff} = 3.97\mu_{\rm B}$ *and a Kondo-temperature of* $T_{\rm K} = 35$K*, for Kanamori* $\mu_{\rm eff} = 3.14\mu_{\rm B}$ *and* $T_{\rm K} = 227$K*. The DFT+DMFT data are compared to the uncorrelated and "bubble" susceptibilities, i.e. calculated respectively from the bare and "dressed" Green's functions, neglecting the effect of vertex corrections. Fig.* **b** *shows the decay in imaginary time* τ *of the local spin susceptibility at two temperatures* $\beta = 4$eV *(dashed lines) and* $\beta = 30$eV *(full lines), for density-density (red) as well as Kanamori (blue). The fact that* $\chi_{\rm loc}(\tau=\beta/2)$ *is going to zero much more slowly than* β *implies the presence of persistent local moments at these temperatures.*

In the paramagnetic phase, iron is therefore a bad metal with a strong electron-electron scattering and robust local magnetic moments. The local susceptibility nicely fits to Wilson's formula (Wilson, 1975)

$$\chi_{\rm loc}^{\omega=0}(T) = \frac{\mu_{\rm eff}^2}{3(T+2T_{\rm K})}, \tag{9.3}$$

as shown in Fig. 9.6a and b. Here, $\mu_{\rm eff}$ is the local moment and, indeed, the estimated values are in excellent agreement with the experimentally ordered ferromagnetic moment. $T_{\rm K}$ is the

Kondo temperature and indicates the screening of the local moment, as well as the onset of a Fermi liquid behavior. As our results show, this would only occur far below T_C, if no long-range order would set it. At T_C, the paramagnetic phase of iron is therefore still closer to a local moment than to an itinerant electron description. This indicates that electronic correlations are much more important around T_C than for the low temperature spin-polarized ferromagnetic solution, which is not too far from a single-electron Slater determinant.

9.4.2 Nickel as the "van-Hove magnet"

The situation in nickel is shown in Fig. 9.7 and it is totally different. The absolute value of the local spin susceptibility (Fig. 9.7a) is way smaller than in iron. Also for nickel, it follows the Wilson law and, surprisingly, this is already the case for the non-interacting susceptibility. We can explain this by the particular shape of the DOS of nickel with its van Hove singularity, appearing in the t_{2g} sector (see Fig. 9.7d) slightly below the Fermi level ($E_F = 0$). As shown in Fig. 9.7c, the corresponding band forms a hollow on the hexagonal face of the Brillouin zone, inside which the dispersion is essentially flat, except for a slow modulation between the six minima and the shallow maximum around the L point. Though this singularity is integrable in three dimensions, it induces a "pre-localisation" effect of the Bloch electrons which, for geometrical reasons, have a band velocity

$$\boldsymbol{v} = 1/\hbar \nabla_{\boldsymbol{k}} \epsilon(\boldsymbol{k}) \tag{9.4}$$

close to zero. This reflects directly in an apparent Curie law of the non-interacting spin susceptibility, governed by the distance in energy from the flat band (Dzyaloshinskii, 1996; Vonsovskii et al., 1993). Including electronic correlations, the local susceptibility in Fig. 9.7b keeps its $1/T$-behavior but is strongly enhanced (by a factor of 2-3). We stress that such enhancement is much stronger than what is to be expected from the quasiparticle normalization $Z \sim 0.8$ ($Z = (1-\alpha)^{-1}$ with $\alpha = \partial \mathrm{Im}\Sigma(i\nu_n)/\partial(i\nu_n)|_{\nu_n \to 0}$ in Fig. 9.2d). This indicates the fundamental importance of vertex corrections to the susceptibility of nickel, despite its large filling.

The second fingerprint of pronounced band effects in nickel is the kink in the spin susceptibility. This is present in the $U_{ijkl} = 0$ as well as in the interacting case (see Fig. 9.7a and b) and separates two "Wilson"-like behaviors with different slopes of $1/\chi_{\mathrm{loc}}^{\omega=0}(T)$. The kink can be traced back to the fact that the chemical potential is $\sim 0.17eV$ below the sharp upper edge of the t_{2g}-DOS and $\sim 0.05eV$ above the van-Hove singularity (see Fig. 9.7c and d). The former acts as a source of pre-localization too (for a demonstration see the analysis under pressure and the inset to Fig. 9.9b). Since the two singularities are different, their influence to $\chi_{\mathrm{loc}}^{\omega=0}(T)$ is not symmetric, resulting in two different $1/T$-behaviors: decreasing T from high temperatures, we switch from one to the other when the larger of the two energy scales, i.e. $\sim$1,700K, is crossed (see Fig. 9.9a).

It is important to note that the inclusion of interactions does not alter this picture, apart from lifetime effects and broadening which make the kink much smoother and its position slightly normalized. The kink in the local susceptibility directly translates via the Bethe-Salpeter equation to a kink in the ferromagnetic susceptibility. It clarifies the experimentally observed

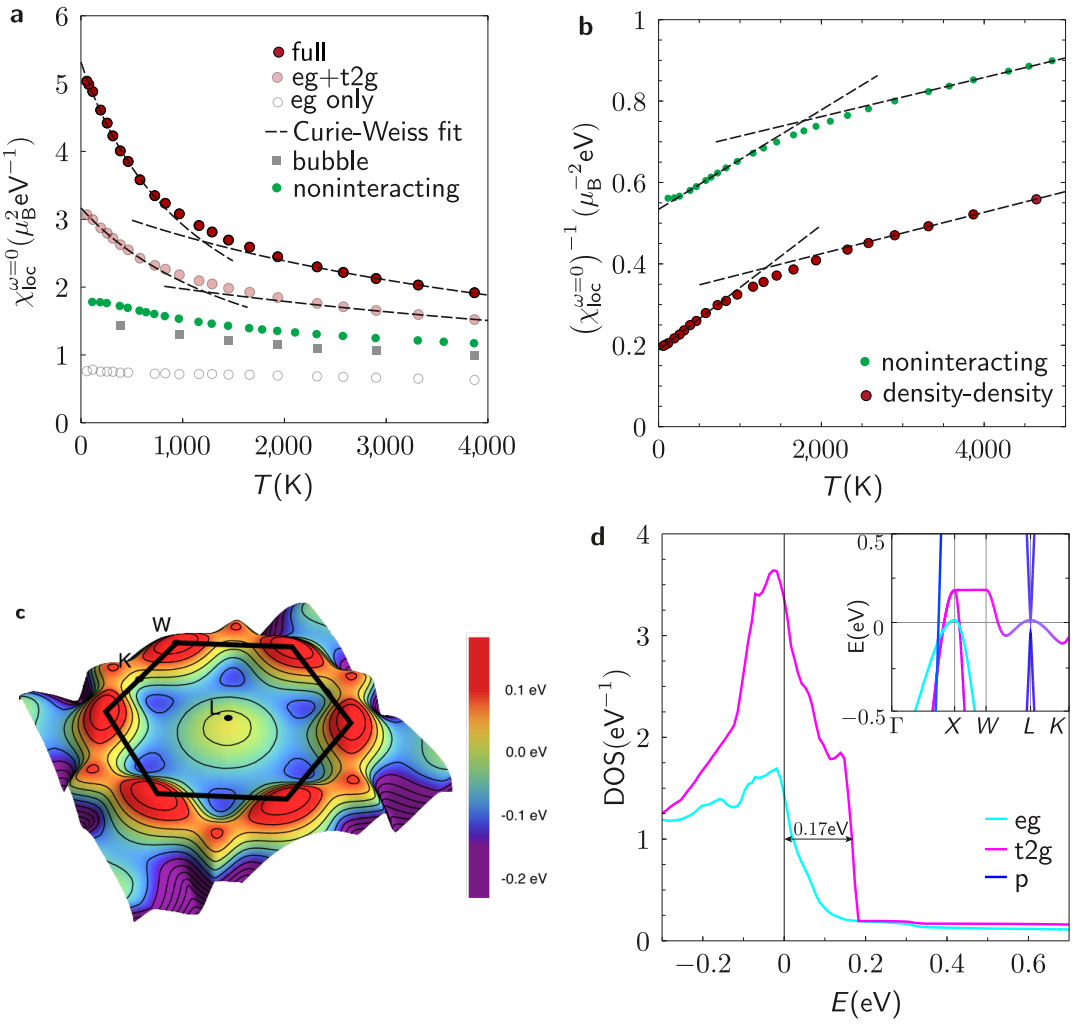

Figure 9.7: Paramagnetic spin response of nickel at ambient pressure. a, *Temperature dependence of the static local spin susceptibility* $\chi_{\rm loc}^{\omega=0}(T)$ *of nickel in DFT+DMFT, compared to the "bubble" approximation and to the non-interacting one. In order to show that the characteristic temperature dependence of the non-interacting susceptibility originates from the* t_{2g}*-sector and its van-Hove singularity, we also plot the intra-orbital contribution to the full* $\chi_{\rm loc}^{\omega=0}(T)$ *("full"), considering the cases where either the 5 orbital-diagonal terms of* $\chi_{\rm loc}$ *are summed ("*$e_g + t_{2g}$*"), or only the two* e_g*-terms are retained ("*e_g *only"). This shows the more conventional Pauli spin response of the* e_g *part is in agreement with the fact that the* e_g*-DOS is much smoother around* $E_F = 0$*.* **b,** *Inverse susceptibility for the non-interacting and DFT+DMFT case. This illustrates the main peculiarity of nickel, namely that already the non-interacting spin response is characterized by a "*$1/T$*" law. As explained in the text, this is due to "pre-localized" moments arising from the vicinity to the van-Hove singularities.* **c,** *Electronic band dispersion of nickel on the hexagonal face of the Brillouin zone, close to the L point. The extended flat region around the shallow maximum at L is responsible for the van-Hove singularity.* **d,** t_{2g}*- and* e_g*-DOS for energies close to* $E_F = 0$*. In the inset, the electronic state dispersion of nickel, close to the W-L-K region and to the top of the band is shown. The distance of the sharp step in the* t_{2g} *orbitals at* $E = 0.17$eV *corresponds to the kink of the non-interacting susceptibility in* **b** *at* $T = 2,000$K*.*

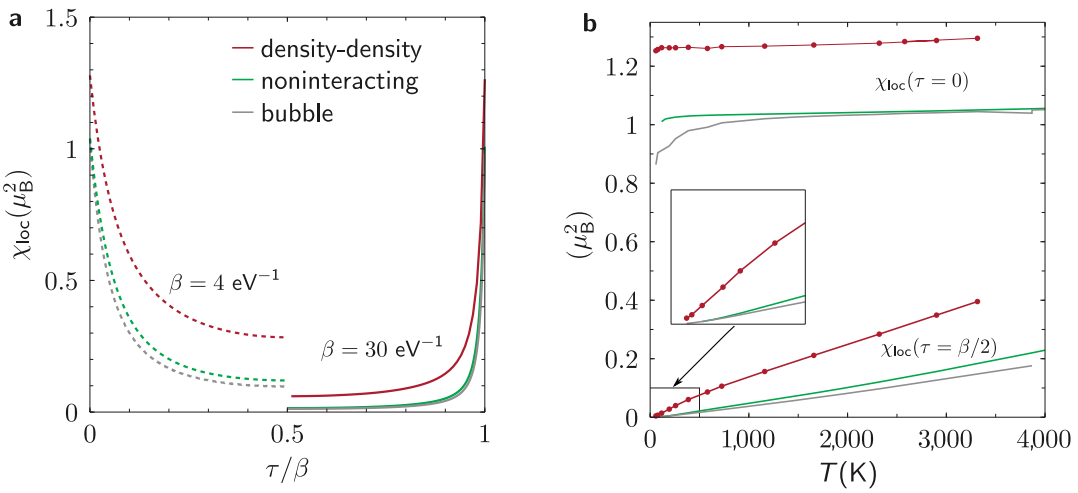

Figure 9.8: **a,** $\chi_{\rm loc}(\tau)$ *for* $\beta = 4eV^{-1}$ *(dashed) and* $30eV^{-1}$ *(solid).* **b,** *instantaneous* ($\tau = 0$) *and long-time* ($\tau = \beta/2$) *values of* $\chi_{\rm loc}(\tau)$. *From the latter one can clearly see that the moment is eventually screened, at temperatures much lower than* T_C. *The comparison with the non-interacting and with the "bubble" results shows also that vertex corrections are important and the DFT+DMFT result cannot be obtained by using "dressed" quasiparticle propagators (see also* **b**).

kink at ∼1,200K (Sucksmith and Pearce, 1938), reported almost eighty years ago but so far, to the best of our knowledge, without explanation.

Since in nickel the "Wilson" behavior is already present in $\chi_{\rm loc}^{\omega=0}(T)$ at $U_{ijkl} = 0$, a direct interpretation in terms of a Kondo effect is difficult. Let us hence turn to the imaginary time τ dependence of the local susceptibility, shown in Fig. 9.8a and b. Without interaction, there is a rapid drop of $\chi_{\rm loc}(\tau)$ for $\tau \to \beta/2$. This indicates the absence of long-lived local moments. A drop is present with interaction as well, but on much larger time scales and from larger $\chi_{\rm loc}(\tau = 0)$ values. This confirms the presence of correlation-enhanced (Prokopjev and Reser, 1991; Toschi et al., 2012) local moments in nickel and the τ-dependence reveals their screening properties. Since there remains a finite unscreened moment $\chi_{\rm loc}(\tau = \beta/2)$ even at $\beta = 30$eV^{-1} (370K), the screening is not complete. Only at much lower temperatures (of the order of 100K) this moment eventually gets completely screened, see inset of Fig. 9.8b. The existence of such a two stage screening can be clarified invoking the few charge carriers available for screening, as in Nozières exhaustion scenario (Burdin et al., 2000; Nozieres and Blandin, 1980). Also the local spin being larger than 1/2 (Nevidomskyy and Coleman, 2009) and the fact that d electrons act both as localized moments and itinerant ones can contribute. The latter screen the former. This leads to different energy scales for the onset of screening and for complete screening (Held et al., 2013), with the range in-between strongly affected by the van Hove peak in the d-electron spectral function.

9.4.3 A unified picture

A van-Hove singularity is actually also present in the bcc-DOS of iron (see Fig. 9.10). The reason why this does not influence the physical properties as for nickel is the different occupation of the d-shell of the two materials. Due to the proximity to half-filling, in iron the physics is dominated by correlation-induced band normalization and strong electron-electron scattering. This means that, even though the van-Hove singularity does give a $1/T$-behavior

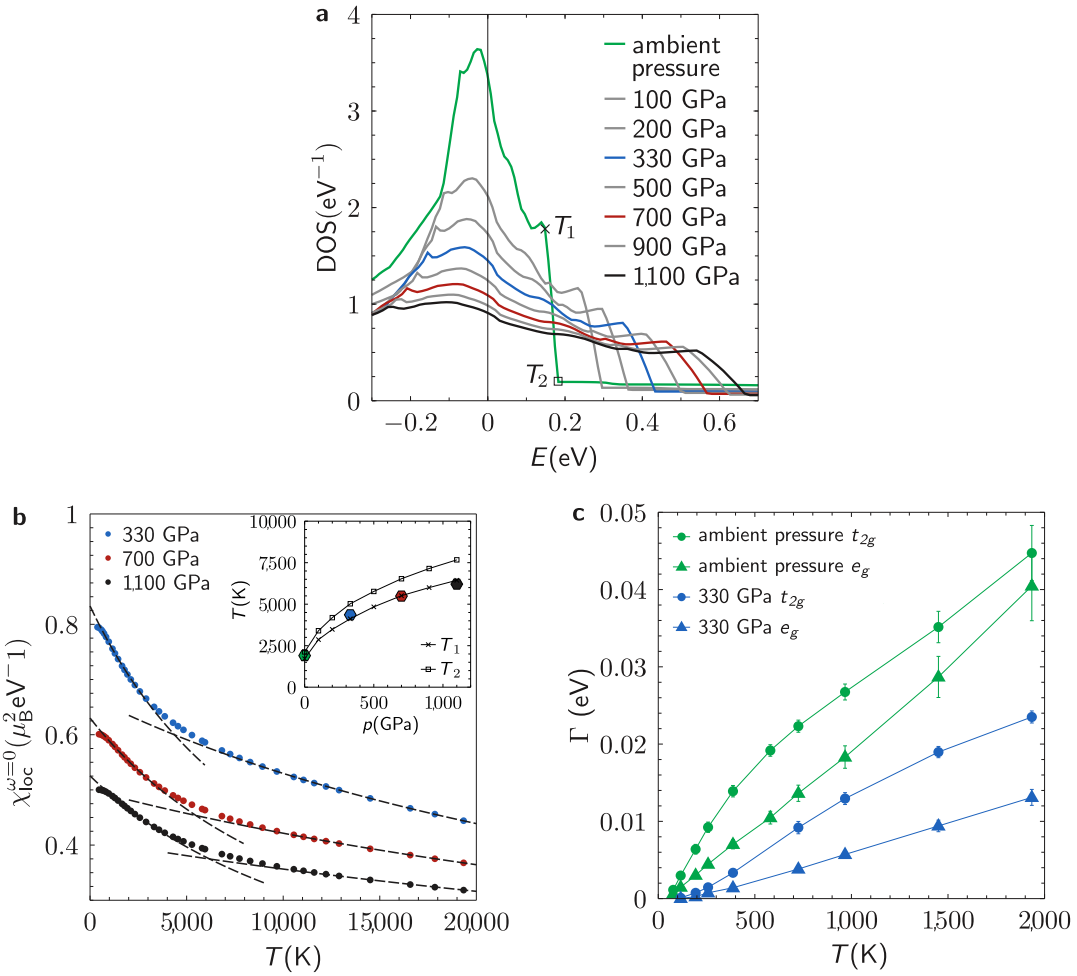

Figure 9.9: Nickel under pressure. a, *The t_{2g}-DOS of nickel at different values of the pressure. The van-Hove peak and the sharp edge are smoothed with increasing pressure, but the Fermi level (E_F=0) remains close to these two singular points. The cross at temperature T_1 marks the beginning of the DOS-steps, whereas the square at T_2 marks is its ending. Their evolution with pressure is shown in the inset to* **b**. **b,** *Non-interacting local spin susceptibility versus temperature at high pressures. The dashed lines are least-square fits of the high- and low-temperature region, which uncover the separation between the two "Wilson"-like behaviors, shifting towards higher temperatures compared to ambient pressure. The position of this kink (shown as hexagons in the inset) scales with the energy distance between E_F and the sharp edge of the t_{2g}-DOS.* **c,** *A consequence of the sharp features at the top of the band is the deviation of the quasiparticle scattering rate from the T^2-law predicted by the Landau theory. Here this is shown for pure nickel, by plotting the scattering rates of one of the degenerate t_{2g} and one of the degenerate e_g orbitals, both at ambient pressure and at 330 GPa. The error bars come from averaging over different fit parameters (number of Matsubara frequencies and order of fit-polynomial).*

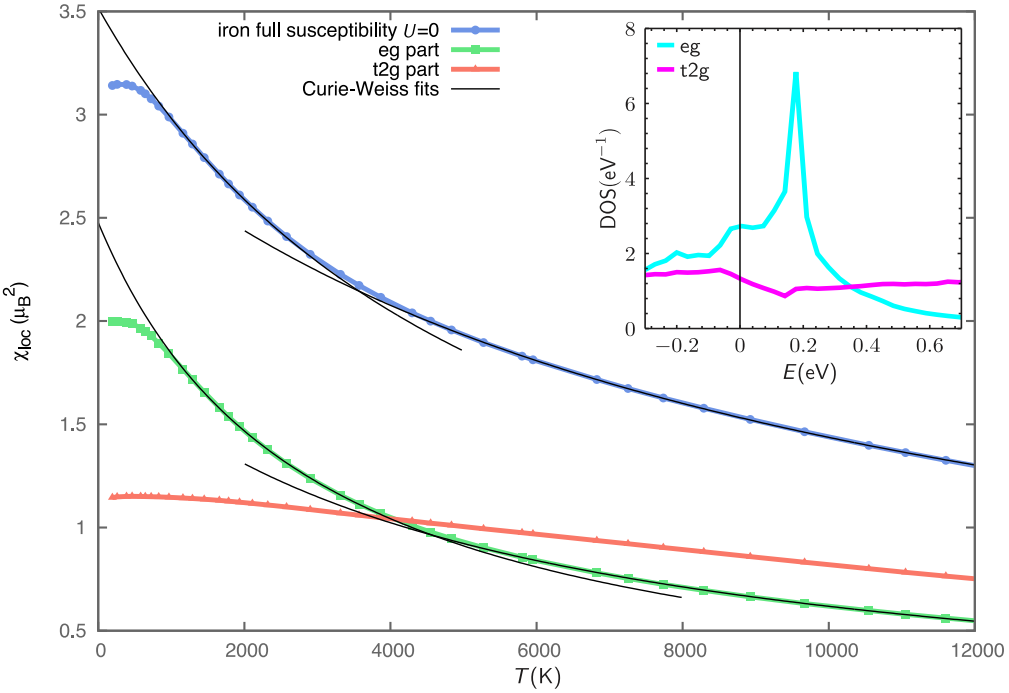

Figure 9.10: *The non-interacting susceptibility of iron, as the sum of e_g and t_{2g} contributions, and the non-interacting DOS as inset.*

for the non-interacting $\chi_{\text{loc}}^{\omega=0}(T)$ as well as a kink visible on a small scale (see Fig. 9.10), this has hardly any influence in the actual behavior in the presence of the interaction.

Nickel is instead close to 9 d-electrons and moreover the individual occupation of its five d-orbitals is almost maximized. Hence, the entire manifold of electronic states is practically occupied and the majority of the active electrons lives close to van-Hove singularity and to the sharp feature at the top of the t_{2g}-DOS. As a result, its physics is distinct from the more common case of a strongly-correlated metal with sharp features in the DOS located far away from the band edges (bcc-iron). This difference between iron and nickel does not only concern the formation of local moments but it also leads to different microscopic mechanisms for ferromagnetism. In the case of iron, ferromagnetism is driven by Hund's rule coupling which forms a large local moment of the d-electrons that are close to half filling. These Hund's moments then only need a bit of hopping to order (Held and Vollhardt, 1998). For nickel on the other side, its peculiar DOS is essential not only for the formation of the local moments but also for their ferromagnetic long range order. This is the flat band (Mielke and Tasaki, 1993), or more generally asymmetric DOS route (Ulmke, 1998; Wahle et al., 1998) to ferromagnetism. In contrast to the aforementioned work, Hund's coupling plays also an important role in nickel. It enhances the local moments and strongly affects T_C (see Supplementary note 2 of (Hausoel et al., 2017)). Such a mixture of Hund's rule and flat band ferromagnetism has recently also been observed in $BaRuO_3$ (Han et al., 2016).

9.5 Iron and nickel at Earth's core conditions

The most important implication of our results for nickel comes from the observation that even at a pressure of hundreds of GPa, the position and the shape of these sharp features in the DOS do not change dramatically. Nickel remains in its fcc structure up to even larger pressures (Kuwayama et al., 2008; McMahan and Albers, 1982; Mohammed et al., 2010) and its magnetic moments, though smaller, are much more robust than those of iron (Torchio et al., 2014). Consequently, this physics is still active at the pressures of the inner Earth's core, at which instead iron is already a perfect Fermi-liquid (Pourovskii et al., 2013, 2016). The non-Fermi liquid mechanism identified here hence calls for including nickel in the current models of geomagnetism.

9.5.1 Nickel at Earth's core pressures

Inspired by our improved understanding of the different nature of magnetism in iron and nickel, we discuss now the physics of Ni under high pressures. Indeed, if the non Fermi-liquid properties of nickel survive the extreme conditions of the Earth's core, our conclusions would be also important to the recent debate about geomagnetism. The key observation is that the van-Hove singularity in nickel does not dramatically change its position with pressure. As shown in Fig. 9.9a, it gets gradually smoothed out but it survives pressures of even hundreds of GPa. At the same time, the sharp edge of the t_{2g}-DOS moves away from the Fermi level but its influence can be clearly observed in the non-interacting $\chi^{\omega=0}_{\rm loc}(T)$ at all values of the pressure considered here. In Fig. 9.9b the kink is indeed still visible at high pressure. In the inset we compare the kink position with the distance – converted in temperature – between $E_{\rm F}$ and the edge of the t_{2g}-DOS (see Fig. 9.9a). They scale the same way with pressure, confirming our interpretation in terms of sharp features of the DOS.

We now analyze the electron-electron scattering rate

$$\Gamma = -Z{\rm Im}\Sigma(i\nu_n \to 0), \tag{9.5}$$

as possible non-quadratic temperature dependencies of this quantity signal deviations from the Landau theory description of Fermi liquids. Γ of pure fcc nickel is shown in Fig. 9.9c as a function of temperature at ambient pressure and 330 GPa, characteristic of the Earth's inner core. In both cases we observe non Fermi-liquid behavior in a large interval of temperatures. A technical comment is in order here: extracting the scattering rate from the Matsubara axis at these elevated temperatures poses well-known difficulties (Pourovskii et al., 2016). We therefore first checked that a three-orbital model with the same filling of nickel, the same bandwidth of the ambient pressure case and no singularity and no asymmetry in the DOS gives a nicely T^2 Fermi-liquid scattering rate (not shown). This confirms that it is possible to reliably extract the scattering rate from our DFT+DMFT calculations – at least for temperatures up to 2-3,000K – without artifacts. As a matter of fact, even by considering error bars estimated from several polynomial fits to ${\rm Im}\Sigma(i\nu_n \to 0)$ (denoted by the vertical bars in Fig. 9.9c), the non-quadratic temperature behavior is clearly recognizable.

Hence we find that, even though judging from the self-energy nickel may seem to be a much more conventional metal than iron (see Fig. 9.2c and d), its scattering rate has a non-Fermi liquid behavior at ambient pressure as well as at 330 GPa. This deviation from the standard linear temperature dependence is caused by the van-Hove singularity (Dzyaloshinskii, 1996)

and it is so robust that it is still visible at Earth's core pressures, where the sharp features in the DOS are weakened but not yet completely gone.

9.5.2 CPA+DMFT

The coherent potential approximation (CPA) can be combined with DMFT to take into account substitutional disorder, see e.g. Ref. (Poteryaev et al., 2015) and references therein. Take a binary alloy of two components A_xB_{1-x} with concentrations x and $1-x$.

If the concentration of A is much larger than that of B, one assumes that the dispersion and lattice structure of A is preserved for the whole structure to a good approximation, and that the substituents B are randomly distributed over the lattice sites of A. The substituents B usually have a different number of valence electrons than A. This is accounted for by introducing a level shift ϵ_B at every B site. This shift is estimated from the shift of the static crystal field (center of mass of the density of states) of B as compared to the parent A in a supercell calculation. For the determination of the CPA shifts we used a Fe-hcp supercell with 16 atoms, replacing one of them by Mn or Ni (6.25% admixture).

Following Vekilova et al. we used the volume established within the Preliminary reference Earth model (PREM) (Dziewonski and Anderson, 1981; Vekilova et al., 2015) to be 7.05Å/atom. Since Mn has one $3d$-electron fewer than Fe, and Ni has one $3d$-electron more than Fe, we obtain shifts of $\epsilon_{\mathrm{CPA,Ni}} = -1.67\mathrm{eV}$ for nickel, and $\epsilon_{\mathrm{CPA,Mn}} = +0.94\mathrm{eV}$ for manganese.

Within the DMFT the impurity problem is subsequently solved for each site A and B, and an average is performed over the Green's functions according to their concentrations

$$G_{\mathrm{CPA}} = xG_A(\tau) + (1-x)G_B(\tau). \tag{9.6}$$

This gives a disorder independent mean-field, that closes the DMFT self-consistency loop. We have benchmarked our implementation against Ref. (Poteryaev et al., 2015) and reproduced some of the results reported there.

9.5.3 Disordered iron-nickel alloy

The inner Earth's core contains about 20% nickel in addition to solid iron and, at these extreme pressure and temperature conditions, they form a disordered alloy. Therefore, in order to understand whether or not nickel should actually be considered in theories of geomagnetism, one has to study a disordered iron-nickel alloy under pressure. In particular, it should be seen if, even under extreme conditions, the electronic scattering rate is large and non Fermi-liquid, as in pure fcc Ni where the van-Hove singularity mechanism is active. The electronic properties of an alloy are fundamentally different from those of a perfect crystal. In order to take the nontrivial disorder effects into account, we performed calculations for nickel alloys of various concentrations at the Earth's pressure within a Coherent Potential Approximation (CPA)+DMFT scheme.

The identification of the correct crystalline structure of iron at Earth's core conditions is still a subject of debate (see (Pourovskii et al., 2013) and references therein, as well as (Belonoshko et al., 2017)). In this work we will consider an hcp-Fe/Ni alloy, since hcp-Fe (ϵ-Fe) emerges as the most stable structure, according to several studies ((Anzellini et al., 2013; Kuwayama et al., 2008; Vočadlo et al., 2003)). The blue curve in Fig. 9.11a shows the DOS

of hcp-iron at core pressure. The vertical dashed lines in the case under pressure show the position of the local levels, after the shift of the CPA+DMFT algorithm that simulates the presence of the dopant atoms. For the iron-nickel alloy, the shift is towards the top of the hcp band and brings the local levels of Ni close to the sharp structures resembling those of pure fcc nickel (shown in Fig. 9.9a). We also considered the alloy with manganese, for reference purposes. In that case, the CPA shift has the opposite sign and it does not bring the energy levels close to any special structure in the DOS, therefore the alloy with Mn is expected to have more standard electronic properties than that with Ni.

The first indication that the hcp-iron-nickel alloy shares part of the anomalous behavior of fcc nickel comes from its non-interacting spin susceptibility (Fig. 9.11b). While pure hcp iron, as well as the alloy with Mn, displays a Pauli-like spin susceptibility in the absence of electron-electron interaction, the alloy with nickel (both with 5 and 20% nickel content) shows the "Wilson"-like behavior which characterizes pure fcc nickel (see Fig. 9.9b). Note that the absolute values of $\chi_{\mathrm{loc}}^{\omega=0}(T)$ depend mainly on the filling, as already observed for pure iron and nickel. Fig. 9.11c confirms that, when taking the electron-electron interaction into account, 20% nickel leads to a linear and large quasiparticle scattering rate at high temperatures. This confirms the close resemblance of the iron-nickel disordered alloy to pure fcc nickel, for what concerns the non Fermi-liquid nature of the scattering. The purple solid circles shown in Fig. 9.11c approach the gray curve at high temperatures (or even go somewhat above it), which refers to pure fcc nickel at 330 GPa. This demonstrates that the anomalous effect of nickel is relevant also in the case of the alloy at the Earth's core conditions.

9.5.4 Molecular Dynamics+DMFT

Since the CPA can account only for substitutional disorder, we have performed additional molecular dynamics (MD) simulations combined with DMFT to estimate effects of thermal disorder. Following Pozzo et al. (Pozzo et al., 2012) we used a canonical ensemble at 6000K and a run time of 20 ps and a time step of 1 fs. Configurations were written every 50 fs, so in total 20.000 configurations were generated. These calculations were performed with an fcc Ni supercell at 330 GPa containing 27 atoms. Subsequently, for the last six MD configurations we performed an additional static calculation and a local orbital projection as for the bulk. These inputs were used to perform a DMFT calculation for all 27 Ni atoms in the unit cell. We used a temperature of about 6000K ($\beta = 2\mathrm{eV}^{-1}$) also in the DMFT. Since the crystal structure of the MD configurations is not cubic anymore we used the spherically averaged Coulomb interaction matrix for Ni, with $U_{\mathrm{S}} = 2.71\mathrm{eV}$ and $J_{\mathrm{S}} = 1.0\mathrm{eV}$. As expected from the structural changes in each configurations the spectrum, self-energies and fillings vary somewhat between atoms. The fillings of the atoms in each studied configuration vary between 8.8 and 8.9 electrons (bulk: 8.85), where the filling is equally distributed between the orbitals. The atom-averaged filling in each studied configuration gives 8.84-8.86, basically on top of the bulk result. Averaging the spectra and self-energies over all 27 impurity problems shows that the cell-averaged results are again very close to the bulk fcc Ni result. In Fig. 9.12 we show the DMFT spectrum and electronic self-energy for the MD configuration at 19.80ps compared to the bulk result obtained using the same parameters. The data shown is a goods representative of all MD+DMFT results we obtained for this system.

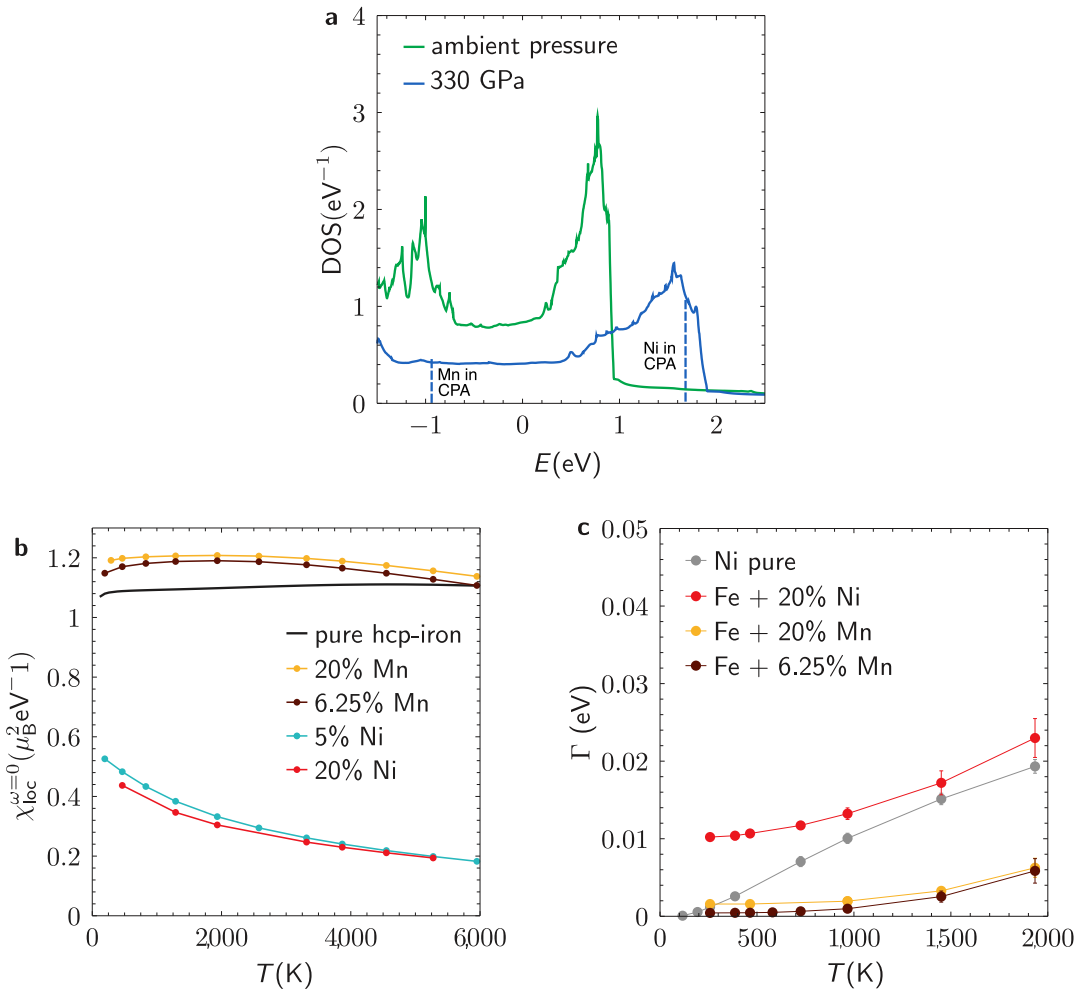

Figure 9.11: Iron/nickel alloy under pressure. a, *DOS of the ε (hcp) phase of iron at ambient and Earth's core pressure (green and blue lines, respectively). $E = 0$ corresponds to the chemical potential of hcp-iron. The vertical dashed lines indicate the energies at which the local levels of Ni and Mn are shifted within the Coherent Potential Approximation (CPA) + DMFT scheme. In contrast to the shift for the Fe/Mn alloy (used here as a reference example), that for Fe/Ni brings the local levels of nickel close to the peak at the top of the hcp band. Since the latter is similar to the sharp features of pure fcc nickel (shown in Fig. 9.9a), the non Fermi-liquid effects observed in the pure fcc material are expected to survive in the iron-nickel alloy.* **b,** *Non-interacting local spin susceptibility for pure hcp-iron and for the alloys of hcp-iron with Mn and Ni, all at Earth's core pressure, i.e.* 330 GPa. *The iron-nickel alloy strongly deviates from standard Pauli behavior of good Fermi liquids. The example of Mn is on the contrary much closer to the Fermi-liquid result of hcp-iron.* **c,** *The scattering rate (averaged over all d-orbitals) of the nickel-alloy at high temperatures within CPA+DMFT is remarkably similar to the corresponding one of pure fcc nickel at these pressures and much larger than that of the Fe/Mn alloy, taken here as a reference.*

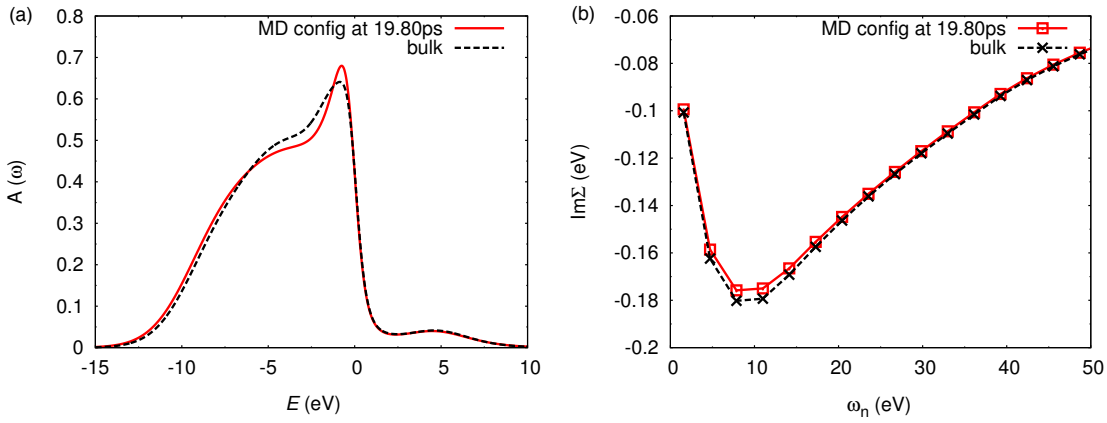

Figure 9.12: ***Molecular Dynamics Simulations.*** *(a) DMFT spectrum and (b) electronic self-energy averaged over the 3d orbitals for the MD configuration at 19.80ps compared to the bulk result obtained using the same parameters.*

9.6 Discussion

The disorder, that we have treated here at the CPA level, turned out to have a crucial effect. A comparable amount of nickel combined with hcp iron in a translationally invariant crystalline structure gives more Fermi-liquid results, as interestingly pointed out in a recent paper by Vekilova, *et al.* (Vekilova et al., 2015). The latter approach has the advantage over CPA+DMFT that non-local changes to the band structure-induced by the presence of the nickel atoms are fully taken into account. By going beyond the state-of-the-art implementation of CPA+DMFT, which is the one we followed here, it will be possible in the future to fully describe this difficult interplay between many-body and disorder effects.

The linear-in-T scattering rate of the iron-nickel alloy at core pressure in a large window of temperatures suggests a small thermal conductivity. Molecular dynamics followed by real-space DMFT calculations of large nickel supercells, shows that the van-Hove singularity in the spectrum and the scattering rate are not dramatically modified by the inclusion of thermal disorder. Our results may therefore play a role in models of the geodynamo, recently questioned because of the large thermal conductivity of iron (Pozzo et al., 2012). Whether or not this can be reconciled with iron alone is at the moment under debate(O'Rourke and Stevenson, 2016; Pourovskii et al., 2016), but according to the current understanding there would be too little energy left for convection in the total heat budget (Olson, 2013). In light of our results, it will be interesting to reconsider the contribution of nickel to the total thermal conductivity of the core. The next challenge will thus be to include electronic correlations also in the ab-initio study of the liquid phase of iron and nickel and determine if a more consistent explanation of the geodynamo can be obtained.

Chapter 10

Summary

This completes our journey from novel double-Dirac fermions in the material Bi_2CuO_4, as well as Higgs- and Goldstone bosons in excitonic magnets, down to the Earth's core and the geodynamo.

For this purpose, I first introduced the models and methods, which were used in the scope of this thesis. I briefly discussed the microscopic framework of the many-body Schrödinger equation, which is way too complicated for practical calculations of systems of scientifically and technically relevant size, therefore abstracted models have to be deduced. Those models try to capture the main macroscopic quantum properties of materials, and omit parts not affecting the physics significantly. I introduced the dynamical mean field theory for the Hubbard model, which treats the on-site electronic correlations in an exact way, and applies a mean-field approximation to the non-local parts. I also discussed the Anderson impurity model, that serves as an auxiliary model for DMFT.

Then followed a detailed derivation of the continuous-time quantum Monte Carlo technique in hybridization expansion, building on standard lectures on solid state theory, before discussing several algorithmical improvements, like the superstate-sampling and sliding techniques, and a recently discovered inconsistency of Green's function estimators in systems with finite baths.

I explained the DMFT for general one- and two-particle interaction terms on the impurity, which appear for multi-orbital Hubbard models of real materials. I showed how to validate the results of those complicated and cumbersome calculations as well as derived and discussed the symmetry properties, which these results have to fulfill, in order to reduce numerical instabilities and improve the precision.

The second part, which presents physical applications, starts with unconventional fermions. The spatial symmetry of the vacuum permits the existence of Dirac, Weyl and Majorana fermions, whereas the lowered symmetries of solids allow further fermionic excitations. I showed the example of double-Dirac fermions in the material Bi_2CuO_4. However, due to strong electron-electron interactions, the material is deep in the Heisenberg limit and orders antiferromagnetically. We propose to apply hydrostatic pressure to reduce the strength of electronic correlations, drive the material back to metallic phase and make the double-Dirac fermions observable.

I derived and discussed the properties of Golstone and Higgs bosons in condensed matter within the framework of Ginzburg-Landau theory and identified them in a model of an excitonic insulator.

The last chapter treats the effects of electronic correlations and magnetism in the metals iron and nickel. It is well known, that iron is a correlated metal due to its strong electron-electron interaction. Nickel however is a correlated metal, because van-Hove singularities close to the Fermi level slow down the electrons, inducing local magnetic moments, which are typical for a correlated metal. Under pressure, iron makes a structural phase transition from bcc to hcp lattice

structure, and looses some of its strongly correlated nature. Nickel instead has already fcc structure at standard conditions for temperature and pressure and keeps its strongly correlated nature even at the high pressure and temperature at the inner core of the Earth. We also find, that in an alloy of hcp-iron and nickel, which is believed to exist in the outer core of the Earth, this mechanism is at work and therefore possibly contributing to the generation of the Earth's magnetic field.

Appendix A

Some Green's and spectral functions

Figures A.1, A.2 and A.3 show, how properties of spectral functions are encoded in imaginary time Green's function. For this purpose, some spectral functions are drawn, which consist of Gaussian peaks. The position of certain peaks is modified, and the corresponding modification of $G(\tau)$ is observed. This illustrates the issue that features of $A(\omega)$ far away from $\omega = 0$ are encoded in small modifications of $G(\tau)$.

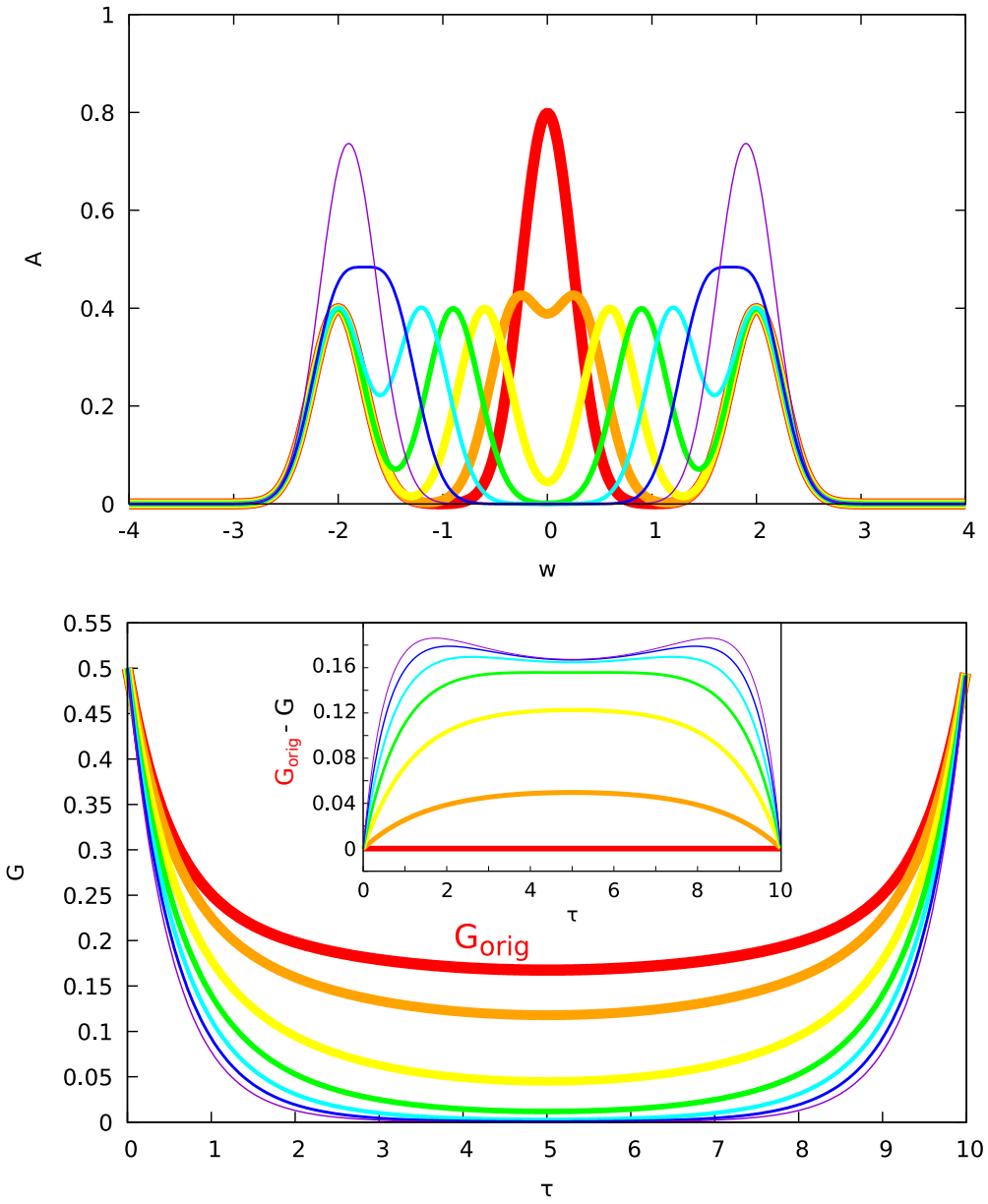

Figure A.1: *The starting point is a spectral function with three peaks at $\omega = -2$, $\omega = 0$ and $\omega = 2$ (red curve). The middle peak splits up into two, where one of them moves left and the other right (orange and yellow curve), until the whole object becomes a two peak structure (purple curve). The change of $A(\omega)$ at the Fermi level makes a significant change of $G(\tau)$. It goes from metallic ($G(\tau = \beta/2) \neq 0$) to insulating ($G(\tau = \beta/2) \approx 0$).*

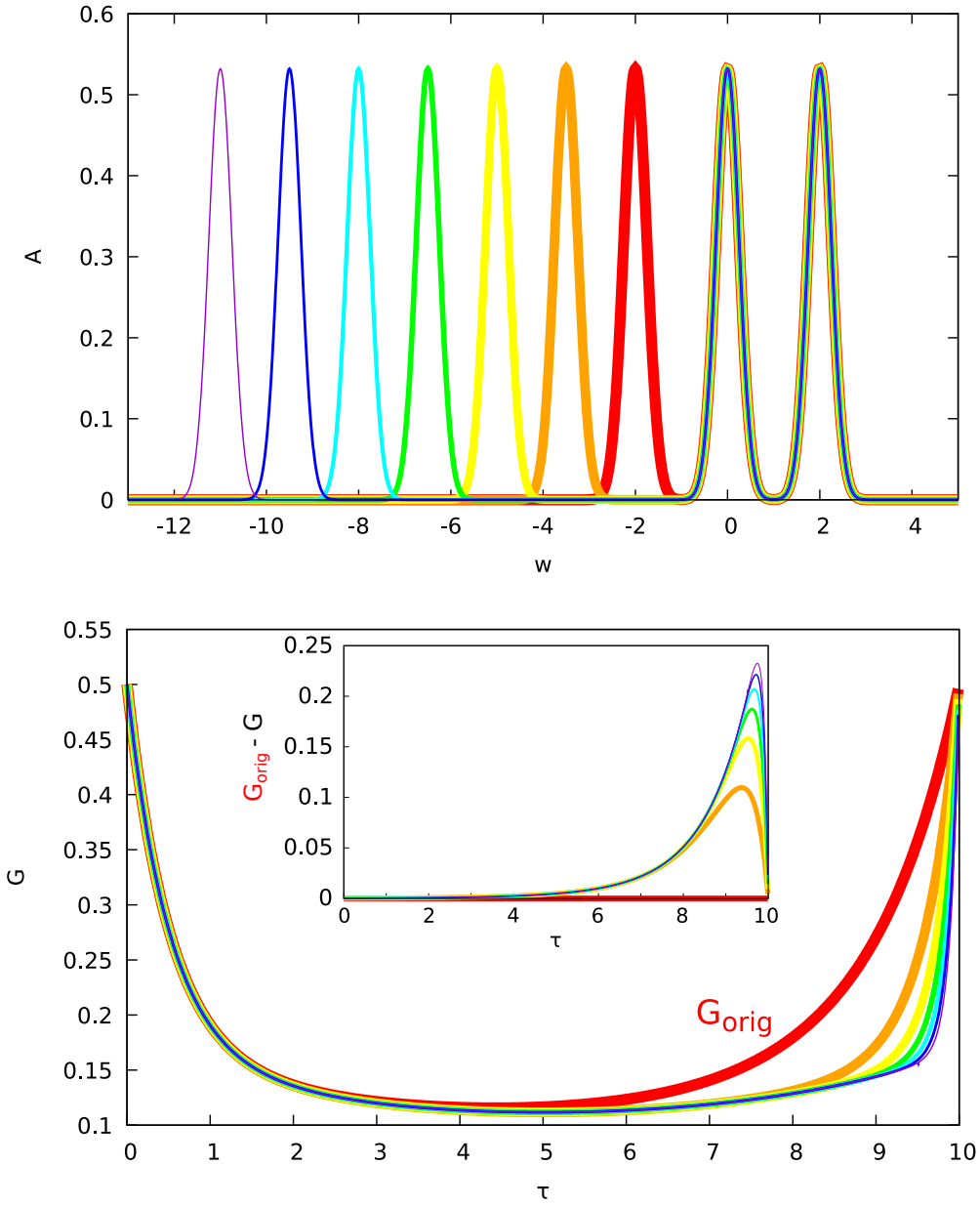

Figure A.2: *Here we start with three peaks at $\omega = -2$, $\omega = 0$ and $\omega = 2$ (red curve). The peaks at $\omega = 0$ and $\omega = 2$ stay where they are, and the peak at $\omega = -2$ moves to the left. One sees, that $G(\tau)$ only changes in the lower right edge, and its changes more, the closer the peak is at the Fermi level.*

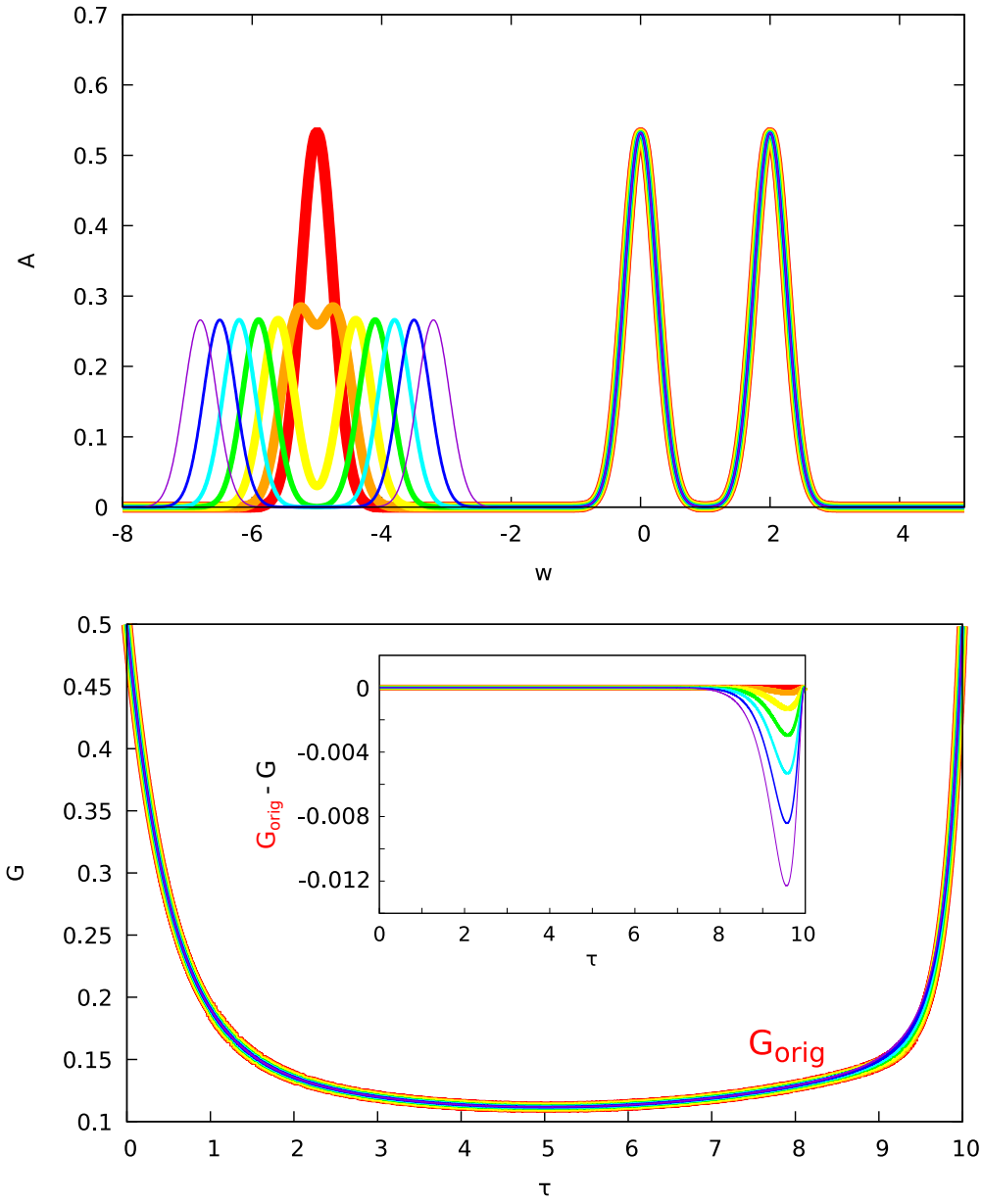

Figure A.3: *Now comes the worst situation, namely the encoding of some detail far away from the Fermi level. We leave the $\omega = 0$ and $\omega = 2$ peaks where they are, and make a splitting of a peak at $\omega = -5$, which could be a multiplet splitting in a material due to the Coulomb interaction. The change in $G(\tau)$ is tiny, making a difference of $G - G_{orig} \approx 0.012$ for the largest splitting, whereas a typical splitting of multiplet in a material is rather given by the yellow curves, which is $G - G_{orig} \approx 0.002$. It is clear, that this information is very easily blurred out by the error bars of a Monte Carlo method.*

Appendix B

Dyson's series

B.1 Interaction representation and the integral equation

In this appendix I derive the expansion of a partition function $Z = \mathrm{Tr}\left[\mathrm{e}^{-\beta H}\right]$ with respect to a part V of its Hamiltonian

$$H = H_0 + V. \tag{B.1}$$

The actual distribution of the terms does not influence the derivations here, since H_0 is not assumed to commute with V. The trace of the partition function

$$\begin{aligned} Z &= \mathrm{Tr}\left[\mathrm{e}^{-\beta H}\right] && \text{(B.2)} \\ &= \sum_N \langle N| \, \mathrm{e}^{-\beta H} \, |N\rangle && \text{(B.3)} \end{aligned}$$

can be seen such, to calculate the expectation value of the Boltzmann weight $\mathrm{e}^{-\beta H}$ with all the many-body states $|N\rangle$. An alternative interpretation of this formula is that the ket $|N\rangle$ is time-evolved from 0 to β with an imaginary time-evolution of $\mathrm{e}^{-\beta H}$; this corresponds to the Schrödinger picture, where the full time-dependence is in the states.

Full Hamiltonians of many-body systems have horribly expensive time-evolutions, which are not possible to calculate. For this purpose the interaction representation was invented, where the partition function is rewritten to have its Boltzmann weight and the time-evolutions only with respect to H_0:

$$\begin{aligned} Z &= \mathrm{Tr}\left[\mathrm{e}^{-\beta H}\right] && \text{(B.4)} \\ &= \mathrm{Tr}\left[\mathrm{e}^{-\beta H_0}\mathrm{e}^{\beta H_0}\mathrm{e}^{-\beta H}\right] && \text{(B.5)} \\ &= \mathrm{Tr}\left[\mathrm{e}^{-\beta H_0} A(\beta)\right]. && \text{(B.6)} \end{aligned}$$

The auxiliary operator

$$A(\beta) = \mathrm{e}^{\beta H_0}\mathrm{e}^{-\beta H} \tag{B.7}$$

is still impossible to calculate, since it contains an exponential of the full Hamiltonian.[1] We are going to find an expansion with respect to V. The differential equation for A is

[1] Note that it is not possible to write $\mathrm{e}^{-\beta H} = \mathrm{e}^{-\beta H_0}\mathrm{e}^{-\beta V}$, since $[H_0, V] \neq 0$.

$$\frac{\mathrm{d}A(\beta)}{\mathrm{d}\beta} = \left(\frac{\mathrm{d}}{\mathrm{d}\beta}\mathrm{e}^{\beta H_0}\right)\mathrm{e}^{-\beta H} + \mathrm{e}^{\beta H_0}\left(\frac{\mathrm{d}}{\mathrm{d}\beta}\mathrm{e}^{-\beta H}\right) \tag{B.8}$$

$$= \left(H_0\mathrm{e}^{\beta H_0}\right)\mathrm{e}^{-\beta H} + \mathrm{e}^{\beta H_0}\left(-H\mathrm{e}^{-\beta H}\right) \tag{B.9}$$

$$= \mathrm{e}^{\beta H_0}(H_0 - H)\mathrm{e}^{-\beta H} \tag{B.10}$$

$$= \mathrm{e}^{\beta H_0}(-V)\mathrm{e}^{-\beta H_0}\mathrm{e}^{\beta H_0}\mathrm{e}^{-\beta H} \tag{B.11}$$

$$= -V(\beta)A(\beta). \tag{B.12}$$

In eq. (B.11) the well known time-evolution of an operator in the interaction representation naturally arises as

$$V(\tau) = \mathrm{e}^{H_0\tau}\, V\, \mathrm{e}^{-H_0\tau}. \tag{B.13}$$

We integrate the differential equation

$$\mathrm{d}A(\beta) = -V(\beta)A(\beta)\mathrm{d}\beta \tag{B.14}$$

$$(A(\beta) - A_0) = -\int_0^\beta \mathrm{d}\tau_1 V(\tau_1)A(\tau_1), \tag{B.15}$$

where in (B.15) the differential was relabelled $\mathrm{d}\beta \to \mathrm{d}\tau$, and obtain the integral equation

$$A(\beta) = A_0 - \int_0^\beta \mathrm{d}\tau_1 V(\tau_1)A(\tau_1). \tag{B.16}$$

B.2 Solution by a series expansion

The solution of (B.16) can be found by a series expansion ansatz

$$A(\tau) = \sum_{n=0}^{\infty} A^{(n)}(\tau), \tag{B.17}$$

with zeroth order term $A^0(\tau) = A_0$. Inserting this into (B.16) gives

$$\sum_{n=0}^{\infty} A^{(n)}(\beta) = A_0 + \int_0^\beta \mathrm{d}\tau' V(\tau') \sum_{n=0}^{\infty} A^{(n)}(\tau'). \tag{B.18}$$

One compares the terms of both sides with the same number of $V(\tau)$ and finds the recursion relation for the coefficients of the series to be

$$A^{(n)}(\tau) = \int_0^\tau \mathrm{d}\tau' V(\tau')A^{(n-1)}(\tau'). \tag{B.19}$$

Let us write the first few coefficients of the expansion:

$$A^{(0)}(\beta) = A_0 \tag{B.20}$$
$$A^{(1)}(\beta) = \int_0^\beta \mathrm{d}\tau_1 V(\tau_1) A^{(0)}(\tau_1) \tag{B.21}$$
$$= \int_0^\beta \mathrm{d}\tau_1 V(\tau_1) A_0 \tag{B.22}$$
$$A^{(2)}(\beta) = \int_0^\beta \mathrm{d}\tau_1 V(\tau_1) A^{(1)}(\tau_1) \tag{B.23}$$
$$= \int_0^\beta \mathrm{d}\tau_1 V(\tau_1) \int_0^{\tau_1} \mathrm{d}\tau_2 V(\tau_2) A_0 \tag{B.24}$$
$$A^{(3)}(\beta) = \int_0^\beta \mathrm{d}\tau_1 V(\tau_1) A^{(\tau_2)}(\tau_1) \tag{B.25}$$
$$= \int_0^\beta \mathrm{d}\tau_1 V(\tau_1) \int_0^{\tau_1} \mathrm{d}\tau_2 V(\tau_2) \int_0^{\tau_2} \mathrm{d}\tau_3 V(\tau_3) A_0 \tag{B.26}$$

Note due to the integration boundaries the times are naturally ordered $0 < \tau_1 < \beta$, and $0 < \tau_2 < \tau_1 < \beta$, as well as $0 < \tau_3 < \tau_2 < \tau_1 < \beta$.

The times in the integration measure

$$\iiint_{0<\tau_1<\cdots<\tau_n<\beta} \mathrm{d}\tau_1 \ldots \mathrm{d}\tau_n \tag{B.27}$$

can be relabeled to any permutation of $\{1, \ldots, n\}$

$$\iiint_{0<\tau_{\pi(1)}<\cdots<\tau_{\pi(n)}<\beta} \mathrm{d}\tau_{\pi(1)} \ldots \mathrm{d}\tau_{\pi(n)}. \tag{B.28}$$

In doing so one can sum up all $n!$ combinatorically possible orderings of the times, which corresponds to integrating over the hypercube $\tau_i \in [0, \beta] \ \forall \ i = 1, \ldots, n$, and correcting this by the normalization factor $1/n!$. Since one has to ensure, that the times of the $V(\tau)$ are always time-ordered, the time ordering operator T_τ is introduced

$$\frac{1}{n!} \int_0^\beta \mathrm{d}\tau_1 \cdots \int_0^\beta \mathrm{d}\tau_n \, \mathcal{T}_\tau. \tag{B.29}$$

With this integration measure, the terms of the expansion can be rewritten:

$$A^{(0)}(\beta) = A_0 \tag{B.30}$$
$$A^{(1)}(\beta) = \frac{1}{1!} \int_0^\beta \mathrm{d}\tau_1 \, \mathcal{T}_\tau V(\tau_1) A_0 \tag{B.31}$$
$$A^{(2)}(\beta) = \frac{1}{2!} \int_0^\beta \mathrm{d}\tau_1 \int_0^\beta \mathrm{d}\tau_2 \, \mathcal{T}_\tau [V(\tau_1) V(\tau_2)] A_0 \tag{B.32}$$
$$A^{(3)}(\beta) = \frac{1}{3!} \int_0^\beta \mathrm{d}\tau_1 \int_0^\beta \mathrm{d}\tau_2 \int_0^\beta \mathrm{d}\tau_3 \, \mathcal{T}_\tau [V(\tau_1) V(\tau_2) V(\tau_3)] A_0. \tag{B.33}$$

The introduction of time-ordering made the factorials appear and it possible to identify the expansion coefficients to be those of an exponential. Therefore the auxiliary operator is

$$A(\beta) = A_0 \, \mathcal{T}_\tau \exp\left[- \int_0^\beta \mathrm{d}\tau V(\tau) \right]. \tag{B.34}$$

B.3 Summary and discussion

Insert (B.34) in (B.6) to find the famous Dyson series

$$Z = \mathrm{Tr}\left[\mathrm{e}^{-\beta H}\right] \tag{B.35}$$

$$= \mathrm{Tr}\left[\mathrm{e}^{-\beta H_0}\mathcal{T}_\tau \exp\left[-\int_0^\beta \mathrm{d}\tau V(\tau)\right]\right] \tag{B.36}$$

with a Hamiltonian $H = H_0 + V$. The factor A_0 was dropped, since for physical observables $\langle B\rangle = \frac{1}{Z}\mathrm{Tr}\left[\mathrm{e}^{-\beta H}B\right]$ it cancels any way.

Practically when one wants to use Dyson's equation for a partition, there are two choices:

1. Expand with eq. B.26. The V-operators are time ordered and time integration of each operator is performed from its left to its right neighbour.

2. Expand with eq. B.33. Now each operator is integrated from $[0, \beta]$, which is compensated by a factorial $1/n!$. The time ordering operator brings the V-operators in correct order.

In any case the V-operators always have to be time-ordered,

Appendix C

Grassmann calculus

C.1 General properties

Grassmann variables θ_i anticommute with themselves

$$\theta_i\theta_j + \theta_j\theta_i = 0, \tag{C.1}$$

commute with every (bosonic) observable $\hat{A}$

$$\theta\hat{A} = \hat{A}\theta \tag{C.2}$$

and anticommute with fermionic operators $\hat{\psi}$

$$\theta\hat{\psi} + \hat{\psi}\theta = 0. \tag{C.3}$$

From this follows, that their square is always zero

$$\theta^2 = 0. \tag{C.4}$$

One can define a formal complex conjugation $\theta \leftrightarrow \bar{\theta}$, which has the same properties as complex conjugation of complex matrices and operators

$$\overline{(\lambda\theta_1 + \mu\theta_2)} = \lambda^*\bar{\theta}_1 + \eta^*\bar{\theta}_2 \tag{C.5}$$

$$\overline{\theta_1\theta_2} = \bar{\theta}_2\,\bar{\theta}_1, \tag{C.6}$$

with complex number λ and η. Since later quantum mechanic fermionic operators will be mapped to Grassmann variables ($\bar{\theta}$ to the creators, θ to the annihilators), I employ that Grassmann variables come in conjugated pairs from the beginning on. Then a general function of two variables is

$$f(\bar{\theta}, \theta) = f_0 + f_1\bar{\theta} + \tilde{f}_1\theta + f_2\bar{\theta}\theta \tag{C.7}$$

with complex numbers f_0, f_1, $\tilde{f}_1$ and f_2.

Derivatives are done equivalently to complex numbers, where the derivation-operator anticommutes with Grassmann variables and also with itself

$$\theta_i \frac{\partial}{\partial \theta_j} + \frac{\partial}{\partial \theta_j} \theta_i = \delta_{ij} \tag{C.8}$$

$$\frac{\partial}{\partial \theta_i} \frac{\partial}{\partial \theta_j} + \frac{\partial}{\partial \theta_j} \frac{\partial}{\partial \theta_i} = 0, \tag{C.9}$$

which have to be understood such that they are applied to a function.[1] The derivative of the general function C.7 therefore is

$$\frac{\partial}{\partial \theta} f(\bar{\theta}, \theta) = \tilde{f}_1 - f_2 \bar{\theta} \tag{C.10}$$

$$\frac{\partial}{\partial \bar{\theta}} f(\bar{\theta}, \theta) = f_1 + f_2 \theta. \tag{C.11}$$

An integral has to have the following properties. It must be a linear operation, i.e. $\int \mathrm{d}\theta (f(\theta) + g(\theta)) = \int \mathrm{d}\theta\, f(\theta) + \int \mathrm{d}\theta\, g(\theta)$. It must be translationally invariant $\int \mathrm{d}\theta f(\theta + \theta_0) = \int \mathrm{d}\theta f(\theta)$, and the result of $\int \mathrm{d}\theta f(\theta)$ must not depend on θ any more. The only possible way to define the integration is

$$\int \mathrm{d}\theta\, \theta = 1 \tag{C.12}$$

$$\int \mathrm{d}\theta\, 1 = 0, \tag{C.13}$$

up to a multiplicative constant. This means, for Grassmann numbers integration and differentiation are the same

$$\int \mathrm{d}\theta = \frac{\partial}{\partial \theta}. \tag{C.14}$$

C.2 Change of variables

As a first step let us take a one dimensional function

$$\int \mathrm{d}\theta f(\theta) \tag{C.15}$$

and change the variable via

$$\theta = \theta' A + B. \tag{C.16}$$

We want the transformation to conserve parity, i.e. the result also to be a Grassmann number. For this purpose, A has to be a complex number and B a Grassmann number. Using that integration and differentiation are the same, the substitution gives

[1] $\left(\theta_i \frac{\partial}{\partial \theta_j} + \frac{\partial}{\partial \theta_j} \theta_i\right) f = \theta_i \frac{\partial f}{\partial \theta_j} + \delta_{ij} f - \frac{\partial f}{\partial \theta_j} \theta_i = \delta_{ij} f$

$$\int \mathrm{d}\theta f(\theta) = \frac{\partial}{\partial\theta} f(\theta) \tag{C.17}$$
$$= \frac{\partial\theta'}{\partial\theta}\frac{\partial f}{\partial\theta'} \tag{C.18}$$
$$= \frac{\partial\theta'}{\partial\theta}\int \mathrm{d}\theta' f(\theta(\theta')) \tag{C.19}$$
$$= \left(\frac{\partial\theta}{\partial\theta'}\right)^{-1}\int \mathrm{d}\theta' f(\theta(\theta')). \tag{C.20}$$

The general transformation formula can be derived the same way. I assume the product $\prod_i \frac{\partial}{\partial\theta_i}$ to be ordered.

$$\int \mathrm{d}\theta_1 \dots \mathrm{d}\theta_N f(\boldsymbol{\theta}) = \prod_{i=1}^{N}\frac{\partial}{\partial\theta_i} f(\boldsymbol{\theta}) \tag{C.21}$$
$$= \prod_{i=1}^{N}\frac{\partial}{\partial\theta_i} f(\theta'_1(\theta_1,...,\theta_N),\dots,\theta'_1(\theta_1,...,\theta_N)) \tag{C.22}$$
$$= \prod_{i=1}^{N}\sum_{j=1}^{N}\frac{\partial\theta'_j}{\partial\theta_i}\frac{\partial}{\partial\theta'_j} f(\theta'_1(\theta_1,...,\theta_N),\dots,\theta'_1(\theta_1,...,\theta_N)) \tag{C.23}$$
$$= \sum_{\substack{\text{permutations } \pi \\ \text{of } \{1,\dots,N\}}} \operatorname{sign}(\pi)\prod_{i=1}^{N}\frac{\partial\theta'_i}{\partial\theta_{P_i}}\frac{\partial}{\partial\theta'_i} f \tag{C.24}$$
$$= \det\left(\frac{\partial\theta'_j}{\partial\theta_i}\right)\prod_{k=1}^{N}\frac{\partial}{\partial\theta'_k} f \tag{C.25}$$

Some remarks about the derivation. In (C.22) I write f as a function of the new variables $\boldsymbol{\theta'}$, in order to apply the chain rule in C.23. Each term in the product of derivatives now becomes a sum of N terms. In C.24 this product of sums was multiplied out. The derivatives $\partial\theta'_j/\partial\theta_i$ commute and thus can be ordered as desired (from the restriction C.16 follows, that the derivative of a transformed Grassmann number with respect to a Grassmann number is a complex number). The order of the derivation operators $\frac{\partial}{\partial\theta'_i}$ is important since they anticommute. In order to factorize them out, they must be ordered, which gives a sign according to the permutation P of $\{1,...,N\}$ they appear in. A little reflection shows, that all terms with two derivation operators of the same kind disappear, and each permutation comes exactly once. So ordering them gives the sign of the respective permutation. In C.25 the derivatives and the signs were cast into a determinant, which is the Jacobi determinant. In contrast to complex numbers, where the Jacobi determinant appears, here is a inverse Jacobian.

To clarify the procedure, I will also explicitly show $N = 2$:

$$\int \mathrm{d}\theta_1 \mathrm{d}\theta_2 f(\theta_1,\theta_2) = \frac{\partial}{\partial\theta_1}\frac{\partial}{\partial\theta_2} f(\theta_1,\theta_2) \tag{C.26}$$

$$= \frac{\partial}{\partial\theta_1}\frac{\partial}{\partial\theta_2} f(\theta_1'(\theta_1,\theta_2),\theta_2'(\theta_1,\theta_2)) \tag{C.27}$$

$$= \frac{\partial}{\partial\theta_1}\left(\frac{\partial\theta_1'}{\partial\theta_2}\frac{\partial}{\partial\theta_1'} + \frac{\partial\theta_2'}{\partial\theta_2}\frac{\partial}{\partial\theta_2'}\right) f(\theta_1'(\theta_1,\theta_2),\theta_2'(\theta_1,\theta_2)) \tag{C.28}$$

$$= \left(\frac{\partial\theta_1'}{\partial\theta_1}\frac{\partial}{\partial\theta_1'} + \frac{\partial\theta_2'}{\partial\theta_1}\frac{\partial}{\partial\theta_2'}\right)\left(\frac{\partial\theta_1'}{\partial\theta_2}\frac{\partial}{\partial\theta_1'} + \frac{\partial\theta_2'}{\partial\theta_2}\frac{\partial}{\partial\theta_2'}\right) f(\boldsymbol{\theta'}) \tag{C.29}$$

$$= \left(\frac{\partial\theta_1'}{\partial\theta_1}\frac{\partial}{\partial\theta_1'}\frac{\partial\theta_2'}{\partial\theta_2}\frac{\partial}{\partial\theta_2'} + \frac{\partial\theta_2'}{\partial\theta_1}\frac{\partial}{\partial\theta_2'}\frac{\partial\theta_1'}{\partial\theta_2}\frac{\partial}{\partial\theta_1'}\right) f(\boldsymbol{\theta'}) \tag{C.30}$$

$$= \left(\frac{\partial\theta_1'}{\partial\theta_1}\frac{\partial\theta_2'}{\partial\theta_2} - \frac{\partial\theta_2'}{\partial\theta_1}\frac{\partial\theta_1'}{\partial\theta_2}\right)\frac{\partial}{\partial\theta_1'}\frac{\partial}{\partial\theta_2'} f(\boldsymbol{\theta'}) \tag{C.31}$$

$$= \det\begin{pmatrix} \frac{\partial\theta_1'}{\partial\theta_1} & \frac{\partial\theta_2'}{\partial\theta_1} \\ \frac{\partial\theta_1'}{\partial\theta_2} & \frac{\partial\theta_2'}{\partial\theta_2} \end{pmatrix} \frac{\partial}{\partial\theta_1'}\frac{\partial}{\partial\theta_2'} f(\boldsymbol{\theta'}) \tag{C.32}$$

$$= \det\left(\frac{\partial(\theta_1',\theta_2')}{\partial(\theta_1,\theta_2)}\right)\frac{\partial}{\partial\theta_1'}\frac{\partial}{\partial\theta_2'} f(\boldsymbol{\theta'}) \tag{C.33}$$

This makes it clearer, that the sign comes from reordering the derivation operators. Therefore the transform of the integration variable goes like

$$\prod_i \mathrm{d}\theta_i = \det\left(\frac{\partial\theta_j'}{\partial\theta_i}\right)\prod_k \mathrm{d}\theta_k'. \tag{C.34}$$

C.3 Gaussian integrals and Hubbard Stratonovich transformation

Compared to Gaussian integrals with complex numbers

$$\int \mathrm{d}x\, \mathrm{e}^{-az^2} = \sqrt{\frac{\pi}{a}}, \tag{C.35}$$

Gaussian integrals with Grassmann numbers are easy, since the expansion of the exponential truncates to

$$\int \mathrm{d}\bar\theta \mathrm{d}\theta\, \mathrm{e}^{-a\bar\theta\theta} = \int \mathrm{d}\bar\theta \mathrm{d}\theta \left(1 - a\bar\theta\theta\right) = a. \tag{C.36}$$

C.3.1 Plain Gaussian integral

The generalization to N variables gives

$$\int \prod_{j=1}^{N} \mathrm{d}\bar\theta_j \mathrm{d}\theta_j\, \mathrm{e}^{-\sum_j a_j\bar\theta_j\theta_j} = \prod_{j=1}^{N} a_j. \tag{C.37}$$

Now consider a general Gaussian integral with a matrix $\boldsymbol{M}$ in the exponent. We insert two unity-operators $\mathbb{1} = U^\dagger U$, where U is the matrix that diagonalizes $\boldsymbol{M}$ to the diagonal matrix $\boldsymbol{M'}$.

$$Z(M) = \int \mathrm{d}\theta_1 \mathrm{d}\bar{\theta}_1 \ldots \mathrm{d}\theta_N \mathrm{d}\bar{\theta}_N \exp\left(\sum_{ij=1}^{N} \bar{\theta}_i M_{ij} \theta_j\right) \tag{C.38}$$

$$= \int \mathrm{d}\theta_1 \mathrm{d}\bar{\theta}_1 \ldots \mathrm{d}\theta_N \mathrm{d}\bar{\theta}_N \exp\left(\sum_{ijklmn=1}^{N} \bar{\theta}_i U^{\dagger}_{ij} U_{jk} M_{kl} U^{\dagger}_{lm} U_{mn} \theta_n\right) \tag{C.39}$$

This defines the transformation of variables to go to the diagonal basis of $\boldsymbol{M}$; the Jacobian is one, since the transformation is unitary.

$$\bar{\theta}'_j = \sum_i \bar{\theta}_i U^{\dagger}_{ij} \tag{C.40}$$

$$M'_{jm} = \sum_{kl} U_{jk} M_{kl} U^{\dagger}_{lm} \tag{C.41}$$

$$\theta'_m = \sum_n U_{mn} \theta_n \tag{C.42}$$

The result is

$$Z(M) = \int \mathrm{d}\theta_1 \mathrm{d}\bar{\theta}_1 \ldots \mathrm{d}\theta_N \mathrm{d}\bar{\theta}_N \exp\left(\sum_{jm=1}^{N} \bar{\theta}'_j M'_{jm} \theta'_m\right) \tag{C.43}$$

$$= \prod_i M'_{ii} \tag{C.44}$$

$$= \det \boldsymbol{M}. \tag{C.45}$$

C.3.2 Gaussian integral with source terms

Now let's consider the generalized Gaussian integral with source terms η and $\bar{\eta}$

$$Z_G(\boldsymbol{M}, \boldsymbol{\eta}, \bar{\boldsymbol{\eta}}) = \int \mathrm{d}\theta_1 \mathrm{d}\bar{\theta}_1 \ldots \mathrm{d}\theta_N \mathrm{d}\bar{\theta}_N \exp\Big[E_{\mathrm{G}}\Big[\boldsymbol{M}, \bar{\eta}, \eta, \bar{\theta}, \theta\Big]\Big] \tag{C.46}$$

$$= \int \mathrm{d}\theta_1 \mathrm{d}\bar{\theta}_1 \ldots \mathrm{d}\theta_N \mathrm{d}\bar{\theta}_N \exp\left[\sum_{ij=1}^{N} \bar{\theta}_i M_{ij} \theta_j + \sum_i \left(\bar{\eta}_i \theta_i + \bar{\theta}_i \eta_i\right)\right]. \tag{C.47}$$

We need to find the change of variables θ and $\bar{\theta}$, that maps this integral on the one in the previous paragraph. For this purpose define the inverse of the matrix $M^{-1} = \Delta$ with $\sum_j M_{ij}\Delta_{jk} = \delta_{ik}$, and determine the maxima of the argument E_G of the exponential in C.47.

$$\frac{\partial E_G}{\partial \theta_j} = 0 \tag{C.48}$$

$$-\sum_i \bar{\theta}_i M_{ij} - \bar{\eta}_j = 0 \tag{C.49}$$

$$-\sum_{ij} \bar{\theta}_i M_{ij} \Delta_{jk} - \sum_j \bar{\eta}_j \Delta_{jk} = 0 \tag{C.50}$$

$$\bar{\theta}_k = -\sum_j \bar{\eta}_j \Delta_{jk} \tag{C.51}$$

And the other one:

$$\frac{\partial E_G}{\partial \bar{\theta}_i} = 0 \tag{C.52}$$

$$\sum_j M_{ij}\theta_j + \eta_i = 0 \tag{C.53}$$

$$\sum_{ij} \Delta_{ki} M_{ij} \theta_j - \sum_i \Delta_{ki}\eta_i = 0 \tag{C.54}$$

$$\theta_k = -\sum_i \Delta_{ki}\eta_i \tag{C.55}$$

The transformed exponent becomes (indices suppressed)

$$E'_G = \bar{\theta} M \theta + \bar{\eta}\theta + \bar{\theta}\eta \tag{C.56}$$

$$= (\bar{\theta}' - \bar{\eta}\Delta) M (\theta' - \Delta\eta) + \eta(\theta' - \Delta\eta) + (\bar{\theta}' - \bar{\eta}\Delta)\eta \tag{C.57}$$

$$= \theta' M \bar{\theta}' - \bar{\theta}' M \Delta\eta - \bar{\eta}\Delta M \theta' + \bar{\eta}\Delta M \Delta\eta \tag{C.58}$$

$$+ \bar{\eta}\theta' - \bar{\eta}\Delta\eta + \bar{\theta}'\eta - \bar{\eta}\Delta\eta \tag{C.59}$$

$$= \theta' M \bar{\theta}' - \bar{\eta}\Delta\eta \tag{C.60}$$

Therefore the generalized integral is

$$Z_G(\boldsymbol{M}, \boldsymbol{\eta}, \bar{\boldsymbol{\eta}}) = \int \mathrm{d}\theta_1 \mathrm{d}\bar{\theta}_1 \ldots \mathrm{d}\theta_N \mathrm{d}\bar{\theta}_N \, \exp\left(\sum_{ij=1}^{N} \bar{\theta}_i M_{ij} \theta_j + \sum_i \left(\bar{\eta}_i \theta_i + \bar{\theta}_i \eta_i \right) \right) \tag{C.61}$$

$$= \int \mathrm{d}\theta'_1 \mathrm{d}\bar{\theta}'_1 \ldots \mathrm{d}\theta'_N \mathrm{d}\bar{\theta}'_N \, \exp\left(\sum_{ij=1}^{N} \bar{\theta}'_i M_{ij} \theta'_j - \sum_{ij} \bar{\eta}_i \Delta_{ij} \eta_j \right) \tag{C.62}$$

$$= \det \boldsymbol{M} \, \exp\left(- \sum_{ij} \bar{\eta}_i \Delta_{ij} \eta_j \right), \tag{C.63}$$

using result C.45 from the last subsection.

C.3.3 Gaussian expectation values - two point function

Now we calculate the expectation value of two Grassmann variables

$$\left\langle \bar{\theta}_a \theta_b \right\rangle = \int \mathrm{d}\bar{\theta}_1 \mathrm{d}\theta_1 \ldots \mathrm{d}\bar{\theta}_N \mathrm{d}\theta_N \; \bar{\theta}_a \theta_b \, \exp\left(\sum_{ij=1}^{N} \bar{\theta}_i M_{ij} \theta_i \right) \tag{C.64}$$

with a Gaussian weight. The restrictions $1 \leq a \leq N$ and $1 \leq b \leq N$ must be satisfied. We start from eq. C.61 and generate $\bar{\theta}_a \theta_b$ by deriving with respect to the corresponding source terms.

$$\frac{\partial}{\partial\bar{\eta}_b}\frac{\partial}{\partial\eta_a}Z_{\mathrm{G}}(\boldsymbol{M},\bar{\boldsymbol{\eta}},\boldsymbol{\eta})|_{\bar{\boldsymbol{\eta}}=\boldsymbol{\eta}=0} \tag{C.65}$$

$$= \int \mathrm{d}\theta_1\mathrm{d}\bar{\theta}_1\ldots\mathrm{d}\theta_N\mathrm{d}\bar{\theta}_N\ \frac{\partial}{\partial\bar{\eta}_b}\Big(-\bar{\theta}_a\Big)\exp\left(\sum_{ij=1}^{N}\bar{\theta}_i M_{ij}\theta_j+\sum_i\Big(\bar{\eta}_i\theta_i+\bar{\theta}_i\eta_i\Big)\right)|_{\bar{\boldsymbol{\eta}}=\boldsymbol{\eta}=0}$$

$$= \int \mathrm{d}\theta_1\mathrm{d}\bar{\theta}_1\ldots\mathrm{d}\theta_N\mathrm{d}\bar{\theta}_N\ \bar{\theta}_a\frac{\partial}{\partial\bar{\eta}_b}\exp\left(\sum_{ij=1}^{N}\bar{\theta}_i M_{ij}\theta_j+\sum_i\Big(\bar{\eta}_i\theta_i+\bar{\theta}_i\eta_i\Big)\right)|_{\bar{\boldsymbol{\eta}}=\boldsymbol{\eta}=0}$$

$$= \int \mathrm{d}\theta_1\mathrm{d}\bar{\theta}_1\ldots\mathrm{d}\theta_N\mathrm{d}\bar{\theta}_N\ \bar{\theta}_a\theta_b\exp\left(\sum_{ij=1}^{N}\bar{\theta}_i M_{ij}\theta_j+\sum_i\Big(\bar{\eta}_i\theta_i+\bar{\theta}_i\eta_i\Big)\right)|_{\bar{\boldsymbol{\eta}}=\boldsymbol{\eta}=0}$$

$$= \int \mathrm{d}\theta_1\mathrm{d}\bar{\theta}_1\ldots\mathrm{d}\theta_N\mathrm{d}\bar{\theta}_N\ \bar{\theta}_a\theta_b\exp\left(\sum_{ij=1}^{N}\bar{\theta}_i M_{ij}\theta_j\right) \tag{C.66}$$

$$= \langle\bar{\theta}_a\theta_b\rangle\det\boldsymbol{M} \tag{C.67}$$

Since we already know the value of $Z_{\mathrm{G}}(\boldsymbol{M},\bar{\boldsymbol{\eta}},\boldsymbol{\eta})$ to be C.63, we can evaluate its derivative an alternative way:

$$\frac{\partial}{\partial\bar{\eta}_b}\frac{\partial}{\partial\eta_a}Z_{\mathrm{G}}(\boldsymbol{M},\bar{\boldsymbol{\eta}},\boldsymbol{\eta})|_{\bar{\boldsymbol{\eta}}=\boldsymbol{\eta}=0}=\frac{\partial}{\partial\bar{\eta}_b}\frac{\partial}{\partial\eta_a}\det\boldsymbol{M}\exp\left[-\sum_{ij}\bar{\eta}_i\Delta_{ij}\eta_j\right]|_{\bar{\boldsymbol{\eta}}=\boldsymbol{\eta}=0} \tag{C.68}$$

$$=\det\boldsymbol{M}\ \frac{\partial}{\partial\bar{\eta}_b}\sum_i\bar{\eta}_i\Delta_{ia}\exp\left[-\sum_{ij}\bar{\eta}_i\Delta_{ij}\eta_j\right]|_{\bar{\boldsymbol{\eta}}=\boldsymbol{\eta}=0} \tag{C.69}$$

$$=\det\boldsymbol{M}\ \left(\Delta_{ba}+\sum_j\Delta_{bj}\eta_j\right)\exp\left[-\sum_{ij}\bar{\eta}_i\Delta_{ij}\eta_j\right]|_{\bar{\boldsymbol{\eta}}=\boldsymbol{\eta}=0} \tag{C.70}$$

$$=\det\boldsymbol{M}\ \Delta_{ba} \tag{C.71}$$

Comparing the results of the two calculations gives simply

$$\Big\langle\bar{\theta}_a\theta_b\Big\rangle=\Delta_{ba}. \tag{C.72}$$

Note that the indices are exchanged, since in the source terms the conjugated θ appears with the unconjugated η, and vice versa.

C.3.4 Gaussian expectation values - Wick's theorem

A general expectation value of Grassmann numbers with Gaussian weight gives Wick's theorem

$$\Big\langle\bar{\theta}_{i_1}\theta_{j_1}\ldots\bar{\theta}_{i_P}\theta_{j_P}\Big\rangle=\frac{\partial}{\partial\bar{\eta}_{j_1}}\frac{\partial}{\partial\eta_{i_1}}\cdots\frac{\partial}{\partial\bar{\eta}_{j_P}}\frac{\partial}{\partial\eta_{i_P}}\exp\left(-\sum_{ij=1}^{N}\bar{\eta}_j\Delta_{ji}\eta_i\right) \tag{C.73}$$

$$=\sum_{\substack{\text{permutations }\pi\\ \text{of }\{1,\ldots,N\}}}\operatorname{sign}(\pi)\Delta_{\pi(i_1)i_1}\Delta_{\pi(i_2)i_2}\ldots\Delta_{\pi(i_P)i_P} \tag{C.74}$$

$$=\sum_{\substack{\text{permutations }\pi\\ \text{of }\{1,\ldots,N\}}}\operatorname{sign}(\pi)\Big\langle\bar{\theta}_{i_1}\theta_{\pi(i_1)}\Big\rangle\Big\langle\bar{\theta}_{i_2}\theta_{\pi(i_2)}\Big\rangle\ldots\Big\langle\bar{\theta}_{i_P}\theta_{\pi(i_P)}\Big\rangle. \tag{C.75}$$

Again $P \leq N$ must hold. It states, that the expectation value of a product of $2P$ Grassmann numbers equals the product of all combinatorically possible 2-operator expectation values, plus the sign that stems from shifting the operators to their according partners.

C.4 Coherent states with Grassmann numbers

A fermionic coherent state is defined as

$$|c\rangle = \mathrm{e}^{\hat{c}^\dagger c} |0\rangle \tag{C.76}$$
$$\langle \bar{c}| = \langle 0| \mathrm{e}^{\bar{c}\hat{c}}, \tag{C.77}$$

with operators $\hat{c}^\dagger$ and $\hat{c}$, and Grassmann numbers c and $\bar{c}$. Their order is important, since they anticommute. Due to $cc = 0$ and $\bar{c}\bar{c} = 0$, the expansions of the exponentials are truncated

$$|c\rangle = (1 + \hat{c}^\dagger c) |0\rangle \tag{C.78}$$
$$= |0\rangle + |1\rangle c \tag{C.79}$$
$$\langle \bar{c}| = \langle 0| (1 + \bar{c}\hat{c}) \tag{C.80}$$
$$= \langle 0| + \bar{c} \langle 1| . \tag{C.81}$$

Fermionic coherent states seem not to be eigenstates of the creation and annihilation operators, because they have finite sums, but indeed they are:

$$\hat{c} |c\rangle = \hat{c}(1 + \hat{c}^\dagger c) |0\rangle \tag{C.82}$$
$$= c |0\rangle \tag{C.83}$$
$$= c(1 + \hat{c}^\dagger c) |0\rangle \tag{C.84}$$
$$= c |c\rangle . \tag{C.85}$$

Analogously

$$\langle c| \hat{c}^\dagger = \bar{c}\bar{c} \tag{C.86}$$

holds. The overlap between a coherent state and a state in occupation number basis is

$$\langle n|c\rangle = \langle n| (|0\rangle + |1\rangle c) \tag{C.87}$$
$$= \begin{cases} \langle 0|0\rangle = 1 & \text{for } n = 0 \\ \langle 1|1\rangle c = c & \text{for } n = 1 \end{cases} \tag{C.88}$$
$$= c^n, \tag{C.89}$$

as well as

$$\langle \bar{c}|m\rangle = (\langle 0| + \bar{c} \langle 1|) |m\rangle \tag{C.90}$$
$$= \bar{c}^m \tag{C.91}$$

The basis of coherent Grassmann states is overcomplete

$$\langle \bar{c}|c\rangle = (\langle 0| + \bar{c}\,\langle 1|)(|0\rangle + |1\rangle\, c) \tag{C.92}$$
$$= 1 + \bar{c}c = \mathrm{e}^{\bar{c}c} \tag{C.93}$$

A representation of the Kronecker delta is

$$\delta_{nm} = \int \mathrm{d}\bar{c}\mathrm{d}c\, \mathrm{e}^{-\bar{c}c} c^n \bar{c}^m. \tag{C.94}$$

Proof.

$$\int \mathrm{d}\bar{c}\mathrm{d}c\, \mathrm{e}^{-\bar{c}c} c^n \bar{c}^m = \int \mathrm{d}\bar{c}\mathrm{d}c\, (1-\bar{c}c) c^n \bar{c}^m \tag{C.95}$$
$$= \int \mathrm{d}\bar{c}\mathrm{d}c\, (c^n \bar{c}^m - \bar{c}c c^n \bar{c}^m) \tag{C.96}$$
$$= \begin{cases} \int \mathrm{d}\bar{c}\mathrm{d}c\, (1-\bar{c}c) = 1 & n=0, m=0 \\ \int \mathrm{d}\bar{c}\mathrm{d}c\, (\bar{c} - \bar{c}c\bar{c}) = 0 & n=0, m=1 \\ \int \mathrm{d}\bar{c}\mathrm{d}c\, (c - \bar{c}cc) = 0 & n=1, m=0 \\ \int \mathrm{d}\bar{c}\mathrm{d}c\, (c\bar{c} - \bar{c}cc\bar{c}) = 1 & n=1, m=1 \end{cases} \tag{C.97}$$
$$= \delta_{nm} \tag{C.98}$$

□

Now rewrite the desired expression using the overlaps between occupation number and coherent states C.89 and C.91

$$\int \mathrm{d}\bar{c}\mathrm{d}c\, \mathrm{e}^{-\bar{c}c} c^n \bar{c}^m = \int \mathrm{d}\bar{c}\mathrm{d}c\, \mathrm{e}^{-\bar{c}c} \langle n|c\rangle \langle \bar{c}|m\rangle \tag{C.99}$$
$$= \langle n| \int \mathrm{d}\bar{c}\mathrm{d}c\, \mathrm{e}^{-\bar{c}c} |c\rangle \langle \bar{c}|\, |m\rangle \tag{C.100}$$
$$= \delta_{nm} \tag{C.101}$$

to find the desired result

$$\Rightarrow \mathbb{1} = \int \mathrm{d}\bar{c}\mathrm{d}c\, \mathrm{e}^{-\bar{c}c} |c\rangle \langle \bar{c}| \tag{C.102}$$
$$= \sum_{c\bar{c}} |c\rangle \langle \bar{c}|\,, \tag{C.103}$$

where in the last line a shorthand notation $\sum_{c\bar{c}} \equiv \int \mathrm{d}\bar{c}\mathrm{d}c\, \mathrm{e}^{-\bar{c}c}$ was introduced.

From the structure of C.97 can be seen, that if one wants to exchange the order of $c^n\bar{c}^m \to \bar{c}^m c^n$, one of the Grassmann numbers must receive a minus sign. The only significant change in C.97 will be, that in the fourth line the order of the single $c\bar{c}$ will change; this will generate an additional sign by the integration, which has to be compensated by a minus sign in either c^n or $\bar{c}^m$. Therefore two further representations of the Konecker delta are

$$\delta_{nm} = \int \mathrm{d}\bar{c}\mathrm{d}c\, \mathrm{e}^{-\bar{c}c} (-\bar{c})^m c^n \tag{C.104}$$
$$= \int \mathrm{d}\bar{c}\mathrm{d}c\, \mathrm{e}^{-\bar{c}c} \langle -\bar{c}|m\rangle \langle n|c\rangle \tag{C.105}$$

or

$$\delta_{nm} = \int \mathrm{d}\bar{c}\mathrm{d}c\, \mathrm{e}^{-\bar{c}c}\bar{c}^m(-c)^n \tag{C.106}$$

$$= \int \mathrm{d}\bar{c}\mathrm{d}c\, \mathrm{e}^{-\bar{c}c}\, \langle \bar{c}|m\rangle\, \langle n|-c\rangle \tag{C.107}$$

respectively.

A trace in the basis of Grassmann coherent states is performed like

$$\mathrm{Tr}[A] = \sum_{\bar{c}c} \langle -\bar{c}|\, \hat{A}\, |c\rangle. \tag{C.108}$$

Proof. With this formula we change the basis of the well-known formula for the trace. We start with the well-known formula for the trace and insert the alternative representation C.105 of the delta function, which gives

$$\mathrm{Tr}[A] = \sum_{mn} \langle m|\, \hat{A}\, |n\rangle\, \delta_{nm} \tag{C.109}$$

$$= \sum_{mn} \langle m|\, \hat{A}\, |n\rangle \int \mathrm{d}\bar{c}\mathrm{d}c\, \mathrm{e}^{-\bar{c}c}\, \langle -\bar{c}|m\rangle\, \langle n|c\rangle \tag{C.110}$$

$$= \sum_{mn} \int \mathrm{d}\bar{c}\mathrm{d}c\, \mathrm{e}^{-\bar{c}c}\, \langle -\bar{c}|m\rangle\, \langle m|\, \hat{A}\, |n\rangle\, \langle n|c\rangle \tag{C.111}$$

$$= \int \mathrm{d}\bar{c}\mathrm{d}c\, \mathrm{e}^{-\bar{c}c}\, \langle -\bar{c}|\, \hat{A}\, |c\rangle \tag{C.112}$$

$$= \sum_{\bar{c}c} \langle -\bar{c}|\, \hat{A}\, |c\rangle \tag{C.113}$$

□

Matrix elements of normal ordered operators (all the creators to the left, all the annihilators to the right) are given by replacing the operators with the corresponding Grassmann numbers:

$$\langle \bar{c}|\, \hat{A}\Big[c^\dagger, c\Big]\, |c\rangle = \langle \bar{c}|c\rangle\, A[\bar{c}, c] \tag{C.114}$$

$$= \mathrm{e}^{\bar{c}c} A[\bar{c}, c] \tag{C.115}$$

C.5 The path integral

Now all ingredients are prepared to write the path integral of the partition function

$$Z = \mathrm{Tr}\Big[\mathrm{e}^{-\beta\hat{H}}\Big] \tag{C.116}$$

$$= \int \mathrm{d}\bar{c}\mathrm{d}c\, \mathrm{e}^{-\bar{c}c}\, \langle -\bar{c}|\, \mathrm{e}^{-\beta\hat{H}}\, |c\rangle \tag{C.117}$$

$$= -\int \mathrm{d}\bar{c}\mathrm{d}c\, \mathrm{e}^{\bar{c}c}\, \langle \bar{c}|\, \mathrm{e}^{-\beta\hat{H}}\, |c\rangle\,, \tag{C.118}$$

where in the last line a substitution $\bar{c} \to -\bar{c}$ was done. The exponential is divided into N slices

$$\mathrm{e}^{-\beta\hat{H}} \to \left(\mathrm{e}^{-\Delta\tau\hat{H}}\right)^N \tag{C.119}$$

of width $\Delta\tau = \beta/N$. This is an approximation for finite N, but becomes exact again in the limit of $N \to \infty$. In between the slices a $\mathbb{1}_j = \int \mathrm{d}\bar{c}_j \mathrm{d}c_j \, \mathrm{e}^{-\bar{c}_j c_j} \, |c_j\rangle \langle \bar{c}_j|$ is inserted.

$$Z_N = -\int \mathrm{d}\bar{c}_N \mathrm{d}c_0 \, \mathrm{e}^{\bar{c}_N c_0} \, \langle \bar{c}_N | \tag{C.120}$$

$$\mathrm{e}^{-\Delta\tau \hat{H}} \underbrace{\int \mathrm{d}\bar{c}_{N-1} \mathrm{d}c_{N-1} \, \mathrm{e}^{-\bar{c}_{N-1} c_{N-1}} \, |c_{N-1}\rangle \langle \bar{c}_{N-1}|}_{\mathbb{1}_{N-1}} \tag{C.121}$$

$$\mathrm{e}^{-\Delta\tau \hat{H}} \underbrace{\int \mathrm{d}\bar{c}_{N-2} \mathrm{d}c_{N-2} \, \mathrm{e}^{-\bar{c}_{N-2} c_{N-2}} \, |c_{N-2}\rangle \langle \bar{c}_{N-2}|}_{\mathbb{1}_{N-2}} \tag{C.122}$$

$$\mathrm{e}^{-\Delta\tau \hat{H}} \underbrace{\int \mathrm{d}\bar{c}_{N-3} \mathrm{d}c_{N-3} \, \mathrm{e}^{-\bar{c}_{N-3} c_{N-3}} \, |c_{N-3}\rangle \langle \bar{c}_{N-3}|}_{\mathbb{1}_{N-3}} \tag{C.123}$$

$$\dots \tag{C.124}$$

$$\mathrm{e}^{-\Delta\tau \hat{H}} \underbrace{\int \mathrm{d}\bar{c}_1 \mathrm{d}c_1 \, \mathrm{e}^{-\bar{c}_1 c_1} \, |c_1\rangle \langle \bar{c}_1|}_{\mathbb{1}_1} \tag{C.125}$$

$$\mathrm{e}^{-\Delta\tau \hat{H}} \, |c_0\rangle \tag{C.126}$$

By imposing antiperiodic boundary conditions, i.e. by setting $c_0 = -c_N$, the Nth time slice equals the 0th time slice

$$-\int \mathrm{d}\bar{c}_N \mathrm{d}c_0 \, \mathrm{e}^{\bar{c}_N c_0} \, \langle \bar{c}_N | \dots | c_0 \rangle = \int \mathrm{d}\bar{c}_N \mathrm{d}c_N \, \mathrm{e}^{-\bar{c}_N c_N} \, \langle \bar{c}_N | \dots | c_0 \rangle \tag{C.127}$$

and the full object can compactly be written as

$$Z_N = \int \prod_{j=1}^{N} \mathrm{d}\bar{c}_j \mathrm{d}c_j \, \mathrm{e}^{-\bar{c}_j c_j} \, \langle \bar{c}_j | \, \mathrm{e}^{-\Delta\tau \hat{H}} \, |c_{j-1}\rangle \, . \tag{C.128}$$

The matrix elements evaluate to

$$\langle \bar{c}_j | \, \mathrm{e}^{-\Delta\tau \hat{H}} \, |c_{j-1}\rangle = \mathrm{e}^{\bar{c}_j c_{j-1}} \mathrm{e}^{-\Delta\tau H[\bar{c}_j, c_{j-1}]} + \mathcal{O}\Big((\Delta\tau)^2\Big) \tag{C.129}$$

in leading order. To obtain the path-integral, which is an exact representation of quantum mechanics, we can now take the limit $N \to \infty$:

$$Z = \lim_{N\to\infty} Z_N \tag{C.130}$$

$$= \lim_{N\to\infty} \int \left(\prod_{j=1}^{N} \mathrm{d}\bar{c}_j \mathrm{d}c_j \right) \exp\left[\sum_{j=1}^{N} -\bar{c}_j c_j + \bar{c}_j c_{j-1} - \Delta\tau H[\bar{c}_j, c_{j-1}] \right] \tag{C.131}$$

$$= \lim_{N\to\infty} \int \left(\prod_{j=1}^{N} \mathrm{d}\bar{c}_j \mathrm{d}c_j \right) \exp\left[-\sum_{j=1}^{N} \Delta\tau \left(\frac{\bar{c}_j (c_j - c_{j-1})}{\Delta\tau} + H[\bar{c}_j, c_{j-1}] \right) \right] \tag{C.132}$$

$$= \int \mathcal{D}\bar{c}\mathcal{D}c \exp\left[-\int_0^\beta \mathrm{d}\tau \, \left(\bar{c}\partial_\tau c + H[\bar{c}, c] \right) \right] \tag{C.133}$$

$$= \int \mathcal{D}\bar{c}\mathcal{D}c \exp[-S[\bar{c}, c]] \tag{C.134}$$

with the action

$$S[\bar{c}, c] = \int_0^\beta \mathrm{d}\tau \; (\bar{c}\partial_\tau c + H[\bar{c}, c]) \tag{C.135}$$

and an abbreviation for the integrals

$$\int \mathcal{D}\bar{c}\mathcal{D}c \equiv \lim_{N\to\infty} \int \left(\prod_{j=1}^{N} \mathrm{d}\bar{c}_j \mathrm{d}c_j \right) \tag{C.136}$$

The boundary conditions for the continuum version of C.127

$$c(\tau) = -c(\tau + \beta) \tag{C.137}$$
$$\bar{c}(\tau) = -\bar{c}(\tau + \beta) \tag{C.138}$$

encode the well known antiperiodicity of fermionic Greens functions.

C.6 From imaginary time to Matsubara

We look at the action

$$S[\bar{c}, c] = \int_0^\beta \mathrm{d}\tau \; \bar{c}(\tau)[\partial_\tau - \mu]c(\tau) \tag{C.139}$$

and write the operators in Fourier representation

$$c(\tau) = \frac{1}{\sqrt{\beta}} \sum_n c(i\omega_n) \mathrm{e}^{-i\omega_n \tau} \tag{C.140}$$
$$\bar{c}(\tau) = \frac{1}{\sqrt{\beta}} \sum_n \bar{c}(i\omega_n) \mathrm{e}^{i\omega_n \tau}. \tag{C.141}$$

One finds

$$\frac{1}{\beta} \int_0^\beta \mathrm{d}\tau \sum_n \bar{c}(i\omega_n) \mathrm{e}^{i\omega_n \tau} [\partial_\tau - \mu] \sum_m c(i\omega_m) \mathrm{e}^{-i\omega_m \tau} \tag{C.142}$$
$$= \frac{1}{\beta} \int_0^\beta \mathrm{d}\tau \sum_n \bar{c}(i\omega_n) \mathrm{e}^{i\omega_n \tau} \sum_m [-i\omega_m - \mu] c(i\omega_m) \mathrm{e}^{-i\omega_m \tau} \tag{C.143}$$
$$= \frac{1}{\beta} \int_0^\beta \mathrm{d}\tau \sum_{nm} \bar{c}(i\omega_n) [-i\omega_m - \mu] c(i\omega_m) \mathrm{e}^{-i(\omega_n - \omega_m)\tau} \tag{C.144}$$
$$= \sum_{nm} \bar{c}(i\omega_n) [-i\omega_m - \mu] c(i\omega_m) \delta_{nm} \tag{C.145}$$
$$= \sum_n \bar{c}(i\omega_n) [-i\omega_n - \mu] c(i\omega_n) \tag{C.146}$$

The integral over τ evaluates to a Kronecker delta[2]. The integration measure does not change, since the Fourier transform is unitary. Therefore

[2] $\int_0^\beta \mathrm{d}\tau \, \exp[i(\omega_n - \omega_m)\tau] = \int_0^\beta \mathrm{d}\tau \, \exp\left[i(\frac{\pi}{\beta}(2n+1) - \frac{\pi}{\beta}(2m+1))\tau\right]$
$= \int_0^\beta \mathrm{d}\tau \, \exp\left[i\frac{2\pi}{\beta}(n-m)\tau\right] = \frac{\beta}{2\pi i(n-m)} \left[\exp\left[i\frac{2\pi}{\beta}(n-m)\tau\right]\right]_0^\beta$
$= \frac{\beta}{2\pi i(n-m)} (\exp[i2\pi(n-m)] - 1) = \begin{cases} \lim_{\phi\to 0} \frac{\beta}{2\pi i\phi}(1 + i2\pi\phi - 1) = \beta, & n = m \\ 0, & n \neq m \end{cases}$

$$Z = \int \mathcal{D}\bar{c}\,\mathcal{D}c\,\exp[-S[\bar{c},c]] \tag{C.147}$$

with the action

$$S[\bar{c},c] = \sum_n \bar{c}(i\omega_n)[-i\omega_n - \mu]c(i\omega_n) \tag{C.148}$$

C.7 From Matsubara to imaginary time

The Matsubara object

$$S_{\mathrm{hyb}}[\bar{\boldsymbol{c}},\boldsymbol{c}] = \sum_n \bar{c}(i\omega_n)[-i\omega_n + \epsilon_p]^{-1}c(i\omega_n), \tag{C.149}$$

wants to be Fourier transformed to imaginary time. For this purpose its Matsubara operators are written in Fourier representation

$$\bar{c}(i\omega_n) = \frac{1}{\sqrt{\beta}}\int_0^\beta \mathrm{d}\tau\,\bar{c}(\tau)\mathrm{e}^{-i\omega_n\tau} \tag{C.150}$$

$$c(i\omega_n) = \frac{1}{\sqrt{\beta}}\int_0^\beta \mathrm{d}\tau\,c(\tau)\mathrm{e}^{i\omega_n\tau}, \tag{C.151}$$

which gives

$$S_{\mathrm{hyb}}[\bar{\boldsymbol{c}},\boldsymbol{c}] = \frac{1}{\beta}\sum_n \int_0^\beta \mathrm{d}\tau \int_0^\beta \mathrm{d}\tau'\bar{c}(\tau)c(\tau')\mathrm{e}^{i\omega_n(\tau-\tau')}[-i\omega_n + \epsilon_p]^{-1}. \tag{C.152}$$

In order to perform the sum over all Matsubara frequencies, object (C.152) is continued to the complex plane, multiplied with the Fermi function, which has it poles with residues of $-1/\beta$ at the fermionic Matsubara frequencies. Using the theorem of residues, the sum of all residues equals zero (since the objects decays to zero for $z \to \infty$ fast enough). From this can be deduced, that the Matsubara sum equals the residue of this object

$$S_{\mathrm{hyb}}[\bar{\boldsymbol{c}},\boldsymbol{c}] = \mathrm{Res}_{z\to\epsilon_p}\left[\frac{1}{\beta}\int_0^\beta \mathrm{d}\tau \int_0^\beta \mathrm{d}\tau'\bar{c}(\tau)c(\tau')\mathrm{e}^{z(\tau-\tau')}[-z+\epsilon_p]^{-1}\frac{1}{\mathrm{e}^{\beta z}+1}\right]\cdot(-\beta) \tag{C.153}$$

$$= -\lim_{z\to\epsilon_p}(z-\epsilon_p)\left[\int_0^\beta \mathrm{d}\tau \int_0^\beta \mathrm{d}\tau'\bar{c}(\tau)c(\tau')\mathrm{e}^{z(\tau-\tau')}[-z+\epsilon_p]^{-1}\frac{1}{\mathrm{e}^{\beta z}+1}\right] \tag{C.154}$$

$$= \int_0^\beta \mathrm{d}\tau \int_0^\beta \mathrm{d}\tau'\bar{c}(\tau)c(\tau')\mathrm{e}^{\epsilon_p(\tau-\tau')}\frac{1}{\mathrm{e}^{\beta\epsilon_p}+1} \tag{C.155}$$

at $z = \epsilon_p$ multiplied with $-\beta$.

Publications

- **A Hausoel**, M. Karolak, E. Sasioglu, A. Lichtenstein, K. Held, A. Katanin, A. Toschi, G. Sangiovanni, Local magnetic moments in iron and nickel at ambient and Earth's core conditions, Nat Commun **8**, 16062 (2017).
- M. Wallerberger, **A. Hausoel**, P. Gunacker, A. Kowalski, N. Parragh, F. Goth, K. Held, G. Sangiovanni, w2dynamics: Local one-and two-particle quantities from dynamical mean field theory, Computer Physics Communications, 235:388 - 399.
- P. Gunacker, M. Wallerberger, E. Gull, **A. Hausoel**, G. Sangiovanni, K. Held, Continuous-time quantum Monte Carlo using worm sampling, Phys. Rev. B **92**, 155102 (2015).
- P. Gunacker, M. Wallerberger, T. Ribic, **A. Hausoel**, G. Sangiovanni, K. Held, Worm-improved estimators in continuous-time quantum Monte Carlo, Phys. Rev. B **94**, 125153 (2016).
- D. Geffroy, J. Kaufmann, A. Hariki, P. Gunacker, **A. Hausoel**, J. Kunes, Collective modes in excitonic magnets: Dynamical mean-field study, Phys. Rev. Lett. **122**, 127601 (2019).
- D. Di Sante, **A. Hausoel**, P. Barone, J. M Tomczak, G. Sangiovanni, R. Thomale, Realizing double Dirac particles in the presence of electronic interactions, Phys. Rev. B **96**, 121106(R) (2017).
- A. Hariki, **A. Hausoel**, G. Sangiovanni, J. Kuneš, DFT+ DMFT study on soft moment magnetism and covalent bonding in $SrRu_2O_6$, Phys. Rev. B **96**, 155135 (2017).
- A. Kowalski, **A. Hausoel**, M. Wallerberger, P. Gunacker, G. Sangiovanni, State and superstate sampling in hybridization-expansion continuous-time quantum Monte Carlo, Phys. Rev. B **99**, 155112 (2019).

Bibliography

Abrikosov, A. A., Gorkov, L. P., and Dzyaloshinski, I. E. (2012). *Methods of quantum field theory in statistical physics*. Courier Corporation.

Anderson, P. W. (1972). More is different. *Science*, 177(4047):393–396.

Antipov, A. E. and Krivenko, I. (2015). pomerol: 1.1.

Anzellini, S., Dewaele, A., Mezouar, M., Loubeyre, P., and Morard, G. (2013). Melting of iron at earth's inner core boundary based on fast x-ray diffraction. *Science*, 340(6131):464–466.

Arute, F., Arya, K., Babbush, R., Bacon, D., Bardin, J. C., Barends, R., Biswas, R., Boixo, S., Brandao, F. G., Buell, D. A., et al. (2019). Quantum supremacy using a programmable superconducting processor. *Nature*, 574(7779):505–510.

Augustinský, P. and Kuneš, J. (2013). Improved Green's function measurement for hybridization expansion quantum Monte Carlo. *Comput. Phys. Commun.*, 184(9):2119–2126.

Balents, L. (2000). Excitonic order at strong coupling: Pseudospin, doping, and ferromagnetism. *Phys. Rev. B*, 62:2346–2357.

Bányai, L. and el Sayed, K. (1994). Time reversal and many-body non-equilibrium green functions. *Annals of Physics*, 233(2):165–181.

Belonoshko, A. B., Lukinov, T., Fu, J., Zhao, J., Davis, S., and Simak, S. I. (2017). Stabilization of body-centred cubic iron under inner-core conditions. *Nature Geoscience*, 10(4):312–316.

Belozerov, A., Katanin, A., and Anisimov, V. (2018). Effect of density of states peculiarities on hund's metal behavior. *Physical Review B*, 97(11):115141.

Belozerov, A., Leonov, I., and Anisimov, V. (2013). Magnetism of iron and nickel from rotationally invariant hirsch-fye quantum monte carlo calculations. *Physical Review B*, 87(12):125138.

Boehnke, L., Hafermann, H., Ferrero, M., Lechermann, F., and Parcollet, O. (2011). Orthogonal polynomial representation of imaginary-time green's functions. *Phys. Rev. B*, 84:075145.

Boehnke, L. V. (2015). *Susceptibilities in materials with multiple strongly correlated orbitals*. PhD thesis, Universität Hamburg, Von-Melle-Park 3, 20146 Hamburg.

Bradlyn, B., Cano, J., Wang, Z., Vergniory, M., Felser, C., Cava, R. J., and Bernevig, B. A. (2016). Beyond dirac and weyl fermions: Unconventional quasiparticles in conventional crystals. *Science*, 353(6299).

Bradlyn, B., Elcoro, L., Cano, J., Vergniory, M., Wang, Z., Felser, C., Aroyo, M., and Bernevig, B. A. (2017). Topological quantum chemistry. *Nature*, 547(7663):298–305.

Bruus, H. and Flensberg, K. (2004). *Many-body quantum theory in condensed matter physics: an introduction*. Oxford university press.

Bryan, R. K. (1990). Maximum entropy analysis of oversampled data problems. *European Biophysics Journal*, 18(3):165–174.

Buckminster Fuller, R. (1969). Operating manual for spaceship earth. *New York: EP Dutton & Co., text available at http://www.bfi.org/node/422 (8 September 2009)*.

Burdin, S., Georges, A., and Grempel, D. (2000). Coherence scale of the kondo lattice. *Physical Review Letters*, 85(5):1048.

Christensen, L. (2019). *Robot Navigation in Distorted Magnetic Fields*. PhD thesis.

Coleman, P. (2015). *Introduction to many-body physics*. Cambridge University Press.

Di Sante, D., Hausoel, A., Barone, P., Tomczak, J. M., Sangiovanni, G., and Thomale, R. (2017). Realizing double dirac particles in the presence of electronic interactions. *Physical Review B*, 96(12):121106.

Drchal, V., Kudrnovskỳ, J., and Turek, I. (2013). Effective magnetic hamiltonians from first principles. In *EPJ Web of Conferences*, volume 40, page 11001. EDP Sciences.

Dziewonski, A. M. and Anderson, D. L. (1981). Preliminary reference earth model. *Physics of the earth and planetary interiors*, 25(4):297–356.

Dzyaloshinskii, I. (1996). Extended van-hove singularity and related non-fermi liquids. *Journal de Physique I*, 6(1):119–135.

Eberhardt, W. and Plummer, E. (1980). Angle-resolved photoemission determination of the band structure and multielectron excitations in ni. *Physical Review B*, 21(8):3245.

Elias, D., Gorbachev, R., Mayorov, A., Morozov, S., Zhukov, A., Blake, P., Ponomarenko, L., Grigorieva, I., Novoselov, K., Guinea, F., et al. (2011). Dirac cones reshaped by interaction effects in suspended graphene. *Nature Physics*, 7(9):701–704.

Fu, L. and Kane, C. L. (2008). Superconducting proximity effect and majorana fermions at the surface of a topological insulator. *Physical review letters*, 100(9):096407.

Garcia-Munoz, J. L., Rodriguez-Carvajal, J., Sapina, F., Sanchis, M. J., Ibanez, R., and Beltran-Porter, D. (1990). Crystal and magnetic structures of bi 2 cuo 4. *Journal of Physics: Condensed Matter*, 2:2205.

Geffroy, D., Hariki, A., and Kuneš, J. (2018). Excitonic magnet in external field: Complex order parameter and spin currents. *Phys. Rev. B*, 97:155114.

Geffroy, D., Kaufmann, J., Hariki, A., Gunacker, P., Hausoel, A., and Kuneš, J. (2019). Collective modes in excitonic magnets: Dynamical mean-field study. *Physical review letters*, 122(12):127601.

Geggel, L. (1998). *Earth's Core Has Been Leaking for 2.5 Billion Years and Geologists Don't Know Why*. https://www.livescience.com/65968-earth-leaky-core.html (last accessed June 2020.).

Georges, A. and Kotliar, G. (1992). Hubbard model in infinite dimensions. *Phys. Rev. B*, 45:6479–6483.

Georges, A., Kotliar, G., Krauth, W., and Rozenberg, M. J. (1996). Dynamical mean-field theory of strongly correlated fermion systems and the limit of infinite dimensions. *Reviews of Modern Physics*, 68(1):13.

Ghanem, K. (2017). *Stochastic analytic continuation: A Bayesian approach*. PhD thesis, Universitätsbibliothek der RWTH Aachen.

Ghanem, K. and Koch, E. (2020). Average spectrum method for analytic continuation: Efficient blocked-mode sampling and dependence on the discretization grid. *Physical Review B*, 101(8):085111.

Gubernatis, J. E., Jarrell, M., Silver, R. N., and Sivia, D. S. (1991). Quantum monte carlo simulations and maximum entropy: Dynamics from imaginary-time data. *Phys. Rev. B*, 44:6011–6029.

Gull, E., Millis, A. J., Lichtenstein, A. I., Rubtsov, A. N., Troyer, M., and Werner, P. (2011). Continuous-time monte carlo methods for quantum impurity models. *Reviews of Modern Physics*, 83(2):349.

Gunacker, P., Wallerberger, M., Gull, E., Hausoel, A., Sangiovanni, G., and Held, K. (2015). Continuous-time quantum monte carlo using worm sampling. *Phys. Rev. B*, 92:155102.

Halperin, B. I. and Rice, T. M. (1968). *Solid State Physics*, volume 21, page 115. Academic Press, New York.

Han, Q., Dang, H. T., and Millis, A. (2016). Ferromagnetism and correlation strength in cubic barium ruthenate in comparison to strontium and calcium ruthenate: a dynamical mean-field study. *Physical Review B*, 93(15):155103.

Haule, K. (2007). Quantum Monte Carlo impurity solver for cluster dynamical mean-field theory and electronic structure calculations with adjustable cluster base. *Phys. Rev. B*, 75(15):155113.

Hausoel, A., Karolak, M., Şaşıoğlu, E., Lichtenstein, A., Held, K., Katanin, A., Toschi, A., and Sangiovanni, G. (2017). Local magnetic moments in iron and nickel at ambient and earth's core conditions. *Nature communications*, 8(1):1–9.

Hausoel, A., Wentzell, N., and Strand, H. (2019). w2dynamics_interface: 2.20.

Held, K. (2007). Electronic structure calculations using dynamical mean field theory. *Advances in physics*, 56(6):829–926.

Held, K., Peters, R., and Toschi, A. (2013). Poor man's understanding of kinks originating from strong electronic correlations. *Physical review letters*, 110(24):246402.

Held, K. and Vollhardt, D. (1998). Microscopic conditions favoring itinerant ferromagnetism: Hund's rule coupling and orbital degeneracy. *The European Physical Journal B-Condensed Matter and Complex Systems*, 5(3):473–478.

Himpsel, F., Knapp, J., and Eastman, D. (1979). Experimental energy-band dispersions and exchange splitting for ni. *Physical Review B*, 19(6):2919.

Hoshino, S. and Werner, P. (2016). Electronic orders in multiorbital Hubbard models with lifted orbital degeneracy. *Phys. Rev. B*, 93(15):155161.

Hubbard, J. (1963). Electron correlations in narrow energy bands. *Proceedings of the Royal Society of London. Series A. Mathematical and Physical Sciences*, 276(1365):238–257.

Hüfner, S. and Wertheim, G. (1974). X-ray photoemission studies of the 3d metals from mn to cu. *Physics Letters A*, 47(5):349–350.

Hüfner, S. and Wertheim, G. (1975). Multielectron effects in the xps spectra of nickel. *Physics Letters A*, 51(5):299–300.

Jarrell, M. and Gubernatis, J. (1996). Bayesian inference and the analytic continuation of imaginary-time quantum monte carlo data. *Physics Reports*, 269(3):133 – 195.

Jeon, S., Zhou, B. B., Gyenis, A., Feldman, B. E., Kimchi, I., Potter, A. C., Gibson, Q. D., Cava, R. J., Vishwanath, A., and Yazdani, A. (2014). Landau quantization and quasiparticle interference in the three-dimensional dirac semimetal cd 3 as 2. *Nature materials*, 13(9):851–856.

Kaneko, T. and Ohta, Y. (2014). Roles of hund's rule coupling in excitonic density-wave states. *Phys. Rev. B*, 90:245144.

Kaneko, T., Zenker, B., Fehske, H., and Ohta, Y. (2015). Competition between excitonic charge and spin density waves: Influence of electron-phonon and hund's rule couplings. *Phys. Rev. B*, 92:115106.

Khaliullin, G. (2013). Excitonic magnetism in van vleck–type d^4 mott insulators. *Phys. Rev. Lett.*, 111:197201.

Kim, J., Daghofer, M., Said, A. H., Gog, T., van den Brink, J., Khaliullin, G., and Kim, B. J. (2014). Excitonic quasiparticles in a spin-orbit mott insulator. *Nature Communications*, 5:4452.

Klier, J., Gornyi, I. V., and Mirlin, A. D. (2015). Transversal magnetoresistance in weyl semimetals. *Phys. Rev. B*, 92:205113.

Koch, E. (2019). Exact diagonalization and lanczos method. In *Many-Body Methods for Real Materials, Modeling and Simulation Vol. 9*, chapter 7. Forschungszentrum Jülich.

Kogar, A., Rak, M. S., Vig, S., Husain, A. A., Flicker, F., Joe, Y. I., Venema, L., MacDougall, G. J., Chiang, T. C., Fradkin, E., van Wezel, J., and Abbamonte, P. (2017). Signatures of exciton condensation in a transition metal dichalcogenide. *Science*, 358(6368):1314–1317.

Kondo, J. (1964). Resistance minimum in dilute magnetic alloys. *Progress of theoretical physics*, 32(1):37–49.

Kotliar, G., Savrasov, S. Y., Haule, K., Oudovenko, V. S., Parcollet, O., and Marianetti, C. (2006). Electronic structure calculations with dynamical mean-field theory. *Reviews of Modern Physics*, 78(3):865.

Kowalski, A., Hausoel, A., Wallerberger, M., Gunacker, P., and Sangiovanni, G. (2019). State and superstate sampling in hybridization-expansion continuous-time quantum monte carlo. *Phys. Rev. B*, 99:155112.

Kraberger, G. J., Triebl, R., Zingl, M., and Aichhorn, M. (2017). Maximum entropy formalism for the analytic continuation of matrix-valued green's functions. *Phys. Rev. B*, 96:155128.

Kudrnovskỳ, J., Drchal, V., Turek, I., Khmelevskyi, S., Glasbrenner, J. K., and Belashchenko, K. D. (2012). Spin-disorder resistivity of ferromagnetic metals from first principles: The disordered-local-moment approach. *Physical Review B*, 86(14):144423.

Kuneš, J. (2014). Phase diagram of exciton condensate in doped two-band hubbard model. *Phys. Rev. B*, 90:235140.

Kuneš, J. and Augustinský, P. (2014). Excitonic condensation of strongly correlated electrons: The case of $pr_{0.5}ca_{0.5}coo_3$. *Phys. Rev. B*, 90:235112.

Kuneš, J. (2015). Excitonic condensation in systems of strongly correlated electrons. *J. Phys. Condens. Matter*, 27(33):333201.

Kunes, J. (2019). supp stuff. Supplemental Material.

Kuneš, J. and Augustinský, P. (2014). Excitonic instability at the spin-state transition in the two-band Hubbard model. *Phys. Rev. B*, 89(11):115134.

Kuneš, J. and Geffroy, D. (2016). Spontaneous Spin Textures in Multiorbital Mott Systems. *Phys. Rev. Lett.*, 116(25):256403.

Kuwayama, Y., Hirose, K., Sata, N., and Ohishi, Y. (2008). Phase relations of iron and iron–nickel alloys up to 300 gpa: Implications for composition and structure of the earth's inner core. *Earth and Planetary Science Letters*, 273(3-4):379–385.

Läuchli, A. M. and Werner, P. (2009). Krylov implementation of the hybridization expansion impurity solver and application to 5-orbital models. *Physical Review B*, 80(23):235117.

Laughlin, R. B. and Pines, D. (2000). From the cover: The theory of everything. *Proceedings of the national academy of sciences of the United States of America*, 97(1):28.

Leonov, I., Poteryaev, A., Anisimov, V., and Vollhardt, D. (2011). Electronic correlations at the α- γ structural phase transition in paramagnetic iron. *Physical review letters*, 106(10):106405.

Lichtenstein, A., Katsnelson, M., and Kotliar, G. (2001). Finite-temperature magnetism of transition metals: An ab initio dynamical mean-field theory. *Physical Review Letters*, 87(6):067205.

Lieb, E. H. and Wu, F.-Y. (1994). Absence of mott transition in an exact solution of the short-range, one-band model in one dimension. In *Exactly Solvable Models Of Strongly Correlated Electrons*, pages 9–12. World Scientific.

Liechtenstein, A. I., Katsnelson, M., Antropov, V., and Gubanov, V. (1987). Local spin density functional approach to the theory of exchange interactions in ferromagnetic metals and alloys. *Journal of Magnetism and Magnetic Materials*, 67(1):65–74.

Luttinger, J. M. (1961). Analytic properties of single-particle propagators for many-fermion systems. *Phys. Rev.*, 121:942–949.

Mårtensson, N., Nyholm, R., and Johansson, B. (1984). Four-hole satellites in the l 3 vv auger and the valence-band spectra from nickel. *Physical Review B*, 30(4):2245.

McMahan, A. and Albers, R. (1982). Insulating nickel at a pressure of 34 tpa. *Physical Review Letters*, 49(16):1198.

Merchant, P., Normand, B., Krämer, K. W., Boehm, M., McMorrow, D. F., and Rüegg, C. (2014). Quantum and classical criticality in a dimerized quantum antiferromagnet. *Nature Physics*, 10:373.

Metzner, W. and Vollhardt, D. (1989). Correlated lattice fermions in d=∞ dimensions. *Physical review letters*, 62(3):324.

Mielke, A. and Tasaki, H. (1993). Ferromagnetism in the hubbard model. *Communications in mathematical physics*, 158(2):341–371.

Mishchenko, A. S. (2012). 14 stochastic optimization method for analytic continuation. *Correlated Electrons: From Models to Materials*.

Mohammed, Y. S., Yan, Y., Wang, H., Li, K., and Du, X. (2010). Stability of ferromagnetism in fe, co, and ni metals under high pressure with gga and gga+ u. *Journal of magnetism and magnetic materials*, 322(6):653–657.

Mott, N. (1961). The transition to the metallic state. *Philosophical Magazine*, 6(62):287–309.

Moyoshi, T., Kamazawa, K., Matsuda, M., and Sato, M. (2018). Inelastic neutron scattering study on the electronic transition in $(\mathrm{pr}_{1-y}\mathrm{y}_y)_{1-x}\mathrm{ca}_x\mathrm{coo}_3$ single crystals. *Phys. Rev. B*, 98:205105.

Nakajima, N., Hatta, S., Odagiri, J., Kato, H., and Sakisaka, Y. (2004). Valence-band satellites in ni: A photoelectron spectroscopic study. *Physical Review B*, 70(23):233103.

Nasu, J., Watanabe, T., Naka, M., and Ishihara, S. (2016). Phase diagram and collective excitations in an excitonic insulator from an orbital physics viewpoint. *Phys. Rev. B*, 93:205136.

National Geographic (1998). *Earth's interior*. https://https://www.nationalgeographic.com/science/earth/surface-of-the-earth/earths-interior (last accessed June 2020.).

Neto, A. C., Guinea, F., Peres, N. M., Novoselov, K. S., and Geim, A. K. (2009). The electronic properties of graphene. *Reviews of modern physics*, 81(1):109.

Nevidomskyy, A. H. and Coleman, P. (2009). Kondo resonance narrowing in d-and f-electron systems. *Physical review letters*, 103(14):147205.

Nolting, W. (2007). *Grundkurs Theoretische Physik 6: Statistische Physik*, volume 6. Springer.

Nozieres, P. and Blandin, A. (1980). Kondo effect in real metals. *Journal de Physique*, 41(3):193–211.

Okane, T., Kashiwakura, T., Suzuki, S., Sato, S., Kinoshita, T., Kakizaki, A., and Ishii, T. (1993). Angle-resolved resonant photoemission of ni (100) and ni (110) single crystals. *Zeitschrift für Physik B Condensed Matter*, 91(4):437–443.

Olson, P. (2013). The new core paradox. *Science*, 342(6157):431–432.

Otsuki, J., Ohzeki, M., Shinaoka, H., and Yoshimi, K. (2017). Sparse modeling approach to analytical continuation of imaginary-time quantum monte carlo data. *Phys. Rev. E*, 95:061302.

O'Rourke, J. G. and Stevenson, D. J. (2016). Powering earth's dynamo with magnesium precipitation from the core. *Nature*, 529(7586):387–389.

Parcollet, O., Ferrero, M., Ayral, T., Hafermann, H., Krivenko, I., Messio, L., and Seth, P. (2015). Triqs: A toolbox for research on interacting quantum systems. *Computer Physics Communications*, 196:398 – 415.

Parragh, N., Toschi, A., Held, K., and Sangiovanni, G. (2012a). Conserved quantities of s u (2)-invariant interactions for correlated fermions and the advantages for quantum monte carlo simulations. *Physical Review B*, 86(15):155158.

Parragh, N., Toschi, A., Held, K., and Sangiovanni, G. (2012b). Conserved quantities of SU(2)-invariant interactions for correlated fermions and the advantages for quantum Monte Carlo simulations. *Phys. Rev. B*, 86(15):155158.

Pekker, D. and Varma, C. (2015). Amplitude/higgs modes in condensed matter physics. *Annual Review of Condensed Matter Physics*, 6(1):269–297.

Pessa, M., Heimann, P., and Neddermeyer, H. (1976). Photoemission and electronic structure of iron. *Physical Review B*, 14(8):3488.

Philip Warren Anderson (1961). Localized magnetic states in metals. *Physical Review*, 124(1):41.

Po, H. C., Watanabe, H., Zaletel, M. P., and Vishwanath, A. (2016). Filling-enforced quantum band insulators in spin-orbit coupled crystals. *Science Advances*, 2(4):e1501782.

Poteryaev, A. I., Skornyakov, S. L., Belozerov, A. S., and Anisimov, V. I. (2015). Specific heat of a binary alloy within the cpa+ dmft method. *Physical Review B*, 91(19):195141.

Pourovskii, L., Miyake, T., Simak, S., Ruban, A. V., Dubrovinsky, L., and Abrikosov, I. (2013). Electronic properties and magnetism of iron at the earth's inner core conditions. *Physical Review B*, 87(11):115130.

Pourovskii, L., Mravlje, J., Georges, A., Simak, S., and Abrikosov, I. (2016). Fermi-liquid behavior and thermal conductivity of {\epsilon}-iron at earth's core conditions. *arXiv preprint arXiv:1603.02287*.

Pozzo, M., Davies, C., Gubbins, D., and Alfe, D. (2012). Thermal and electrical conductivity of iron at earth's core conditions. *Nature*, 485(7398):355–358.

Prokopjev, Y. I. and Reser, B. (1991). A single-site spin correlation function in paramagnetic iron. *Journal of Physics: Condensed Matter*, 3(32):6055.

Read, N. and Green, D. (2000). Paired states of fermions in two dimensions with breaking of parity and time-reversal symmetries and the fractional quantum hall effect. *Physical Review B*, 61(15):10267.

Rohringer, G. (2013). *New routes towards a theoretical treatment of nonlocal electronic correlations*.

Rohringer, G., Toschi, A., Katanin, A., and Held, K. (2011). Critical properties of the half-filled hubbard model in three dimensions. *Physical review letters*, 107(25):256402.

Ruban, A. V., Khmelevskyi, S., Mohn, P., and Johansson, B. (2007). Temperature-induced longitudinal spin fluctuations in fe and ni. *Physical Review B*, 75(5):054402.

Sakurai, J. J. and Commins, E. D. (1995). Modern quantum mechanics, revised edition.

Sánchez-Barriga, J., Fink, J., Boni, V., Di Marco, I., Braun, J., Minár, J., Varykhalov, A., Rader, O., Bellini, V., Manghi, F., et al. (2009). Strength of correlation effects in the electronic structure of iron. *Physical review letters*, 103(26):267203.

Sandvik, A. W. (1998). Stochastic method for analytic continuation of quantum monte carlo data. *Phys. Rev. B*, 57:10287–10290.

Schäfer, J., Hoinkis, M., Rotenberg, E., Blaha, P., and Claessen, R. (2005). Fermi surface and electron correlation effects of ferromagnetic iron. *Physical Review B*, 72(15):155115.

Schickling, T., Bünemann, J., Gebhard, F., and Boeri, L. (2016). Quasiparticle bands and structural phase transition of iron from gutzwiller density-functional theory. *Physical Review B*, 93(20):205151.

Schulz, A., Courths, R., Schulz, H., and Hufner, S. (1979). Ups investigation of fe single crystals. *Journal of Physics F: Metal Physics*, 9(2):L41.

Sémon, P., Yee, C.-H., Haule, K., and Tremblay, A.-M. (2014). Lazy skip-lists: An algorithm for fast hybridization-expansion quantum monte carlo. *Physical Review B*, 90(7):075149.

Sémon, P., Yee, C.-H., Haule, K., and Tremblay, A.-M. S. (2014). Lazy skip-lists: An algorithm for fast hybridization-expansion quantum monte carlo. *Phys. Rev. B*, 90:075149.

Shinaoka, H., Dolfi, M., Troyer, M., and Werner, P. (2014). Hybridization expansion monte carlo simulation of multi-orbital quantum impurity problems: matrix product formalism and improved sampling. *Journal of Statistical Mechanics: Theory and Experiment*, 2014(6):P06012.

Shinaoka, H., Nomura, Y., Biermann, S., Troyer, M., and Werner, P. (2015). Negative sign problem in continuous-time quantum monte carlo: Optimal choice of single-particle basis for impurity problems. *Physical Review B*, 92(19):195126.

Sommer, T., Vojta, M., and Becker, K. (2001). Magnetic properties and spin waves of bilayer magnets in a uniform field. *Eur. Phys. J. B*, 23(3):329–339.

Sponza, L., Pisanti, P., Vishina, A., Pashov, D., Weber, C., Van Schilfgaarde, M., Acharya, S., Vidal, J., and Kotliar, G. (2017). Self-energies in itinerant magnets: a focus on fe and ni. *Physical Review B*, 95(4):041112.

Sucksmith, W. and Pearce, R. (1938). The paramagnetism of the ferromagnetic elements. *Proceedings of the Royal Society of London. Series A. Mathematical and Physical Sciences*, 167(929):189–204.

Tanaka, A., Jo, T., and A. Sawatzky, G. (1992). Configuration interaction in ni metal and ni alloys and high-energy spectroscopy. *Journal of the Physical Society of Japan*, 61(8):2636–2639.

Tikhonov, A. N. (1943). On the stability of inverse problems. In *Dokl. Akad. Nauk SSSR*, volume 39, pages 195–198.

Torchio, R., Mathon, O., and Pascarelli, S. (2014). Xas and xmcd spectroscopies to study matter at high pressure: probing the correlation between structure and magnetism in the 3d metals. *Coordination Chemistry Reviews*, 277:80–94.

Toschi, A., Arita, R., Hansmann, P., Sangiovanni, G., and Held, K. (2012). Quantum dynamical screening of the local magnetic moment in fe-based superconductors. *Physical Review B*, 86(6):064411.

Troyer, M. and Wiese, U.-J. (2005). Computational complexity and fundamental limitations to fermionic quantum monte carlo simulations. *Physical review letters*, 94(17):170201.

Tsubouchi, S., Kyômen, T., Itoh, M., Ganguly, P., Oguni, M., Shimojo, Y., Morii, Y., and Ishii, Y. (2002). Simultaneous metal-insulator and spin-state transitions in $pr_{0.5}ca_{0.5}coo_3$. *Phys. Rev. B*, 66:052418.

Ulmke, M. (1998). Ferromagnetism in the hubbard model on fcc-type lattices. *The European Physical Journal B-Condensed Matter and Complex Systems*, 1(3):301–304.

Valli, A., Bahlke, M. P., Kowalski, A., Karolak, M., Herrmann, C., and Sangiovanni, G. (2020). Kondo screening in co adatoms with full coulomb interaction. *arXiv preprint arXiv:2004.06677*.

Vekilova, O. Y., Pourovskii, L., Abrikosov, I., and Simak, S. (2015). Electronic correlations in fe at earth's inner core conditions: Effects of alloying with ni. *Physical Review B*, 91(24):245116.

Vočadlo, L., Alfè, D., Gillan, M., Wood, I., Brodholt, J., and Price, G. D. (2003). Possible thermal and chemical stabilization of body-centred-cubic iron in the earth's core. *Nature*, 424(6948):536–539.

Vonsovskii, S., Katsnel'son, M., and Trefilov, A. (1993). Localized and itinerant behavior of electrons in metals. *Physics of Metals and Metallography(Russia)(USA)*, 76(3):247–299.

Wahle, J., Blümer, N., Schlipf, J., Held, K., and Vollhardt, D. (1998). Microscopic conditions favoring itinerant ferromagnetism. *Physical review B*, 58(19):12749.

Wallerberger, M. (2016). *w2dynamics: continuous time quantum Monte Carlo calculations of one-and two-particle propagators*. PhD thesis, PhD thesis.

Wallerberger, M., Hausoel, A., Gunacker, P., Kowalski, A., Parragh, N., Goth, F., Held, K., and Sangiovanni, G. (2019). w2dynamics: Local one- and two-particle quantities from dynamical mean field theory. *Computer Physics Communications*, 235:388 – 399.

Wan, X., Turner, A. M., Vishwanath, A., and Savrasov, S. Y. (2011). Topological semimetal and fermi-arc surface states in the electronic structure of pyrochlore iridates. *Physical Review B*, 83(20):205101.

Wang, R.-P., Hariki, A., Sotnikov, A., Frati, F., Okamoto, J., Huang, H.-Y., Singh, A., Huang, D.-J., Tomiyasu, K., Du, C.-H., Kuneš, J., and de Groot, F. M. F. (2018). Excitonic dispersion of the intermediate spin state in $lacoo_3$ revealed by resonant inelastic x-ray scattering. *Phys. Rev. B*, 98:035149.

Wang, X., Millis, A. J., et al. (2011). High-frequency asymptotic behavior of self-energies in quantum impurity models. *Physical Review B*, 84(7):073104.

Watanabe, H. and Murayama, H. (2012). Unified description of nambu-goldstone bosons without lorentz invariance. *Phys. Rev. Lett.*, 108:251602.

Werner, P., Comanac, A., de' Medici, L., Troyer, M., and Millis, A. J. (2006). Continuous-Time Solver for Quantum Impurity Models. *Physical Review Letters*, 97(7):076405.

Werner, P. and Millis, A. J. (2007). High-spin to low-spin and orbital polarization transitions in multiorbital mott systems. *Phys. Rev. Lett.*, 99:126405.

Wieder, B. J., Kim, Y., Rappe, A., and Kane, C. (2016). Double dirac semimetals in three dimensions. *Physical review letters*, 116(18):186402.

Wilson, K. G. (1975). The renormalization group: Critical phenomena and the kondo problem. *Reviews of modern physics*, 47(4):773.

Wohlfarth, E. P. (1986). *Handbook of magnetic materials*, volume 2. Elsevier.

Yamaguchi, T., Sugimoto, K., and Ohta, Y. (2017). Low-Energy Excitation Spectra in the Excitonic Phase of Cobalt Oxides. *J. Phys. Soc. Japan*, 86(4):043701.

Zhang, F., Manoun, B., Saxena, S., and Zha, C. (2006). Structural behavior of sr2bi2o5 at high pressures. *Journal of Solid State Chemistry*, 179(2):544–550.

Acknowledgements

Even though a monograph, it is not possible to accomplish a thesis on one's own. At this place, I want to thank all people, who helped me make this work possible, in one or another way.

First of all I thank my supervisor **Prof. Dr. Giorgio Sangiovanni** for accepting me as his PhD student. The way he lectures and talks about physics motivated me to look into many-body quantum physics in the first place, and his lively group and collaborators, as well as the challenging topics made me devote many years to that research. He very early gave me the opportunity to give lectures and organize excercise groups, as well as to travel to countless international conferences. He accepted my tendencies to work independently, learn in autodidactic ways and solve problems stand-alone; I wonder where this will lead me. I will never forget the invitations to Campello and twice to Rome. Grazie di tutto, professore!

Not less I thank my inofficial co-supervisor **Prof. Dr. Alessandro Toschi** for the many invitations to Vienna, for endless explainations (initiated by a single question) and debates also about non-physical topics. He tought me how to find proper Italian food in a town and reminds to follow the rules of Italian food and drink culture. I also will never forget our research stay for 2.5 months in New York City, or your tours off the tourist paths in Rome: the Jewish district, the catacombs of the vatican, the churches and many more! Grazie mille, professore!

I also acknowledge the nice and inviting atmosphere in the AG Sangiovanni in Würzburg. To **Michael Karolak** for the collaboration on the massive nickel/iron project, recurring debates about the unsolved riddles surrounding us, and all the stories from legendary Soviet theoretical physics he passed on from his supervisors. To **Alexander Kowalski** for implementing my ideas about superstate-sampling at the beginning of his master studies. I thank **Domenico di Sante** for the fantastic conference in his home region of Abruzzo, for the shared lecture "Computational Materials Science" in the winter term 2016/17, and many Hamiltonians he prepared for me. As we all know, Hamiltonians are very important! Furthermore I thank **Niklas Wagner** for continuing with the unconventional fermions, **Philipp Eck** for explaining Brillouin zones and single-particle physics to me (messing around with many-particle stuff one easily looses control over the single-particles...), and **Severino Adler** for joining in with my cumbersome spin-orbit calculations, as well as his ability to motivate others.

I also thank **Florian Goth** for the administration of the computer machines and discussions about technical and algorithmical questions. **Manuel Weber**, **Johannes Hofmann** and **Stefan Beyl** for discussing Monte Carlo techniques more broadly, and **Marcin Raczkowski** for co-orgainizing the "Young scientist's meeting" with me.

I had the continuous opportunity to visit Vienna and work at its technical university. There I especially thank **Markus Wallerberger** for his explainations about the (pythonesque) interor of w2dynamics, about computational physics in general and also touching deep and general philosophical questions. I will never forget our evening-discussions in dark Viennese restaurants with beer and wine. **Thomas Schäfer** always picked the perfect wine for every occasion and transfered some of his wine-enthusiasm to me. Thanks **Georg Rohringer** for making me visit Moscow and

showing me this fascinating metropolis. I thank **Patrik Gunacker** for explaining his worms to me in every detail, and last but not least, my New York City roommate **Patrick Chalupa** for the great time in the US.

I thank **Prof. Dr. Oppermann**, for whom I had the honor to teach several excercise groups, for inspiring me by his way of doing and thinking about theoretical physics. I thank the **University of Würzburg** for not allowing cumulative dissertations. Some time ago the terms insanity, loss of control and despair were only abstract for me, but during the writing of the thesis, they were filled with life more than I ever could have imagined!

Da das Leben nicht nur aus Physik und Wissenschaft besteht, möchte ich an dieser Stelle auch weiterführende Danksagungen verewigen.

Ich muss auch meinen früheren Mathematik- und Physiklehrern **Bruno Handwerker** ("Für die Wissenschaft!") und **Hans-Werner Neumann** ("Klar kann man radioaktiven Staub mit einem trockenen Tuch wegwischen!") danken, die mich vor langer Zeit für ihre Fächer eine Art von Begeisterung entfachen konnten, die bis heute anhält und von der ich noch immer zehre. Sie wussten, Motivation entstammt der *Meta*physik. **Professor Dr. Lembeck** ist die zentrale Figur, welche mich vor langer Zeit für Philosophie, Wissenschaftstheorie und Sprache begeistern konnte!

Ich danke **Simon**, **Moritz**, **Kevin** und **Sebastian** für endlos viele durchfeierte Nächte, und speziell **Simon** für die Einladungen zum Vorglühen.

Ich danke der *Crew* des Spieleabends: **Heiko** ("Das ist ein Witz!"), **Björn**, unseren Dichter **Jo**, meinen Namensvetter **Andy**, **Christian** ("Wir müssen die Sitzreiehenfolge auswürfeln!"), **Anne**, **Gerald**, **Sebastian** (auch für die Einführung in die Sterne-Küche!), **Martin**, **Stefan** (ebenfalls für die Woche in London!), **Andy** und **Ines**. Die Abende waren immer Fixpunkte im Kalender, auf die ich mich schon im Voraus freute!

Außerdem danke ich **Armin** dafür, mich in die Studentenverbindung Cheruskia eingeführt zu haben und **Dirk** für lange philosophisch-existenzielle Diskussionen nachts am Main und die vielen Buchtipps! Weiterhin danke ich allen Mitgliedern des Kanu-Club Würzburg für die vielen Stunden auf dem Wasser, auch wenn ich in letzter Zeit nicht schaffte oft zu kommen, sowie **Anti**, **Michi**, **Marc** und **Anne**, den ehemaligen Leitern der Jugendgruppe DéjàWü, welche ebenfalls einen Fixpunkt in frühen Studentenjahren darstellte. Zum Schluss kommt noch der harte Kern der ewigen Würzburger Studenten, **Benedikt** und **Holger**, sowie **Jürgen** und **Stefan**; ich hoffe sehr, dass es uns gelingt, die Kaffee-Gruppe in eine Wander-Gruppe umzuwandeln.

Mein höchster Dank gilt allerdings meiner Familie, insbesondere meinen Eltern **Elisabeth** und **Karl**, für ihre uneingeschränkte Unterstützung während meines Studiums und auch immer und überall sonst!